Glacier erosion at convergent margins: a numerical and field study in the Chugach-St. Elias Mountains of South Alaska

Yann Merrand

A dissertation

submitted in partial fulfillment of the

requirements for the degree of

Doctor of Philosophy

University of Washington

2013

Reading Committee:

Bernard Hallet, Chair

David Montgomery

Edwin Waddington

Program Authorized to Offer Degree:

Earth and Space Sciences

University of Washington

Abstract

Glacier erosion at convergent margins: a numerical and field study in the Chugach-St. Elias Mountains of South Alaska

Yann Merrand

Chair of the Supervisory Committee:
Professor Bernard Hallet
Earth and Space Sciences

The Saint Elias range of South Alaska is known for its rapid erosion and uplift (order of 1 cm/yr), extreme relief at Mt. St. Elias reaching ~5800 m within 15 km of Pacific waters, and long history of tidewater glaciation extending to the Pliocene. The region is a natural laboratory to examine the coupling between tectonics, climate and topography, and the evolution of mountain ranges under the influence of glacial ice. To better understand the spatial and temporal distribution of glacial erosion and the parameters that control the landscapes they generate, I have built a physically based 2-dimensional model of glacial erosion forced by climate on glacial cycle time scale and applied it to the Seward-Malaspina glacier system. This numerical model should also prove useful in interpreting the growing thermochronological record of exhumation within the range, the sedimentary record in the Northeast Pacific and the climatic signature contained in the spatial and temporal distribution of sediment depocenters.

The model integrates the seasonal evolution of glacial mass balance and basal hydrology, as well as accounts for ice dynamics, thermal regime, bedrock erosion by glacier quarrying and abrasion, sediment transfer, and tidewater processes. Field measurements of basin-wide erosion rates, glacier mass balance, ice velocity and glacier

geometry conducted during the course of this study and as well as glaciological data available in the scientific literature are used to constrain model parameters. In addition, seismic profiling of Vitus Lake in front of the massive Bering-Bagley glacier system allowed computing a basin wide erosion rate of almost 6mm/yr averaged over 30 years of sediment accumulation for arguably the largest temperate glacier in the world. Model results indicate that ice flux per unit glacier width and sliding velocity, controlled by mass balance and valley width, exert an important influence over the distribution of glacier erosion. Yet, basal effective pressure as dictated by subglacial hydraulics and sediments protecting the substrate often overcome all other parameters in dictating erosional patterns, thereby suggesting that accounting for the degree of decoupling between ice and the bed and the presence of sediment is necessary to capture the essence of the distribution of glacial erosion in numerical models. Integration of these factors over glacial cycles allows establishing the spatial distribution of erosion for Seward-Malaspina Glacier that is consistent with long-term denudation revealed by the thermochronological data available for the region.

Acknowledgements

I dedicate this dissertation to Austin Post who left us last Fall. Austin was a giant whose history, knowledge and boundless enthusiasm were only matched by his humanity.

I would like to thank my committee chair, Professor Bernard Hallet whose inspiration, guidance and NSF grants EAR-9628675 and 1009812 made this work feasible. In addition, the other members of my reading committee, Professor David Montgomery and Professor Edwin Waddington gave important advice to make this manuscript more incisive and readable. Jay Fleisher, Dennis Trabant, Bruce Molnia, Howard Conway, and Austin Post, in particular, generously shared data and equipment that allowed this endeavor to be more successful. Michele Koppes, Lew Hunter, Ian Willis, David Morse, Toni Gades, and many other students and faculty helped to collect data. Harvey Greenberg assisted with GIS modeling and supported Gretchen Moore who processed the acoustic survey data. Paul Jacobson made important suggestions toward glacier modeling. Wendell Tangborn and Al Rasmussen offered challenging and stimulating ideas. Many more faculty, students and staff in the Earth and Space Science department at UW supported my efforts in numerous ways. Michael Herder provided expert boat handling and a sense of adventure that made many outings a success. Dick Sylvester graciously taught me acoustic survey methods. The staffs and logistical capabilities of the USGS, BLM and St. Elias National Park greatly facilitated access to remote and pristine public land.

Finally, I would like to thank my family without whose support and enduring patience I wouldn't be writing these words today.

Table of content

List of figures

11

List of Tables

Chapter 1   Introduction and regional setting

1.1   Introduction

Today's relatively warm interglacial climate is not representative of mean Quaternary climate because for most of the Quaternary temperatures were lower and glaciers more extensive (Porter, 1989). The dissected coasts of mid to high latitudes and most incised orogens are the expression of this greater mean Quaternary level of glacierization. These dramatic landscapes, which often exhibit great relief, underscore the importance of glaciers in shaping the earth surface in these regions and in contributing to the sediment fluxes that control geochemical cycles. In part inspired by Molnar and England's (1990) puzzle about whether climate change is the cause or the result of accelerated uplift of mountain ranges in the Quaternary, researchers began investigating with renewed interest how landscape results from the interaction between regional tectonics and climate. Understanding topography as the product of climatic, surface and geologic processes over time has, however, been a goal of geomorphologists since Davis' paper on geographical cycles (1899). Early workers showed that climate and uplift combined to create landforms but they did not consider possible feedback between forcing mechanisms.

Critical wedge theory first suggested a system in which surface processes could influence tectonics. Both theory and laboratory sand-box experiments show that under time invariant conditions at system boundaries, accretionary wedges thicken and build topographic slope to attain critical taper; body forces are then balanced by internal material strength and traction on the basal boundary. Critically tapered wedges are at

failure everywhere and slide stably on weak decollements; they grow in a self-similar fashion to accommodate on-going accretion and retain a critical taper (Chapple, 1978; Davis et al., 1983; Dalhen et al., 1984; Dalhen, 1990). Perturbation of boundary conditions at the interface between the crust and the atmosphere, by removal or deposition of overburden, alters the pressure-dependent yield strength of crustal material thereby influencing crustal deformation. This feedback suggests that increasing the ratio of material export to import would change gravitational stresses and impact the spatial pattern of uplift. For the last two decades, landscape evolution modelers have implemented schemes of erosion and sediment transfer to probe the strength of coupling between climate, tectonics, and topography (Dalhen and Suppe, 1988; Koons, 1989; Summerfield, 1991; Beaumont et al., 1992; Anderson, 1994; Gilchrist et al., 1994; Kooi and Beaumont, 1994; Masek et al., 1994;Tucker and Slingerland, 1994). However, only a few workers (Tomkin and Braun, 2002; Tomkin and Roe, 2007; Herman and Braun, 2008) have thus far modeled these couplings in glacial environments despite the often-discussed connections between relief generation, glaciations, distribution of detrital deposits, continental weathering, and ocean and atmospheric chemistry (Raymo and Ruddiman, 1988).

Competing processes can lead to steady-state dynamics by dampening system response to forcing, thereby driving self-regulation, which is expressed in the balance of system attributes. For example, erosional flux out equals tectonic influx in orogens that have reached steady state (Willett and Brandon, 2002). The steady state is a useful idealization to analyze controls on competing processes of downwasting and uplift because it assumes that the accretionary wedge has reached a stable configuration and

that system dynamics arise from the coupling between atmospheric and tectonic forcing. Quasi-steady-state accretionary wedge deformation is quite likely in the Chugach-St. Elias range, given, a) high rates of uplift at the Alaska Syntaxis that are likely sustained for millions of years due to relatively constant plate convergence over long time scales ($10^6 - 10^7$ yr; Plafker, 1994) and evidence of sustained and rapid glacial incision fueled by heavy precipitation and cool climate for ~5 millions years (Lagoe et al., 1993; Hallet et al., 1996; Sheaf et al., 2003); b) a mountain belt morphology characterized by modest dimension in the direction of convergence since the windward side of range width parallel to the direction of convergence is less than 50 km, thereby suggesting when considered jointly with the high rates of convergence and erosion that climate-driven exhumation controls the distribution of thickening in the range; and c) extreme relief. Mean landscape form becomes time invariant once an equilibrium between climatically modulated erosion and tectonically sustained topography has evolved; however, advection of topography toward the accretionary backstop through shortening implies that true topographic steady state isn't likely except for major features while secondary landforms may not attain steady state (Willett and Brandon, 2002). Negative and positive feedback responses arise from the interaction between climate, tectonics and topography that results from linkages between precipitation, erosion and crustal deformation (Ahnert, 1970; Saltzman and Verbisky, 1992; Beaumont et al., 1991; Montgomery and Brandon, 2002). For over a century, researchers have noted that topography controls erosion rates (Gilbert, 1877). The functional relationship between erosion rate and elevation through topographic slope and precipitation is the source of feedback on the elevation of fluvial landscapes; although erosion increases with local slope, the distribution of precipitation

18

with elevation can either decrease or increase depending on climatic regime. In turn, perturbation of gravitational stresses controlling the distribution of crustal deformation through erosion and deposition provides a feedback, which is opposite to that arising due to the linkage between relief and erosion. Similarly to non-glacial landscapes, the couplings between climatically controlled erosion and crustal thickening take on significance in tectonically convergent temperate glacial regions: a negative feedback on the lowering of topography arises in regions where rock uplift does not compensate for intense glacial erosion. In such uplift-deficient systems the land surface subsides with time leading to an increasingly deficient glacial mass balance and vanishing glacier extent once the surface has descended significantly below the snow line, which in turn slows erosion. The opposite is true when a positive feedback enhances erosion wherever it does not keep up with the uplift. The topography of tectonically active glacial regions thus results from uplift and climatically induced self-regulation of erosive regime. Uplift creates topography, which captures precipitation and affects local climate (Brozovic et al., 1997; Anders et al., 2006) that itself also controls the spatial distribution of uplift (Beaumont et al., 1992; Willett et al., 1993). The tendency toward topographic steady state due to climate-uplift interactions raises the possibility of inferring spatial patterns of uplift from patterns of glacial erosion. Once a steady-state relief has been attained and a dynamic equilibrium controls landforms "in which every slope and every form is adjusted to every other" (Hack, 1960), glaciers set the lowering rate of the landscape through valley incision and consequent oversteepening of threshold interfluves. The general hypsometry of a glaciated mountain range at convergent margins is likely to reflect the regional balance of tectonic forcing and glacial erosion fueled by climate (fig. 1.1). In

addition, overdeepenings and fjords, and morphometric indices such as basin slope

distribution and relief are also closely related to the elements of climate that determine

the state and erosive regime of glaciers. Perhaps fueled by a pronounced interest in the

alpine environment, there already exist numerous observations about glacial landforms

and their relevance as climatic indexes. For example, moraine distributions and

morphology have long been recorded to infer glacial chronology and climatic history.

Researchers have also proposed that a "glacial buzz saw" exerts a first order control on

the elevation of mountain ranges (Porter, 1989; Brozovic et al., 1997; Mitchell and

Montgomery, 2006). In particular, cirque floor elevations have been shown
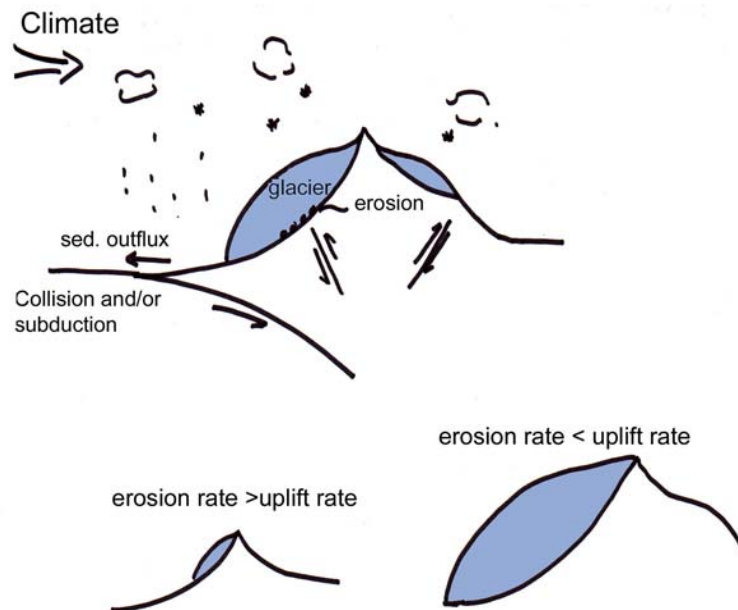
Figure 1.1: Regulation of erosive regime by glaciers in regions under tectonic compression results from the linkage between basin hypsometry and glacier mass balance. Lowered topography sustains smaller, less erosive glaciers and vice versa.

to reflect gradients in precipitation and topographic surfaces that are sub-parallel to

modern and past glacial equilibrium line altitudes (Flint, 1957; Peterson and Robinson,

1969; Porter, 1964 and 1977). More recently, workers have analyzed digital models of

topography (Brozovic et al., 1997; Whipple et al., 1999; Meigs and Sauber, 2000; Montgomery et al., 2001; Brocklehurst and Whipple, 2002 and 2004; Mitchell and Montgomery, 2006; Egholm et al., 2009; Anders et al., 2010; Sternai et al. 2010) and used thermochronometry (Meigs and Sauber, 2000; Spotila et al., 2004; Spotila and Berger, 2010) to further examine the correlation between ELA and mountain range elevation. Their findings suggest that glaciers dictate the elevation of the valley floors near the ELA, where they are particularly erosive, and that the higher relief is limited by the strength of rocks subject to landsliding and frost action, and the spacing between adjacent cirques and valleys. Other characteristics of glacial landscapes also reflect the combined effects of climatic and tectonic forcing; fjord morphology (depth and length), slope distributions, the location of overdeepenings and sills, stepped longitudinal profiles, the distribution of basin area with altitude, and relief are the collective expression of this forcing which is usually modulated by relative sea level in the glacial coastal environment.

In order to investigate the relative importance of climate dependent controls on the pattern and rates of erosion, and on the resulting topography, I constructed a numerical model of glacial erosion and applied it to the Seward-Malaspina Glacier system at the convergent margin between North America and the Pacific plate. The model comprises two main parts, one simulating a glacier and the other simulating erosion and sediment production and transport. The glacier part includes climate cycles and runoff generation, ice dynamics, sub-glacial thermal regime, subglacial hydrology, and calving in the tidewater environment. The second part of the model contains modules representing bedrock abrasion and quarrying coupled to glacier runoff, subaerial erosion

21

of interfluves, subglacial sediment mobilization, submarine sedimentation, and crustal response to denudation as glaciers advance and recede while denuding the landscape (fig. 1.2). An original objective of this model is to explicitly represent the dependence of the glacial quarying rate on subglacial hydrology through both stress partitioning on the bed and sediment mobilization. Existing models of glacial erosion simply assume bedrock erosion rates to be proportional to the ice sliding velocity or other simple basal characteristics, such as basal power (MacGregor et al., 2000; Tomkin and Braun, 2002; McGregor et al., 2009; Herman et al., 2011; Headley et al., 2012), and is supported by empirical research such as that at Variegated glacier (Humphrey and Raymond, 1994) and theoretical understanding of glacial abrasion (Hallet, 1979). This simple approach
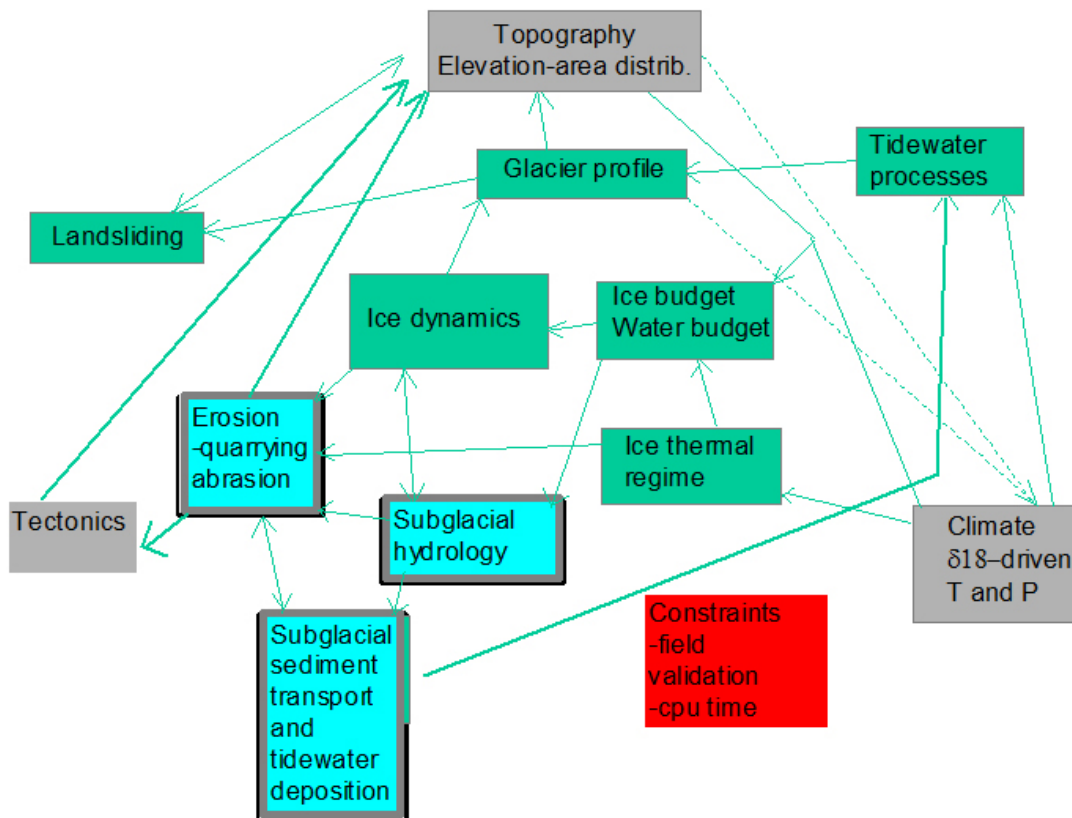
Figure 1.2: Flow chart for the glacier surface process model developed in Chapters 3 and 4.

does not, however, represent the dominant most erosive process at the glacial interface adequately. This process is most likely to be glacial quarrying (e.g. Hallet, 1996; Iverson, 2012), which depends sensitively on the state of stress at the basal interface (Iverson, 1991, 2012; Hallet, 1996). Including the dependence of quarrying on hydrologically-modulated basal effective pressure and its transients is likely to result in a modeled distribution of erosion rates in space and time that differs substantially from that modeled assuming that erosion rates scale solely with sliding rates. Other novel features of my glacial erosion model include accounting for 1) the presence of rock debris, the product of glacial erosion at the glacial interface, and the cessation of bedrock erosion where sediment accumulates significantly; 2) erosion, transport and accumulation of sediment by subglacial water flow, and 3) the control of tidewater processes on glacial extent as a function of global sea level change, proglacial sediment deposition and remobilization, and mass balance, which are important for coastal glacier systems.

The field component of this project largely consisted of adding additional data to the set of glacier erosion rates in South Alaska; thus, I documented sediment accumulation in a large proglacial lake in front of the massive Bagley-Bering Glacier system (5000 km^2) to infer rates of glacial erosion based on several decades of lacustrine deposition and fluxes of sediment to the ocean during the years following the 1994 glacial surge at Bering Glacier (Chapter 2).

Starting in 2003, NSF funded the St. Elias Erosion and tectonics Project (STEEP), a large multi-disciplinary research effort to examine the interplay of climate and tectonics at the Chugach-St. Elias mountain range along the southern coast of Alaska. This program resulted in a large collection of scientific articles that document the combined

effects of tectonics, climate and glaciation in the region.

1.2   The Chugach-St. Elias ranges of South Alaska

The Chugach-St. Elias mountain range of the South Alaska continental margin is

a spectacular topographic barrier that presents a nearly continuous 500 km long

orographic obstacle to air masses traveling north from the Gulf of Alaska; it reaches up to

5960 m high at Mt. Logan and features some of the most dramatic relief in the world at

Mt. St. Elias (5500 m) located only 15 km from sea level at Icy Bay. High rates of

oblique tectonic convergence (~3.7 cm/a; DeMets et al., 1990; Elliott et al., 2010) largely

localized within a ~100 km region and the numerous large subduction earthquakes over

the past century attest to exceptional tectonic activity in this region (three earthquakes of

magnitude 8 in the last 100 years; Nishenko and Jacob, 1990). The extent of ice cover in
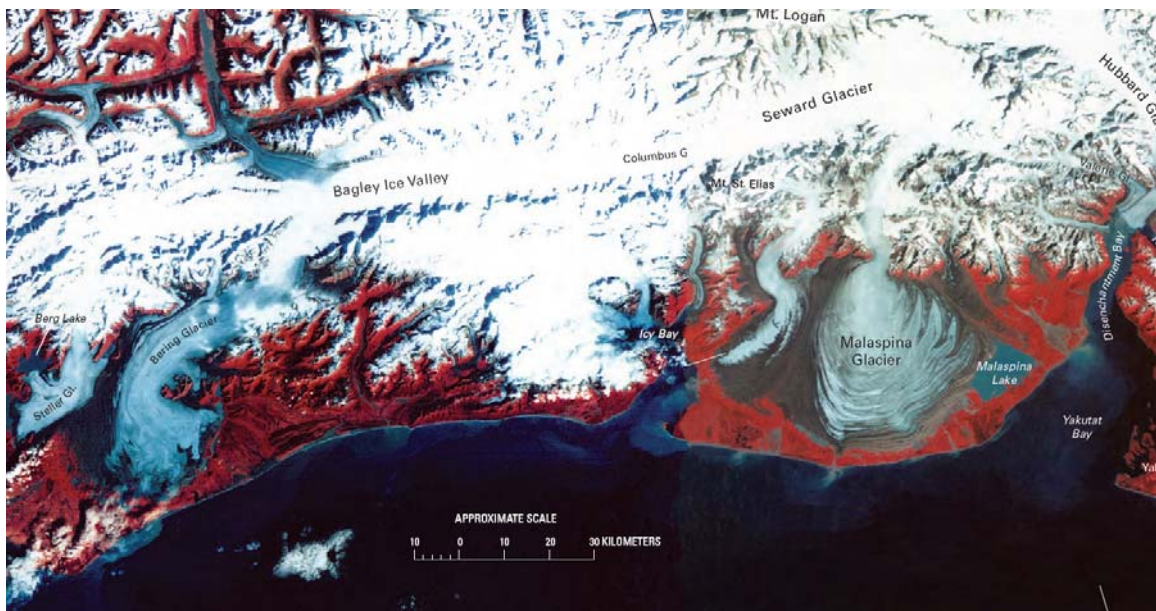
**Figure 1.3: The Bering-Bagley and Seward-Malaspina glaciers region of South
Alaska.**

the Chugach-St. Elias mountain is ~37,000 km^2 (Molnia, 1989) while the combined

drainage area of the Bagley-Bering and Seward-Malaspina systems alone totals almost

10,000 km^2 (Molnia, 2001). It is the most extensive region covered by temperate glaciers

on Earth today, it currently contributes more to sea level rise than any other regions

except for the Greenland and Antarctic ice sheets (Gardner et al., 2013), and it provides

an ideal laboratory to study the nature of feedback between crustal deformation and mass

removal by glacial systems (fig. 1.3).

1.2.1 Structural and tectonic setting

The uplift of the Chugach-St. Elias range is associated with the docking of the

Yakutat terrane at the South Alaskan continental plate margin that started in the late

Miocene (Plafker et al., 1994; Bruhn et al., 2004) (fig. 1.4). The Yakutat bloc is an

assemblage of Eocene marine basalt and siliciclastic rocks deposited from late Mesozoic

through the present. The microplate translated northward from the Cordilleran margin

along the western American continental boundary. Southeast of the study region, the

relative plate motion between the Pacific and NA plates is accommodated mostly by

right-lateral displacement on the Fairweather fault (Plafker et al., 1978; Savage et al.,

1988) whereas to the west, the Pacific plate subducts at the Aleutian megathrust (Plafker

et al., 1994). In the transition zone between transcurrent motion and subduction, the

Alaska syntaxis, transpression results in a broad belt of late Cenozoic folds and dip-slip

to dextral-oblique thrusts (O'Sullivan et al., 1995; Doser and Lomas, 2000) (fig. 1.4).

Extension of the magnetic slope anomaly under the Prince William Terrane suggests that

the Yakutat block may have subducted ~200 km in a direction parallel to the Transition

Fault under the Alaska syntaxis (Griscom and Sauer, 1990). In the study region, the

Yakutat block is thought by some authors to underthrust as far as the Chugach - St. Elias
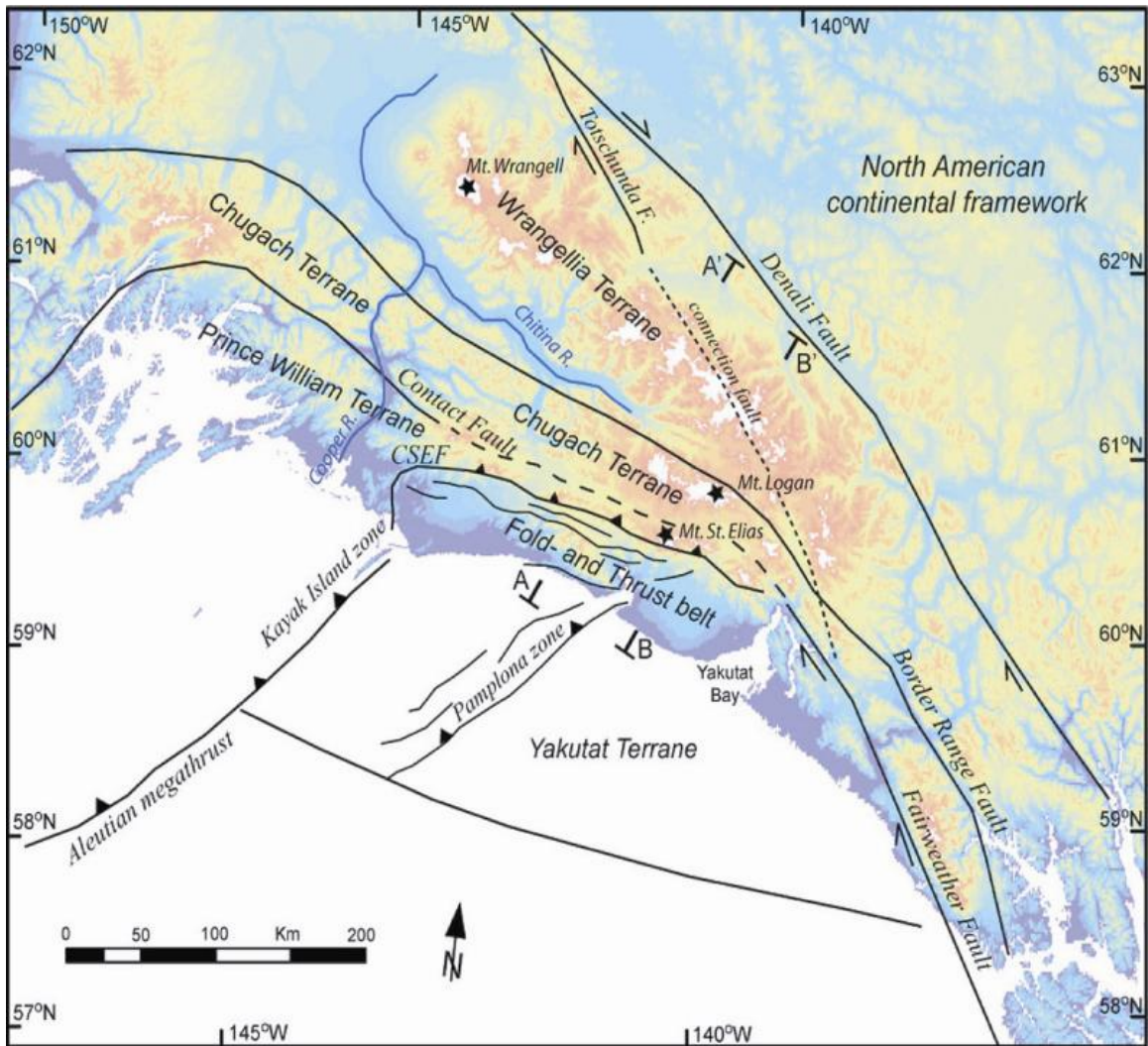
Figure 1.4: Accretionary complex at the Alaska syntaxis. Figure taken from Enklemann et al., 2010.

Fault (Estabrook et al., 1992). Total relative convergence since docking of the Yakutat

terrane off South Alaska would amount to ~600 km if rates of plate motion have

remained constant since Miocene time as suggested by Plafker (1994). The down-going

Pacific plate is inferred by reflection/refraction surveys to dip ~10° to 20 km depth

(Bayer et al., 1978; Brocher et al., 1994), steepening to ~30$^{\text{o}}$ by 40 km depth (from

seismic data in Page et al., 1989).

Large coseismic deformation during the 1899 and 1979 Yakataga/Malaspina area

earthquakes (respectively magnitude 8.1 and 7.5) and their aftershocks were associated

with rupture on the Chugach - St. Elias and other faults to the south which contributed

several meters of uplift per event (Nishenko and Jacob, 1990; Estabrook et al., 1992). The

direction of maximum compressive stress derived from earthquake focal mechanisms,

structure orientations and dike swarms parallels the direction of convergence between the

Pacific and North American plates (Nakamura and Uyeda, 1980; Biswas et al., 1986;

Zoback et al., 1989; Doser et al., 1997). Very Long Baseline Interferometry and GPS data

indicate maximum displacements in the direction of convergence relative to Fairbanks of

3.1-4.4 cm/yr near the coast around Cape Yakataga (Ma et al., 1990; Sauber et al., 1997;

Fletcher and Freymueller, 1999; Elliott et al. 2010). Plate velocity decreases to 1.6 cm/yr

at the Border range fault and 0.1-0.4 cm/yr just south of the Denali fault (Sauber et al.,

1997). The coupling between the Pacific Plate and the Yakutat block is not well known

and their relative motion is inferred to range from less than 1 cm/yr up to 3 cm/yr

(Plafker et al., 1994; Doser and Lomas, 2000; Gulick et al., 2007). These estimates imply

that 3.5-1.5 cm/yr of convergence occur across the St. Elias range in the study area.

1.2.2   Uplift rates and marine terrace emergence

The marine terrace uplift rate computed from emergence rate is ambiguous

because it is contaminated both by fluctuating sea level and isostasy. Average uplift rates

since the Late Pliocene in the Pamplona zone on the continental shelf are computed to be

1.5 mm/yr; however, these structures accommodate little shortening (2-10 km) compared

to onshore structures (Bruns and Schwab, 1983; Worthington et al., 2008). The Holocene uplift history of the region, as seen in marine terraces radiocarbon dated as 11,000 y.b.p. to the recent past (Robinson mountains, Middleton Island, Lituya Bay), is suggestive of maximum rock uplift rates of ~10 mm/yr (Plafker and Rubin, 1978; Plafker et al., 1981). The marine terrace emergence signal likely contains a component of isostatic rebound in response to 1) erosional unloading since the terraces are close to the mountain front and the base level of erosive systems fluctuates well below present sea level over glacial cycles; and 2) reduction in ice load on various time scales. A notable example of the latter in a nearby region southeast of the study area, is the rapid glacial rebound at Glacier Bay since the Little Ice Age (LIA), over 100 years ago (reaching ~3 cm/yr, Larsen et al., 2005). In turn, the mean uplift rate of terraces dated from 5000 y.b.p. to 1100 y.b.p. also equals 10 mm/yr, and 5000 year old terraces emerged during the high sea level stand of the Hypsythermal period more than ~7000 years after the late Pleistocene deglaciation. Deglaciation of the continental shelf after the Last Glacial Maximum (LGM) was probably rapid as is typical of tidewater glaciers retreating off their terminus pinning point; thus, Bering Glacier is thought to have retreated inland from the modern shoreline by 16,000 y.b.p. (Shennan, 2009). This suggests that most of the regional rebound due to deglaciation after the LGM probably had occurred by 5000 y.b.p.. Several glacial fluctuations of similar magnitude to that of the LIA have also been noted in southern Alaska between 5000 and 1000 y.b.p. (Wiles and Calkin, 1994; Molnia et al., 1995; Barclay et al., 1997; Calkin et al., 2001) so relative sea level probably fluctuated considerably irrespective of tectonic uplift of the region over that time period.

1.2.3 Topography and structure

The topography of the study region changes rapidly along strike. The maximum elevation decreases east to west, from ~6000 m at Mt. Logan/St.Elias and the Alaska Syntaxis, to 2000 m east of the Copper river (fig. 1.5). The area between the Chugach-St. Elias fault (CSEF) and the continental shelf is a relatively low relief surface that is at most a few hundred meters above sea level in the Malaspina and Bering foreland and rises abruptly to ~1500 m in the Robinson Mountains; it progressively descends to 500-1000 m further to the west (Fig. 1.5 & 1.6; DEM not corrected for ice cover). The
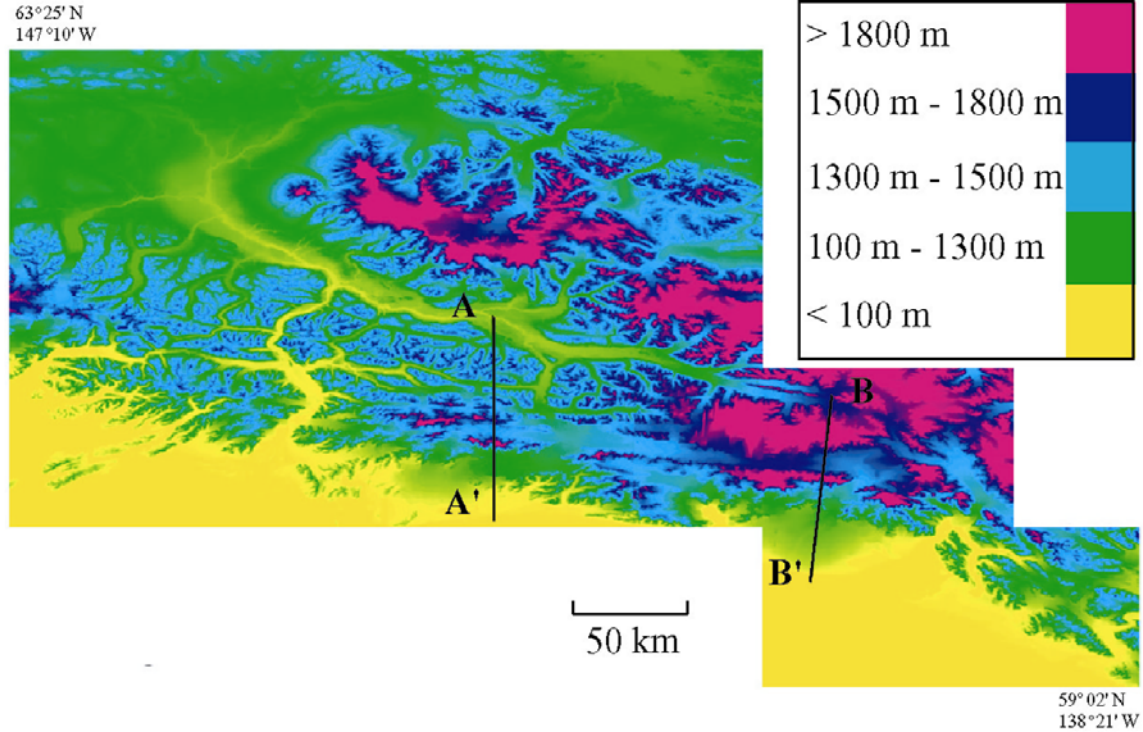
Figure 1.5: Topography of the Chugach St. Elias Mountains (linear stretch, 90 m DEM). Elevation transects are shown in Figure 1-6. Cross-section AA' is slightly west of Bering Glacier while BB' is near Mt. St. Elias and Mt. Logan. Cross section BB' runs nearly down the centerline of Malaspina lobe.

continental shelf is extensively folded in the west (the Pamplona zone) whereas it is

relatively undisturbed in front of the Malaspina lowland. Two major marine valleys with

a maximum relief of 200 m cross the continental shelf at the outlets of the large drainages

of Bering-Bagley and Seward-Malaspina glaciers (Carlson et al., 1982). The Waxell-

Miller-St.Elias ridge (WMSE) is a nearly continuous (>250 km long, 2000-5500 m in

elevation) strike-parallel linear feature that is on the edge of the hanging wall of the

CSEF (fig. 1.6).
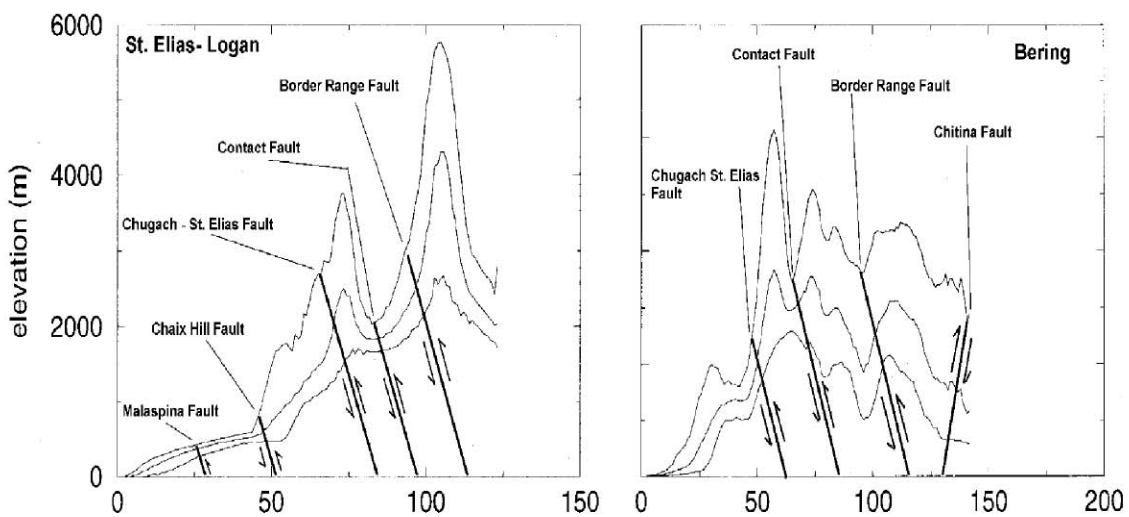
**Figure 1.6: Maximum, mean and minimum surfaces on transects averaged over 30
km transverse swaths of the St. Elias-Logan (transect B'B) and Bering Glacier
(transect A'A) regions. Transects locations in figure 1-5. Fault locations inferred
from Plafker et al., 1994.**

Just to the North, a major transverse drainage (the Bagley-Seward ice

accumulation area) follows the trace of the Contact fault, the suture between the Prince-

William and Chugach terranes. High topography, including the Mt. Logan and King

Peak, characterize the hanging wall of the Border Range Fault, the suture between the

Chugach and Wrangellia composite terranes. The accumulation area of the two major ice

30

drainages in the region (Seward-Malaspina and Bagley-Bering glaciers) is in the lee of the topographic crest of the WMSE but on the windward side Mt. Logan. As they drain to the Gulf of Alaska, these massive glaciers funnel through relatively narrow gorges through the WMSE ridge, especially for Seward Glacier where the drainage narrows to a width of 4 km.

1.2.4   Climate, glaciers, and erosion rates

Interaction between the North Pacific polar front prescribed by the Aleutian low, the frequent storm systems that sweep over the range from the Gulf of Alaska, and the physiography of the region combine to deliver generous precipitation South of the range divide. High precipitation (3.7 m/yr at sea level in Yakutat), frequent cloud cover (~330 days/yr in Yakutat) and moderately cool temperatures (~$3.5\,^{\circ}$C mean annual temperature in Yakutat at sea level) result in the most extensive temperate glacial cover on Earth. Basin averaged erosion rates, measured mostly on the basis of post Little Ice Age (end of the LIA occurred in the late 1800's in South Alaska) sedimentation in fjords, are quite high; they would be the highest rates for a time scale of 100 years recorded anywhere if solely the product of concurrent glacier incision (order of 10 mm/yr; Hallet et al., 1996). These modern rates cannot be imparted strictly to glacial erosion for they also reflect the paraglacial cycle, the product of hillslope relaxation and sediment remobilization incurred after deglaciation, and the mobilization of sediments stored under the ice (Koppes and Hallet, 2006; Meigs et al., 2006; Cowan et al., 2010). On a longer time scale (10^{4} years), the erosion rate averaged over the orogen, as inferred from sedimentation on the continental shelf over the course of the Holocene after deglaciation of the continental shelf, is estimated to be 5.1 mm/yr (Sheaf et al., 2003). Longshore currents from East to

West in the Gulf of Alaska in response to the Alaskan gyre transport a significant but undetermined amount of sediment to the West, which implies that this estimate may be a minimum denudation rate in the St. Elias Mountains during the Holocene.

The Yakataga formation, a 5000 m thick glaciomarine sequence found offshore and up to ~1800 m elevation in the foothills is thought to span the last ~5 Ma. through the present; its initiation marks the onset of tidewater glaciation in North America (Lagoe et al., 1989; Eyles et al., 1991; Lagoe et al., 1993; Rea and Snoeckx, 1995). The friability of the Yakataga formation lithologies (shale, siltstone, diamicton) and of other lithologies that have been subjected to considerable tectonism contributes to the rapid erosion by the massive, fast-moving glacier in this region. Simple theoretical considerations suggest that, to a first approximation, the rate of glacial erosion scales with glacier sliding velocity. Fast sliding is indeed a major component of ice motion (sliding velocity >>50% of mean ice velocity) for many South Alaskan glaciers (Rasmussen, 1989; Nolan et al., 1995; Krimmel, unpublished report, 1985; Raymond and Harrison, 1987). The rapid sliding is due primarily to the temperate nature of the ice, the large ice flux dictated by great snow fall, and the massive size of the glaciers that is conducive to high basal water pressures (as such pressures tend to develop to permit water drainage to the glacier front). Extreme sliding speeds arise during transient events such as surges, which are common in this region. Interestingly, massive floods of sediment-laden water that evacuate large volumes of debris from the orogen often punctuate these events.

1.2.5 Exhumation rates

Until recently, few thermochronological studies of rocks in the Chugach-St. Elias Mountains had been published. Most of the samples processed came from the east side of Yakutat Bay where dextral motion on the Fairweather Fault is the dominant tectonic signal (fig. 1.4). K-Ar cooling ages derived from annealing of fission tracks in apatite range from 1.3-40 Ma (O'Sullivan and Currie, 1996; O'Sullivan et al., 1997), whereas ([U-Th])/He ages in apatite are significantly younger at 0.4 Ma (Berger and Spotila, 2008). Although these data do not show abrupt age discontinuities across faults, overall cooling ages become younger to the South between the range crest in the hanging wall of the CSEF and the Gulf of Alaska. Older apatite and zircon cooling ages, to the North of the Border Range Fault, are from the Mt. Logan Batholith (153 Ma, K-Ar hornblende; Dodds and Campbell, 1988) and King Peak pluton (50 Ma, K-Ar biotite). The Pliocene-Pleistocene exhumation rate, estimated using an assumed paleothermal gradient of 36° C/km, is 0.3 mm/yr at Mount Logan. More recently, thermochronological data acquired by Berger, Spotila, Enkelmann and other workers on the maritime side of the range near the Bering-Steller glacier area show typical rates of 2 mm/yr with enclaves showing maximum rates of ~5.5 mm/yr (Berger et al., 2008; Enkelmann et al., 2008 and 2009). In the absence of structural evidence for tectonic unroofing, cooling and exhumation most likely result from erosion. South of the Border Range fault, erosion is inferred to predate 4.5 Ma (the age of the oldest apatite sample), which similarly to the Logan data, suggests an association between more rapid erosion and underthrusting of the Yakutat terrane starting ~ 7.5 Ma (O'Sullivan, 1997). Pollen studies in the region N of the St. Elias Mountains also suggest development of a topographic barrier around ~ 7 Ma as reflected by an increasingly colder, xeric environment on the downwind side of the

range (White et al., 1997). Although there were major uncertainties in the timing of initiation of glacimarine sedimentation in the Gulf of Alaska (6-4 Ma, depending on interpretation), recent work at ODP887 in the Gulf of Alaska (Murray-Patton sea mounts) clearly identifies the beginning of increased sedimentation and ice rafting at ~5.5 Ma (Rea et al., 1995; Krissek, 1995). The evidence suggests that surface uplift accelerated erosion in the Late Miocene, as supported by O'Sullivan and coworkers, and a cooling climate accelerated denudation at ~5.5 Ma. Importantly, the onset of ice rafting also signals the presence of glaciers that reached the sea, and presence of sufficient high elevation areas to support these glaciers during the relatively warm period that predated the Quaternary. A long history of high mountains, and erosive glaciers that reach the sea implies quasi steady state conditions with erosion and rock uplift compensating for one another and sustaining the large-scale topography.

Chapter 2   Bering Glacier (Alaska): Sediment Budget during a Surge Cycle, 1968 –1999

2.1 Introduction

Rates of sediment production by glaciers figure prominently in many glacial-geological questions. For example, extensive generation of fresh mineral surfaces in the form of glacial flour and its subsequent weathering has been invoked in driving climate change scenarios (Molnar and England, 1990; Blum, 1997). Dramatic atmospheric CO_2 drawdowns caused by the weathering of silicates have been called upon in theories ranging from the climatic cooling of the Quaternary to the snowball earth of the Neoproterozoic (Chamberlin, 1899; Raymo et al, 1988; Hoffman, 1998). Some of the fundamental assumptions of these conceptual models are that glaciers are more efficient at eroding landscapes and producing large volumes of fine-grained sediment with large surface areas than rivers; therefore, increases in the global level of glacierization during the Quaternary increased rates of erosion and production of fine-grained sediment, which in turn weathered thereby depleting the atmospheric carbon reservoir. Assessing the role that glacial erosion play in these hypotheses requires that we understand first modern rates of sediment production and next. their fluctuations as climate changes.

The respective erosional capacity of fluvial and glacial systems has been discussed with renewed interest in the recent past (Hicks et al, 1990; Harbor and Warburton, 1993; Hallet et al, 1996; Elverhoi et al, 1998; Koppes and Montgomery, 2009). Besides bearing on the question of which environment shows greater potential for the genesis of Quaternary relief, this debate is also relevant to understanding whether sediment flux

varies as global ice volume cycles with climate (Broecker et al, 1958; Molnar and England, 1990; Summerfield and Kirkbride, 1992; Willenbring and von Blanckenburg, 2010). Unfortunately, poor knowledge of sediment budgets as well as the difficulty of comparing fluvial to glacial basins with the same environmental conditions (rock competence, climate, tectonics, etc) renders this issue elusive.

Studies of the evolution of glacial landscapes and mountain belts shaped by glaciers are also concerned with the magnitude and distribution of glacial erosion. In particular, to appraise the balance between tectonics and erosion and its implications for the long-term evolution of glacial landscapes necessitates reasonable estimates of mass fluxes at the earth surface over glacial cycle time scales of 10^5 years (Merrand and Hallet, 2000). Glaciers of South Alaska are among the most erosive systems on earth today; basin-wide effective erosion rates of the order of 10^1-10^2 mm/yr have been inferred on the basis of sediment accumulation in fjords respectively on shorter time scales of 10^1-10^2 years (Hallet et al, 1996; Hunter et al, 1995). With the exception of steep basins recently impacted by volcanism (Koppes and Montgomery, 2009), these modern erosion rates exceed those for small mountainous basins, which are known to be very erosive (Milliman and Syvitski, 1992). Exceptionally high sediment yields in the St. Elias Mountains can be attributed to a number of causes that include very erosive glaciers, and soft lithologies that are pervasively fractured by active tectonics, and the rapid transfer of ice from the high lands to the ocean during the major Little Ice Age retreat that locally started in the late 19th century. As discussed in chapter 1, exhumation rates derived from thermochronology on glacial cycle time scales (~ 3mm/yr) in South Alaska are a fraction of the lowest modern sediment evacuation rates. In view of this apparent discrepancy in

the data between short and long time scales, more robust estimates of glacial erosion rates are needed to better define the erosional export of material at the surface of this convergent orogen.

With a drainage area of ~4700 km^2, Bering/Bagley Glacier is likely the largest temperate valley glacier on earth. This surging glacier terminates in Vitus Lake, an ice-marginal basin that is documented to be a site of rapid sedimentation. Seismic reflection profiles acquired in 1991 and 1993 by USGS workers show over 100 m of sedimentation on top of a prominent reflector that is inferred to be the surface overridden by the glacier during its penultimate surge in 1967 (Molnia and al, 1996). Vitus Lake is an ideal setting to quantify sediment yield for a complete surge-non-surge cycle of a massive temperate glacier. Since 1994, I have constructed a sediment budget for Bering Glacier through the monitoring of sediment fluxes out of the system (Merrand and Hallet, 1996), and repeated bathymetric surveys in the proglacial lake complex as well as a high-resolution seismic reflection survey in 1999. As the sediment output reflects erosion from such an extensive glacial drainage basin, it bears directly on the crustal interplay between tectonics and erosion that gives rise to some of the most spectacular relief on Earth, with Mt. St. Elias rising over 5489m (18,008') within 15 km of Pacific Ocean waters.

2.2   Measuring sediment yields and inferring erosion rates

Extrapolating modern sediment fluxes to infer long-term rates of denudation has long been a challenge for geomorphologists. Indeed, significant uncertainties are characteristic of long-term estimates of sediment yields for large basins in active orogens. Tectonics and climate cycles affect sediment production, transport and storage at all

latitudes; in particular, examples of climatically perturbed sediment yields abound in glacial landscapes. The paraglacial cycle, i.e. the Holocene remobilization of glacial sediment, reflects a progressive decrease in storage of sediment in subaerial basins over a 10^3-10^4 yr time scale since the LGM (Church and Rider, 1972; Church and Slaymaker, 1989; Jordan and Slaymaker, 1991) and illustrates the impossibility of inferring bedrock erosion rates from basins storing much sediment based on sediment yields alone. In turn, the sediment flux transients accompanying the rapid retreat of calving glaciers such as that occurred after the Little Ice Age probably reflect an increase in sediment production over a 10^1-10^2 yr time scale (Koppes and Hallet, 2002 and 2006) and illustrate the need to carefully identify the time scale over which rates of denudation can be determined (Fernandez et al., 2011). The great difficulty in accounting for sinks and sources of sediment over an averaging window has led to the amalgamation of erosion with sediment entrainment into part of the literature. Herein, I use the term erosion to represent only the detachment of bedrock fragments from the bedrock. In order to average out natural fluctuations in sediment output over longer time scales field workers have measured sedimentation in terrain traps. Assuming the chronology of deposition is known, rigorously accounting for sediment storage upstream from the trap can still be a difficult task. The major issues to insure a meaningful sampling of sediment traps include 1) the efficiency of basins in trapping sediment for the entire period considered, 2) establishing the chronology of deposition to provide a basis for the estimate of a rate of erosion, and 3) assessing whether transient output is indeed averaged in the sedimentary record over the time window of interest.

Interpretation of the sediment yield emanating from glaciers in temperate climates

where storage is limited is often less ambiguous than for climatically perturbed basins of lower latitudes. The time necessary to deliver supraglacial and englacial debris to the terminus scales with the residence time of ice, but this debris amounts only to a small fraction (2-5%) of the total sediment load of glaciers (Drewry, 1986; Hunter et al, 1996). The bulk of the sediment (95-98%) is located at or near the glacier bed and ~85% is evacuated through glacifluvial transport on much shorter time scale. At Bering-Bagley Glacier, climate, more specifically melt water production and rain, controls the rate of sediment evacuation from the glacier bed and delivery to the proglacial environment. Field observations relevant to assessing basal sediment storage under temperate glaciers are few; however, workers who have accessed the glacier sole a distance away from the terminus have found little sediment (Hooke et al, 1985; Humphrey et al, 1993; Humphrey and Raymond, 1994). Theoretical considerations also suggest that, contrarily to polar systems, temperate glaciers store little sediment subglacially (Alley et al, 1997). Subglacial streams have great sediment transport capacity due to high, flashy seasonal discharge and steep head gradients that it is difficult to conceive significant subglacial sediment accumulation, except along the margin of valleys and fjords that are not traversed by subglacial rivers (Cowan et al., 2010). Although isolated pockets such as closed depression or overdeepenings can collect loose material, given enough time even they will eventually build a reverse slope shallow enough to allow channelized flow and sediment transport.

2.3 Bering Glacier: a natural laboratory to study erosion by massive temperate glaciers

Bering Glacier is located in the Chugach-St. Elias Mountains on the south Alaska coast. Its accumulation area (the Bagley Icefield) is composed of two ~10 km wide troughs that trend parallel to range strike over the trace of the Contact fault (fig. 2.1). To
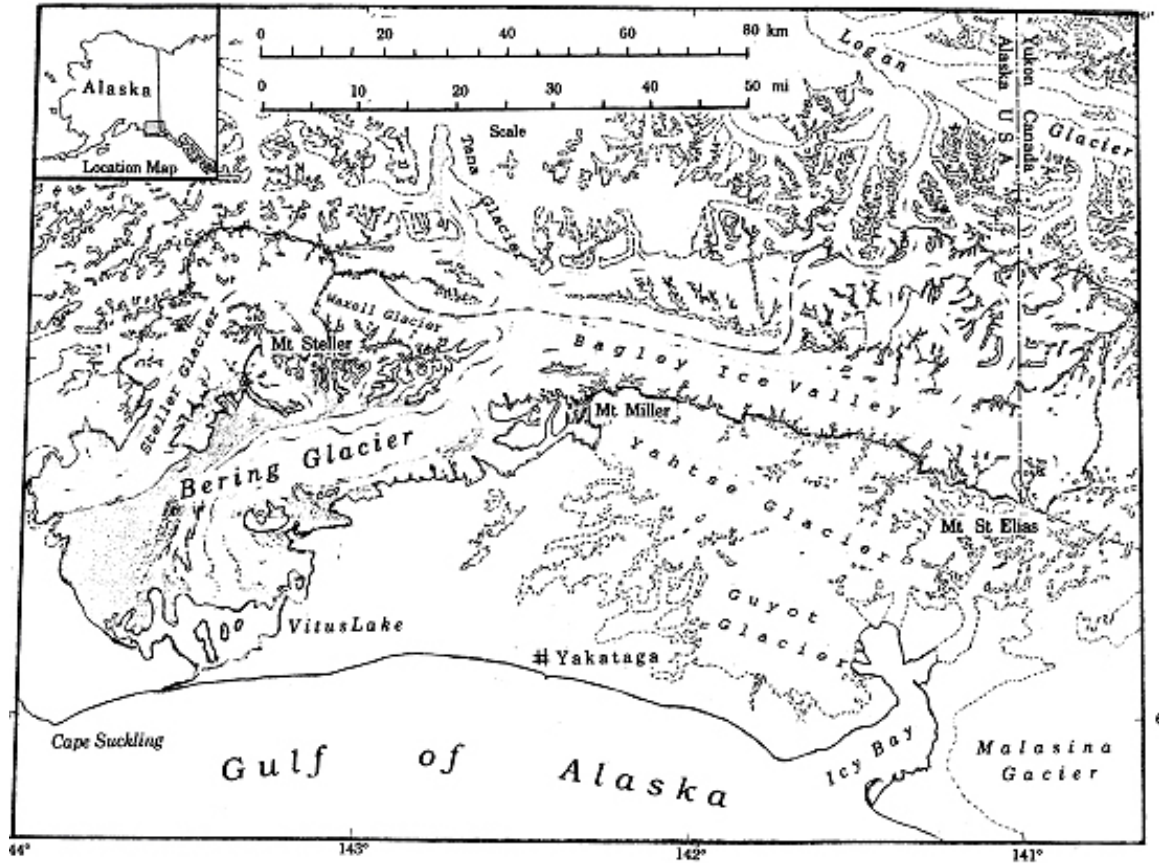
Figure 2-1: The accumulation area of Bering Glacier stretches from Mt. St. Elias to Mt. Steller over the trace of the Contact fault. Mt St. Elias rests on the hanging wall of the Chugach-St. Elias fault (CSEF) that connects to the Aleutian trench via many splay faults between Cape Suckling and Malaspina Glacier. The Bering Glacier lobe is thought to overly one of the major splay fault breaking through the Steller-St. Elias ridge (Bruhn et al., 2009)

the east the glacier originates between Mt. St. Elias and Mt. Logan at Columbus Glacier and ultimately flows ~180km to the ocean. At the confluence of the West and East Bagley streams, the ice slices through Waxell Ridge and eventually spills onto a glacial outwash foreland that is nested between the folded rocks of the Robinson Mountains and

40

Kayak Island. On the foreland it coalesces on the west with Steller Glacier forming a large piedmont lobe. From head to terminus, the ice flows over flysch and basalts that have been metamorphosed into the St. Elias metamorphic complex and intruded by small plutons on the Bagley Icefield; in the upper ablation area the ice slides over flysch and basalt and lower it slides over younger Cenozoic sedimentary rocks that include the Yakataga fm, and Holocene deposits (Plafker et al, 1994). An estimate of erosion rate at Bering Glacier is thus characteristic of fast-moving, massive, temperate glacier over a wide range of lithologies.

Researchers infer an ice-free marine embayment for the early part of the Holocene (Muller et al, 1991; Molnia and Post, 1995; Muller and Fleischer, 1995; Crossen and Lowell, 2010; Pasch et al., 2010). Fossil shells, dating ~13000-5000 y.b.p., indicate a marine environment for the first half of the Holocene while evidence of forest occupation imply the formation of a foreland as early as 4000 y.b.p. Following a readvance ~1500 y.b.p., the glacier reached a Neoglacial maximum ~250 ago, after which it started retreating around the turn of the 20th century. Although the Bagley Icefield has deflated an estimated 150 m since the LIA according to trimlines on the mountain front, the terminus of Bering Glacier has oscillated between ~1-10 km from the 1900 ice limit over the course of the 20th century. As recently as during the 1967 surge, Bering Glacier reached within 3 km of the 1900 moraine. Glacier recession into the overdeepening on the Bering foreland resulted in the formation of a large ice-marginal lake complex of which the largest, Vitus Lake, extends 20km along the ice front. It is not clear how long the glacier has terminated in Vitus Lake; however, aerial photographs by Bradford Washburn show its terminus there in 1938. Based on aerial photographs, historical

records and dendrochronological studies, it has been determined that Bering glacier surged in 1900, 1920,1938, 1957, 1967 and 1993 (Molnia and Post, 1995). Whereas in 1992 the ice front had retreated ~12 km following the 1967 surge, by 1996 the terminus position had re-advanced by as much as 9 km in Vitus Lake. The last surge (1993-1994) started in winter, a little below the ELA and propagated both toward the terminus and upward to an elevation of 2000 m, over 50km up the Bagley Icefield from the confluence. Local velocities of up ~100 m a day were recorded during the surge near the terminus; as the ice is relatively thin here, they directly reflect rapid sliding (Austin Post, personal communication). Variations in speed during the spring melt also reflect accelerated sliding in the region of the rising snowline. The spatial-temporal variations in sliding speed are likely to span at least 2 orders of magnitude over several decades as has also been noted at Variegated Glacier (Humphrey and Raymond, 1994). Although the glacier sliding rate is one of the principal controls of erosion rates, the functional relationship between these two rates is in all likelihood non-linear (see below) and it lacks solid support from extensive empirical data. It is thus desirable to obtain erosion rate estimates that are characteristic of a wide range of dynamic behavior such as exists at Bering Glacier.

Sliding rates and decoupling of a glacier from its bed depend sensitively on basal water pressure and storage. Basal water pressure and storage capacity depend on the closure rates of cavities and tunnels under the ice, melting rates along basal conduits, and water input at the ice surface during melt and rainfall events. According to Nye's solution for the creep of ice in cylindrical channels, the closure rate of the subglacial network increases with ice thickness to the 3rd power, assuming zero water pressure. Using

realistic rheological parameters for ice, all channels under at least 300m of temperate ice would be closed shut within 10 days if no further melting occurred, and it would take no more than a couple of days for closure to occur under 500m of ice. Thick glaciers are thus much more likely to undergo fast hydraulic network closure between peaks in discharge than thin glaciers. The decrease in network transport capacity results in rapid basal water pressure increases during periods of high melt and precipitation, which leads to extensive cavitation and fast sliding. Low effective pressure and large water pressure transients favor glacial quarrying, which is inferred to be the most efficient mechanism of glacial erosion. The erosional budget of massive temperate glaciers could thus be expected to have a much greater relative contribution from glacial quarrying than abrasion. Ice thickness exceeds 300 m for more than 80% of Bering glacier and exceeds ~900m thick near the Bagley Icefield confluence with Bering Glacier (Molnia and Post, 1995; gravity survey, this study). Bering Glacier is thus a good proxy to study erosion by large temperate ice masses, for which ice thickness is commonly on the order of 1 km such as that was found at the lower latitude of their range during Pleistocene glaciations.

2.4   Vitus Lake: morphology and late Holocene evolution

The Vitus Lake complex is a large ice marginal body of brackish water that is composed of several basins stretching in the ice flow direction. From east to west the basins are: Tsivat Lake and Tsiu Lake, Taxpayers' Bay, East Vitus Lake, MacMurdo Sound, and Tashalich Arm (fig. 2.2). In front of the ice, maximum water depth ranges from a few 10's of meter to over 200m deep, and the basins deepen from east to west.
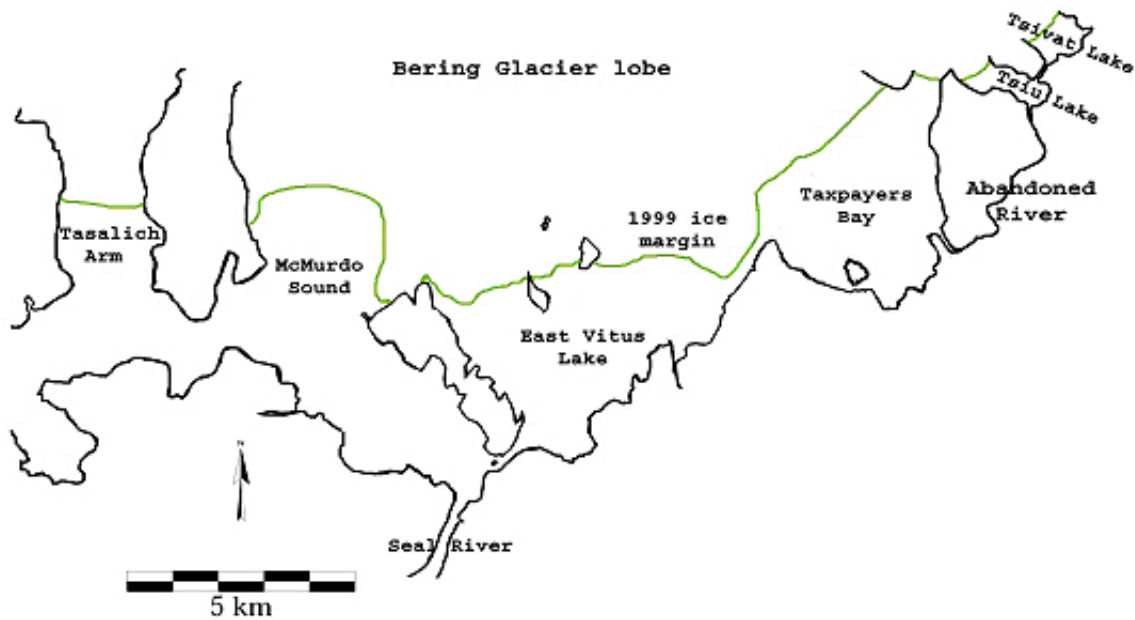
Figure 2-2: The Vitus Lake proglacial basin complex with the 1999 ice margin (green line). Although other outlets were active in the past, today the Seal River is the only connection to the Gulf of Alaska.

Ice penetrating radar soundings of the terminal piedmont lobe indicate some basins to be at least as deep as 330m below sea level (Molnia et al., 1991; Trabant et al, 1991; Trabant and Molnia, 1992; Molnia and Post, 1995; Conway et al., 2009). Most of the ice-covered foreland is below sea level (as far as 60 km upstream from the terminus) forming an over deepened region 700 km^2 in surface area that stretches between the mountain front and Bering trough on the continental shelf. Bedrock crops out in West Vitus right in the middle of the foreland (Molnia et al., 1996), suggesting that a fjord sill anchors the alluvial plain. Early Holocene sediments probably underlie portions of the terminal lobe as is shown by the presence of Holocene marine shells, dated from ~13,000 b.p. to ~5000 yr b.p., in situ and in reworked deposits on the Bering foreland (Pasch et al., 2010).

The extent of the lake varies with terminus position during surges and the following retreats. The lake was almost entirely filled with ice in 1967 whereas there were 200 km^2 of open water in 1993 just prior to the latest surge (Molnia et al, 1994). Despite ice margin oscillations during surges, overall Bering glacier has slowly retreated since the LIA. Rock wall trim lines show ~150m of ice surface deflation (probable Little Ice Age surface profile) near the modern ELA. The ice front has oscillated over a range of 5-11km upstream from the 1900 LIA retreat ice margin on the coastal plain. The sediment trapping efficiency of the Vitus overdeepening has improved in the last few decades since the ice front has retreated in deeper basins. Comparison of aerial photographs (1938-1998) shows that large banks of rock debris have accreted on the southern shore of the lake. As new land stabilizes and develops a thick cover of vegetation, the southern shore of the lake migrates northward since the glacier retreats and cannot remobilize sediment deposited during its furthest advances (1920, 1940, 1967).

The deep subglacial basins (up to 300-500 m below sea level) are separated by highs in the substrate that reach above water level and line up with medial moraines at the ice surface and islands within the lake in front of the ice (Conway et al., 2009; Molnia and Snyder, 2012). From East to West, maximum water basin depth increased from 50m to 180m in 1993 (from ~10m to 180m in 1999), thereby implying either a greater sediment load and/or a lesser capacity to move sediment in eastern basins. The relief of subglacial topography across the flow in the lower reaches of the glacier is as large as ~200m and it averages ~100m. Spot ice-penetrating radar data of the glacial interface with the substrate acquired by USGS workers in 1991 (Trabant and Post, personal

45

communication) and surface elevation show that transverse bed slopes between basins can exceed 11 times the transverse ice surface gradient, suggesting that subglacial drainage channels are hydrologically isolated when approaching the terminus in the outer basins (Tsivat, Tsiu, MacMurdo, and Tashalich). A steeper ice surface gradient on the east side of the glacier where it exits the mountain front (at Grindle Hills where the Bering lobe spreads eastward) probably drives much water at the glacier bed toward the eastern sector of the terminus. A region of low subglacial laterally confined topography (2 basins) reaching ~300 m below sea level stretches from below Grindle Hills toward the eastern sector of the ice front (Conway et al., 2009) and the area of the terminus from which spectacular outburst floods emanated in summer 1994. Each proglacial basin is presumably the outlet for significant drainage of subglacial water and sediments; however, only the eastern sector of the terminus (Tsivat Lake) has shown evidence of large water discharge near the surface (Fleischer et al, 1998; A. Post, personal communication), and shows massive infilling whereas bathymetric elevation of the western sector has changed little between 1993 and 1999. Alternatively, the basins to the West are much deeper and wouldn't necessarily show large water discharge.

The sub-bottom elevation spot data show the adverse slope of the trough (dipping upglacier) to be 2-6 times the ice surface slope in the 3 most eastern basins (Tsivat, Tsiu and Taxpayers' Bay). Freezing of the subglacial network on the reverse slope of overdeepenings is thought to occur whenever viscous dissipation does not provide enough heat to keep up with a rise in melting temperature under rapidly decreasing ice overburden. Such circumstances are met when the magnitude of the bed slope reaches between 1.2-1.7 times the surface slope (Rothislberger and Lang, 1987; Hooke et al,

1990; Alley et al., 1998). Supercooled artesian water and its associated surface crystal deposits have been observed at several locations of the eastern Bering ice margin (Fleisher et al, 2000; Molnia, personal communication) and some overturned icebergs exhibit debris-rich basal ice that may have formed by basal freezing. Significant sediment storage is thus possible in the over-deepened section of the eastern sector; yet this area is also the scene of recurrent outbursts of heavily sediment-laden water similar to the 1994 jokulhaups (Fleisher et al, 2000; AGU Bering Glacier Special Session, 1996). This suggests that storage ultimately depends on the frequency and sediment transport capacity of sudden large discharges. During typical, non-flooding conditions subglacial water may be diverted toward the far eastern margin where several artesian fountains with supercooled water have been active through the years; however, water pressure approaching or exceeding the overburden pressure is likely responsible for large discharges to pass beyond the overdeepening during flood outbursts thereby suggesting that most of the sediment may be preferentially flushed during glacier surges. Water in crevasses and supraglacial lakes on a pervasively crevassed surging glacier indicating near flotation conditions are a common occurrence on the Bering terminus. Although there is no confirmation of surface water upstream from the location of the August 1994 outbursts, aerial photographs of the central part of the terminus in May 1994 show a ~10 km^2 region with water-filled crevasses. The middle basins (East Vitus and McMurdo Sound) have slopes that are opposite the ice surface slope but appear shallow enough in their upper reaches that freezing of the subglacial channel network is not expected where sub-bottom data is available; however, reverse bottom slope may well steepen further upstream. Finally, the bed in the westernmost basin is sub-parallel to the ice surface,

47

favoring sediment evacuation from the glacier bed. Evolving ice surface gradient between the surge and inter-surge years is expected to affect the steepest reverse bed slope that can be sustained before freeze-on comes into play. Glacier surface slopes tend to increase during non-surge years as excess accumulation is stored in the upper reaches of the glacier and the ice pulsed during the previous advance wastes away (Variegated Glacier). Surface reconstructions of Bering Glacier based on morainal deposits show a steeper lower ablation area (last ~20km) as ice retreats in non-surge years (Molnia and Post, 1985). A comparison of 1972 to 1992 surface elevation data shows ice slopes of the central lobe of, respectively, 0.014 and 0.021. The steepening of driving gradient by 50% when ice is at its most retracted position may translate into lesser subglacial sediment storage during non-surge years in the eastern portion of the lobe since it is otherwise susceptible to freezing of subglacial channels. Alternatively flood outbursts during surges may remobilize sufficient material stored subglacially to steepen the adverse slope beyond what may be sustained by the steeper ice surface gradient characteristic of periods between surges.

2.5   Mass exchange with the ocean

Since the early 1950's, Vitus Lake has only one outlet to the Gulf of Alaska, the Seal River (Molnia and Post, 1985). The lake traps essentially all of the coarse sediment as long as the shallow sill (~10m deep) at the river outlet is not overridden by ice during a surge. Satellite images, including those acquired during non-surge periods, show suspended sediments streaming out of the Seal River; large sediment plumes can be seen offshore as they are entrained to the West by the Alaskan gyre. Loss of suspended

sediment out of the system is likely most significant as the terminus closes in on the river outlet during surges. Faced with the possibility of significant sediment evacuation along the Seal River, it was necessary to assess the effectiveness of Vitus Lake as a sediment trap.

2.5.1   Sediment evacuation through the Seal River

Beginning in 1994 through 1999, I monitored the Seal River to quantify sediment leakage to the Gulf of Alaska (Merrand and Hallet, 1994). On short time scales (hours to month) lake level is controlled by subglacial discharge and tides. Lake level rises in early summer (~mid-June) as melt water starts draining out of the glacier. The Seal River is an 8 km long tidal stream, which undergoes reverse flow into the lake at high tide. Suspended sediment concentration and river stage are the 2 flow characteristics that are needed to compute sediment flux out of Vitus Lake.

2.5.2   Methods and results: continuous parameter monitoring, GPS surveys and discharge computations. Modeling of discharge and sediment flux

In order to monitor mass exchange through the Seal River, we need water discharge and suspended sediment concentration. I assume that all bedload is retained within the lake. We installed a gauging station 1 km down from the lake outlet in the narrowest stretch (200 m wide) of the river. We named the gauging station B.S. (Big Schist) for the giant schist erratic right at water edge upon which we built a small wooden stand in an attempt to protect the datalogger and power source from water damage. Water flow through this rectilinear river reach is fully rough as large eddies imprint the water surface at all times. Vigorous mixing processes prevents settling of particles up to sand

sizes (this was confirmed by the presence of fine sand in water samples brought back to

the laboratory); surveys of the river cross-section at B.S in 1994, 1996 and 1999

confirmed its stable geometry. Hourly measurements of stage, turbidity (proxy for

suspended sediment concentrations), electrical conductivity (proxy for dissolved load)

and water temperature have been recorded since the beginning of this study. The Seal

River is a very harsh environment for sensitive instrumentation. Indeed obtaining

consistent and systematic data has proven to be a great challenge; as a result most records

are interrupted after a few months to half a year worth of data. Only once did the

instrumentation remained functional the entire year (1998). The wooden stand had to be

rebuilt every year due to massive floods that were induced by the surge (jokulhaups) and

large rain storms, icebergs raking the river banks on their way to shipping lanes in the

Gulf of Alaska as well as on their way back toward the lake during rising tides, trees

uprooted by advancing ice and the occasional brown bear pawing. Fortunately

duplication of all sensors allowed us to gather valuable information for at least part of the

year. For the sake of being succinct only the most complete part of the record obtained is

included in this report; however, through 1999 the following periods were monitored

successfully: 7/8-8/20/1994, 7/20-9/23/1995, 8/10/1996-2/01/1997, 7/15-8/15/1997, and

6/05/1998-7/30/1999, and 08/01/1999 –01/14/2000. Details of the methods, in particular

that used to transform turbidity data into suspended sediment concentrations, are given by

Merrand and Hallet (1996). The stage record for 1998-1999 illustrates well the controls

on water flux through the Seal River (fig. 2.3). Stage (panel a) readily appears to result

from superposition of 1) rain event and melt caused by high temperature (panel c and b)

and 2) tidal cycles (panel d). Water level at B.S. reaches a maximum in early August and
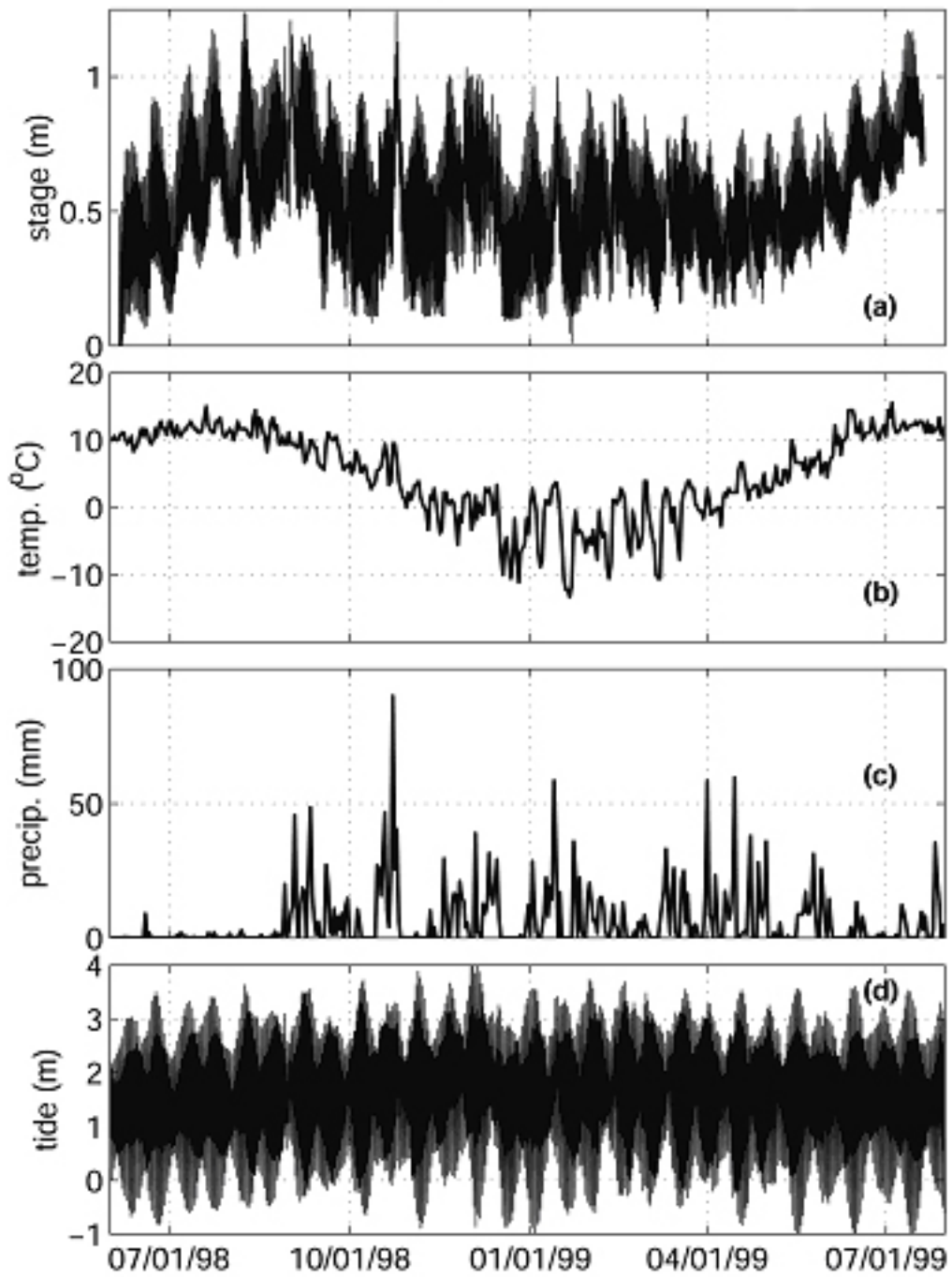
Figure 2-3: Seal River stage for 1998-99. The contributions to water fluxes are described in the text.

a broad low in late winter. It lags air temperature during spring and summer (panel b)
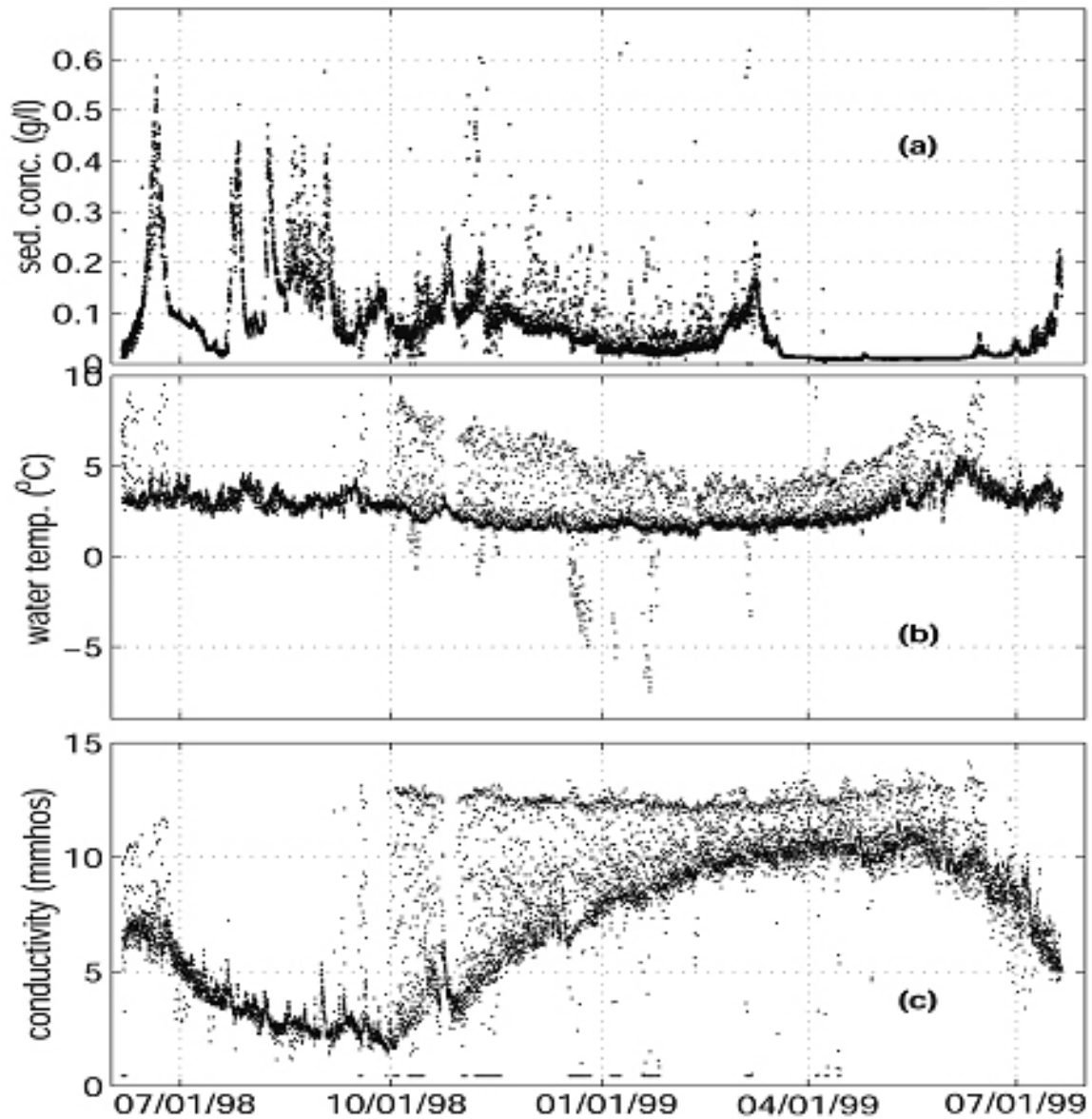
Figure 2-4: Record of suspended sediment concentrations, water temperature and conductivity in the Seal River during 1998-99.

thus reflecting the importance of subglacial network reorganization in regulating water

flux at the terminus. In turn temperature lows during winter are highly correlated with discharge minima indicating depleted basal water storage, as well as no or negligible input of surface water. Large precipitation events result from the greater influence of the Aleutian pressure lows over artic highs, and are thus accompanied by anomalously high temperatures and rain. These storms occur in all seasons (although summer 1998 was very dry) and they are closely reflected in the stage record. A low in melt water production during winter is mitigated by higher than average tide amplitudes about the winter equinox. Although I monitored turbidity only at one location (fig. 2.4), collection of samples at the water surface as well as integrated over depth along the river cross-section allows to relate the continuous point sampling to a cross sectional average. Suspended sediment concentrations of samples collected at the surface are essentially the same as those that are integrated over water depth thereby confirming the turbulence and well-mixed character of flow. The ionic load (fig. 2.4) is greatly dominated by chlorine and sodium due to seawater intrusion into the lake thereby rendering the conductivity data meaningless to assess dissolved mass transfer from the Bering Glacier drainage area to the ocean. Fortunately, the dissolved load of glaciers is a small fraction of the total sediment yield (less than a few percent of the total sediment load in Alaska; Hallet et al., 1996) and it is therefore neglected in this study for the purpose of computing erosion rates.

Varying lake level at the river outlet and tidal cycles render the task of constructing a stage-rating curve for the sampling site problematic because water surface slope in the Seal is a function of two independent variables: elevation of the water surface at the lake and that at the river mouth at the ocean. Thus we had to measure slope, and

compute discharge via Manning's equation and measurements of channel geometry. This

equation relates mean flow velocity to hydraulic radius, surface slope and flow resistance

at the channel boundary: $\overline{U} = \dfrac{R^{\frac{2}{3}} S^{\frac{1}{2}}}{n}$. The roughness coefficient n was back calculated

on the basis of discharge measurements performed with USGS workers in 1994 (Molnia

et al, 1994) near the instrumentation site BS. In order to determine water surface slope

expediently, I assume that water level at the river mouth varies with local tides and is

unaffected by the discharge in the Seal River. I monitored stage at the Seal River mouth

for only a few tidal cycles per year, and established the amplitude and timing of tides at

the Seal River and compared them to one of the nearest NOAA tidal gauge ~100km away

in Yakutat. I then compute stage at the Seal River mouth for the remainder of the year by

assuming that the relationship between these 2 locations remains the same for the

duration of the record. To compute the water surface slope, which is used to derive water

discharge, I established the absolute elevation of the water surface at both sampling

points using differential GPS surveys with Trimble 4000SSE geodetic quality survey

receivers. I opted to conduct fast-static positioning due to relatively short baselines (~8

km), the ease of conducting fast-static surveys and the quality of data obtained in this

fashion. In order to obtain the highest precision available I conducted multiple 24-hour

static surveys of the base station (at Moose International on Taxpayers' Bay, fig. 2.1);

this data was then processed with GIPSY-OASIS II (via JPL mail-in analysis service).

The fast-static data was then analyzed with Trimble's standard software while treating the

base station as a known position. The largest uncertainty involved in measuring surface

elevation (~10 cm) by this method rests with changes in stage occurring during surveys which have an average duration of ~15 minutes.

To estimate sediment fluxes during times I did not acquire data, I model discharge by computing glacier runoff due to ablation and liquid precipitation. This method neglects the transfer of water from the ice surface to the glacier terminus, thus does not account for the exact timing of water flux pulses due to the evolution of basal water storage. Yet, this is still a useful approximation because Vitus Lake is a reservoir between the terminus and the Seal River; it dampens the flashiness of melt water pulses thus in the process counteracting the scaling of sediment pulses with discharge cycles at the terminus. I couple a degree-day scheme to the distribution of area with elevation to model glacier mass balance and runoff. The procedure has been shown to deliver comparable results to surface energy models while it has the advantage of using many fewer poorly known parameters (Braithwaite, 1995; Johanneson et al, 1989). The method consists of computing 1) the fraction of precipitation falling as snow by determining whether temperature is greater than a threshold for solid precipitation (1°C) and 2) the ablation, which is assumed to scale with the number of degree-days when temperature at the surface is greater than the melting point for water. Two ablation coefficients are necessary (one for ice and one for snow) to relate degree-days to melting (Anderson et al, 1998; this study). The model is forced with time series of daily mean temperature and total precipitation collected near sea level at Bering Glacier (BLM weather station at Moose International), and weather stations data from Cordova and Yakutat. I assume a normal distribution of temperature about the daily mean and compute a standard deviation on the basis of available hourly time series. The absence of high elevation

55

meteorological stations requires modeling temperature and precipitation as a function of elevation. The distribution of temperature with elevation is simulated with a standard lapse rate for maritime regions (5.5°C per 1000m). Modeling precipitation with elevation is constrained by a scattering of observations at elevations above sea level; it is therefore treated as a dependent variable with the constraints imposed by topography to determine the location of a maximum, a 100-year accumulation record at 5500m on Mt. Logan (Holdsworth et al, 1989) and 1967 winter balance data for the south side of the range (Marcus and Raggle, 1970). Finally, I adjust the degree-day coefficients in view of mass balance information consisting of net snow accumulation above the 1992 Mt. Spur tephra (September 1992- Late August 1992) and the location of the ELA. I also account for calving losses simply by using Brown et al's (1982) relation where calving rate is proportional to water depth at the terminus. The elevation-area distribution for the basin is obtained from the 90m DEM. Mass balance is then integrated over the basin hypsometry so that ice discharge at the terminus equates calving. This simple model does not include the thermal insulation provided by debris cover, which is potentially important for a fraction of the ablation area (~10%). Runoff obtained in this fashion is immediately transferred to the terminus thereby not accounting for possible groundwater flow or storage under the ice. Finally, to obtain sediment fluxes for the periods of missing data, I use the mean concentration for the fraction of the melt season on record.

2.5.3 Sediment flux to the ocean

To compute sediment loss to the ocean I continue assuming that all bedload remains trapped into Vitus Lake due to its great depth relative to the lake outlet (~10m). I multiply water discharge with suspended concentration to derive the sediment yields of

Table 1	Sediment flux (megatons/yr)
1994-95	28.5 ± 11
1995-96	17.1 ± 7
1996-97	3.9 ± 1.6
1997-98	2.5 ± 1
1998-99	2.6 ± 1
1999-2000	$1.9 \pm .8$

table 1. As expected, sediment flux through the Seal River was greatest during the period of the surge that was witness to flash floods during the 1994 melt season. The suspended load remained high through the end of summer 1995 as glacier extent reached a maximum, then immediately decreased by an order of magnitude for the remainder of the study. The errors in computing discharge and approximating sediment concentration are estimated to be ~ 40% of the sediment volume transferred to the ocean.

2.6 Sedimentation in Vitus Lake

2.6.1 Methods and results

From 1993 to 1995 ice discharged rapidly into the lake complex almost filling Vitus basin in the process (ice-free portion was reduced from 200km^2 to 40km^2) (Molnia et al, 1996). Stagnant ice and rafting icebergs had to waste away before a meaningful

bottom profiling survey could be conducted. In the mean time retreat of the ice front was documented and, in order to determine changes in shape and depth of the lake floor, the bathymetry of Vitus basin was recorded every year of the study in conjunction with USGS researchers. I also conducted vertical profiling of the water column (conductivity, temperature, turbidity) at the terminus in all basins in an attempt to determine the main subglacial water outlets draining Bering Glacier. The western basins proved too deep to be monitored successfully. We did not find large point sources of water discharge in the central sector. In contrast, major water outlets from the glacier were well documented in the eastern basins (Fleisher et al, 2000; Molnia et al, 1996). The jokulhlaups that occurred in 1994 and 1995 almost filled Tsiu and Tsivat lakes (Fleisher et al, 2000; Merrand and Hallet 1996, Molnia et al, 1996). A 1.5 km^2 sandur, composed of silt, sand and gravel, formed within just a few days in Tsivat Lake during the 1994 flood outburst (Fleisher et al, 2000). Sediment transfer of flood deposits via Abandoned River, a former ice-marginal channel reoccupied during the flood outbursts, to the central basins was monitored in 1997-1998. Water sediment concentrations averaged 9g/l over the course of the melt season, which translated into large sediment fluxes from the eastern basin to the central basins (11 megatons for 6/11-11/07/1997).

By summer 1999 the ice retreated sufficiently to allow sub-bottom profiling of lake deposits although ~35% of the 1992 lake was still under ice (an estimated 15% of the 1992 lake was under ice in 2013). We collected ~180 km of seismic data in order to quantify the accumulation of sediment within Vitus Lake. The subsurface reflection record is an acoustical profile of the lake floor and sub bottom stratigraphy along the survey track lines. To characterize sedimentation over such a large area as well as

58

possible with limited time and resources we opted for establishing track line down a

centerline along each basin long axis and a zigzagging pattern about the centerline. Track

line turn angle was 30-60° (fig 2.5). The small survey vessel was a 6 m, fiberglass boat

based in Yakutat; it has a shallow draft that permits entering eastern Vitus Lake and a

custom-made solid canopy to protect the equipment from the elements. I used
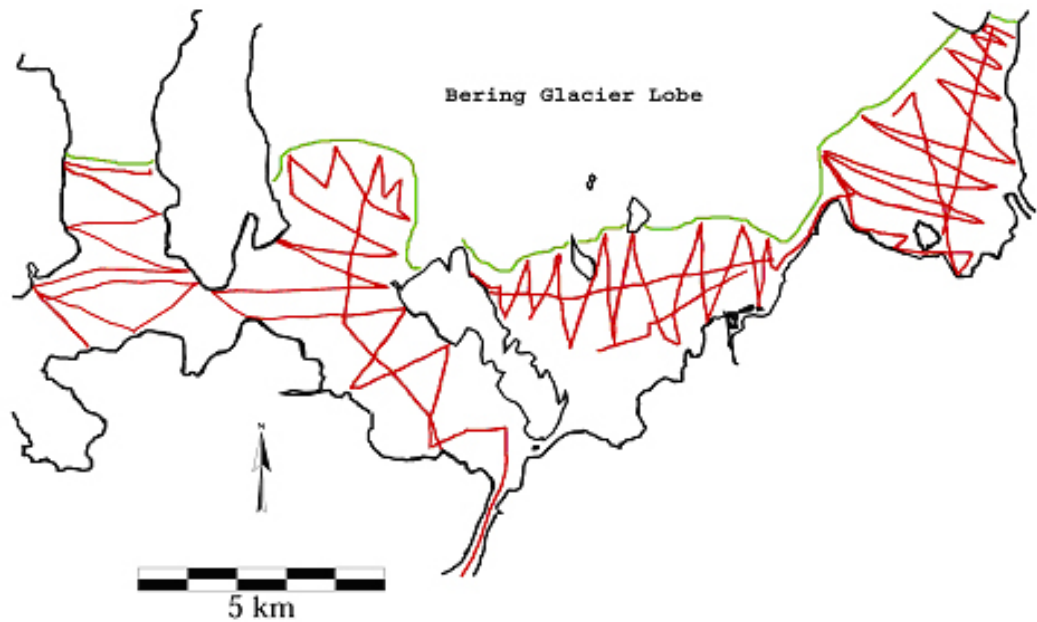
Figure 2-5: Tracklines for sediment profiling in Vitus Lake. The 1999 ice front is the green line.

a Datasonic Model 1200 Bubble Pulser suitable for collecting high-resolution acoustic

reflection data in the shallow target environment at Vitus Lake and for penetrating glacial

tills and gravels more effectively than with high frequency/high energy seismic reflection

systems. The Bubble Pulser is medium frequency (350-800 Hz) and has low output

acoustic energy (20 joules). It is capable of excellent subsurface penetration, particularly

in glacial sediment; yet it provides good vertical resolution (15-30 cm). The maximum

subsurface penetration achieved was approximately 120 m of fine-grained acoustically

transparent sediment. The hydrophone array and the acoustic source were towed 25 m and 5 m, respectively, astern the vessel in open water and closer to the boat whenever we encountered iceberg jams. The reflection data were displayed on an EPC Model 1086 thermal graphic recorder and archived on a Sony Model 208A, 8-channel, DAT recorder. The graphic recorder display and the firing interval for the acoustic energy source were set according to water depth and thickness of the sediment pile (.4-.6s). Throughout the 6-day survey, location markers were simultaneously set at 2-minute intervals on the GPS record, the graphic recorder output as well as the digital record. The estimated positional accuracy is $\pm$ 50m.

The seismic reflection signature of the soft Yakataga formation (mudstone, siltstone and diamicts) and compacted erosional detritus is very similar which effectively prevents bedrock to be differentiated from very consolidated and/or coarse deposits. I analyzed the seismic data to identify the acoustic signature of different sediment types and their depositional environments. In particular, I searched for strong continuous reflectors that should separate material deposited during different glacier advances. Lacustrine sediment overridden by ice should be compacted and draped by a veneer of diamicton similar to what can be observed subaerially on islands (0.5-1m of till). The reflectivity of diamicton and compacted sediment is markedly different from that of the fine-grained material deposited via settling in a distal lacustrine environment prior to and during the latest advance. Although coarser materials deposited in a proximal environment, such as during the 1968-93 retreat, also have high reflectivity and could thus be confused with glacial till, processes of deposition in fans and deltas from a retreating point source do not produce continuous horizons of great extent. Therefore, a

transparent silt-size sediment package should be readily identifiable above the surface

overridden during the greater 1967 advance. Rafting icebergs can locally scour this

package while proglacial outwash and gravity flows deposited during the previous retreat

could also be found above this surface.

Indeed a continuous, highly reflective horizon in the substratum can be followed
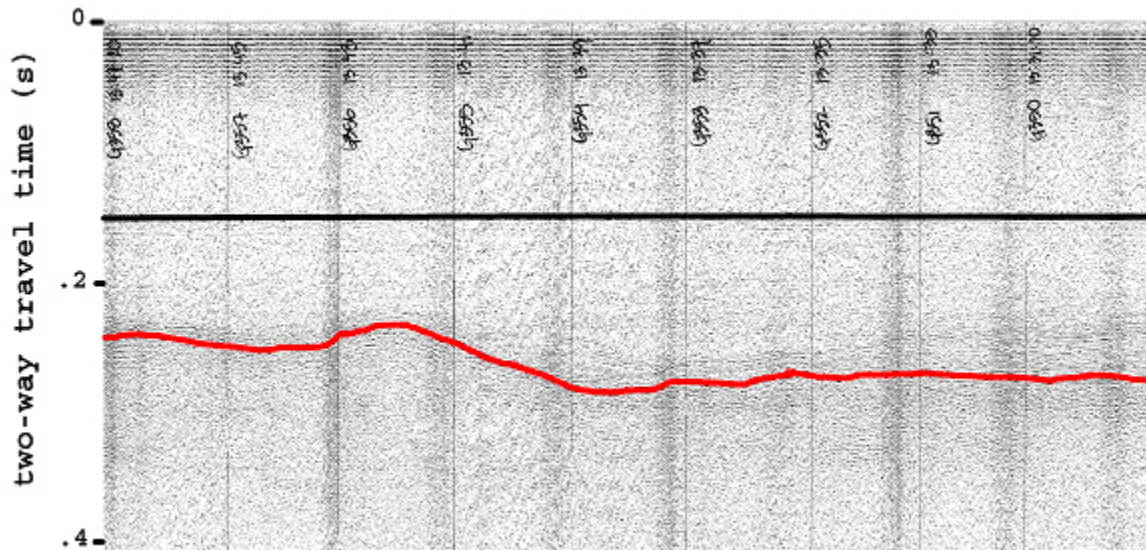
Figure 2-6: 1967 surge surface (red bottom reflector) and sediment surface in McMurdo Sound (bathymetry in black). Transparent material is stacked above more reflective ice proximal sediment above the 1967 surge horizon.

over much of 3 out of 4 basins surveyed with the bubble pulser (Taxpayer's Bay, East

Vitus basin, and McMurdo Sound); it is topped by a thick package of material that is

mostly acoustically transparent in East Vitus Lake and McMurdo Sound although some

discontinuous reflectors are sometimes present within it (fig 2.6). This strong continuous

reflector is also often overlain with a unit characterized by low amplitude, discontinuous

reflective horizons. This unit is inferred to be coarse-grained sand and gravel outwash. In

Taxpayer's Bay, only the upper few meters of the package overlying the basal reflector

are truly transparent whereas most of the package is moderately reflective and composed

of truncated horizons (fig. 2.7). Thus, the seismic profile reveal at least 3 separate seismic facies with the following interpretation: 1) acoustically transparent material composed of silt and mud deposited by settling through the water column, 2) low amplitude, chaotic and hummocky package above and possibly below the 1967 surface comprised of outwash and possibly slump material, and 3) highly reflective continuous and hummocky reflectors bounding an incoherent package of faint acoustic signature thought to be glacial till; however, as noted above, differentiating between till and outwash is seldom straightforward.

I am confident that reflector at the base of the recent sediments is the 1967 surge surface because it merges with the surface of the moraines built during the previous major advance (1967-68) at the south end of Taxpayer's Bay and East Vitus Lake (fig 2.7). Similarly the southern tip of island surfaces (Whaleback and Pointed islands) last
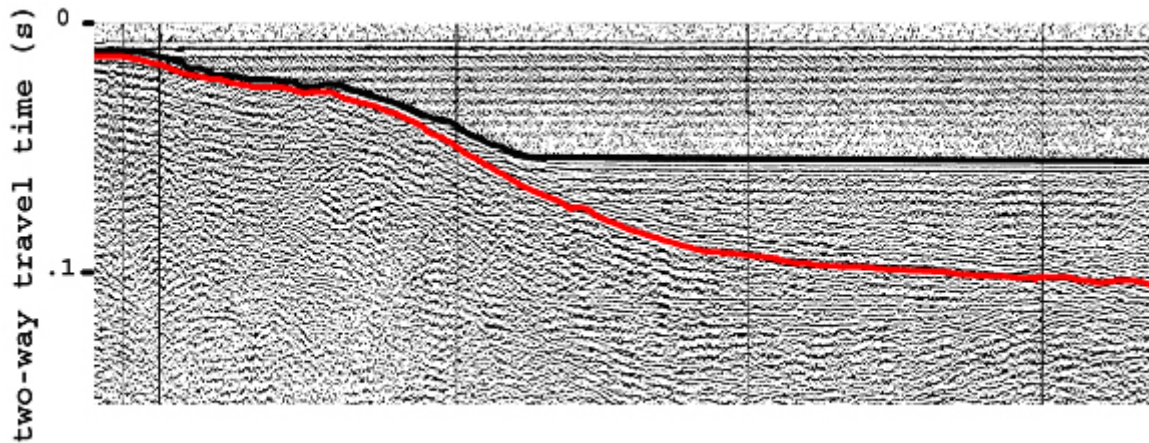
Figure 2-7: 1967 surge surface (red) and bathymetry in Taxpayer's Bay. The penultimate surge surface rises out of the southern end of Taxpayer's Bay to form a prominent subaerial moraine (~10 m high).

overridden during the 1967 surge merges with the surface of interest in the substratum

(fig 2.8). The 1993-95 surge deposited fairly continuous 1 to 2m-thick moraines on land

along its subaerial margin, but submerged moraines are visible in only a few places

(notably in Taxpayer's Bay). Backfilling behind shoals during retreat can be seen in some

locations and may contribute to the apparent lack of a widespread and prominent
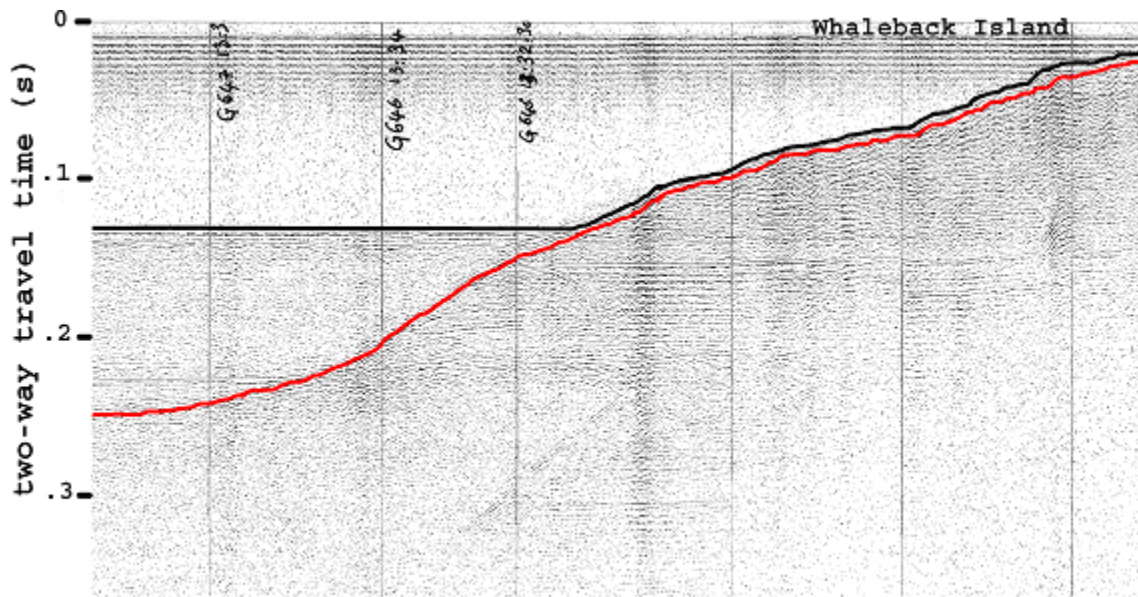
Figure 2-8: Surface overridden during the 1967 surge (red) in East Vitus Lake nearly merges with the surface of Whaleback Island. Whaleback Island was completely overridden by ice during the 1993-1994 surge.

terminus deposit. The layer above the 1967 surface appears to thin upstream from shoals

(fig. 2.9), which implies that material deposited prior to the 1993 advance was

remobilized during the surge. Thus, the continuous sub bottom is well defined through

most of the basin and its relationship to surfaces shaped during the penultimate and the

last surge allow to infer with confidence that sediment overlying this continuous reflector

was deposited in Vitus Lake after Bering Glacier began retreating from the 1967 surge.

The situation is more complex in the westernmost basin, Tashalich Arm, since the 1993-

1994 glacier surge equaled that of 1967 which failed to leave submarine moraines that are

distinguishable today. Several discontinuous unconformities present over much of the

basin may correspond to earlier surges/advances and
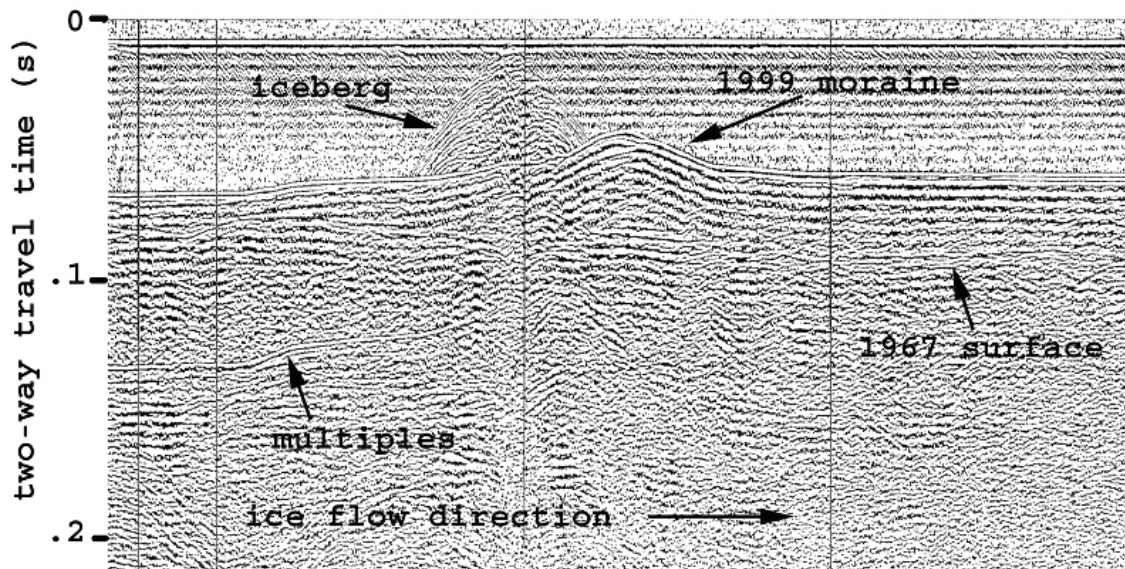
Figure 2-9: Acoustic profile in Taxpayer's Bay showing the terminal shoal built during the most recent surge, and the surface overridden during the penultimate surge (1967). While material above the continuous reflector thins from right to left North of the submarine shoal. The 1967 surface shows hummocks of low amplitude (at ~0.08 s from the top of the profile).

appear to be truncated by more recent events. The difficulty of identifying a clear 1967

surface in the westernmost basin is taken into account in the analysis of the record of

deposition; it has minor consequences because the bulk of the sediment accumulation

since 1967 occurred in other basins. The sub-bottom reflector identified as the 1967 bed

surface and the lake bottom were digitized in ArcInfo. Triangular Irregular Networks

(TIN) defining the bathymetry and subsurface elevation over the entire lake system were

rasterized into 10x10 m cells. Two-way travel times were transformed to elevation

relative to mean water level with a geoacoustic model accounting for sediment and lake

water properties (Hamilton and Bachman, 1982). I used mean values of lake water

conductivity (1.5 mS/cm) and temperature (1.5°C) to derive a constant sound velocity in

water (1420 m/s) and to compute bathymetry. Low conductivity combines with low

temperature to lower sound speed and easily cancel the opposing effect of pressure in

water that is at most 210 m deep. I calculated the constant ratio of sound speed in lake

bottom sediment (a medium-size silt of 5 on the phi scale) to bottom water sound speed.
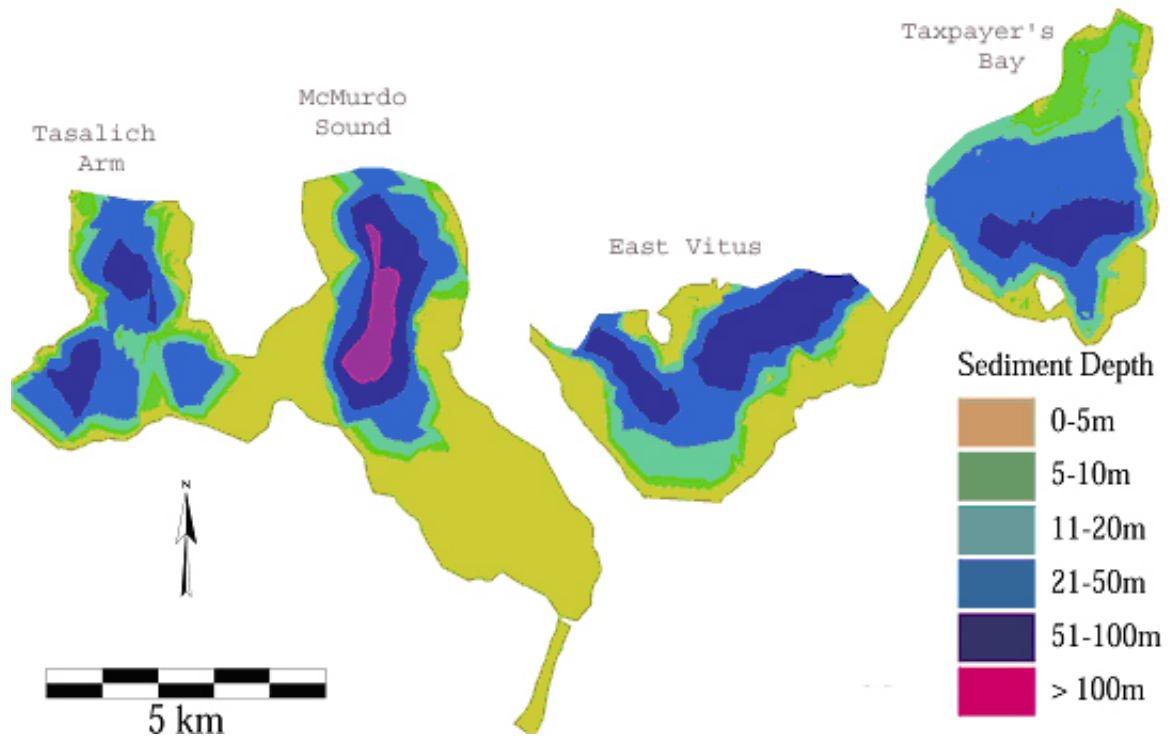
Figure 2-10: Isopach map of sediment thickness above inferred 1967 surge surface in Vitus Lake.

Finally, I discretized travel time to integrate the velocity-depth function and compute

subbottom reflector elevation (Hamilton, 1985). Differencing these two surfaces yielded

the distribution and thickness of sediment deposited in Vitus Lake since 1967 (fig. 2.10).

As noted earlier, the easternmost basin of the lake complex (Tsiu and Tsivat lakes; fig.

2.2 and 2.11) nearly filled with sediment deposited during and immediately after the 1993-94 surge. Tsivat Lake practically disappeared in 1994 and became largely the site of a large sub aerial sediment delta. Sediment is transported out of these lakes toward Taxpayer's Bay via Abandoned River (fig. 2.2), a steep bouldery channel that was reactivated when advancing ice closed the ice marginal channel between the eastern lakes and Taxpayer's Bay. Continuous monitoring of turbidity and stage ~200 m downstream
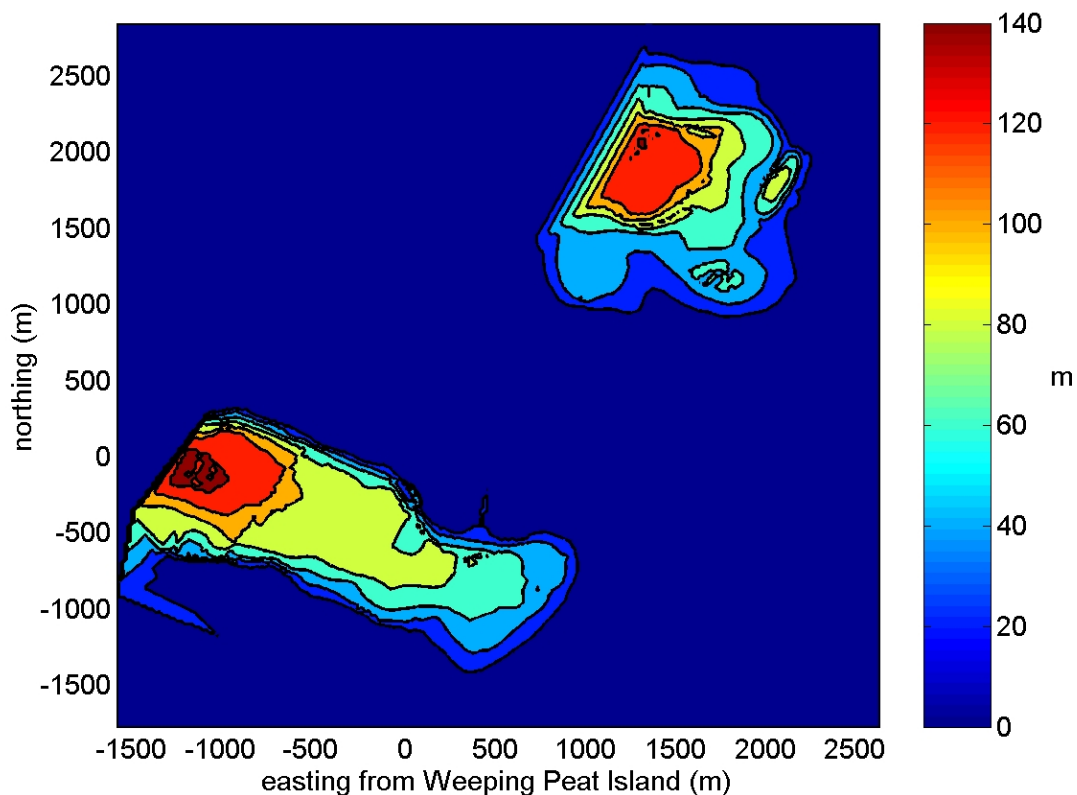
Figure 2-11: Sediment accumulation in Tsiu Lake (lower left corner) and Tsivat Lake (upper right corner) for the 1992-96 period based on differential bathymetry. These small basins separated by Weeping Peat Island were almost filled in during the floods punctuating the 1993-1994 surge.

from the Tsiu lake outlet confirmed high sediment flux for much of the duration of the study (sediment concentrations up to 15g/l); however, conditions were too extreme for the instrumentation and the location too remote to enable the acquisition of sufficient data

to compute sediment transfer between reservoirs. The difficulty of reaching these basins

with the survey boat forced us to forego plans to profile them with the seismic system.

Instead, to estimate lake sedimentation, I relied on bathymetric data collected in both

basins with an inflatable craft in 1996 (with Austin Post, USGS), and baseline

bathymetry recorded by P.J. Fleisher and co-workers in 1992. The subaerial delta is of

low relief (a fraction of 1m above the lake level) and I neglected the fraction above water

level in the analysis. Differencing the bathymetries allowed computing the volume of

sediment accumulation for the 1992-96 years in the easternmost sector of the Bering

terminus (fig. 2.11).

Table 2	Basin Area (km2)	Sed. Volume (km3) above 67 surface *	Mean Sed. Thickness (m)	Max. Water Depth (m)
MacMurdo Sound	22.1	.44 ± .15	20	120
East Vitus	15.3	.4 ± .11	26	90
Taxpayer's Bay	14.4	.37 ± .11	25	35
Tashalich Arm	11.8	.27 ± .13	23	210
Tsiu Lake and Tsivat Lake	3.21	.22 ± .05	68	20

* These sediment in Tsiu and Tsivat Lakes were deposited during the 1992-1996 period

The largest basin, McMurdo Sound, features the thickest and largest sediment pool in the

lake (max. 120 m; table 2). East Vitus Lake features 2 large sediment pools that together

collect the 2nd largest volume. A significant amount of the material found in the eastern

part of East Vitus was transferred via the Narrows from Taxpayer's Bay; very turbid

water exited the Narrows and sediment was often seen flocculating as it encountered

waters under greater tidal influence in East Vitus Lake (large gradients in conductivity

were recorded across this migrating boundary between clear and turbid water). The 3rd largest volume of material in the lake is in Taxpayer's Bay; much of it appears to be coarse debris delivered by Abandoned River from the Eastern sector. In turn, Tashalich Arm features a moderately thin layer (4-15m) of laminated sediment that overlaps a thick, consolidated and disturbed material of uncertain age. Although Tsiu and Tsivat lakes are the smallest sediment reservoirs of the lake system, they have the thickest accumulation of new sediment. They also contained the smallest sediment volume of the entire lake complex, which is likely not representative of sediment flux into the basins since much sediment is transferred to Taxpayer's Bay. Unfortunately, trying to put bounds on the transfer of sediment from Tsiu and Tsivat lakes to Vitus Lake over the time period of the study is an uncertain endeavor. If I assume that the suspended sediment load estimated from continuous monitoring at Abandoned River from June to November 1998 (11 megaton of sediment) is representative of the yearly sediment transfer from the Eastern sector to Taxpayer's bay for the 1992-96 period, I compute a Bering Glacier sediment output into Tsiu/Tsivat basin that is marginally greater than the amount computed through differential bathymetry alone (~19% greater); however, sediment transport out of the 2 eastern lakes could potentially be much greater than suggested by the 1998 sediment transfer estimate because significant increases in water discharge and sediment concentration are probable during floods. Another line of evidence pointing to greater sediment delivery in Tsiu/Tsivat basins than suggested by the volumes reported in table 2 (Tsiu/Tsivat basins account for 1/5 of total sediment volume) is that the Abandoned River water discharge is approximately 1/3 the magnitude of the Seal River discharge (Josberger et al., 2006; this study), which suggests these basins receive a greater fraction

68

of sediment volume since sediment delivery should scale with water flux in this glacifluvial dominated system. Total post-1967 sediment volume in the entire lake system, excluding the 1967-1991 deposition in the smallest eastern basin, is $1.80 \pm .36$ km^3.

2.6.2   Uncertainty of the methods and sediment volume

Several potentially significant sources of uncertainty can be assessed: The nearly horizontal lake bottom across sediment pools and low amplitude subsurface relief result in low sediment thickness gradients which help mitigate the positioning error. Assuming that a 50 m wide column of mean sediment thickness around the perimeter each basin is equivalent to the maximum volume error that can be imparted to positioning, results in a conservative error estimate of a few 1000th of a percent. Respectively, the error induced by the density of seismic tracklines and by selecting accurately the chosen reflectors in ArcInfo is estimated to be 10% and 2-5% depending on sediment thickness.

The fraction of the sediment package composed of coarser and denser material varies between basins, which may result in different estimates of sound velocity since the speed of sound in sediment is a strong function of bulk density, which can be empirically modeled from particle size (Hamilton and Bachman, 1982). For the first estimate of sediment volumes (Table 2), I assumed that silt-size material entirely composed the sediment package above the inferred 1967 surface even though almost all profiles showed the presence of more reflective and discontinuous seismic facies (sand, gravel and diamicton), especially in East Vitus Lake and Taxpayer's Bay. Computing sediment volume by using an acoustic velocity resulting from coarse sand (1820 m/s at the

69

interface between silt and sand size material) for the bottom 20% of the sediment column suggests that sediment volume could be underestimated by up to ~5%. The total error induced by the sampling and data processing methods therefore amount to ~20% of the sediment volume.

In order to provide a robust approximation of sediment volume and of multi-decadal erosion rate, I exclude part of the sediment from the volume estimate. In places, more reflective chaotic facies in the acoustic profiles make identifying the 1967 surface an uncertain proposition. Thus, I exclude 50% of the sediment package in Tashalich Arm due to the lack of a decisive relationship with a continuous sub horizon; yet, I retain the acoustically transparent material in that part of the basin that was overridden by ice in 1993-1994. I also exclude the coarser fraction of the material in the lower part of the profiles taken in East Vitus Lake for the same reason as above (~15% of sediment package in the lake). I include all sediment in McMurdo basin due to its clearly unconsolidated lacustrine appearance in the seismic data, and in Taxpayer's Bay since much of the material is coarser debris transferred from the eastern part of the lobe. The Taxpayer's Bay sediment volume is in fact an underestimate due to the difficulty of identifying a basal reflector underneath part of the Abandoned River fan and the relevant reflector beneath disturbed material in front of retreating ice. Moreover, the sediment volume initially computed for Tsiu and Tsivat lakes does not account for deposition that occurred from 1968 to 1992, although part of it is bound to have found its way to Taxpayer's Bay after the basin was almost filled in 1994. The revised total volume of material in the Bering Glacier proglacial lake complex is $1.61 \pm .32$ km^3, which is 11% smaller than the original estimate.

2.7 Erosion and sedimentation at Bering Glacier

Spot comparison of 1991 and 1993 Vitus Lake bathymetry acquired by USGS workers (Molnia et al, 1996; map of Bering Glacier lobe by Austin Post, unpublished) to 1999 data suggests that approximately 50% of the sediments deposited since 1968 in MacMurdo Sound, East Vitus, and Taxpayer's Bay were deposited in or around the 94 surge. In turn, the same comparison in Tashalich Arm showed no deposition after 1993. The differential bathymetry method (1993-1996) used for the eastern most basin (Tsiu Lake and Tsivat Lake) doesn't allow the same comparison because the surface overridden in 1967 is unknown. High rates of sedimentation in deep pools in the 3 before-mentioned basins could result either from glacier advance closer to the deep part of the basin or because of an increase in sediment delivery by large water discharges during the surge. In a few places, the 1993 bathymetric surface may be distinguishable due to the presence of more reflective horizons indicating a change in depositional environment and delivery of coarser material as the terminus rapidly moved toward the southern end of the lake during
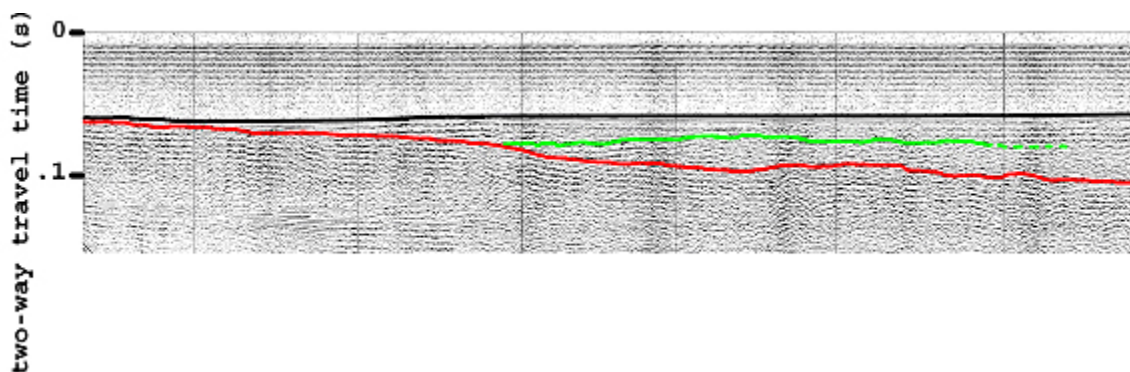
Figure 2-12: 1993 surge surface (green) in Taxpayer's Bay approximately halfway between the 1967 surge surface and 1999 bathymetric profile. Ice flow direction is from right to left.

the surge. In such cases, the sediment deposited during the surge amounts to approximately half of the total package (fig. 2.12). The disproportionate amount of sediment pulsed during the surge is consistent with the temporal evolution of suspended sediment fluxes through the Seal River (table 1). Even though proximity to the terminus necessarily implies greater local sedimentation, jokaulhops may well have occurred in parts of the lobe other than the Eastern sector since an unobserved peak in water discharge was recorded in mid-August 1994 at the Seal River station (Merrand and Hallet. 1996), whereas a corresponding abrupt stage rise was not recorded at that time in Tsiu/Tsivat Basins (unpublished data from Dennis Trabant, USGS). It should also be noted that the sediment record contains two early retreat phases since it includes deposition that occurred during the 1996-99 period. It thus represents slightly more than a single surge cycle of rapid advance and slow retreat. It is also likely that a significant fraction of the new material is reworked sediment that was deposited upstream from the 1999 ice margin during the inter-surge. A few studies of South Alaskan fjords have documented rapid lowering of the glacier bed, up to several meters per years, by glaciers overriding previously deposited outwash (Motyka and Echelmeyer, 2003; Motyka et al., 2006). It is also probable that a fraction of the sediment deposited during the inter-surge was not remobilized during the latest advance and remains under the terminal lobe. The lack of data for regions still under ice at the time of the study offset the inflationary effect of including the years 1996-99 in the volume computation. Surveying Vitus Lake after the ice has retreated near its 1993 margin may provide a better estimate of sediment during the intersurge, yet the sediment has been overridden, deformed and topped with a layer of till which would probably prevent effective identification of the limiting horizon.

The sediment leaked out of the proglacial lake system to the ocean over the course of the study amounts to 4% of the revised sediment volume. It is possible that sediment leakage may have been significant in the early stage of the retreat after the 1967 surge since the ice margin was close to the lake outlet; however, it is probable that little sediment escaped during most of the inter-surge as the ice front retreated farther from the outlet. Aerial photographs taken during the inter-surge period show sediment plumes streaming out of the Seal River and veering westward toward Kayak island; however, sampling of Seal River water during the post-surge years shows that little suspended sediment is needed in surface waters to give a turbid appearance to water exiting the lake complex to the Gulf of Alaska. Assuming that sediment fluxes through the Seal River during the inter-surge years occurred at a rate similar to the post-surge rate measured from 1996-99, total leakage adds up to ~7% of the total sediment yield for the period since 1968. The sudden decrease in sediment leakage in post 93-94 surge years is informative. The glacier had barely began retreating into deeper water by late 1995; it is thus probable that the drop off in Seal River water sediment concentration starting in 1996 results from either or both of waning sediment supply and less flashy discharge. The record does not allow differentiating between these 2 possibilities; however, large water pulses due to heavy summer rain occurred after the surge (in particular in 1997). Since sediment fluxes usually scale with the magnitude of water discharge in transport-limited systems, low sediment yields through the Seal after large rainstorms may suggest that sediment stores available for transport were limited.

2.7.1 Basin wide erosion rate

In order to estimate a time and spatially averaged erosion rate, I calculate the mass of material found in Vitus Lake from sediment density and the volume of sediment. Although a smooth depth function of density is only an approximation, particularly in glacial deposits that vary considerably in lithology and consolidation, I use Hamilton and Bachman's model (1982) to derive a first estimate of mean dry bulk density of 1.73 tons/m^3. To do so, I again assume a conservative mean grain size of 5 phi units, similarly to that used in the sound velocity model. Very few studies report the dry bulk density of glacimarine sediment composed of multiple facies; one such study recorded dry bulk densities ranging from 1.7 to 2.1 tons/m3 in a sediment core collected on the continental shelf off Vancouver Island in British Columbia (Cosma and Hendy, 2008). The core was composed of ~20% clay and ~40% silt and ~40% sand and larger lithic debris. In turn, a few shallow sediment cores (<2.5 m) collected within kilometers from glacier termini in Icy Bay (~150 km East from Vitus Lake) exhibit dry bulk densities ranging from 1.07 to 1.39 tons/m^3 at 2.5 m depth (Jaeger and Nittrouer, personal communication). In view of the dry bulk density reported by Cosma and Henry, the mean density estimate calculated with the Hamilton model is on the lower side of what could be expected for a glacio-lacustrine thick sediment pile of mixed facies. Similarly, the bulk density recorded in shallow core at Icy Bay reflects on homogeneous, not very compacted fine material settling out of fjord water a fair distance away from the ice front. Given the mix of ice proximal and ice distal facies found in the lake complex, I chose to calculate sediment load using a dry bulk density range of 1700-2000 kg/m^3. Accordingly, the sediment load above the 1967 surface in Vitus Lake is $3 \times 10^3 \pm 0.8 \times 10^3$ tons.

In ArcInfo, I computed a Bering Glacier drainage basin area of 4,773 km^2 from the 90 m DEM. I assume a mean basin wide bedrock density of 2.7 tons/m^3, an arguable median density for a wide range of lithologies (from poorly cemented sandstone to mafic rocks). The basin wide erosion rate for the 32 year period between the 2 surges is 7.2 ± 2 mm/yr. I have discussed the possibility of subglacial remobilization of stored sediment, which could be significant in overdeepened regions. Yet, in the absence of great change in mean glacier extent over the 1967-99 period and widely fluctuating precipitation, changes in surface slope according to the phase of the surge are likely to be the main control on storage under the terminal lobe. Change in storage is thus likely cyclical, and there is little reason to think it would be significantly different between surges of similar extent.

2.7.2 Subaerial contribution

The magnitude of subaerial storage change along the lateral margin of the glacier following the ice surface draw down can be assessed to understand what fraction of the sediment yield can be attributed to glacial erosion or remobilization of material by subaerial processes. I estimate the volume of morainal material that could have been transported by marginal water channels toward Vitus Lake assuming that sediment remobilized resulted from lateral moraine slope relaxation between the modern ELA and the terminal lobe, and that the ice surface lowering incurred since the last surge is a linear function of the ice surface draw down that has occurred since the LIA. Remobilized material computed for relaxation of an initial 45° morainal slope to the angle of repose over 130 km of lateral margin would amount to 3% of total sediment volume. 130km of

lateral moraine remobilization is an overestimate since the LIA ELA was far downstream from the present ELA; however it is also likely that ice surface draw down was greater at lower elevations than that observed near the present ELA. Although there is evidence of landslide deposits originated through mass failure of ridge slopes on the glacier surface, we stress that all valleys and many ridges are covered with ice except for the steeper slopes of interfluves. Cold ice protects all topography above ~2500m according to model results (Merrand and Hallet, in prep.) and since glacial erosion of this landscape has occurred over most of the past 5 myr in this very active tectonic region (1cm/yr over the Holocene; Plafker et al., 1989), topographic interfluves are expected to be near a limiting height and to lower at a temporally averaged rate that is similar to the glacier incision rate. No tributary valleys has deglacierized since the LIA thus no large single sediment package possibly impounded behind the lateral ice margin could have been remobilized by surface waters and transported into Vitus Lake. If I assume further that, on the average, ridges lowered at the rate of glacial incision, and I generously approximate the average length of ice-free slopes (2000 m) along 200 km of the glacier margin, I find that another ~2% of the total sediment found in Vitus Lake could be imparted to the lowering of interfluves. The new estimate of glacial erosion rate is then 6.8 ± 1.9 mm/yr. Although these estimates are based on simple idealizations, they likely provide an upper bound on the amount of sediment of non-glacial origin and an order of magnitude of the potential subaerial contribution to the sediment budget at Bering Glacier. I conclude that as long as most of the landscape is covered by ice the subaerial contribution to the sediment budget is minor.

2.7.3   Remobilization of earlier Holocene sediment

The presence of early Holocene marine fossils (7600 to 13200 y.b.p.) on the foreland in reworked subaerial deposits, especially in the western sector at Tashalich Arm, highlights the possibility that a fraction of the sediment found above the 1967 surge surface was stored subglacially for a period much greater than the 32 years of deposition used to compute this sediment budget. The fossils, mostly bi-valves and gastropods, included very delicate shells (Pasch et al., 2010). Approximately 13% of the fossils were whole; the remainder was composed of fragments. The bi-valves occasionally contained fine silt and the fossil fragments had broken edges that showed little wear thereby indicating they were not transported in subglacial melt water channels or within a deforming layer of diamicton. Instead, these observations imply that shells were probably encased in basal ice during transport; such ice can form due glaciohydraulic supercooling, which is known to occur at Bering Glacier. Since glaciohydraulic supercooling occurs on the reverse bed slope of overdeepenings when decreasing ice overburden raises the freezing point of water, basal freezing and entrainment of fossils are likely on the slope rising out of the overdeepening North of Vitus Lake. The location of a shoreline that would have provided a fitting environment for intertidal marine species is uncertain; however, topographic highs in the substrate of a marine embayment may have provided this suitable habitat. One such location has been identified; it is on the western shore of Tashalich Arm where boring and nestling clam fossils (~5000 y.b.p.) have been found in a bedrock outcrop reaching 4 m above present lake level (Molnia and Post, 1995; Shennan, 2009).

Sediment flux in basal ice has been shown to be a small fraction of the total sediment flux of coastal South Alaskan glaciers where glacifluvial sediment transport largely dominates the modes of sediment delivery to the glacier terminus (Hunter et al, 1996a &b). Transport of sediment in basal ice at Muir, Margerie, and Grand Pacific Glaciers at Glacier Bay amounts to <1% to 8% (3% on average) of the sediment volume transferred to the glacier terminus. If I assume that subglacial accretion of older sediment at Bering Glacier is at the upper end of the data range acquired in Glacier Bay and subtract it from the sediment volume above the 1967 reflector in Vitus Lake, the mean glacial erosion rate is reduced to 6 ± 2 mm/yr.

2.8 Discussion and conclusions

Sub-bottom profiling of Vitus Lake, bathymetric surveys of Tsiu and Tsivat Lakes, and monitoring of sediment exiting the lake system allowed to conservatively estimate a sediment flux of $5 \times 10^7 \pm 10^7$ m^3/yr at Bering Glacier between 1968 and 1999. This approximation is within the range of sediment fluxes for South Alaskan glaciers with proglacial sedimentation records longer than 10 years (Hallet et al., 2006); however, it is at the low end of the range of specific yields for South Alaskan glacial systems of comparable size (Bering Glacier specific sediment yield for 1967-1999: 2×10^4 ton/km^2/yr).

Turbidity and water discharge measurements in the Seal River, the only outlet of the system during the course of the study, show that Vitus Lake is an efficient sediment trap except during major subglacial flood outbursts and during surges when the ice front closes in on the distal end of the overdeepening in the Bering Glacier foreland. Sediment flux to the ocean through the Seal River over the entire surge/non-surge cycle was an

estimated 6.5% of the total sediment flux at Bering Glacier from 1967 to 1999. Approximately half of these 6.5% escaped the sediment trap during the 2.5 years following the beginning of the surge.

Survey of the sediments in the lakes reveals that McMurdo Sound is the basin with the greatest glacial sediment volume in the proglacial lake complex (table 2). Although there is no direct information on massive glacial water discharge in McMurdo Sound, the sedimentation record indicates that it is probably where much water and sediment exits the glacier. In spite of exhibiting the highest sedimentation rates, the Tsivat/Tsiu basin is one of two basins showing the smallest post-1967 sediment volume of the lake complex; this is so despite the massive amount of sediment deposited during the well-documented 1994 flood in Tsivat basin. There is however considerable uncertainty in the amount of sediment transferred from the Tsiu/Tsivat basin to Vitus Lake, and hence, the volume of post-1967 deposit delivered to the easternmost basin can only be estimated roughly. Among all basins, Tashalich Arm stands out: it is the deepest basin of the lake complex and it contains the smallest post-1967 sediment volume of all basins. Increasing reflectivity of chaotic horizons imparted to ice-proximal facies in acoustic profiles as one moves East along the ice front and the composition of the large Tsivat Lake sandur (silt, sand and gravel) deposited during the surge indicate that the fraction of coarse material is high in the Eastern basins. Sediment pile architecture in a few locations (Taxpayer's Bay in particular) suggests that thickness approximately doubled during and in the few years after the surge, hinting at the anomalously large transport capacity of subglacial and proglacial waters during this dynamic stage of the glacier.

Excluding half the sediment in Tashalich Arm and 15% of that in East Vitus Lake due to the uncertainty in the timing of deposition of ice proximal sediment, I compute an average glacial erosion rate of 6 ± 2 mm/yr for Bering-Bagley Glacier. Including the estimated contribution from interfluves to sediment volume translates into an erosion rate 5% greater for the entire drainage area upstream from the terminus. This erosion rate is much lower than for South Alaskan glaciers with existing multi-decadal data sets that show rates up to ~5 times greater. Koppes and Hallet (2002) have proposed that increased ice-flux and fast basal sliding during rapid tidewater glacier retreat from the LIA advance explain the very high erosion rates inferred from sedimentation in the region. The Bagley-Bering glacier system hasn't undergone fast or considerable retreat since the beginning of the 20th century, which may account in part for why calculated erosion rates are currently smaller at Bagley-Bering Glacier than for many coastal glaciers that retreated tens of km to the head of fjords since the end of the LIA. In addition, contrarily to retreating coastal glaciers, no tributary ice-free valleys with impounded sediment are within the range of terminus oscillations at Bering Glacier; the subaerial contribution to the sediment budget has thus been kept to a minimum. Subaerial erosion should remain a small component of the total denudation rate until further glacial retreat causes tributary valley to become ice-free and the release of temporary storage for glacial debris. Koppes and Hallet extrapolated modeling result to infer a long term erosion rate of 9 mm/yr for Tyndall Glacier in Icy Bay, which is ~100km east of Vitus lake, which is higher but comparable to the rate computed during this study. I have been very conservative in choosing options that would tend to minimize sediment volume in Vitus Lake and I could not account for material deposited post-1967 upstream from the 1999 margin. A cautious

analysis of the survey data and the lack of survey of sediment still under ice in 1999 could account for most of the remaining discrepancy between the rates of erosion at Bering versus other coastal glaciers in South Alaska. Consequently, 6 mm/yr is likely a lower bound on erosion occurring at Bering Glacier.

On the basis of sedimentation of the continental shelf since deglaciation, Sheaf and co-workers (2003) estimated a denudation rate of ~5 mm/yr for the coastal St. Elias Mountains, in the process discounting deposition in fjords since the LIA and transport off the shelf by longshore currents. This suggests that a rate of 6 mm/yr is in good agreement with Sheaf et al.'s estimate. Exhumation rates derived from bedrock and detrital thermochronology for the Bering-Bagley drainage area range from 1.2 to 3.6 mm/yr (Berger at al., 2008). Although the maximum thermochronological denudation rate for the windward side of the range is up to ~4 mm/yr, the range of data available for the Bering/Bagley basin is a fraction of the erosion rate presented herein; however, denudation rates averaged over the course of the Quaternary reflect on average climatic conditions that are colder than that averaged over the last 3 decades. Also, denudation rates derived from thermochronological data are sensitive to assumptions about particle path and thermal models of the crust. The presence of Yakataga sandstone and other sedimentary rocks in the foothills of the St Elias range suggests that models assuming vertical rock particle trajectories may underestimate exhumation. Alternatively, transients in sediment storage and delivery following the LIA may lead to overestimating incision rates at Bering-Bagley glacier since ice surface deflation may force a change in bed slope configuration. Quantifying erosion rates for massive temperate glacial systems that are

good proxies for lower latitude ice masses during glaciations remains an important

endeavor.

Chapter 3   Modeling erosion

3.1 Introduction

The steep net balance gradients of temperate coastal glaciers generate large ice

fluxes that are facilitated by rapid sliding, which makes them especially well suited to

study the subglacial conditions necessary to sustain high rates of erosion. The first order

approximation in the erosion rule of classical glacial landscape models is to let incision

scale with some measure of glacier sliding rate. This is a logical first attempt at modeling

the problem since all theoretical models suggest that the rate of glacial erosion increase

with the rate of sliding and the few empirical estimates available suggest that erosion

rates increase linearly with sliding rate (Humphrey and Raymond, 1994). Johannes

Oerlemans (1984) first attempted to quantitatively relate glacier dynamics to large-scale

landforms. He didn't ascribe a specific process to detach particles from the bed but

followed Budd et al.'s (1979) experimental approach by making erosion proportional to

the product of sliding velocity raised to a power less than unity (1/3), and effective

normal stress, N, and shear stresses, τ, at the glacier bed [$\dot{e} = f(N, U_s, \tau)$]. Oerlemans

found that basal normal stress doesn't have a significant effect on the distribution of

erosion since different model assumptions about water pressure distribution (constant

basal effective pressure versus lower effective pressure where ice is thickest) didn't

produce significantly different output; however, Oerlemans adopted the widely accepted

formulation in which sliding is inversely proportional to effective pressure. Erosion thus

scales with shear stress to the power of ~2 and effective pressure to the 2/3 power. This

erosion scheme combined with the prescription of a glacier width function that is exponentially decreasing with distance from the ice divide resulted in greater erosion and overdeepenings where ice flux per unit valley width is greatest. The resulting landscape does not differ significantly from that evolving out of a perfectly plastic slip-line model where erosion depends first on basal shear stress (Nye and Martin, 1967); yet, Oerlemans' study is an important first numerical effort toward understanding the genesis of glacier long profiles as the imprint of time-averaged climate on the landscape. Oerlemans also first proposed that glacial erosion is self-limiting unless tectonic processes regenerate the landscape necessary to sustain glaciers; however, Oerlemans' early model and most more recent models didn't attempt to account for the complexity necessary to assess how evolving subglacial hydraulics on seasonal to glacial cycle time scales contribute to the spatial and temporal distribution of erosion as displayed in the landscapes that have been shaped by temperate ice masses. More recent studies by MacGregor et al. (2000, 2009), and Anderson et al. (2006) also successfully modeled major elements of glacial landscapes by assuming erosion increases linearly with sliding. In these studies, and similarly to Oerlemans' test case, the piezometric water surface within the glacier was chosen to be parallel to the ice surface, thus forcing effective pressure to be lowest and sliding velocity greatest where ice is the thickest. In McGregor's model the relationship between sliding ice flux and incision rate is further underscored by the modeled impact of ice flux contributions from tributaries at valley confluences: topographic steps in valley longitudinal profiles

The climatically controlled glacial conditions likely to exert the greatest control on glacial erosion are 1) mass balance convolved with landscape hypsometry that dictates

the extent of glacier cover and ice discharge per unit width, and 2) the local state of stress at the glacier-substrate interface, and, in particular, its variation with thermal regime and subglacial hydrology. Although, the important role of water storage and transfer under temperate glaciers with respect to sliding and sediment evacuation has long been recognized, the effect of subglacial runoff and storage on the basal stress regime and on glacial erosion has received little attention. A novel dimension of my research is the explicit representation of subglacial hydraulics in a glacial model of landscape generation including, in particular, its role in decoupling ice from the bed, localizing the stresses imparted to the substrate (Rothlisberger and Iken, 1981; Iverson, 1991; Hallet, 1996) and evacuating the sediments produced by erosion.

To model numerically topographic evolution of an orogen in regions such as the South Alaska coast where glaciers are the dominant geomorphic agents, I assume major glacial growth and decay cycle over a 123ky glacial-interglacial period. Modern conditions of climate and glacier extent are assumed to be characteristic of the interglacial, and provide the constraints for calibration, and for evaluation of model performance. Before implementing sediment transfer and processes characteristic of tectonically active tidewater environments, I apply a "stripped-down" version of the model to a landscape of very simple geometry to examine the model's ability to simulate climatic controls on glacial extent and the glaciologic controls on crustal mass fluxes over glacial cycle time scale. This first set of model runs serves to assess and validate the model and its representation of how mass balance, glacial runoff, and thermal regime affect erosion and sediment production. In a second set of model runs, I use this stripped model to examine erosion along a longitudinal profile along the centerline of Seward-

Malaspina Glacier. Eventually, in Chapter 4, I introduce greater complexity step-wise to model landscape evolution for large temperate glacial systems at high latitude such as Malaspina and Bering Glaciers. These more complete models include important feedbacks that arise from interactions between processes, in particular 1) those affecting the location of overdeepenings through influences on runoff and sedimentation, and 2) those affecting local relative sea level by, including uplift, sedimentation, subsidence, and climate which collectively modulate major sinks of ice at calving termini and, hence, control ice extent.

3.2 Model development

3.2.1 Modeling strategy, valley geometry, and initial conditions

Glacial valley cross-sections are easily abstracted as a U-shaped trough and a ridge line separated by bedrock slopes at a threshold angle. I chose to develop the model the glacier and glacial erosion in one-dimension along the length of valleys that are transverse to a range while keeping the 2nd horizontal dimension of the earth landscape, valley width, time invariant. The model is therefore implemented to address the evolution of valley long profile, and ,in particular, the development of overdeepenings. Drainage network development, hypsometry and evolution of valley width are issues that I cannot address systematically with the present model formulation. Although letting basin hypsometry evolve would be very desirable, a multi-dimensional formulation and the associated increase in CPU time would demand significantly simpler formulation of the hydrologic and erosion sub-routines. Nonetheless, a one-dimensional numerical scheme as described above should capture well the important features of glacial valley evolution.

The initial long valley profile assumed for model runs is the inferred profile of the bed of Malaspina glacier based on the modern ice surface elevation and an educated estimate of ice thickness informed by radar observations in the ablation area (D. Trabant, unpublished data; Conway et al., 2009). Glacier width and its temporal evolution are based on a parameterization of valley geometry. Modern elevation-area profile and surface slope distribution are derived from a 90m DEM for the drainage basin. An effective width for the glacial basin is then computed through a summation of glacial area per altitudinal bin. The resulting plan form of the domain modeled is likely to be a good approximation for simple basins where no significant branching in the valley network occurs at lower elevation.

The parameterization of glacier width assumes parabolic valley walls in transverse cross-sections whenever the ice is confined between interfluves:

$$W = aW_{ref} + bW_{ref} \left(\frac{h}{h_{ref}} \right)^{\frac{1}{2}} \qquad \text{(Equation 3.1)},$$

where h is ice thickness, h_{ref} and W_{ref} are respectively the reference ice thickness and width, and the constants a and b are chosen to reflect the wide aspect ratio of large glaciers and the fraction of valley width which depends on a threshold ice thickness (defined as the mean glacier thickness) to be occupied by the glacier. When the glacier is allowed to spread on alluvial plains or the continental shelf, I adopt the quadratic dependence of glacier extent on ice thickness that is consistent with a uniform basal shear stress assumption. The formulation of width then takes the form:

$$W = aW_{ref} + bW_{ref} \left(\frac{h}{h_{ref}} \right)^{2} \qquad \text{(Equation 3.2)}$$

The second horizontal dimension in the ice flow model is incorporated through a valley shape factor. It is important for narrow valley glaciers, and has limited significance whenever the glacier half-width significantly exceeds twice the ice thickness, as is commonly the case for large South Alaskan glaciers. Centerline flow is then a good approximation for most of the glacier width (Raymond, 1980).

For this initial simplified model run, in order to decrease net mass balance to compensate for the lack of a major ice sink at the calving front, the typical maritime topography of South Alaska is raised by a few hundred meters because it lifts the drainage area to a zone of lower precipitation. Thus glacier extent is contained within the bounds of a reasonably sized domain. I also consider glacier width uniform and time invariant during this first set of model runs in order to further simplify the analysis of how ice flux affects valley profile evolution.

3.2.2   Climate forcing and mass balance response

I assume to glacier mass balance to vary in line with the marine isotope record in view of the high correlation between various glacial chronologies and the marine record. I use the SPECMAP $^{18}O/^{16}O$ ratio as the climatic proxy to modulate precipitation and temperature during the course of a climatic cycle (McIntyre et al., 1989; Imbrie et al., 1990). Temperature and precipitation rates are assumed to follow synchronously the benthic foraminifera $\delta^{18}O$ record. The decrease in precipitation rates with temperature represents the lowering of the moisture content of the atmosphere during cooler periods (Cuffey and Clow, 1997; Alley et al., 1993; Manabe and Broccoli, 1985). Departures in $\delta^{18}O$ from interglacial condition are assumed to represent a linear fraction of maximum

changes in sea level (-130m), temperature (-3°C), and precipitation (-20 %), realizing that little is known of the regional variance of these parameters. There is no data showing a change in moisture in the Gulf of Alaska during glacial times yet lower temperatures ought to result in lesser air moisture reaching the accumulation area of glaciers due to lower evaporation over the ocean.

Changes in temperature, precipitation and radiation affect the mass balance of glaciers so that the glacier geometry and velocity field adjust to new` rates of accumulation and ablation. As the dynamics of the ice respond to thickness changes induced by lasting climatic variations, the glacier geometry ideally adjusts so that the cumulative net mass balance vanishes and the glacier profile reaches steady state.

$$\int_s b(y)dS = 0 \qquad\qquad \text{(Equation 3.3),}$$

where $b(y)$ is the specific mass balance at elevation y and S the glacier area, The response time for glaciers to reach this equilibrium after a perturbation can be described simply by the volume response time-scale $\tau_i = -\dfrac{H_{ref}}{a_0}$, where H_{ref} is the reference maximum ice thickness (in meters) and a_0 is ablation (in meters per year) at the terminus in the datum state (Johanneson et al., 1989). This relation arises when expressing volume change in term of maximum ice thickness and equating the net change in ice volume over the initial geometry to that due to the change in glacier surface area ($\int_{S_o} \Delta b(y)ds = \int_{\Delta S} b(y)ds$). It is shown to be a good approximation as long as the initial and final dynamics of the glacier are similar. Assuming a glacial-interglacial range of ice thickness (500-2000 m) and terminus ablation rates (5-10 ma^{-1}) gives glacier response times of 10^1-10^2 years for

glaciers in a maritime setting ($a_0=0$). The shorter characteristic time is relevant to interglacial periods when the ice is thin and ablation the greatest.

Although surface energy models offer considerable physical realism in the analysis of energy exchange at the surface of glaciers, the lack of knowledge of the spatial and temporal variability of model variables, notably the large uncertainty contained in the parameterization of turbulent heat fluxes above the glacier surface, call for a simplified and efficient mean of computing glacier mass balance. Degree day models have been shown to be a good alternative for they give equivalent results and they are formulated in term of the best known meteorological parameters (temperature and precipitation) which are also the driving parameters of models involving climate change schemes (Braithwaite, 1985; Johanneson, 1995b).

Degree-day mass balance methods rest on the strong correlation between air temperature and the melt-rate of ice and snow. It is simplest to assume a linear relationship between the number of positive degree-days and ablation; one coefficient each for the melting of snow and ice are sufficient to relate degree-days to ablation. The distribution of temperature with elevation is modeled with the lapse rate pertinent to the climatic regime (5°C/km in maritime setting) whereas the spatial distribution of precipitation is modeled by assuming a precipitation gradient with elevation that is consistent with sparse available mass balance data: a precipitation curve reaching a maximum at 1000 m elevation reproduces best available net accumulation observations (Marcus and Ragle, 1970; Austin Post, personal communication). For the interglacial temperature sea-level datum of the ~200 km long coastal region that includes Bering and Malaspina Glaciers, I assume a normal distribution about the average of the historical

90

(nearly 60 years) monthly mean temperature for the nearby towns, Yakutat and Cordova.

The monthly standard deviations of temperature are computed from the mean daily

observations over the period of record and are assumed to remain constant with elevation

and through time despite changing climate. The annual temperature time series and its

standard deviation are used to derive the probability of days with temperature below 1^oC

that would permit solid precipitation and greater than 0^oC to induce surface melt. Once

computed, the mass balance is compared to available mass balance data (Marcus and

Ragle, 1970; Holdsworth et al., 1989; Krimmel, personal communication; Meier and

Post, 1962; Post, personal communication; Sharp, 1951 and 1958; Merrand, unpublished

data at Bering Glacier) and model parameters (2 degree-day coefficients and slopes of the

precipitation curve) are tuned until modern mass balance under the current climate is

approximated closely. Integration of the local mass balance over the elevation-area

distribution determined from the glacier hypsometry provides a global check on the

calculated mass balance globally; the steady-state ice flux must vanish at the land-based

terminus.

3.2.3 Glacier profile along the center flow-line

In one-dimension, the vertically integrated equation for glacier mass conservation

is (Paterson, 1994):

$$\frac{\partial h_i(x,t)}{\partial t} = b(x,t) - \frac{\partial q(x,t)}{\partial x} \qquad \text{(Equation 3.4)},$$

where the ice flux per unit width: $q(x) = \int_h u\,dy$. Changes in glacier surface elevation are

related to ice flux divergence and the net source or sink term of water comprised of

precipitation and melt (mass balance). For a glacier in equilibrium with climatic forcing,

91

the first tem in equation 3.4 vanishes and the ice flux is the mass balance flux. For each

glacier cross-section, the balance flux, Q_{bal}, for a full seasonal cycle is the net

accumulation over the upstream glacier surface area: $Q_{bal} = \int_s b(z)dS$, $b(z)$ is the

elevation-dependent net accumulation over S, the glacier surface upglacier of each cross-

section. In the absence of basal sliding and assuming incompressible viscous flow in

simple shear down an infinitely wide channel (laminar flow), the discharge due to

deformation of polycrystalline ice is (Paterson, 1984):

$$Q_{dyn} = \frac{2A}{n+2}\left(f\rho_i g \frac{\partial h_i}{\partial x}\right)h_i^{n+2}W(x) \qquad \text{(Equation 3.5)},$$

where h_i is ice thickness averaged over the glacier width and W is glacier width, f is a

valley cross section shape factor that accounts for valley wall drag in retarding flow, A is

the Arrhenius coefficient of Glen's flow law that is held constant, n is a power coefficient

widely chosen to be 3 according to the mean value found in the literature, ρ_i is ice

density, g is gravitational acceleration, $\frac{\partial h_i}{\partial x}$ is the surface slope averaged over 4 to 10

times the ice thickness (Kamb and Echelmeyer, 1986). The shallow ice approximation

assumes that, for each column of ice, the driving stress is balanced by basal drag;

however, sidewall drag cannot be neglected for many valley glaciers. The valley cross-

section shape factor, f, becomes significant when the valley cross-section aspect ratio

($\frac{h_i}{W}$) increases to values greater than ~0.1 (Paterson, 1994).

Equating balance discharge to the sum of discharges due to internal deformation

and basal sliding (treated in next section) while solving the equilibrium equations for

basal stress with the thin parallel-sided slab assumption [$\tau = \rho g (y_{surf} - y_{base}) \dfrac{dy_{surf}}{dx}$] gives

an ODE in term of ice thickness and surface slope. Mass balance flux is computed on a

staggered grid and passed to a second and third order Runge-Kutta ODE solver (Matlab

ODE23s) to derive a glacier surface profile starting at the terminus where ice thickness is

set at 20 m. At the crest of the range, the left side of the domain, I impose a boundary

condition that represents an ice divide with a vanishing ice surface gradient, and hence

ice flux. At each time increment the scheme is iterated until solutions converge with

residuals set at less than 2% of glacier volume. No greater convergence is sought; first

because no greater accuracy is necessary for our purpose and second because it is

unlikely that the shallow ice approximation applied to glaciers resting on uneven terrain

permits much better accuracy, especially from the mountain front to near the range divide

where topographic gradients are the steepest and most variable. For each time step the

new ice thickness is computed from the previous ice surface, except at t = 0, when ice

thickness is set to 0 and derived from applying mass balance to valley hypsometry and

iterating until steady state is reached.

3.3 Glacier sliding

Due to the relative paucity of direct observations of glacier soles well within ice

margins and the complexity of basal conditions understanding of how glaciers slide over

their beds is limited but several theoretical formulations for sliding have emerged.

The classical theory (e.g. Weertman, Nye), which disregards the important effects

of subglacial hydrology, fail to account for rapid sliding (Bindschadler, 1983; Raymond

and Harrison, 1987) and the seasonal speed up observed on many glaciers during the

onset of melt in spring. Lliboutry (1968) first suggested that the functional form for sliding should account both for basal shear stress and effective pressure because it controls the extent of drowning of roughness elements. Seasonal injection of water at the bed increases cavitation in the lee of bed obstacles once local ice pressure is less than the water pressure, thus changing the extent of separation between the glacier and its bed (Iken et al., 1983). The ice flux due to sliding thus depends on the transient relationship between climatically controlled surface melt or liquid precipitation, and the evolving storage capacity of the subglacial water network, as well as the basal shear stress and bed roughness. Laboratory experiments (Budd et al., 1979), field observations (Bindschadler, 1983), and further theoretical work (Fowler, 1987a) suggested a relation of the form:

$$U_{slid} = A_s \frac{\tau^n}{N} \qquad \text{(Equation 3.6)},$$

where A_s is an adjustable parameter that represent bed and ice properties (water content, ice fabric) and bed roughness, τ is the basal shear stress taken to be the driving stress since longitudinal coupling is ignored, and N, the effective pressure ($N = P_i - P_w$) is the difference between the ice pressure and water pressure. The power-law coefficient n is chosen to be 3, which is a common value used for ice masses characterized by high rate of sliding (Paterson, 1993).

3.4 Glacial Hydrology, water storage and subglacial water pressure

Periods of surface uplift and high surface velocity that last several days commonly occur during periods of great surface melt or rain, especially during spring at the onset of the glacier melt season, or during subglacial water outbursts (Muller and Iken, 1973; Hooke et al., 1983; Iken et al., 1983; Iken and Bindschadler, 1986; Kamb and Engelhardt,

1987; Hooke et al., 1989; Denner et al., 1999; Zwally et al., 2002; Sugiyama et al., 2007).

Many field studies support the notion of linkage between seasonal high rates of sliding

and high subglacial water pressure and increases in subglacial water storage

(Rothlisberger et al., 1979; Holmlund and Hooke, 1983; Iken et al., 1983; Bindschadler,

1983; Iken and Bindschadler, 1986; Kamb et al., 1994; Blake et al., 1994; Raymond et

al., 1995; Jansson, 1996; Iken and Truffer, 1997; Harbor et al., 1997; Hanson et al., 1998;

Harper et al., 2002; Sugiyama and Gudmunsson, 2004; Anderson et al., 2004; Harper et

al., 2005). Drowning of bed roughness by water storage is likely to play a significant role

in reducing basal drag and increasing basal sliding, and hence, glacier flow. These

observations suggest that the rate of water input to base of the glacier relative to the rate

of outflow is critical in determining water pressure and effective bed roughness because it

controls the subglacial and englacial change in water storage. Theoretical models show

that water pressure fluctuations at the base of glaciers result from 1) variations in water

input rate as dictated by seasonal and diurnal climatic cycles, and 2) the storage and

conveyance capacity of temporally varying cavity and tunnel networks. Nye first showed

quantitatively that cavities filled with water close in unless water pressure equals the ice

overburden (Nye, 1953). Heat dissipation by moving water will melt cavity walls thereby

enabling ice conduits to exist when water pressure is somewhat less than ice pressure as

long as water is flowing. The size and geometry of subglacial cavities (up to 10's of m)

and conduits evolve because of a) the melting of walls by the friction and heat dissipation

of flowing water, b) the basal motion over bed topography and c) creep closure due to the

ice overburden exceeding water pressure (Rothlisberger, 1972; Iken, 1981; Rothlisberger

and Lang, 1987; Shreve, 1972; Walder, 1986; Kamb, 1987; Fowler, 1987). Conduit

geometry also affects the changes in melt rate and creep closure of conduit walls associated with discharge fluctuations (Hooke et al., 1990; Hooke, 1998).

3.4.1   Supraglacial and englacial runoff

Generalizations can be made about the seasonal evolution of glacial hydrology, and network morphology starting with the onset of melt and extending through the winter season. Before the melt season, the entire glacier is typically covered with winter snow and little liquid water percolates into the glacier unless an unusually large warm precipitation event occurs. As the melt season progresses, surface melt and rain percolate through the snow and the firn cover down to a saturated zone characterized by lower permeability; water is temporarily stored within the firn aquifer, which dampens the amplitude of diurnal runoff (Fountain, 1989; Schneider, 1999). Surface runoff occurs supraglacially within the firn or on the ice surface down glacier of the snowline until a crevasse and/or moulin captures the melt water and routes it toward the englacial network. It is very unusual for a surface stream to run directly off the glacier onto the surrounding landscape; most melt water eventually reaches the bed and exits the glacier laden with sediments via the subglacial water network outlets at the ice margins. Several authors have noted the weak hydraulic conductivity and probable low flow rate of intergranular veins in ice (Lliboutry, 1971; Fountain and Walder, 1998); these veins are thus not very likely to contribute significantly to the rapid infiltration of surface water to the bed as is the case during significant hydrologic events. Hydro-fracturing of water-filled crevasses, englacial tunnels and passageways melting their way downward have long been inferred to be the main means of water transfer from the surface to the bed. Fluctuations of water levels in moulins as basal water pressures increase suggest their

connectivity to the englacial and subglacial water networks. Englacial tunnels are thought to travel downward into the ice toward the bed in a direction normal to equipotential surfaces, which dip upstream at 11 times the surface slope if water pressure equals the ice overburden (Shreve, 1972; Nye and Frank, 1973; Holmlund and Hooke, 1983; Holmlund, 1988; Raymond and Harrison, 1987; Fountain and Walder, 1998; Alley et al., 2005). Fountain and co-workers (2005) have identified a network of medium size fractures and englacial passages (.3-20 cm wide) in the upper ablation area at Storglaciaren in Norway, some of which actively transported water at the time of investigation. These fractures appear to be the main mean of water transport to the bed due to their frequency (at least 1 fracture per 100 m of ice) and the rarity of larger conduits. Studies of GPR velocity attenuation indicate that temperate glacier ice routinely contains 3-4% liquid water during the melt season (up to 7% around moulins and fracture zones), and 2% water in winter, which ensures some minimal flow during winter. Water content in ice has been shown to increase sharply at the elevation of the piezometric surface within the glacier as reflected by water level in boreholes (up to 4% at ~30m depth; Murray et al., 2000).

3.4.2   Conceptual subglacial hydraulic networks

Besides observations of recently de-glaciated surfaces, and those made in industrial tunnels excavated for water capture or in cavities near the ice margin, relatively little direct evidence exists regarding the morphology of water passageways and their networks in and under glaciers (Vivian and Bocquet, 1973; Walder and Hallet, 1979; Humphrey, 1987; Hooke et al., 1990). Consequently, models of water routing and its evolution are mostly guided by indirect evidence that include observations of water level in moulins near the surface and at depth with video cameras, borehole studies, dye tracing

experiments of supraglacial runoff, variation of pro-glacial discharges, sediment transport and water chemistry measurements, radar investigations, glacial surges and jokulhaups, and theoretical reasoning (Humphrey et al., 1986; Walder, 1986; Kamb, 1987; Fountain, 1993; Sharp et al., 1993; Humphrey and Raymond, 1994; Hubbard et al., 1995; Nienow et al., 1996; Gordon et al., 1998; Gordon et al., 2001; Flowers and Clarke, 2002; Jansson et al., 2003; Schuler et al., 2004; Vaughn and Fountain, 2005).

Field observations suggest that a poorly connected basal hydraulic system often coexists with a fast-flow tunnel network under the glacier. A distributed network of cavities in the lee of bed roughness and their connecting links result in slow water flow ($\sim 10^{-2}$m/s) and high water pressure over most of the bed, especially above the seasonal snow line. The conduits connecting the regions of pressure shadows are much more susceptible to disturbance by advection of the ice over the bed and control the rate of water flow down the hydraulic gradient. In turn, a dendritic system of larger channels (the so-called Rothlisberger or Nye channels) efficiently conveys water from the snow line to the margins characterized by flow velocities $>10^{-1}$m/s (Iken and Bindschadler, 1986; Kamb, 1987; Walder, 1986; Nienow et al., 1996) (fig. 3.1). Since, I consider the case of temperate maritime glaciers with considerable precipitation and melt, I first assume that conditions at the bed are erosion limited with most erosional product efficiently transported to the pro-glacial environment. Observations at Variegated Glacier suggest that at most a few decimeters of debris covered most of the bed (Humphrey and Raymond, 1994). Subglacial fluvial processes in such glaciers are expected to rapidly remobilize sediment overrun by ice during glacial advances such as observed in South Alaska (at rates averaging 2-3 m/yr at Taku glacier; Nolan et al., 1995) as well as other

maritime sub-polar environments (Bjornsson, 1996); hence, the following discussion

concerns non-deformable and effectively impermeable beds. The role of Nye channels

eroded downward into sediment is therefore ignored for the purpose of this
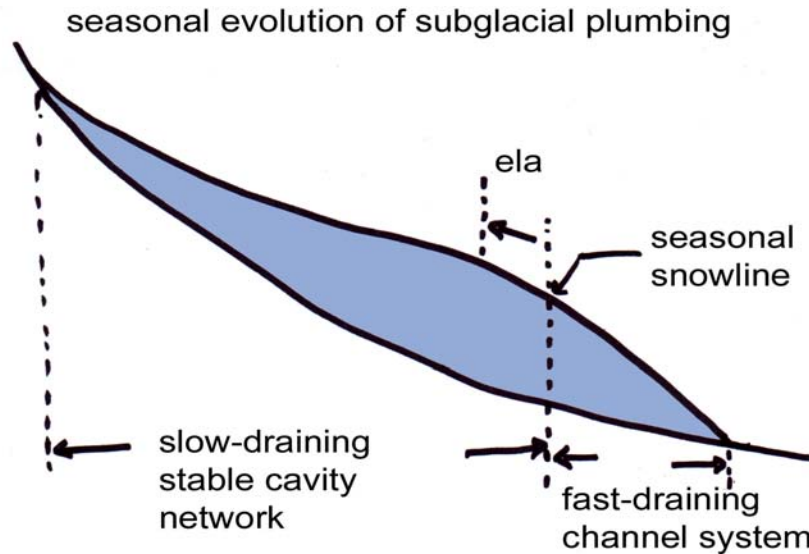
Figure 3.1: The 2 coexisting subglacial hydraulic networks under glaciers meet near the seasonal snowline.

discussion even though they are likely to be of significance during glacial advances over

outwash fans and continental shelves. Similarly, the role of subglacial aquifers in

conducting glacier melt to the pro-glacial environment will be neglected.

Despite the existence of systems of channels and cavities, sheet flow is likely to play a

role in lubricating bed regions not directly connected to the surface and that are remote

from the subglacial hydraulic network. The size of these regions is difficult to assess

because little is known about the frequency of injection points of water at the bed

especially in the accumulation area where little investigative work besides dye tracer

experiments in borehole has been done. The size of these regions subject solely to sheet

flow is likely to expand drastically during winter months in the absence of large surface

liquid input, decrease in bed separation, and slower basal motion. Basal melt generation

due to geothermal heat flux and sliding friction of ice over the bed contributes a small

portion of total subglacial water flux because it is 2-3 orders of magnitude slower than

surface melt and rain in sub-polar regions (10^{-2} m/yr versus 10^0-10^1m/yr); yet, basal melt

can be relatively significant outside the melt season and thus it is represented in the

model.

Although a large fraction of surface runoff probably gets to the bed through

conduits that eventually discharge into the established R channels draining the ablation

area of glaciers, increasing rates of water input at the bed in the spring initially

overwhelm the conveyance capacity of a mostly non-existent hydraulic network. Water is

injected along the bed and driven to the lee of bed roughness by stress gradients, which

causes widespread cavitation, increasing subglacial water storage and raising water

pressures. An overall decrease in effective roughness of the glacier-bed interface results

as bed separation increases and smaller roughness elements become bridged by larger

cavities. With sustained increases in water supply and pressure perturbations as the melt

or rainy season progresses, friction and heating by viscous dissipation in flowing water

enlarges cavities and their links rapidly. In the ablation area with abundant surface melt,

the network enlarges and conveys efficiently the water supplied to it; with continued

enlargement it eventually it reduces the water storage and decreases bed separation.

Subsequently, decreasing fall temperatures reduce liquid input to the subglacial network,

allowing conduit closure and a decrease in bed separation. In turn, the disruption of the

efficient channel network leads to renewed high water pressures (Fountain and Walder, 1998; Willis, 1995).

At any location under a glacier the state of drainage network development dictates local water discharge. Water pressure in conduits is usually less than ice overburden pressure, which implies that tunnels close in unless sustained by melting of conduit walls by heat dissipation of flowing water. Rothlisberger showed that at steady state, as tunnel enlargement by flowing water equals creep closure, water filled cylindrical tunnels show an inverse relationship between water discharge and water pressure gradient. This inverse relationship indicates that as the melt season advances and water discharge increases, larger channels with lower water pressure grow at the expense of smaller ones that have higher pressure (Shreve, 1972; Rothlisberger and Lang, 1987). In turn, Walder (1986) and Kamb and co-workers (1985) showed exactly the opposite for networks of slow draining cavities in the steady state for which discharge increases with water pressure gradient at constant effective pressure. This implies a tendency for stability of the distributed network of small cavities since it is not likely that water would flow against the pressure gradient to coalesce into bigger conduits needing higher water pressure; however, the cavity network becomes unstable and channelized if it is subject to large increases in discharge that cause lots of conduit wall melt (Kamb, 1987). An efficient arborescent network of fast flowing low pressure channels is therefore likely to expand up glacier with increasing discharge during the melt season and, in the process, linking previously poorly connected networks of high pressure cavities (Gordon et al., 1998; Nienow et al., 1998). The pressure over most of the bed above the seasonal snowline arises from water input rate and relative storage change in cavity regions.

Below the snowline, fast draining R channel water pressure is probably not representative of conditions over much of the bed in the ablation zone. Although low to atmospheric water pressures characterize channels during the low discharge mode of the diurnal cycle, adjacent areas exhibits high pressure often near ice overburden pressure (Haut Glacier d'Arolla, Nienow et al., 1998; Cascade glacier, Fountain, 1994; Bench glacier, Harper et al., 2005) indicating that poorly connected regions coexist with fast-draining channels in ablation areas of glaciers. The hydraulic pressure gradient points toward channels during low channel discharge and vanishes in the far field where poorly connected regions remain under high pressure. During high discharge periods like that characteristic of the peak of the diurnal cycle or during unusually warm and/or rainy events, the pressure gradient is reversed and water is driven away from the channel toward the bed. A pressure wave propagating away from channels is likely to also increase separation with the bed and increase connectivity with adjacent regions in the case of a hard substrate. However, below the equilibrium line altitude where subglacial drainage is channelized part of the substrate is covered at least in part with a thin debris layer (0.1-1 m thickness) such as was inferred at Arolla, Cascade, and Columbia Glaciers), in which Darcian flow is inferred (Nienow et al., 1998; Flowers and Clark, 2002). Pressure variations with magnitudes reaching a significant fraction of overburden pressures have been observed to propagate away from channels and dampen greatly within 10's of meters and essentially vanish within ~100 m where pressure is typically near overburden (Fountain, 1994; Hubbard et al., 1995; Nienow et al., 1996). An attempt at representing these subglacial networks in their complex space and time-dependent meter scales variations; hourly to monthly changes) details seems challenging and

fortunately unjustified within the spatial (1 km grid) and temporal (10^2-10^3 yr time steps) scales adopted for this model. Water pressure variations over regions with length scales of a few ice thickness (Balise and Raymond, 1985; Kamb and Echelmayer, 1986; Mair et al., 2001; Nienow et al., 2005) are necessary to induce significant change in surface motion because the basal drag induced by sticky spots in adjacent regions can be felt locally via longitudinal coupling. I solve for water pressure with simple schemes that are guided by the general principles of subglacial hydrology and the terminus boundary condition.

3.4.3 Slow-draining subglacial network and water pressure

To represent a subglacial network that is responsive to the climatic regime, in particular to temperature and liquid water input, I chose to formulate a model that is dependent on seasonal variations, in particular to the evolution of monthly mean surface-water production computed by the degree-day method. The computation of melt also accounts for water production arising from the heat dissipation of internal and basal frictions, and the geothermal flux. Melt water produced by the heat dissipation of viscous deformation equals the product of driving stress average over the ice column and deformational velocity, divided by the latent heat of fusion for ice:

$$Q_{mi} = \bar{\tau}_d \frac{U_d}{L}$$
(Equation 3.8),

Melt from basal friction scales with basal shear stress and sliding speed:

$$Q_{bf} = \bar{\tau}_b \frac{U_s}{L}$$
(Equation 3.9).

Cumulative monthly mean water production by rain, surface, internal and basal melt ranges 3 orders of magnitude along the glacier profile over the course of one year (fig.

3.2). Although local water production decreases along with temperature and precipitation by an order of magnitude during full glacial conditions, the cumulative melt and rain is one order of magnitude greater at the terminus during the full glacial because of greater contributing ice area.

To simplify the numerical model, I assume that the conveyance capacity of the distributed network at steady state is known and equivalent to the mean monthly cumulative melt and rainwater input per unit drainage area since the divide. Since I want to avoid modeling change in basal water storage explicitly yet retain its role in decoupling the ice from the bed within the distributed network region, I further assume
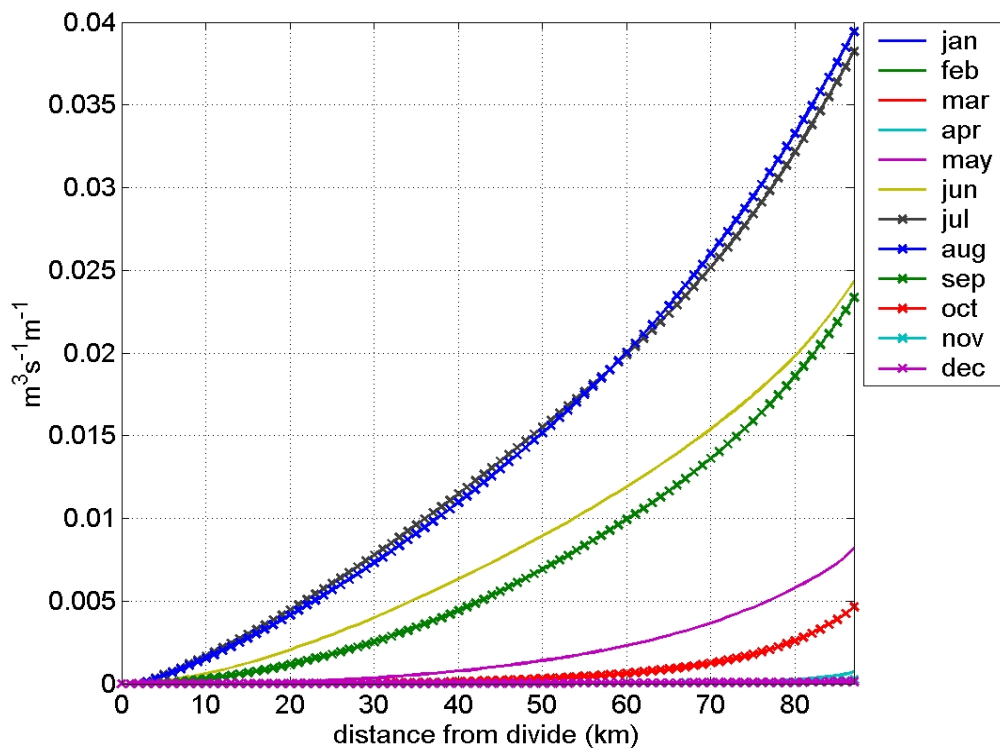
Figure 3.2: Modeled cumulative monthly mean water surface runoff per unit glacier width for this generic run is indicative of the seasonal distribution of melt and rain in South Alaska but not its magnitude.

that subglacial storage variations control directly basal water pressure variations. Therefore, a pressure gradient enabling the hydraulic network to convey the total surface water input corresponds to the steady state mean monthly water discharge. Many previously cited field studies (at Trapridge Glacier, Storglaciaren, Lauteraargletscher, Findelengletscher, Variegated Glacier, and Haut d'Arolla Glacier) propose that increase in storage leads to higher water pressure and vice-versa. In turn, there exist data showing that on some glaciers, surface uplift occurs concurrently with a velocity increase without change in water pressure (Harper et al., 2007), thus suggesting that increases in water storage do not necessary lead to water pressure increases; however, an uplifted glacier surface and increased sliding rate imply further decoupling from the bed with a greater fraction of overburden being supported by basal water. In general, at the length scale necessary for basal conditions to affect sliding rate through further drowning of bed roughness, water pressure is likely to augment even if only slightly. As shown by empirical evidence and theory, sliding has a strongly non-linear dependence on effective pressure, especially in the low range of effective stress and small changes in water pressure averaged over a large area may be difficult to measure properly. I will thus assume that increases in basal water storage lead to higher basal water pressure.

Local and/or short-term departures from the mean water pressure are expected to occur due to the evolving network and the varying discharge, but I prefer to solve first for mean equilibrium conditions over large regions of the bed; conditions that can be perturbed by modeling departure from the mean to represent daily variations. Assuming water incompressibility, conservation of water at steady state means that flux divergence equals the local water input from the surface and from melting due to heat dissipation melt water

105

input. I abstract flow within the subglacial network of cavities and conduits as Darcian

flow in a macro-porous horizon where the effective hydraulic conductivity is modulated

by effective basal pressure and the rate of change of water input at the bed. The Darcian

flux is proportional to the energy slope of the subglacial network modulated by the

effective hydraulic conductivity according to the following non-linear first order ODE:

$$Q_w = -\left[\frac{\alpha}{N^m} e^{-\left| \frac{\partial Iw_i}{\partial t} \right| \frac{\tau}{Iw_0}} \right] \frac{d}{dx} (P_w + \rho_w gz) \qquad \text{(Equation 3.10)}$$

Since I calculate the steady-state discharge at every node independently from the

distribution of water inputs, I numerically integrate the Darcian flow equation from the

junction with the fast flowing subglacial network near the snow line to the divide to solve

for a water pressure distribution that is consistent with Darcy's empirical relation

between total energy slope and water flux. The water pressure boundary condition at the

lower end of the distributed network is the pressure computed at the upper end of the R-

channel network. Next, I use a second and third order Runge-Kutta variable one-step

method (Matlab's built in ODE23s) to solve equation 3.10. Problem stiffness initially

appeared to slow down the numerical procedure considerably and although the solution

overall was stable thanks to the variable step size, a modified scheme to handle stiffness

proved necessary to speed up the process to acceptable CPU time requirements.

The bracketed expression in the equation for Darcian flow, which consists of 2 terms,

represents the effective hydraulic conductivity of the bed-ice interface. To embody the

controls on the conveyance capacity of the basal contact, transmissivity has to be

sensitive to the variables that dictate the enlargement of the hydrological network by

flowing water and its closure by overburden pressure. Therefore, the first term in the

bracketed expression is the negative feedback that arises from the inverse relationship between interface connectivity and effective pressure, $N=P_i -P_w$; thus, embodying the concept that as water pressure decreases, network conductivity decreases since conduits and cavities contract via ice creep. Furthermore, to capture the essence of the effects of flux variations on water pressure, I introduce a storage capacity index in the second term ($I_s = e^{-\left|\frac{\partial Iw_t}{\partial t}\right|\left|\frac{\tau}{Iw_0}\right|}$) that forces the transmissivity of the macro-porous layer to adjust to changes in water flux. Before approaching steady state, conduits and cavities are either enlarging to adapt to an increase in surface input or contracting during a decrease in precipitation and/or melt. A non-dimensional characterization of the ability of the network to convey the water injected at the glacier sole permits accounting crudely for the pressure transients resulting from the lag between changes in water input, and conveyance capacity through change in storage. If the ratio of the monthly mean water flux variation to the mean discharge characteristic of the previous month is much greater than zero ($\frac{\Delta Iw_t}{Iw_0} >> 0$), the relative ability of the network to convey the water coming from different sources is low; therefore, the lower will be the effective conductivity and the greater the water pressure gradient necessary to evacuate the prescribed flux toward the glacier margin (fig. 3.3). The opposite holds true when this ratio approaches zero and the storage capacity index is near unity, thereby meaning the volume of the water network necessary to convey the water supplied to it remains unchanged. In turn, a very large negative relative discharge ratio occurs solely when discharge becomes very small which means the network cannot contract any further because it is inexistent. Thus, the storage capacity index also could approach zero if sheet flow became prevalent over

107

much of the interface and relatively small changes in water input caused significant pressure variations. To resume, high water pressure can result from water injection at the glacier sole both when 1) water discharge is very high, during the melt and rainy season, and network capacity is low, and 2) discharge is very low during winter but network capacity is also very small. To prevent unrealistically low values of I_s, when network disruption and flooding is likely to occur upon a sudden very large relative injection of water, I cap the possible relative discharge fluctuation at an arbitrary maximum value ($\left|\dfrac{\Delta I_w}{I_w}\right| \leq 20$). This maximum value of the relative discharge change corresponds to a minimum value of ~0.1 for the storage capacity index, I_s.

I assume that cavity and tunnel geometry eventually reach equilibrium with concurrent water flux over a time period with the characteristic e-folding time τ that should scale with the time necessary for the closure by creep of a cylindrical channel. The relaxation time of the cavity network τ is estimated to be 3-5 days, approximately the time necessary for water pressure to relax in conduits after the peak of a hydrologic event during spring at Haut Glacier d'Arolla in Switzerland (Mair et al., 2005).

The formulation for conductivity has 2 adjustable parameters (α and m) that control the magnitude and longitudinal gradient of water pressure at the bed. These parameters are of course not independent from one another: a large value of m demands a large value of α and vice versa. Values of m have a decisive role in setting the slope and
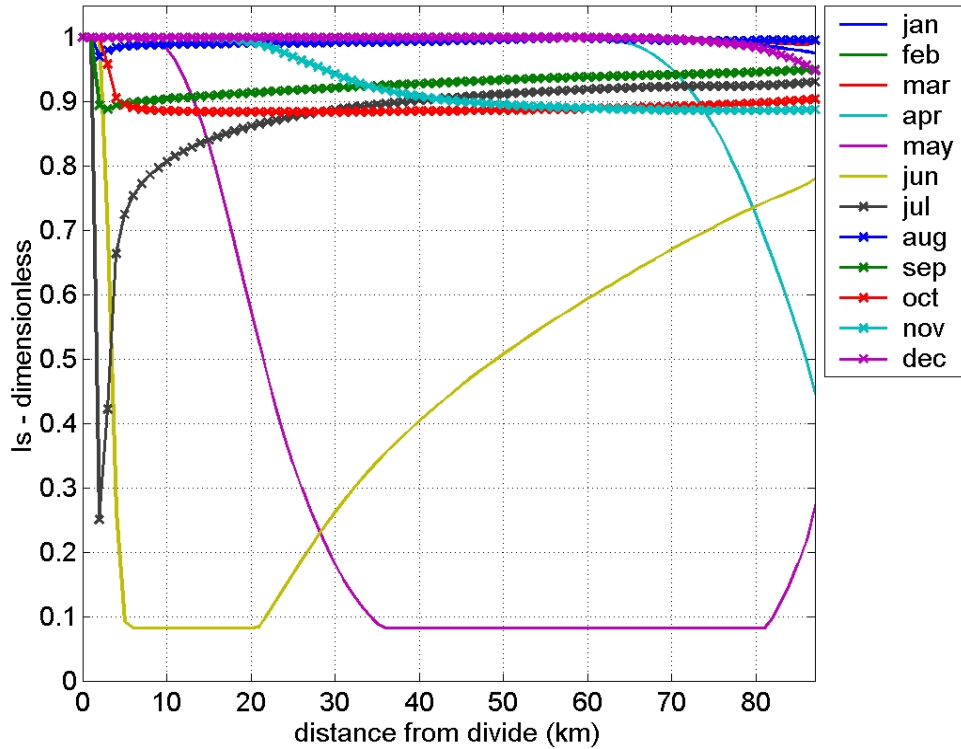
Figure 3.3: Monthly longitudinal profiles of the storage capacity index (I_s) account for the relative conveyance capacity of the subglacial network in the distributed region. The network has the least relative conveyance capacity at the beginning of seasonal melt (April-July).

yearly range of water pressure. At length scales greater than that of most basal

topography ($> 10^3$ m), subglacial passageways follow the direction of steepest decrease in

hydraulic head, which strongly depends on the ice surface slope (Shreve, 1972).

Consequently, the power coefficient m is taken to be 3, so the subglacial hydraulic head

gradient is of the same order of magnitude ($O-10^{-2}$) and sub-parallel to the ice surface

slope. Under large/thick glaciers, the yearly distribution of mean monthly effective

pressure range is likely to be small for the conveyance capacity of the subglacial network

adjusts rapidly to decreases in water input; A value of $m = 3$ dampens system response by

increasing the non-linearity of the functional relationship between overburden pressure

and adaptive conveyance capacity, and thus allows to limit the range of mean effective pressure to ~0.5 MPa over much of the profile (fig. 3.4 and fig. 3.5). In turn, the constant α is chosen to make the magnitude of mean water pressure over most of the glacier profile during the melt season approach ice overburden pressure (effective pressures of 1 to a few bars) thus reflecting observations commonly reported in the literature (Iken and Bindschadler, 1986; Kamb et al., 1994; Fountain, 1994; Jansson, 1996; Sugiyama and Gudmunsson, 2004). These parameter values also insure that water pressure within the distributed network is significantly higher than that in R channels (fig. 3.4) during the entire year.

I let dimensionless α vary 2 orders of magnitude (10^{10}-10^{12}) to characterize the sensitivity of water pressure to this parameter. As α decreases, so does conductivity, which requires greater basal water pressure to force water toward the terminus. As effective pressure approaches 0, lower α values are necessary to lower mean monthly effective pressure. Water pressures are greatest during the ablation season (fig. 3.4 & 3.5). The yearly range of mean effective pressure for the lowest α values is a small fraction of that for high alpha values; effective pressures are then less than 0.5 bars throughout summer over most of the glacier profile in the distributed network region, which seems a little low compared to available data. In turn, intermediate values, on the other hand, constrain effective pressure between 0 and 2 bars over much of the domain during the ablation season (fig. 3.4), which is more consistent with the data available in the literature. These values yield results lacking large departures in monthly mean basal effective pressure throughout the year, yet still allow for large pressure transients on short time scales, and maintain mean water pressures that are always a small fraction of ice

110

pressure (fig, 3.4 & 3.5). Widespread evidence of water standing at the surface and in the

crevasses of temperate coastal glaciers like those of South Alaska during the melt season

suggests that large areas of these glaciers are subject to low basal effective pressure of at
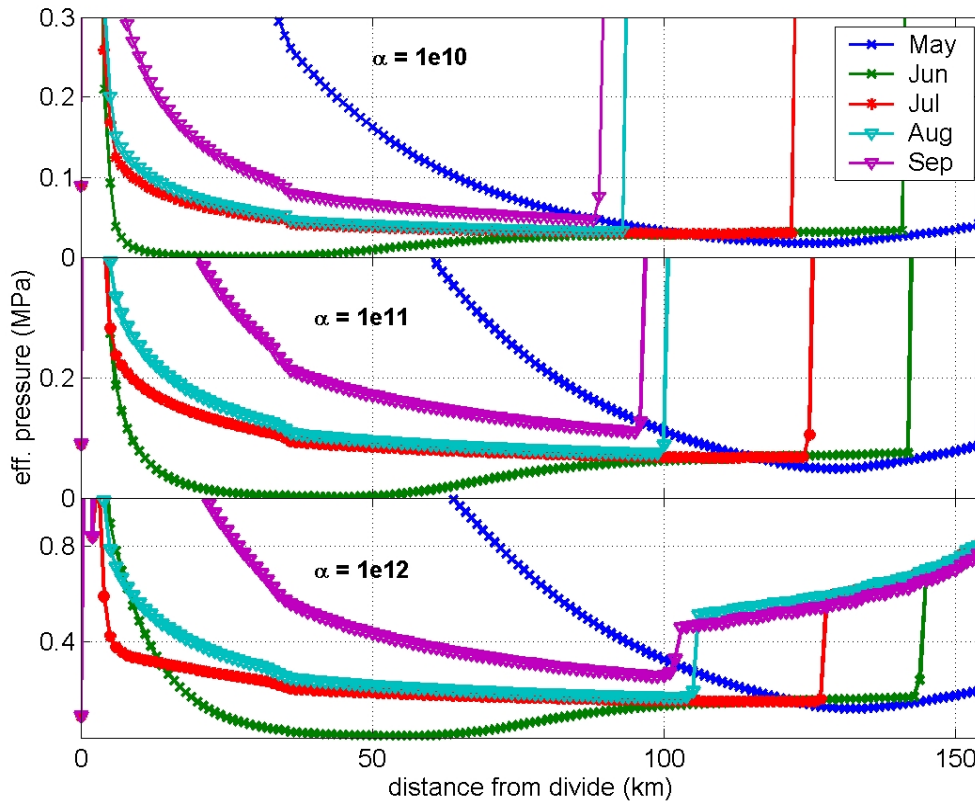
Figure 3.4: Monthly mean longitudinal profiles of effective pressure during the melt season for a range of α value. A value near the middle of the range ($\alpha = 1 \times 10^{10} - 1 \times 10^{12}$) leads to the range of low effective pressures characteristic of maritime glacial systems.

most a few bars during most of the year. Indeed, field borehole studies show as well that

basal water pressures of coastal range and maritime glaciers, and massive glaciers

anywhere in the world are low (<5 bars) throughout much of the year (Harper et al.,

2005; Fahnestock, 1991; Kamb et al., 1994). Effective pressure increases by several bars

(3-4 bars) at the transition between the distributed and the channelized network below the

snowline (fig. 3.4 & 3.5). Water pressure isn't expected to increase so abruptly at the

boundary between networks because regions of high water pressure exists between R-channels and these regions aren't explicitly modeled, as discussed in the following section.

Near the divide where ice is frozen to the bed, effective pressure equals the ice overburden pressure; effective pressure first increases (off the charts in fig. 3.4 through 3.6) and decreases along with ice thickness then starts decreasing where liquid water forms at the bed and water pressure becomes finite. From the drainage divide to the major
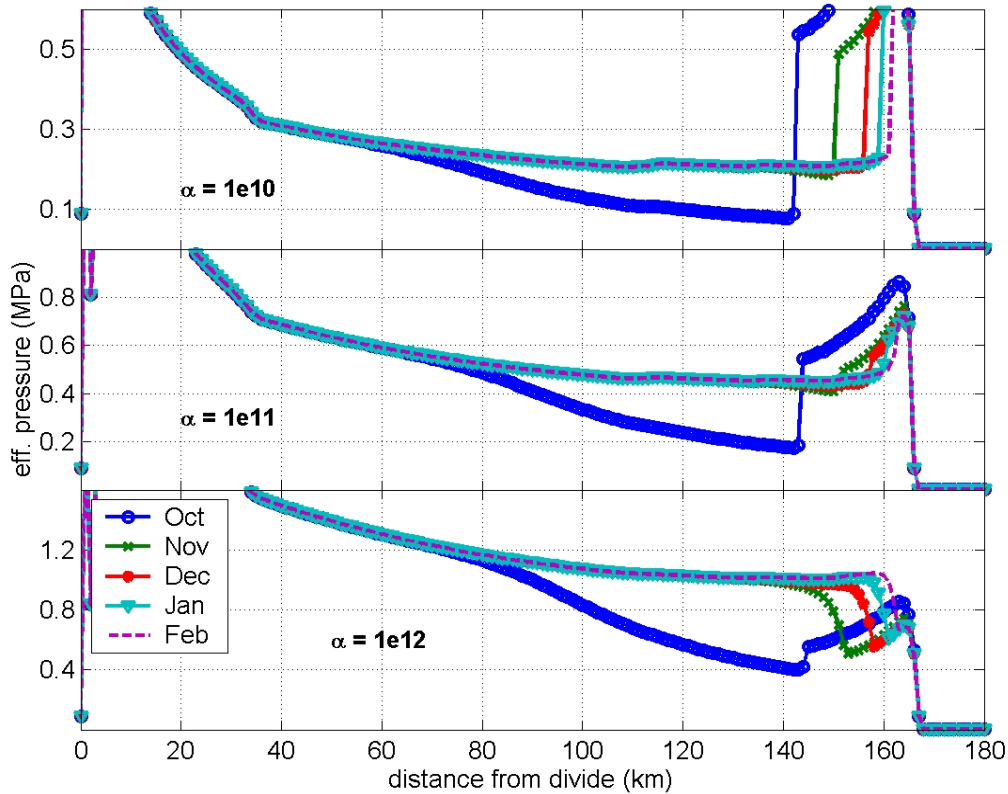
Figure 3.5: Distribution of effective pressure for a range of α value during the accumulation season.

break in slope topography near the mountain front (35 km from the divide), basal effective pressure follows topographic slope, then continues to decrease to reach a broad pressure low between the principal break in basal slope and the seasonal snow line (210-

280 km in figure 3.6). A wave of high water pressure first propagates upstream with the

snowline during the first half of the ablation period (April-July) and then downstream

toward the terminus from August through November. During winter (November –

March), mean effective stress remains low and nearly constant due to the continued

production of water through heat dissipation and geothermal heat.

The corresponding distribution of hydraulic conductivity ($O[10^{-4} - 10^{-6}$ m/s]) is

realistic for most of the profile (fig. 3.7); its magnitude is toward the lower end of

conductivity values back calculated from field observations under glaciers (Fountain,
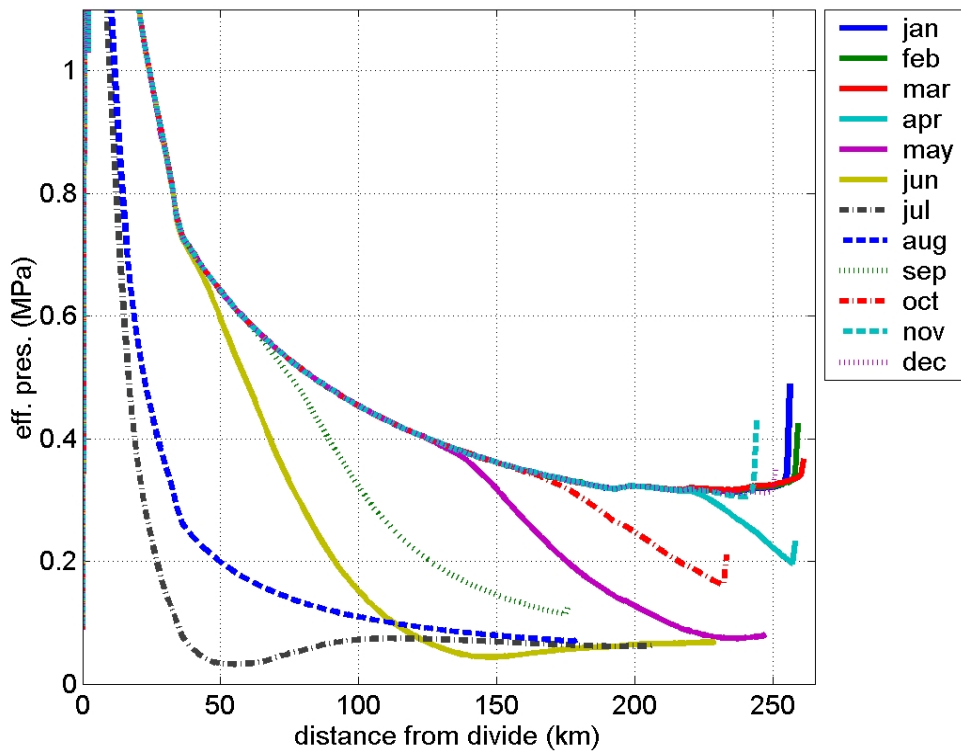
Figure 3.6: Yearly distribution of monthly mean effective pressure in the region characterized by a distributed hydraulic network with α =1x10^{11} during glacial conditions.

1994). Effective conductivity expectedly increases with discharge and water pressure down the profile. Conductivity is very low during winter month as can be expected since cavities and links should close in and network connectivity decrease drastically. The relative connectivity of flow at the network transition is more uncertain because this
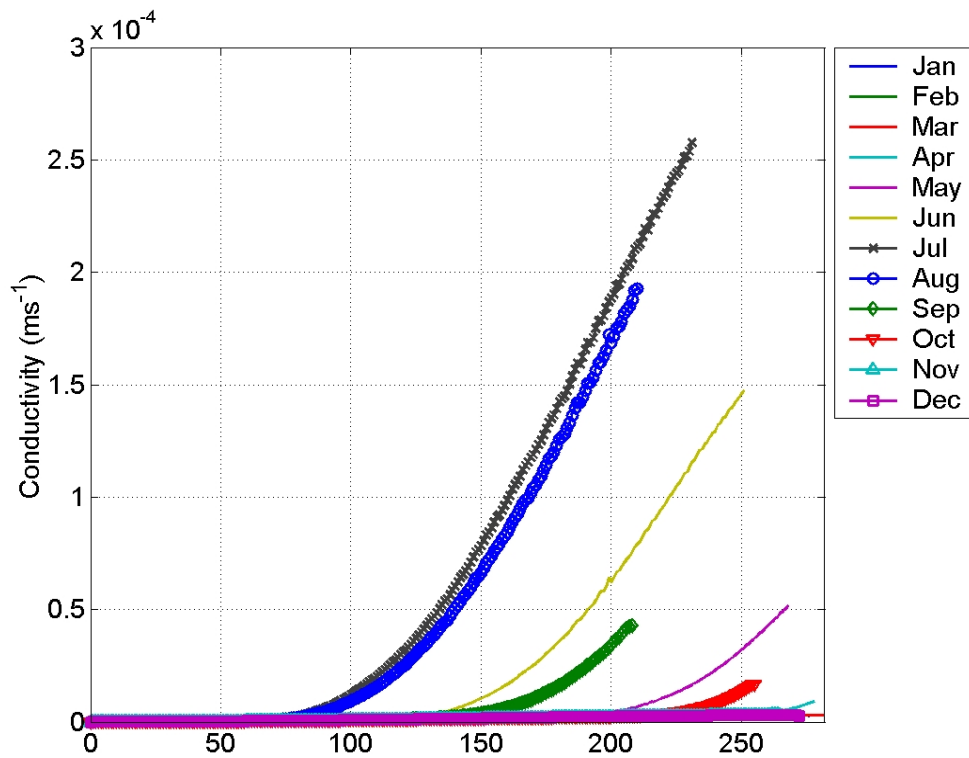
Figure 3.7: Effective hydraulic conductivity of the slow-draining basal networks.

region is seasonally subject to the highest rate of water input along the profile without being channelized, which should lead to high water storage, high degree of decoupling from the substrate and accompanying frequent disruption of an embryonic network. It is thus quite possible that the network transition be characterized by low connectivity but it is also unlikely that a simple model could provide much insight into the rapidly evolving connectivity of flow in that region of the bed.

As anticipated, mean water pressures at the bed are highest during the seasons with the highest melt and rain rates. To first order, the seasonal evolution of water pressure (fig. 3.6) reflects the seasonal evolution of discharge. The overall pressure distribution is grossly similar to that, which could be obtained with a conductivity model without feedback from the overburden pressure and the variations in water injection rate. The modeled departures from the exact pattern suggested by the magnitude of discharge follow to a great extent the progression outlined in the conceptual model. Effective pressures are generally low through the melt season but lowest in late spring/early summer (June) when melting is most abundant relative to the conveying capacity of the hydraulic network and similarly in late summer/early fall (September) during large precipitations events and while melting is still important (fig. 3.6). Although a little greater during winter, effective pressures are still low and less than 0.5 MPa over most of the profile during that season. Thus the differences with the simplest conductivity model independent from ice thickness and melt rate, which is implemented through the formulation of water pressure negative feedback on connectivity and the storage capacity index are a) the smaller range of seasonal departure of mean effective pressure forced through the negative feedback of effective pressure on connectivity and b) the amplification of system response to large changes in water input in the network via the Storage Capacity Index (fig. 3.8). The effect of differential water input on modeled water pressure is significant during the month of May, June and July when mean monthly water pressures are increased by up to nearly one bar. The pattern of water pressure departure from the model output without dependence on relative melt rate reflects that of
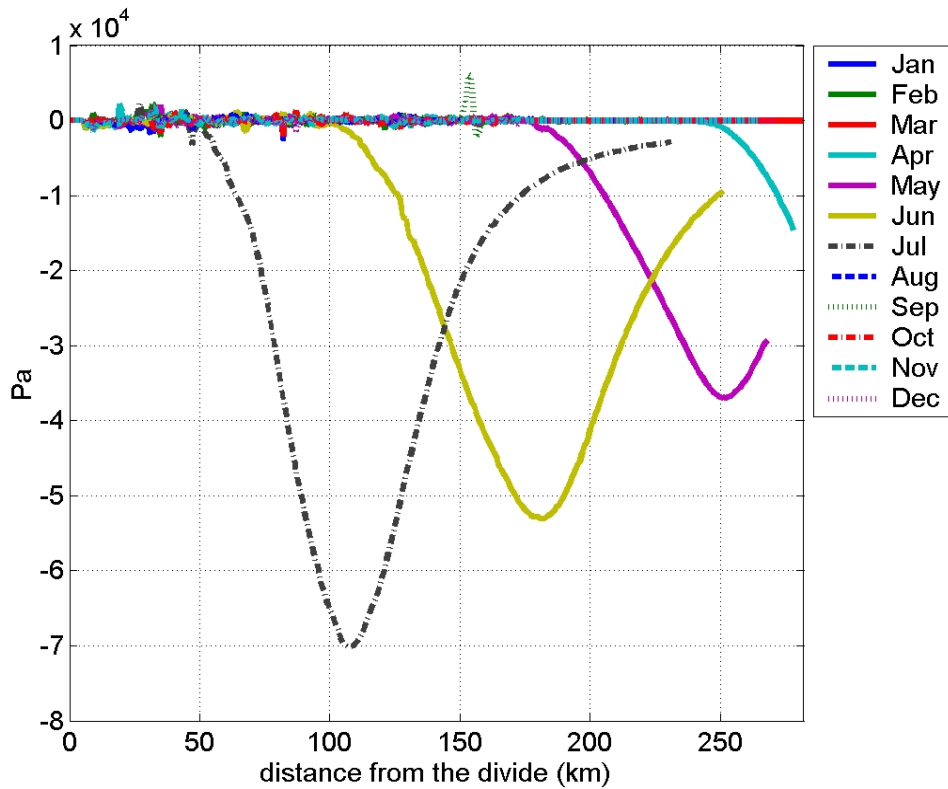
Figure 3.8: Comparison of effective pressure outputs between a conductivity model driven solely by an effective pressure feedback and another that also includes the Storage Capacity Index ($\alpha = 1\mathrm{x}10^{10}$). As expected, a melt rate-dependent hydraulic conductivity induces lower effective pressures during the first half of the melt season.

the Storage Capacity Index: during any single month, the greatest increase in water

pressure occurs where melt rate increases the most relative to that occurring during the

previous month.

Our model of a macro-porous layer characterized by Darcian flow reproduces a

number of known or inferred seasonal characteristics of basal hydrology: 1) a highly

pressurized distributed network of cavities and links at the glacial interface early in the

melt season when cavitation is extensive; 2) likely spatial distribution of effective stress

with regions of low stress, a bar or less during the early melt season, which seem

reasonable for the slow draining regions of the bed above the snowline, and 3) the

resulting piezometric head decreases monotonically in a down glacier direction, as it

must to convey melt water to the terminus (fig 3.9). Water pressures are assumed to

fluctuate about the monthly mean within a range dictated by maximum discharge

variations. Comparison of modeled daily melt generation to continuous monitoring of

water discharge in proglacial streams at Bering Glacier, and data from the literature help

constrain daily fluctuations in water input to one order of magnitude variation. Thus, I

increase water flux ten-fold to compute a new Storage Capacity Index corresponding to

extreme discharge variations and to derive extreme values of effective pressure within the
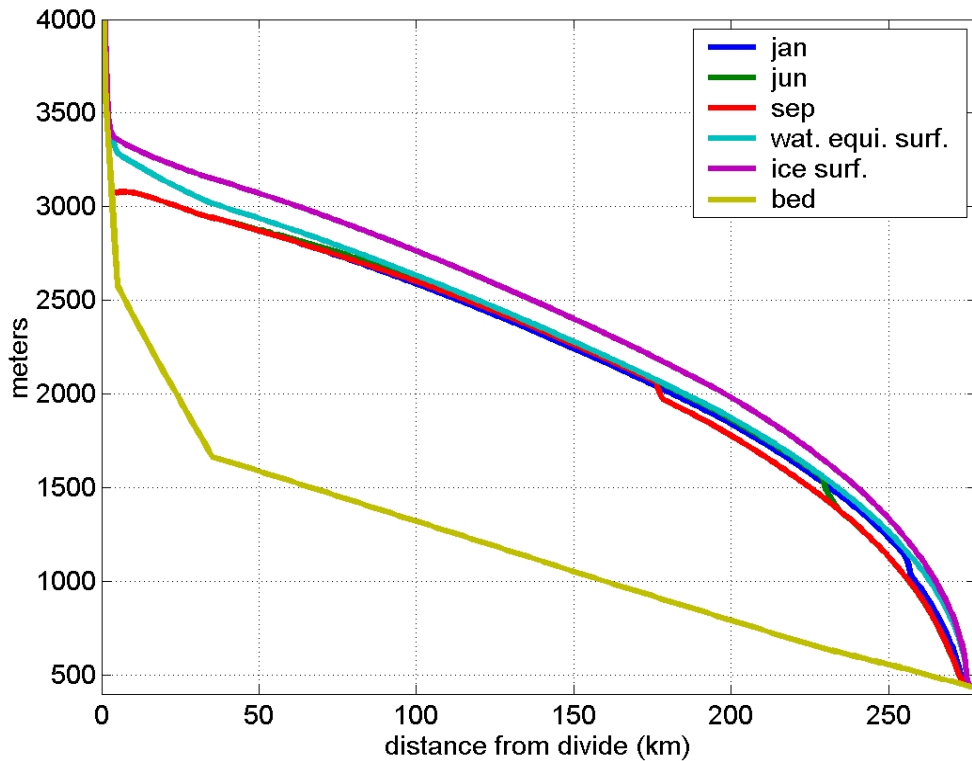
Figure 3.9: Longitudinal profiles of monthly mean piezometric head. During the melt season total head reaches within 5-10 meters of the water equivalent surface, level at which floatation occurs.

distributed network. During the melt season water pressure transients depart from the monthly mean by a few bars at most, which is sufficient to result in basal pressure within a few percent of floatation for large regions of the bed immediately upstream from the network transition. Water pressure transients are significantly larger and reach up to several bars at other times of year.

3.4.4 Fast-draining subglacial network

Modeling a propagating arborescent network of channels draining regions of distributed cavities is the next step to address subglacial flow in the ablation zone where it is well drained along channel axes. Water pressures in R channels provide the boundary condition to that in the distributed cavity network above the snowline as well as to the poorly connected regions in between major channels in the ablation area. Dye tracing experiments at Glacier d'Arolla suggest that the transition from a distributed to a channelized network occurs with the up-glacier retreat of the snowline during the melt season (Nienow et al., 1998). Possible reasons for the location of this transition include the higher melt rate associated with the lower albedo of bare ice and/or saturated snow, as well as the lack of a firn aquifer to dampen the effect of warmer or rainier days, and thus the greater likelihood of sudden large melt input that is necessary to disrupt a stable cavity network. Thus, I assumed that the transition zone to an arborescent channel network migrates up glacier following the upward retreat of the snowline during summer and computed its monthly mean position along the profile with our mass balance model. To represent the physics of water transfer in tunnels I adopt the analysis of Rothlisberger (1972); the analysis that follows is found in much greater detail in several standard glaciology textbooks such as W.S.B. Patterson's (1994) and R. LeB. Hooke's (1998) and

will be purposefully kept minimal here. Neglecting a possible source term contributed by the advection of warm surface water, the head loss down the tunnel alone provides the energy necessary to melt channel walls and keep water at the pressure melting point. At geometric steady state, the rate of wall closure for a unit length of channel equates the rate of wall melt; this insight allowed Rothlisberger to express the water pressure gradient of a cylindrical channel surrounded by ice in terms of its cross section area, water flux, elevation head gradient and effective pressure according to the following first order non-linear ODE for water pressure:

$$\frac{dP_w}{dx} = \left(\frac{2}{1-E}\right)\left[\frac{S}{Q_w}L\rho_i A\left(\frac{P_i - P_w}{n}\right)^n\right] - \rho_w g \frac{dy_b}{dx} \qquad \text{(Equation 3.11)},$$

where E is a dimensionless constant and S is the channel cross-sectional area, which I assume to be circular. L is the latent heat of melting of ice and the other variables are as been defined previously. In turn, the cross-sectional area of a cylindrical pipe can be expressed in terms of water flux and pressure gradient through the following form of Manning's equation:

$$S = \left[\frac{(4\pi)^{\frac{2}{3}}\rho_w g m_r Q_w^2}{\rho_w g \frac{dy_b}{dx} + \frac{dP_w}{dx}}\right]^{\frac{3}{8}} \qquad \text{(Equation 3.12)},$$

where m_r is the effective Manning roughness. For this fast-draining network, I chose water flux to be the cumulative surface water runoff per glacier width divided by an estimate of the numbers of channels likely to drain the glacier front (spacing of 10^2-10^3

meters). Provided an initial guess of channel cross-section that is a function of discharge at the terminus (radius of the order of meters) and known water pressure at the glacier front (atmospheric), I integrate equation 3.12 for water pressure from the terminus to the snowline with a second and third order Runge-Kutta variable one-step method (Matlab's built in ODE23). The resulting water pressure field and piezometric surfaces are well behaved (fig.3.9 and 3.10) and the computed channel dimensions are quite realistic (fig. 3.11).
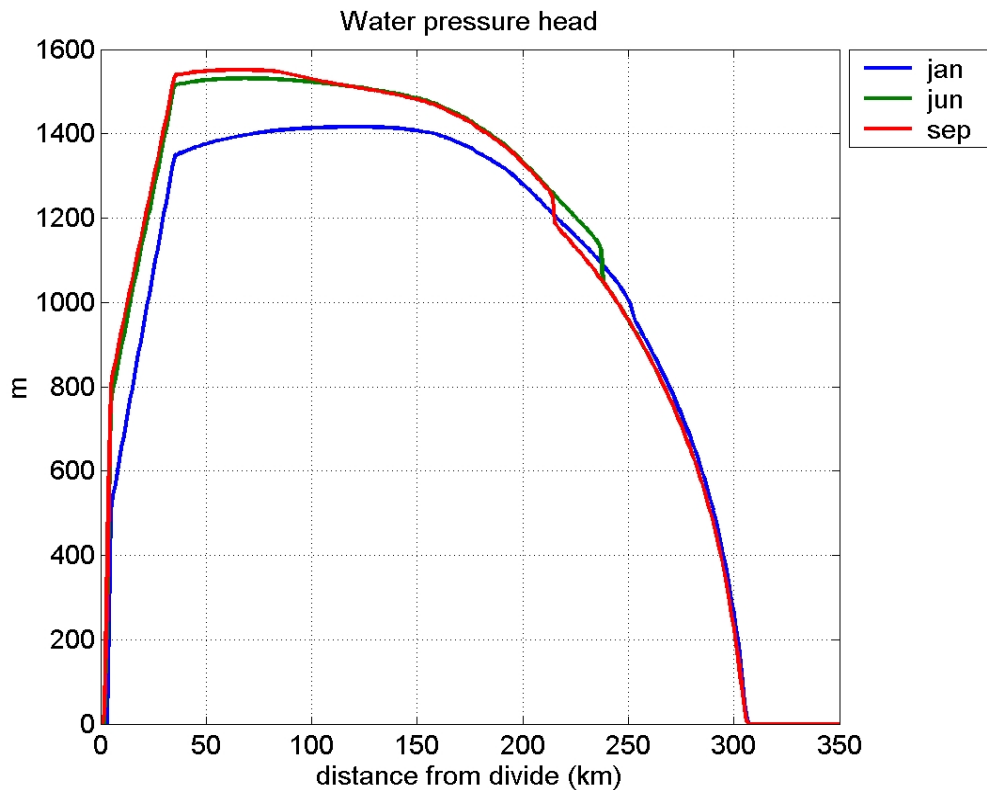
Figure 3.10: Mean monthly hydraulic head. Water pressure is highest where ice is the thickest. As prescribed the network transition retreats uphill with the melt season. Water pressure displayed below the snow line (between 215 and 255 km) is that computed for fast draining cylindrical channels.

Downstream from the network transition, effective pressure increases progressively to reach a maximum within a few kilometers from the terminus; further downstream,

120

effective pressure decreases along with ice thickness to vanish at the terminus (fig. 3.11).

An increase in effective pressure with distance below the snowline is consistent with

increasing glacier surface melt rates with decreasing elevation and with a well established

dendritic network of R channels under decreasing overburden pressure. The seasonal

variation in tunnel water pressure reflects exactly the opposite of that of water discharge;

as can be inferred readily from Rothlisberger's equation, model output shows that
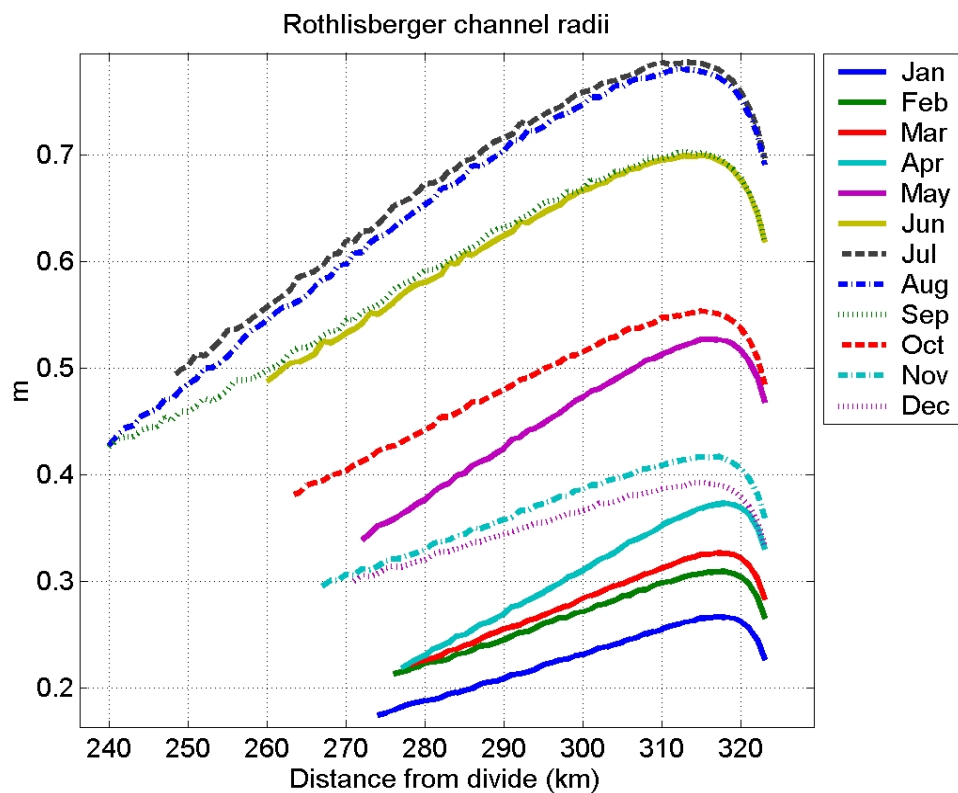
Figure 3.11: Rothlisberger channels extend from the glacier terminus to the seasonal snowline. Channel cross-section decrease a little when nearing the terminus because of steepening pressure gradients (eqn 3.12).

summer with high water flux has the lowest water pressure and vice versa during winter.

The minimum effective pressure is 0.8 MPa and it varies seasonally by 0.3-0.4 MPa.

Computed tunnel effective pressure is a little high compared to some of the available

summer season field observations of boreholes thought to be connected to channels (~0.5 MPa). Adjusting parameters, such as ice viscosity, in the flow equation above didn't substantially affect water pressure distribution. At least one other worker, Roger LeB. Hooke who has studied extensively R channel theory and its variation has noted that the Rothlisberger equation underestimates channel water pressure. However, as already mentioned, much of the bed in the ablation area is in between channels and much closer to overburden pressure than water in R channels. As already mentioned, observations show that water pressure increases away from channels and eventually reaches ice pressure within some 10's of meters. For simplicity, I assign a single water pressure value that varies along the length of the glacier below the snow line; it average half way between computed monthly mean channel pressure and ice overburden pressure. Diurnal water flux variation and other hydrologic events temporarily overwhelm the transport capacity of R channel thereby resulting in large pressure transients reaching buoyancy levels. Attempts at forcing large water pressure changes by routing maximum discharge within the tunnel proved unsatisfactory since maximum departure of only 3-4 bars proved possible by this method. Consequently, I chose to simply assume that water pressure reaches ice overburden pressure over all the bed below the snowline at some point during great discharge variation.

3.5   Thermal regime

Glacier sliding and erosion are very slow, and therefore negligible, whenever the basal contact is subfreezing; it is thus of importance to compute a basal temperature profile. Again, I have elected to model thermal evolution simply, i.e. with a one-dimensional conduction, vertical advection steady-state model that also includes internal

viscous dissipation. The temperature dependence of ice thermal properties, and the latent heat transfers associated with melting and refreezing of ice at the basal contact are neglected. The one-dimensional steady state heat equation takes the form:

$$\frac{\partial^2 T}{\partial y^2} - \frac{v(z)}{\kappa}\frac{\partial T}{\partial y} + \frac{f}{\kappa\rho c} = 0 \qquad \text{(Equation 3.13),}$$

where T is temperature, v is vertical velocity, κ is thermal diffusivity and f is the body source term which for deformation in simple shear is:

$$f = 2\tau\dot{\varepsilon} \qquad \text{(Equation 3.14)}$$

The one-dimensional heat equation can be solved analytically for temperature (Firestone et al., 1990):

$$T(y) = T_s - \frac{Q_{gh}}{\kappa}\int_h^y \frac{1}{F(\eta)}d\eta - \int_h^y \frac{1}{F(\eta)}\int_0^\eta F(\xi)\frac{1}{\kappa}\left(\frac{1}{A}\right)^{\frac{1}{3}}\left(\frac{\partial u}{\partial \xi}\right)^{\frac{4}{3}}d\xi d\eta \qquad \text{(Equation 3.15),}$$

where the integrating factor is:

$$F(y) = \exp\left(-\int_0^y \frac{v(\xi)}{\kappa}d\xi\right) \qquad \text{(Equation 3.16)}$$

K is the heat conductivity and h is the ice thickness. The surface and bottom boundary conditions are T_s, the surface temperature, and Q_{gf}, the geothermal heat flux. Surface temperature is assumed to be air temperature modeled with a lapse rate but modulated by the latent heat of freezing from melt water and rain assumed smeared over a 10m layer of

123

the snowpack. The heat flux is chosen to be 65 Wm^2s^{-1}, a representative value for a convergent margin affected by magmatic processes

The vertical velocity profile is obtained by first deriving the horizontal velocity with the laminar flow assumption. For an infinite isothermal parallel-sided slab deforming in simple shear and frozen to its bed (no x or z dependence and $v=0$), the x-component of the equilibrium equations becomes:

$$\frac{\partial \tau_{yx}}{\partial y} + \rho g \sin \alpha = 0 \qquad \text{(Equation 3.17)}$$

The shear strain rate simplifies to: $\dot{\varepsilon} = \frac{1}{2}\frac{\partial u}{\partial y}$, which according to Glen's flow law can be related to shear stress: $\tau_{xy} = 2\eta\,\dot{\varepsilon}_{xy}$, where η, the effective viscosity is inversely proportional to the coefficient of Glen's law and the 2nd invariant of the stress tensor raised to a power, τ^{n-1}. The distribution of horizontal velocity with depth is:

$$u(x,y) = u_s\left[1 - \left(\frac{h-y}{h}\right)^{n+1}\right] \qquad \text{(Equation 3.18),}$$

where $u_s = \frac{n+2}{n+1}\frac{q}{h}$, the surface velocity is a function of q, the ice flux per unit width. The horizontal velocity is then differentiated with respect to x (neglecting second-order term in $\frac{\partial h}{\partial x}$), and by incompressibility:

$$v(x,y) = v_s\left[1 - \left(\frac{h-y}{y}\right)\left(\frac{n+2}{n+1} - \frac{1}{n+1}\left(\frac{h-y}{h}\right)^{n+1}\right)\right] \qquad \text{(Equation 3.19),}$$

where $v_s = -b(y)$ is the surface velocity for the steady state case (Raymond, 1983).

The major uncertainties in the temperature profiles result from the assumption that temperatures equilibrate with climatic forcing within the time interval used in the computation, the neglect of horizontal advection, the magnitude of the geothermal gradient and the surface boundary condition. Scaling of the various terms of the heat equation show that whereas horizontal advection is a contribution smaller than vertical advection, the body source is several times greater. Neglect of frictional heat wherever ice slides is non-trivial (potentially much greater than geothermal heating), however temperature modeling is needed solely for the location of a change of frozen to wet basal conditions and accurate temperature modeling of the sliding domain is not a pre-requisite. Latent heat of refreezing of surface melt and liquid precipitation modifies surface boundary conditions; however, little surface melt and/or liquid precipitation occur where the basal contact is found to be sub-freezing. Therefore, this effect appears to be small were it matters the most. The assumption of steady state thermal profile within the interval of time between equilibrium conditions can be compared to considering the time necessary for snow to reach the basal contact solely because of vertical advection if vertical velocity decreased linearly with depth. For a surface accumulation rate of 1 m/yr, it would require on the order of 1000 years for a snow packet to reach the bottom of a 500 m thick glacier, which is equivalent to the time step selected for this model. At high elevations, the effect of decreased surface velocity because of smaller mass balance is offset by smaller ice thickness. This assumption is likely to grow worse during cold period when the glacier is thicker and precipitation lesser, but the time necessary to reach thermal equilibrium is at most a small multiple of the time interval chosen for this exercise.

3.6 Subglacial erosion model

For this generic landscape, I first treat the glacial abrasion and detachment of bedrock fragments by plucking; I do not consider their translation to the glacier margins to focus initially on how climatic forcing affects the distribution of bedrock erosion along a glacier. This approach is appropriate for many temperate coastal glaciers that have little sedimentary cover at their base. In a later section, I will address glacial sedimentary processes that interact with the erosion; these include sediment mobilization and transport, which can strongly affect sediment yields from glaciers. Similarly to other subglacial processes, direct observation of glacial erosion is difficult because the glacier bed is rarely accessible; thus, much of our understanding is derived from inferences based on sediment fluxes in the proglacial environment, the morphology of formerly glaciated surfaces (Hallet and Anderson, 1981; Walder and Hallet, 1979) and a few subglacial studies (Boulton et al., 1979; Iverson, 1991; Cohen et al., 2000; Cohen et al., 2006). Efforts have been made to use near-margin subglacial cavities and industrial tunnels to instrument the glacial interface and record conditions leading to quarrying and abrasion (Anderson et al., 1982; Cohen et al., 2000 and 2006).

Theoretical considerations (Boulton, 1974. 1979; Morland and Boulton, 1975; Hallet, 1979, 1981 and 1996; Shoemaker, 1986; Rothlisberger and Iken, 1981, Iverson, 2012) and laboratory experiments (Iverson, 1990, 1991) provide a general framework for our grasp of erosional processes and their relative importance. Quarrying, abrasion, fluvial erosion and chemical dissolution are the generally accepted mechanisms of glacial

126

erosion (Drewry, 1986). Although the rate of chemical denudation of glacial landscape is significantly greater than most environments at equivalent latitudes, chemical dissolution has been shown to be a small contributor to the total glacially derived mineral mass flux except in carbonate regions (Sharp, 1995; Souchez and Lemmens, 1987). The chemical load is also to a great extent the dissolution product of particles already detached from the bed that are further comminuted during subglacial transport. Despite the paucity of quantitative data constraining the different erosional processes, several lines of reasoning help prioritize the physical modes of erosion: glacial plucking of bedrock fragments appears to be a more important mean of lowering the bed than abrasion by particles encased in the glacier sole. Whereas the abrasion process tends to smooth landforms because clasts erode preferentially where ice converges on bed protuberances, quarrying generates roughness by plucking blocks out of the bed where stresses imparted by ice flow on bedforms are great enough to exceed rock strength. Observations of bedrock surfaces recently uncovered by retreating ice show that despite the sand paper like smoothing action of abrasion, the bed of glaciers has much asymmetric roughness over a wide range of length scale (parallel to ice flow: $O[10^{-3}\text{-}10^3 \text{ m}]$). The morphology of the rough and steep lee faces contrasts with the smooth and gently rising stoss faces of bed undulations, thereby highlighting the respective domains of activity of abrasion and quarrying. The role of bed obstacles in controlling the flow of ice and the unlikelihood of creating roughness out of a smooth surface implies that bed roughness is sustained in the course of valley lowering many times greater than the amplitude of bed obstacles; headward retreat of steep lee faces of obstacles due to plucking appears to be a likely and perhaps the only mode of lowering the bed while maintaining roughness. Indeed, surface

exposure dating of glacial landforms in the Puget Sound region, part of the Cordilleran ice sheet of North America where glacial occupation was short lived (~2kyr) during the LGM, shows that by opposition to plucked lee faces where there is no cosmogenic radio nuclides inherited from before the most recent glacial occupation, the age of stoss surfaces has not been reset completely by abrasion (Briner and Swanson, 1998). Briner and Swanson's study, along with a much earlier study of granite domes with sheet structure (Jahns, 1943) suggest that rates of glacial abrasion are an order of magnitude less important than rates of glacial quarrying. Unfortunately, records of sedimentation in sediment traps are too sparse and ambiguous to determine with confidence the fraction of the sediment that is ascribable to the quarrying process; available data indicate that the coarse fraction of the sediment load (sands and gravel) amounts to 30-90% of the total load (Pearce et al., 2003; Loso et al., 2004).

At any particular time, fluvial erosion under glaciers is very localized in fast flow channels and is probably an important factor only near the terminus. Some deglaciated surfaces show evidence of incised subglacial streams of depth ranging up to ten's of meters (from Nye channels to narrow slot canyons) which demonstrates the capacity of water flowing in sub-glacial channels to incise deeply in one place; however, glacial valley cross-sections do not exhibit obvious zones of preferential incision over a likely region of subglacial streams lateral migration which suggests that erosion by water borne particles is either localized when the stream becomes entrenched or of lesser significance when averaged in space and time. Moreover, most bedforms are attributable to the abrasion and plucking processes indicating that these are spatially much more important modes of bed modification. For this work, I chose to ignore chemical and subglacial

fluvial erosion and to model only quarrying and abrasion. The treatment of quarrying takes into account the state of stress at the bed whereas abrasion is treated simply as a linear function of sliding speed.

The quarrying scheme adopted follows directly from Hallet's model of glacial quarrying (Hallet, 1996). Hildes (2001) also described a model of glacial quarrying that shares some features in common with Hallet's but differs in several important ways. In particular, Hildes argues that local topography does not affect significantly the stress regime and can be ignored, which leads him to simply parameterize its effect on the extent of bed separation. The resulting distribution of bed separation is significantly less extensive than that obtained with Hallet's model which may explain in part the smaller erosion rates. After a brief description of the method I adopt for this work, the model is generalized to a range of bedform length scales and of evolving stress states arising because of water pressure variations in time. Paralleling previous idealizations of glacier beds in the literature, the quarrying model assumes a periodic bed topography composed of steps with ledge treads dipping upglacier at a shallow angle β and with steep downstream facing risers (figure 3.12). In agreement with many observations of glacier beds, I assume that steps are elongated in the direction transverse to ice flow, which permits me to assume plane strain and the use of a 2-D model. Although the imposed geometry limits protuberances to angular asymmetric features, it is a useful abstraction for hard beds because staircase morphologies are ubiquitous in glacial landscapes of all lithologies. In particular, periodic step geometry reproduces many of the features of the lee faces of roches moutonnees that present sets of steps carved by plucking (Sugden et al., 1992). It is also a particularly good approximation for sedimentary lithologies since

ledges can evolve from quarried sub-horizontal bedding planes. Furthermore, this bed

geometry allows capturing the essence of stress partitions in a distributed network
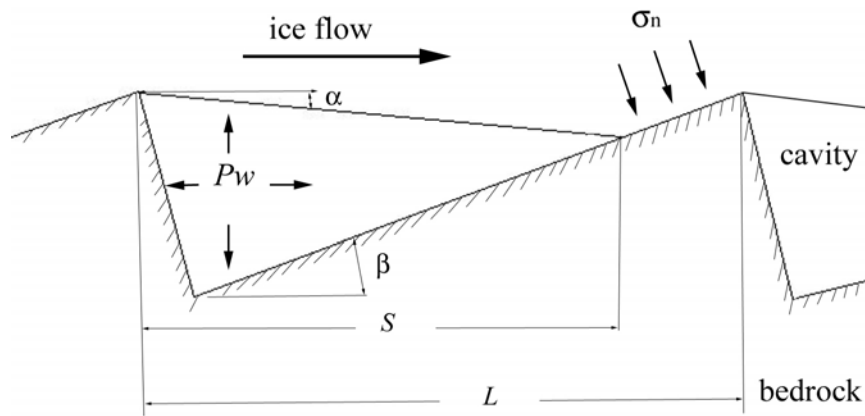
Figure 3.12: Detail of periodic bed geometry. The cavity ice roof is approximated as being straight. The ledge corner is in a state of tension that causes cracks to propagate parallel to the direction of most compressive stress.

of stress partitions in a distributed network of cavities, which would be highly favored by

this configuration of roughness elements. As high water pressure and water storage in

cavities at the glacier sole cause partial ice decoupling from the bed and high rates of

sliding, stresses are concentrated where ice regains contact with the bed, typically high on

the stoss face of bumps or ledges when sliding is fast or water pressures approach the ice

pressure. Under these conditions, the glacier is mostly supported by pressurized water

while ice-bed contact stresses concentrate near the edge of the treads and give rise to

greatest deviatoric tensile stresses a short distance ($O[10^{-2}$ m]) upglacier from the ice

reattachment point with the bed. Stress concentration at the tip of cracks induces crack

propagation and eventual detachment of the block from the bed. I consider only mode I

cracks, which propagate under tension, since shear tractions under glaciers are thought to

be small and could generate stress intensities exceeding mode II fracture toughness only

in the softest rocks (Morland and Boulton, 1975). Although lower stress intensity may be sufficient to induce block fracture due to the existence of planes of lower cohesive strength in the form of contacts and joints that may have weathered in subaerial environments, quarrying also appears to occur in the absence of joints suggesting that fracturing of competent bedrock also has to occur.

Water pressure fluctuations within cavities can increase the range of bed separation or leave ledge risers without lateral confining pressure thereby leading to higher deviatoric stresses about the ledge corner (Rothlisberger and Iken, 1981; Iverson, 1991). Although infiltration of pressurized water into fractures could contribute to greater stress intensity at the tip of cracks and cycling of subglacial pressure may play a role in rock fatigue (Iverson, 1991), these processes are not taken into account here.

Consideration of bed geometry, the rate of sliding and a simple assumption of creep closure rate in a cylindrical cavity without melting permits to formulate a second order polynomial for the extent of bed separation S in terms of effective pressure, sliding velocity, the angle the ledge tread makes with the horizontal and the characteristic length scale of bedforms likely to lead to cavitation according to:

$Sk_{ca}N^3 + k_{ca}N^3(L-S)^2 \tan^2\beta - U_{sl}(L-S)\tan\beta = 0$ (equation 3.20), where k_{ca} is the ice closure rate constant, U_{sl} is the rate of sliding of ice relative to the bed, and S and L are respectively the decoupled and total area per unit width of ledge tread, and β is the departure of the ledge tread makes from the horizontal. Note that solving this polynomial for bed separation requires choosing a representative ledge dimension in the direction of ice flow as well as the angle at which it rises from the horizontal. Note that solving this polynomial for bed separation requires choosing a representative ledge dimension in the

direction of ice flow as well as the angle at which it rises from the horizontal. For simplicity's sake, when attempting to account for the spatial variability of bedforms found under glaciers, I chose to approximate the length of ledges by the wavelength of bottom topography. The great asymmetry of the proposed bed geometry renders this approximation acceptable. Similarly, the tangent of the angle β, can be approximated to bed roughness.

Quarrying rate is assumed to be proportional to crack growth rate and the fraction of the ledge in contact with ice, thereby reasonably assuming that crack propagation is rate limiting, according to:

$$\dot{Q} = k_c \overline{V}_c \left(1 - \frac{S}{L}\right) \qquad \text{(Equation 3.21)},$$

where $\overline{V}_c$ is the crack propagation velocity averaged over a unit area of bed. The dimensionless constant k_e permits tuning the equation 3.21 and to reproduce representative basin wide erosion rates for the region under consideration. The crack propagation velocity V_c takes the form used by Atkinson (1987):

$$V_c = V_i \left[\exp\gamma\left(\frac{K_i^2}{K_{ic}^2} - 1\right) - \exp\gamma\left(\left(\frac{0.3K_{ic}}{K_{ic}}\right)^2 - 1\right) \right] \qquad \text{(Equation 3.22)},$$

where the stress intensity factor $K_i > 1/3K_{ic}$, the critical intensity factor above which cracks grow unstably, and $V_c = 0$ when $K_i < 1/3K_{ic}$. V_i and γ are lithology-dependent material parameters and K_i is a function of the differential stress about the ledge exterior corner and crack length scale. The differential steady state stress about the ledge corner is the difference between the normal stress imparted by ice on the bed and water pressure acting on the ledge riser according to:

$$(\sigma_n - P_w) = N\left(\frac{1}{1-S'}\right)$$
(Equation 3.23),

where σ_n is the average normal stress imparted by ice in contact with the bed and the

dimensionless geometric separation index S' is the fraction of the ledge thread occupied

by the cavity ($S' = \dfrac{S}{L}$). The other symbols are defined as previously. The tensile strength

of ice (~1 MPa) places an upper bound on the maximum allowable differential stress.

At low sliding velocity (or high effective pressure), ice closes cavities and S'

approaches 0. The stress differential equals effective pressure and stress intensity in

cracks is less than the stress corrosion limit in rocks. On the other hand, at very high rate

of sliding and low effective pressure, the ice is nearly fully decoupled from the bed and

S' approaches 1; stresses in the ice at the reattachment point could exceed its tensional

strength and cavities collapse. In the limit, the effective closure rate of cavities vanishes

and the ice either becomes fully decoupled from the bed or the cavity system grows

unstable; $S' = 1$ and $N = 0$, and the right side of equation 3.23 blows up. Hence erosion

by quarrying turns off at both mid to high, and vanishing effective pressures. With a high

degree of bed separation, the rate of crack propagation is high but the size of quarried

blocks also decreases; this dampening of quarrying rates at high degree of decoupling is

captured by the model since quarrying rate is proportional to the fraction of ledge in

contact with the ice. For steady water pressure and low rate of sliding, there exists a

narrow range of effective pressure of at most a few bars over which quarrying occurs

(figure 3.13). This range increases substantially at high glacier velocity. At constant

velocity, the distribution of quarrying rates with N is strongly asymmetric; it rises

progressively with increasing effective pressure to reach a maximum and drops off

abruptly to 0 at greater N. The sharp drop in erosion rates occurs when the stress intensity factor at crack tips decreases below the corrosion limit because cavitation isn't extensive enough to induce significant stress concentration at reattachment points.

Studies of spectral power density of recently deglaciated surfaces show that at all length scale, roughness varies little (Hubbard et al., 2000). I am mostly interested
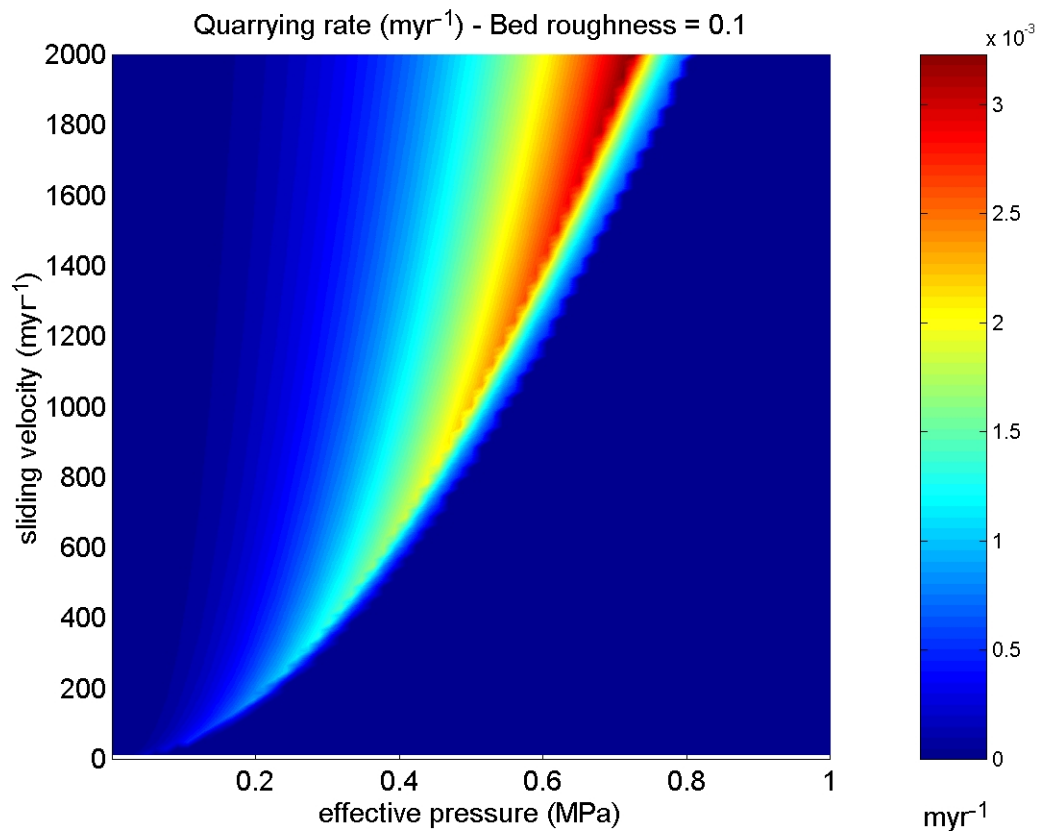
Figure 3.13: Quarrying rates for steady water pressure, constant bed roughness and constant bedform wavelength. The probable effective parameter space under glaciers is the different shades of blue at lower effective pressure. The magnitude of quarrying rates is tuned to produce inferred sediment production rates.

in bed elements presenting significant relief that permit decoupling of the glacier sole. For all but the lower effective pressures, the amount of bed separation for a given

velocity is dependent on bed roughness. The rate of sub-critical crack growth is

dependent on the amplitude to wavelength ratio of bed obstacles (fig. 3.14). At constant

velocity, the maximum in quarrying rate increases both with roughness and effective
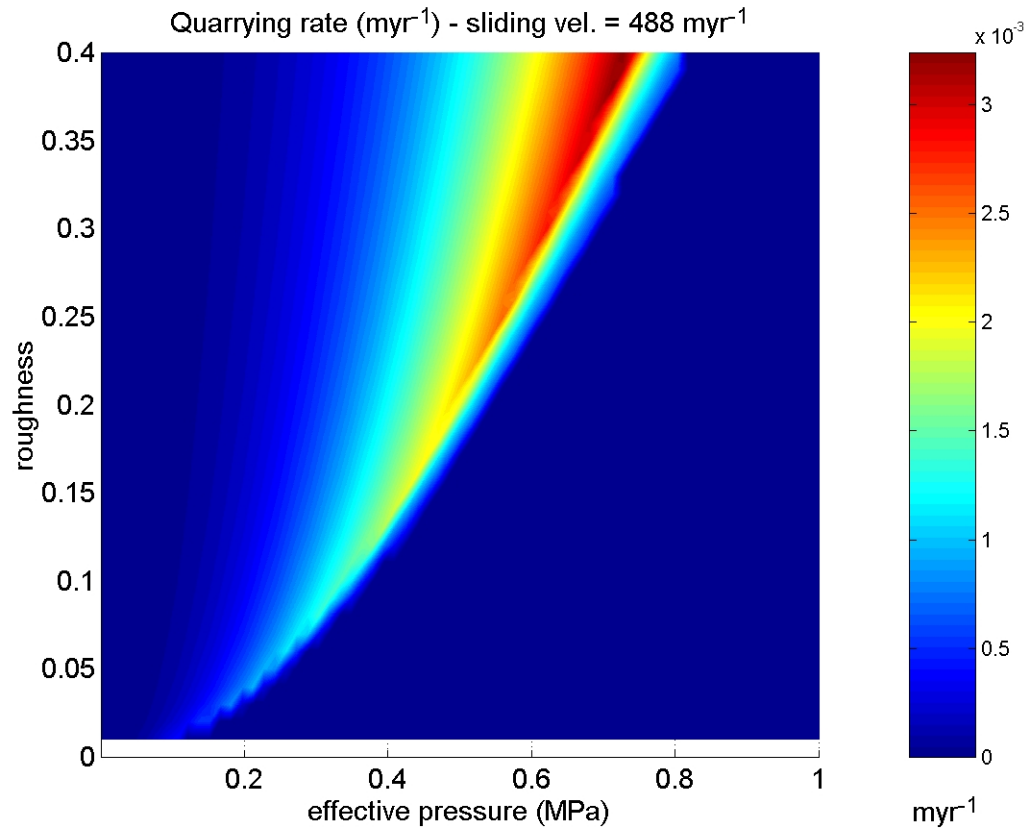
Figure 3.14: Distribution of quarrying rate for a range of likely bed roughness at constant velocity (~490 m/yr).

pressure. The range of effective pressure, at which quarrying is rapid, increases between

~2and 10 bars depending on bed roughness and velocity: a representative density

distribution of bed elements should therefore broaden the range of conditions susceptible

to quarrying of the bed. Predictably, low roughness demands high rates of sliding to

induce significant cavitation and high rates of quarrying (fig. 3.15). In turn, vanishing

effective stress limits erosion at high velocities and high roughness.

135

I have thus far considered bed topography of variable roughness and of constant

wavelength whereas, in fact, for a given sliding rate bed separation is likely to increase
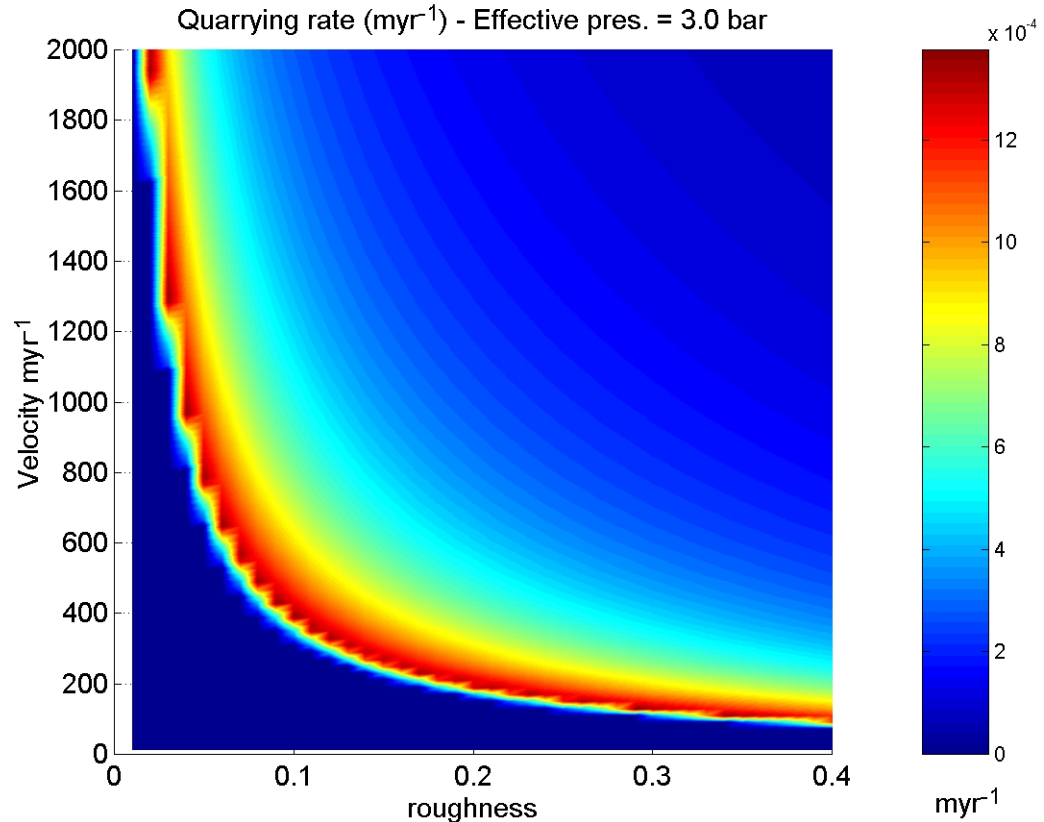
Figure 3.15: Quarrying rates for a range of likely roughness at constant effective pressure. The distribution of quarrying is displaced toward the top right hand corner of the figure with increasing *N*.

with decreasing length scale; it is therefore likely that under uniform condition of ice

pressure, velocity and bed roughness, greater rates of quarrying occur for bed obstacles

with short long axis. At the small end of bedforms dimensions, that which is smaller than

the transition wavelength for sliding (< 1 m), roughness elements of the bed are unlikely

to give rise to significant bed separation because of ice regelating in the pressure shadow

of roughness; however, obstacles with wavelength on the order of meters undergo

significant decoupling even for moderate rates of sliding (O[10^2 myr^{-1}]) (Nye, 1969).

According to our bed separation index, bedforms of most relevant wavelength (from meters to outcrop scale) undergo much separation (*S'*>0.7) at low effective pressure (<5 bars) but only bed obstacles with length scale near the lower end of the range (<10 m long) can undergo similar bed separation at effective pressures approaching 1 MPa. Computing quarrying rates for a uniform set of bed roughness (roughness range: 0.01-0.4) elements with wavelengths ranging between 1 to 30 m, under the typical bed
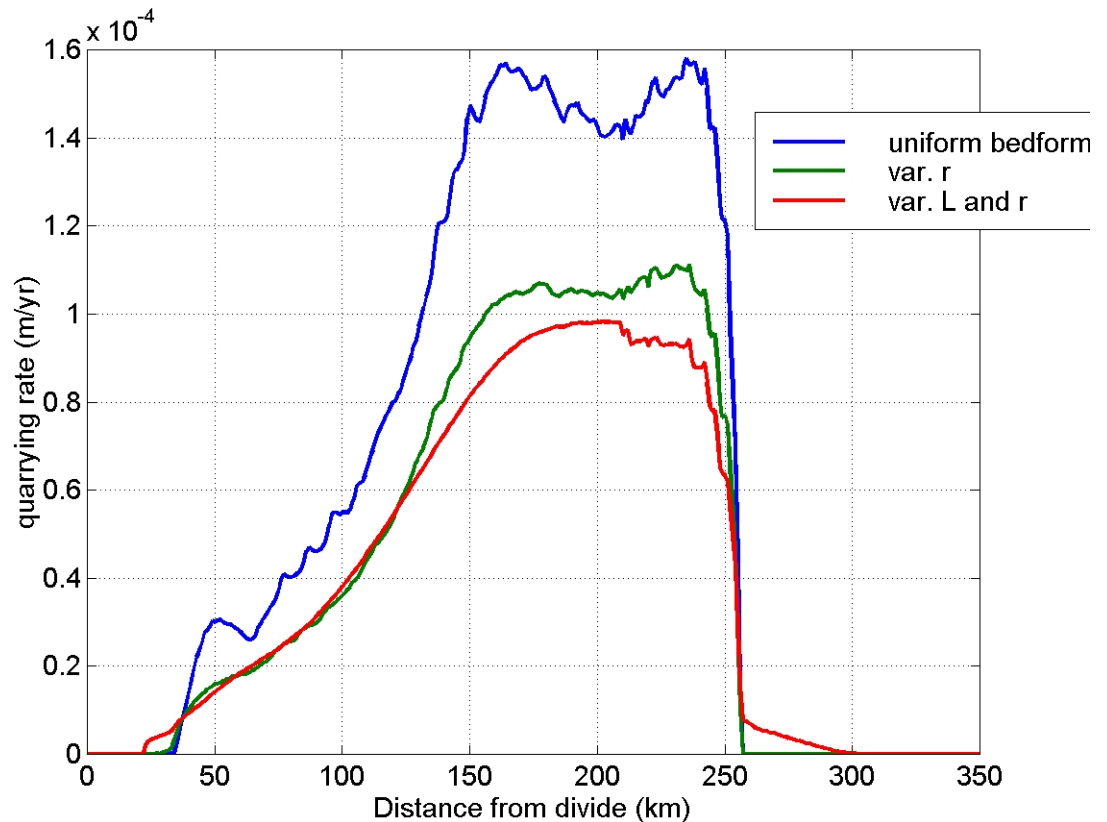
Figure 3.16: Comparison of quarrying rates for glacier bed geometry composed of bed obstacles of uniform geometry with variable roughness and a bed with variable roughness and scale of bed roughness length scale.

conditions modeled in the baseline model, doesn't significantly modify the spatial distribution of erosion (10% difference in quarrying rates between the 2 scenarios

compared) found under condition of variable roughness and constant wavelength (fig. 3.16). It doesn't appear critical to incur the significant CPU time expenditure needed to account for a distribution of bed obstacles wavelength in the quarrying erosion routine. I assume a roughness density distribution heavily skewed toward low mean roughness to represent a possible range of bedform geometry (roughness range: 0.01-0.5, mean: 0.1) and constant wavelength of 10 m. Comparison of quarrying rates of uniform bedforms versus that for elements of variable roughness under moderate conditions of ice flow confirms that a distribution of roughness element significantly change the magnitude of erosion incurred (~33% difference in quarrying rates over much of the profile). It seems therefore worthwhile to account for a representative distribution of bed element roughness while computing erosion by quarrying.

When water pressure in cavities suddenly decrease, perhaps because of a sudden increase in subglacial network connectivity or a rapid decrease in water injection at the bed, the differential stress about the ledge corner increases because a greater fraction of the normal load is taken up by the ledge. Depending on the new water pressure and glacier thickness, it may take from a few hours to several days before cavity size reach equilibrium with the new stress conditions. Accounting for water pressure transients, and balancing forces in the vertical direction about the ledge, permits solving for the transient differential stress about the corner, according to:

$$(\sigma_n - P_w) = (P_w - \Delta P_w)\left(\frac{1}{1 - S'}\right) \qquad \text{(Equation 3.24)},$$

where $P_e - \Delta P_w$ is the new effective stress computed after the water pressure drop, and S' is the bed separation index characteristic of the steady state of stress. Water levels in boreholes below the snow line have been observed to drop many ten's of meters in a few

hours, which implies that water pressure variations of up to 1 MPa are possible within at least part of the network (Nienow et al., 2005; Kamb et al., 1985; Iken and Bindschadler, 1986). It is however unclear whether large water pressure variations are possible or common within the distributed network above the snow line. Assuming for an instant that such large variations are a widespread feature of subglacial hydraulic networks, I find that water pressure fluctuations in cavities significantly increase quarrying rates at all effective pressures (fig. 3.17). When comparing the departure in quarrying rates with the distribution shown in figure 3.13 for the entire parameter space in the steady case, on average the effective pressure range under which active quarrying occurs almost triples over the entire velocity range for a water pressure drop of 1 MPa. The greater the stress decrease in the cavity, the greater the increase in the range of conditions under which quarrying is effective. The horizontal axis in figure 3.16 is characteristic of the steady state effective pressure prior to the perturbation. Thus, although the window of conditions susceptible to quarrying is enlarged because the differential stress about the ledge corner is for all water pressure drops greater than in the steady case, the geometry of the cavity most susceptible to quarrying is still determined by steady state conditions. The effect of water pressure drops on quarrying rate is thus limited by the non- dimensional geometric term on the right-hand side of equation 3.24 and the parameter space considered in the steady case is still relevant for the perturbed state. The range of effective quarrying is greatly expanded by water pressure transients at lower effective pressure and for lower
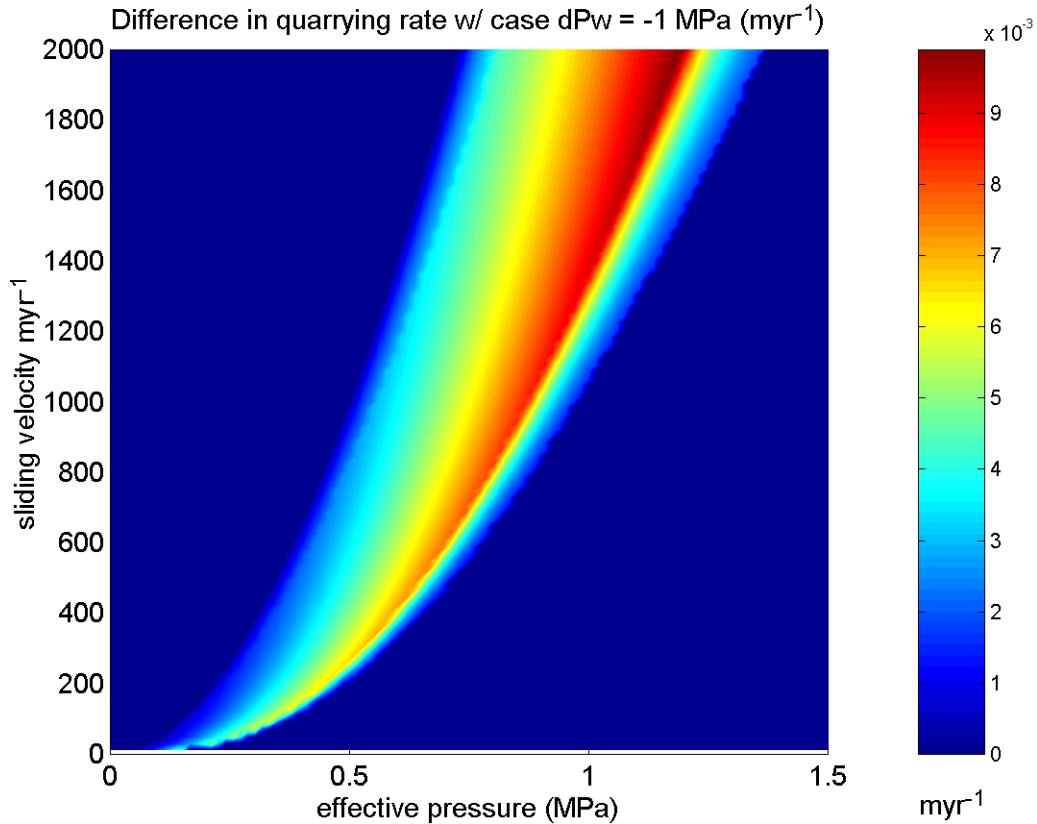
Figure 3.17: Departure in quarrying rates caused by a 1 MPa water pressure drop with bed roughness of 0.1. Reference case is the steady state of stress shown in figure 3.14.

rate of sliding; however, the inverse relation between normal stress and sliding still

precludes an initial cavity geometry that would sufficiently concentrate stresses at high

effective pressure even though the differential stress may be greater after perturbation. I

have so far considered only the case of decreases in water pressure because a positive

fluctuation in cavity pressure does not result in changes in the relevant parameter space

for the erosion controlling variables accounted for in our model. An increase in cavity

pressure would rapidly translate into decreased normal stress and greater bed separation

as if one moved to the left toward decreasing effective stress in the output for the steady case shown in figure 3.13.

To obtain suitable input for the quarrying model, I represent the daily variations of water pressure induced by discharge and other hydrologic events not captured by the monthly averaged climatic forcing by assuming a normal distribution of water pressure within the range dictated by extreme discharge variations. I also assume that the spatial distribution of water pressure fluctuations is centered about the computed monthly mean for each domain cell of the distributed network of cavities and links, whereas it is
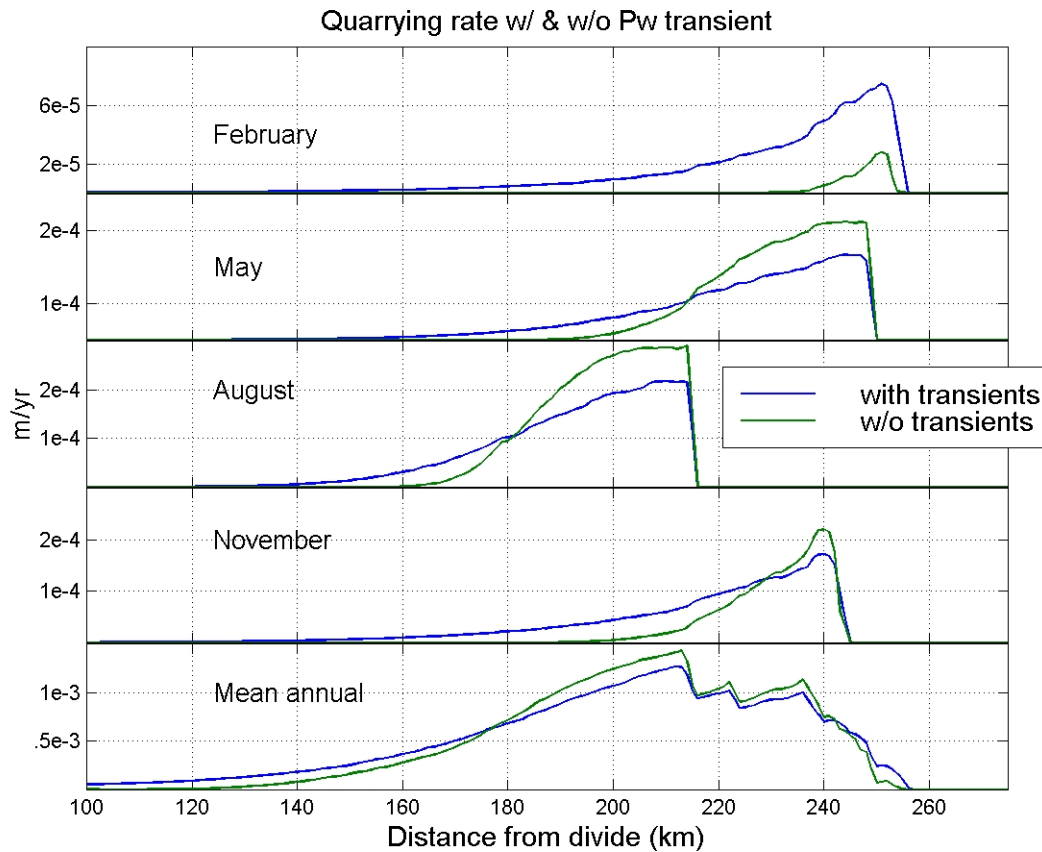
Figure 3.18: Comparison of quarrying model outputs between steady and transient cases (Velocity: 10-200 myr⁻¹; Effective pressure: 2x10⁵-1x10⁶ Pa).

centered about the mid-value between R channel pressure and overburden pressure below

the snowline. To understand further the effect of water pressure fluctuations on the spatial

distribution of quarrying rates in conditions susceptible to arise under the modeled

glacier, I compute quarrying both in the steady and the unsteady cases to compare results

(fig. 3.18). Although a distribution of water pressure about the monthly mean is used in

the steady case to represent a spatial and temporal distribution of steady water pressures,

only in the transient case do I consider changes in the state of stress near the ledge corner

before cavity size relaxes to a new equilibrium. When accounting for stress transients to

compute stress differential about ledges, quarrying is active over a greater fraction of the

longitudinal profile than in the steady case, which is consistent with the earlier

observation that in the transient case, quarrying occurs under a broader range of

conditions. During the winter season, water pressure variations would increase quarrying

substantially; however, large pressure variations in the winter are rare, which may point

to the need for a seasonal modulation of water pressure transients density distribution.

During most of the year, the spatial distribution of quarrying is a little smeared out (lower

magnitude, greater footprint) but the monthly difference is never greater than ~30% and

often significantly less. These differences between the 2 methods result in little change in

the yearly spatial distribution of erosion rates.

     During any given month, quarrying erosion mostly occurs only in the region

between the monthly averaged snowline and the upper slopes of the range (fig 3.19 &

3.20). Despite the prescribed distribution in water pressure between channel pressure and
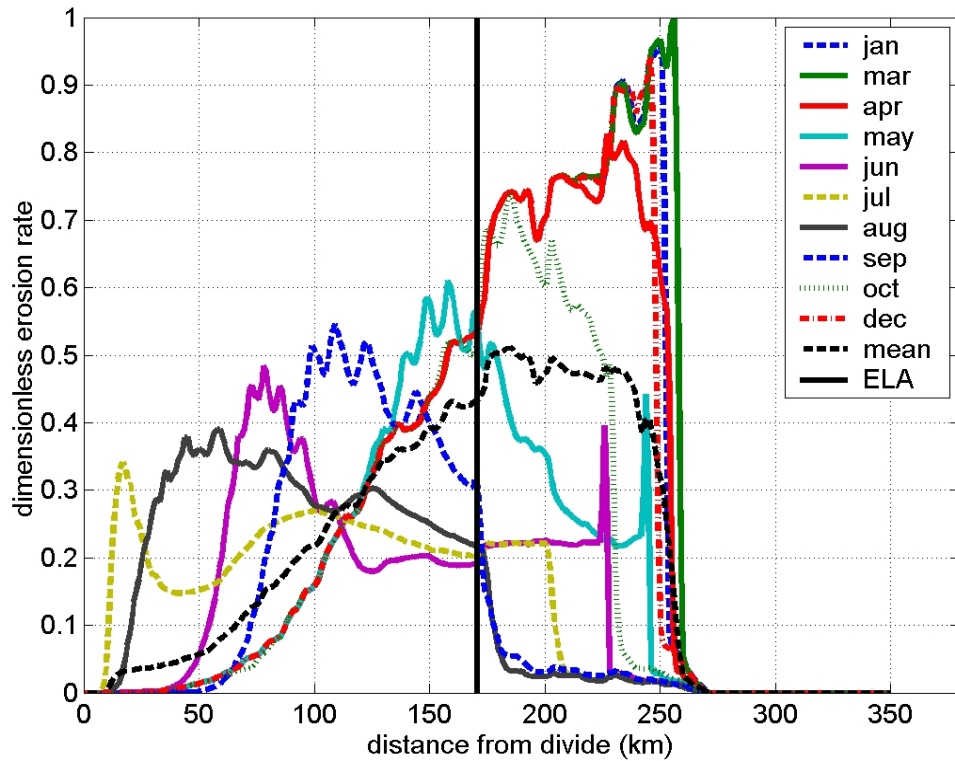
Figure 3.19: Monthly mean distribution of quarrying rates for $\alpha = 5 \times 10^{10}$. Rates of erosion during February and November that are not included in the graph resemble closely the other winter month. Spikes in output at the network transition during June and May result from effective pressure passing briefly through the optimum range of conditions for quarrying.

buoyancy, quarrying essentially shuts off below the monthly snowline because at low

velocity, less than 200 myr^{-1} in this model run, only a small range of low effective

pressures (a few bars at most) enables quarrying (fig. 3.13). Implementing more complex

basin geometries and a mass balance gradient that permit fast sliding may therefore

change the pattern of erosion observed in these model runs. As the melt season

progresses, the peak in erosion migrates upglacier until August when it starts migrating

toward the ablation area. Since the rate of erosion on any given month is strongly

dependent on a small range of effective pressure, especially at lower sliding velocity, the

value of parameter α is critical. When $\alpha = 5\mathrm{x}10^{10}$ as pictured in figure 3.19, and melt

season mean water pressures are very low (<1 bar) in the distributed network, it is less

than the optimum conditions for quarrying (fig 3.13). Very large departures from the

mean can then only be expected during water pressure drops, which probably not very

common given the stable nature of the network. In this example, quarrying rates during
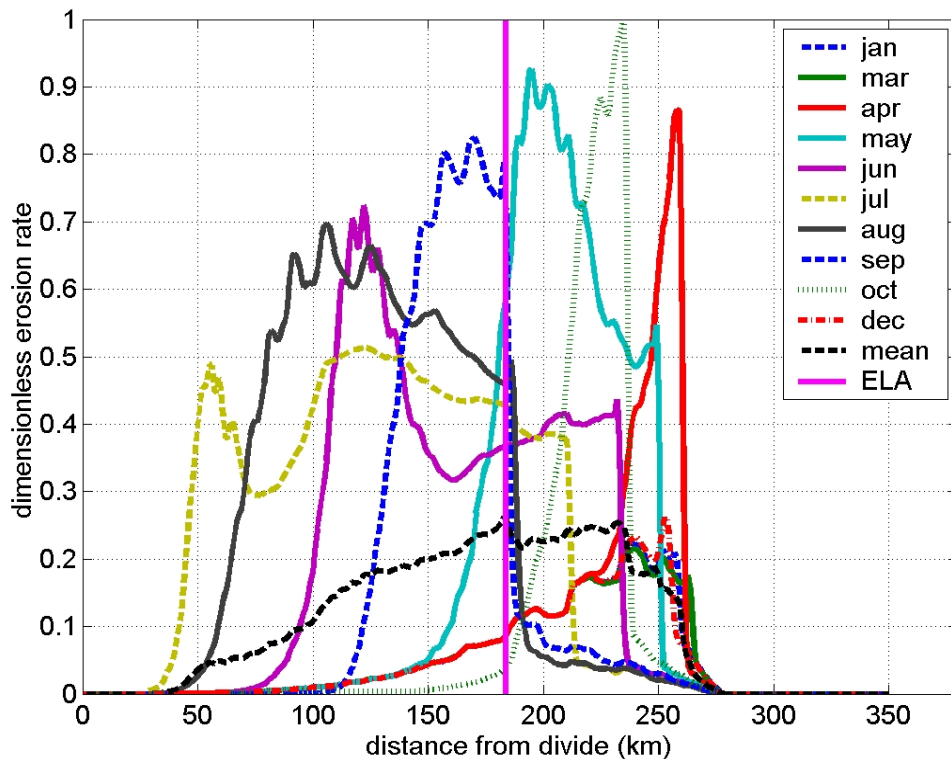
Figure 3.20: Monthly mean distribution of quarrying with $\alpha = 5\mathrm{x}10^{11}$.

the ablation season are lower than during the accumulation season because winter

effective pressures are 3-4 bars. The yearly averaged quarrying rate peaks ~20 km below

the ELA. Setting $\alpha = 5\mathrm{x}10^{11}$, changes the partitioning of quarrying along the glacier

profile (figure 3.20). With smaller α, the locus of erosion migrates upward along with the

snowline, and downward toward the terminus with the seasonal freeze. The amount of

144

erosion during the cold season is then significantly less than during the melt/rainy season because winter effective pressure are around 5 bars. The locus of fastest erosion averaged over a year is near the ELA. In both cases illustrated (fig. 3.19 & 3.20), mean yearly erosion below the ELA is important either because of the fast erosion near the seasonal snowline during the spring speed up or because winter erosion rates are significant. The tendency for a greater proportion of the annual erosion to take place during the melt season continues with increasing values of α. The fastest erosion averaged over a year also remains near the ELA because maximum incision occurs at the snowline where effective pressures are lowest yet not so low as to prevent quarrying. Summing up the sensitivity of the pattern of erosion: the maximum in yearly erosion migrates from a short distance (~20 km) below the ELA to near the ELA as α increases. Although, erosion remains on average greater in the ablation zone irrespective of α, the proportion of erosion occurring in the accumulation area increases with α.

To assess the vanishing values of erosion rates below the seasonal snow line, I increased 2-fold the standard deviation of the assumed Gaussian density distribution for water pressure about R channels, but erosion rates in the ablation region remained less than an order of magnitude smaller than above the snow line. Substituting a uniform probability distribution of water pressure between channel pressure and buoyancy as an end-member case also didn't change results significantly from the reference case.

In regions where the effective pressure is greater than the range at which quarrying is effective yet sliding occurs, abrasion is likely to be significant. The rate of abrasion is simply assumed to scale with the sliding rate:

$$\dot{A} = k_a U_{slid} \qquad \text{(Equation 3.25),}$$

145

where k_a is a constant scaled so that background erosion is ~1 order of magnitude lower than the basin wide quarrying rate (Briner and Swanson, 1998).

Overdeepenings have a finite depth that is self-limiting by two potential negative feedbacks: 1) erosion stops when the effective pressure vanishes and 2) a substantial cover of debris prevents bed erosion. Rothlisberger's (1972) solution for subglacial water flow indicates that water would tend to freeze in channels on a rapidly rising reverse bed slope. A rapid pressure drop due to thinning ice raises the freezing point of water flowing uphill, thus causing it to freeze along channel walls whenever mechanical dissipation is not great enough to sufficiently raise water temperature (Hooke, 1991). If conduits freeze to the point when water is forced along the bed or in a distributed network, the sediment transport capacity of the flow decreases, causing sediments to accumulate. Sediment evacuation out of hollows would then be entirely dependent on entrainment by ice either through shearing of a soft bed or basal freeze-on (Alley et al., 1997; Alley et al., 1998). To implement these feedbacks simply, I define a critical negative bed slope beyond which no further erosion occurs. As suggested by Hooke (1998), it can be simply formulated as the negative multiple of the ice surface slope.

3.7 Model experiments with a land based glacier with no sediment transport

The dynamics of glacial landscapes like those of other geomorphic systems are non-linear and complex. To illuminate the role of cumulative mass balance and runoff on the evolution of glacial longitudinal profiles, streamlined models are used in the next section; they are devoid of most complicating feedback and with basins of simple geometry. I start with a model of a basin of uniform width to eliminate the effect of local

146

topography on flux divergence and compare its longitudinal distribution of erosion with that of a basin with a width distribution that include the principal features found at Seward-Malaspina Glacier.

3.7.1 Erosion by a glacier of constant width

Initial conditions and response to forcing: The main attributes of large basins in South Alaska, with longitudinal scale of 10^5 m and very high relief over short distances at basin headwaters (~5000 m over 25 km), are retained (fig 3.21). Applying South Alaskan climate to the domain (Length = 0-3.5x10^5 m; Width = 5x10^3 m) causes the glacier to expand much beyond the lower domain boundary 35 kyr into a glacial cycle, because there is no accounting for major ice loss caused by calving in tidewater, the topographic gradient of the continental shelf is very low (0.002 slope) and the width is forced to be constant. To contain the glacier in the domain during the glacial maximum and keep CPU time within reasonable bounds demanded increasing mass balance gradients in the ablation area to augment melting. To meet this goal, a small topographic slope was introduced from the mountain front to the distal end of the long profile (0.0047 slope) in the region of the modern continental shelf, which in turn required raising the mountain end of the profile by 1500m to also account for the part of the modern landscape presently below sea level that becomes glaciated during colder climates. These steps proved however insufficient to contain the variations of such a narrow glacier within domain bounds. A more negative mass balance was obtained by raising the modern ELA through raising mean monthly temperature by trial and error (9^oC uniformly added to vertical air temperature profile) and lifting the distribution of precipitation with altitude

147

by approximately 1500 m. The resulting ELA is ~1500 m above that of the modern South Alaskan ELA at Bering and Malaspina glaciers. Mass balance shows maximum net accumulation reaching similar value to the estimated modern amount (2.5 versus 2.35 m.w.e.)

Although steep topography at basin headwaters ($>45^{o}$) prevents thick ice accumulation (Fig 3.21; panel a), it is included in the model because it represents a few percent of the glacierized area (nearly 3% of area in this generic interglacial case and 1-2% in the real world at Malaspina-Seward and Bering-Bagley glaciers) and is a non-negligible source of snow contributing to glacier mass balance. At lower latitude and/or elevation, as shown by W. Tangborn at Cascade Glacier (personal communication), the contribution to glacier mass balance by accumulation on steep topography is not important presumably because much snow deposited on topographic interfluves melts in place and runs off during summer; however, high topography at high latitude doesn't undergo sustained seasonal melt runoff, and most snow deposited on the high peaks is redistributed onto lower topography through wind redistribution and avalanching. Between major glaciations when ice isn't thick enough ($<10^{3}$ m) to fill valleys and drown local topography, the ice surface slope is sub-parallel to topographic slope in all parts of the drainage area. The dependence of sliding velocity on topographic gradients exerts strong control on the velocity distribution (figure 3.21, panel c). Decreasing the dependence of sliding on surface slope by reducing the power exponent on driving stress from 3 to 2 in the formulation of sliding results in qualitatively similar distributions of
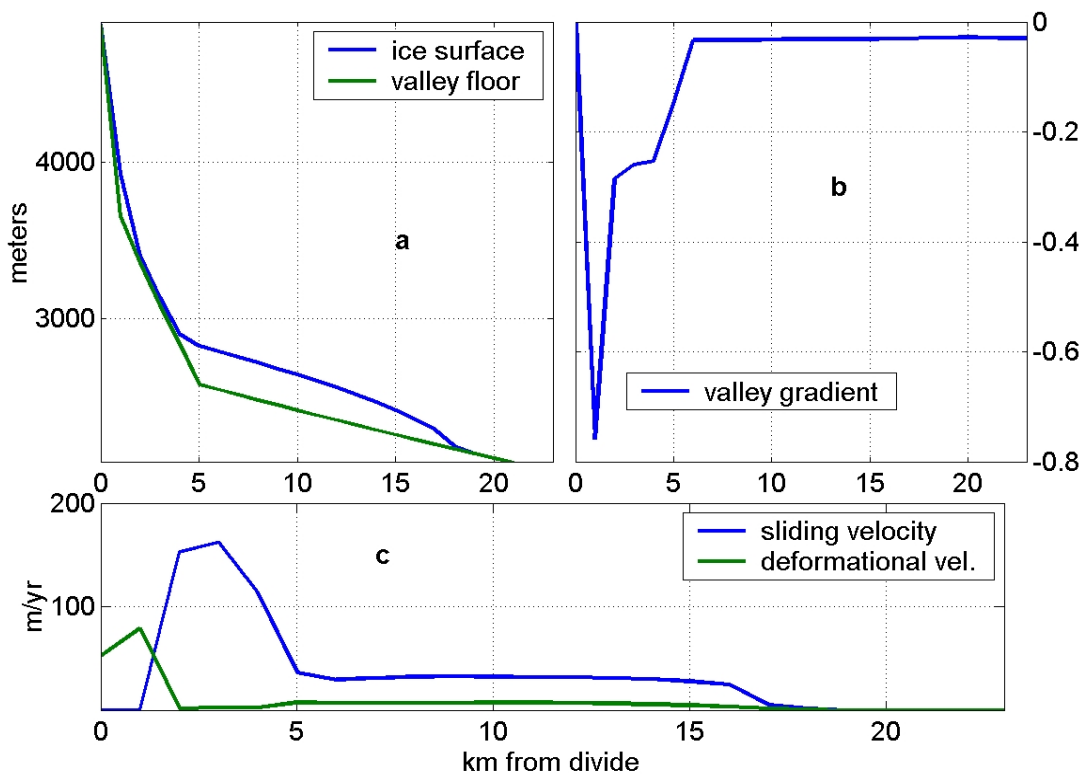
Figure 3.21: a) Initial conditions for a glacier of uniform width (*Wi* = 5 km) for α = 1x10^{11}. Note the important vertical exaggeration (~10X). b) Bed slope. c) The partitioning between basal sliding and deformational velocity is selected to represent a maritime sub-polar glacier.

longitudinal velocity. Greatest ice velocity occurs where slope is also greatest at basin

headwaters and a pronounced transition to lower velocity occurs at the main break in

slope where the glacier is in longitudinal compression. The lack of longitudinal stress

coupling in the model formulation likely exaggerates this transition, rendering it more

abrupt than it is. Although the small aspect ratio of the ice mass at basin headwaters

ensures compliance with the infinite thin slab assumption, the small slope assumption

doesn't hold, which places significant, but difficult to quantify uncertainty on the details

of glacier geometry (thickness) and velocity profile in that region for interglacial climatic

conditions. Fortunately, it is only over the first few spatial increments of the domain (0-5

km) that topographic slopes exceed 10%, and error in ice thickness in this region may
therefore exceed a few percent (Le Meur et al., 2004). Beyond the main break in
topographic slope at 5 km, velocity increases with ice discharge toward the ELA (ELA
located at ~2670m or 10 km down the profile in figure 3.3.1a) and keeps increasing
slightly along with ice surface slope to another maximum located 1 km downglacier of
the ELA in the example shown in figure 3.21. Along with the locus of lowest effective
pressure, the peak in sliding rate migrates upstream with decreasing. Partitioning of mean
annual velocity between deformation and basal motion is adjusted with the sliding
parameter so the yearly sliding flux is at least 2/3 of the total ice flux at the ELA, thereby
reflecting modern observations of velocity partition in south Alaskan maritime glaciers
(Harper et al., 2002). Tuning of the sliding parameter is done during average interglacial
climatic conditions when the generic glacier reaches a thickness and length scale similar
to massive modern Alaskan glaciers like Bering and Seward-Malaspina glaciers (10^2 km
in length and 10^3m maximum thickness). The seasonal pulse of elevated velocity
propagates with the melt season from the terminus upward into the accumulation area and
migrates back toward the terminus with the seasonal freeze up. Velocity during fall
amounts to 0.5-0.7 the peak rate of motion during the early summer speed up, hence in
broad agreement with field observations. During cooler climate and higher level of
glaciation, when the glacier spreads far onto the low gradient part of the domain and ice
thickness is sufficient ($>10^3$ m) to drown local topography, ice surface slope isn't sub
parallel to basal topographic gradient at basin headwaters and total velocity increases
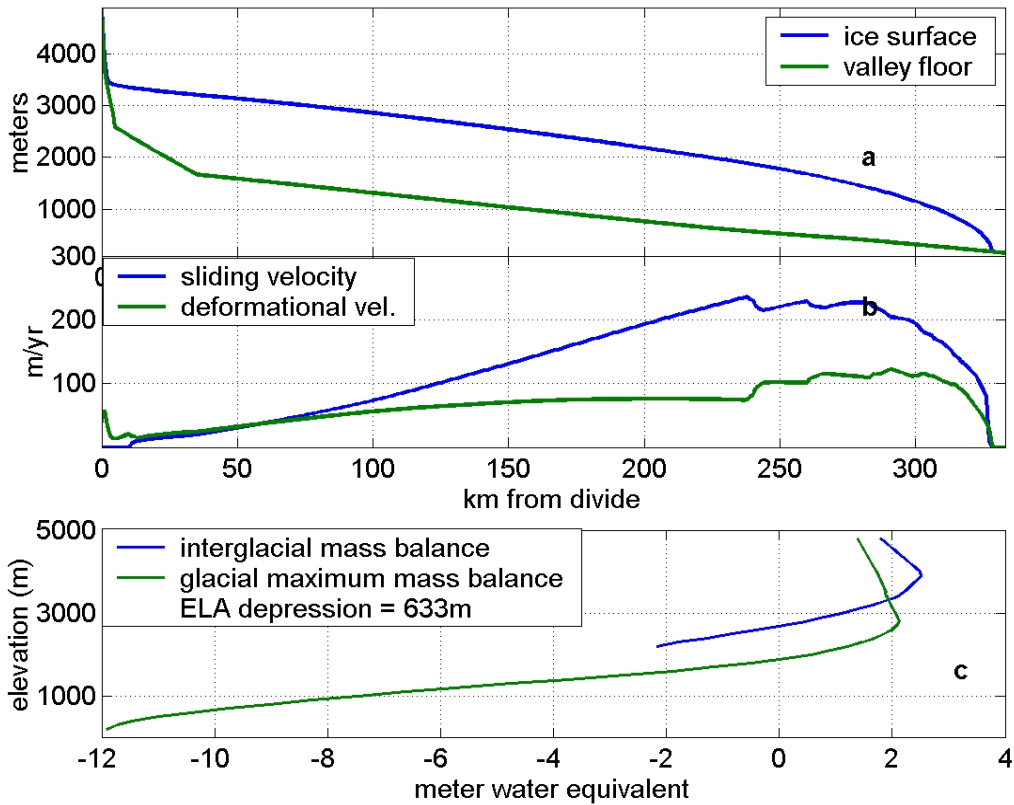
Figure 3.22: Surface and valley profiles (a) and partitioning of velocity (b) during the LGM for a glacier of constant width ($\alpha = 1x10^{11}$). ELA is at 2033 m near 220 km from the range divide in this model run.

monotically from the point where ice isn't frozen to the bed and down the profile to reach a maximum a short distance (at 238km in figure 3.22) beyond the location of the ELA.

Glacier response to climatic forcing and topographic constraints: The fluctuations in glacier extent are always in phase with climate forcing, which follows directly from the steady state assumption (fig. 3.23). The expected rapid transition beyond the major break
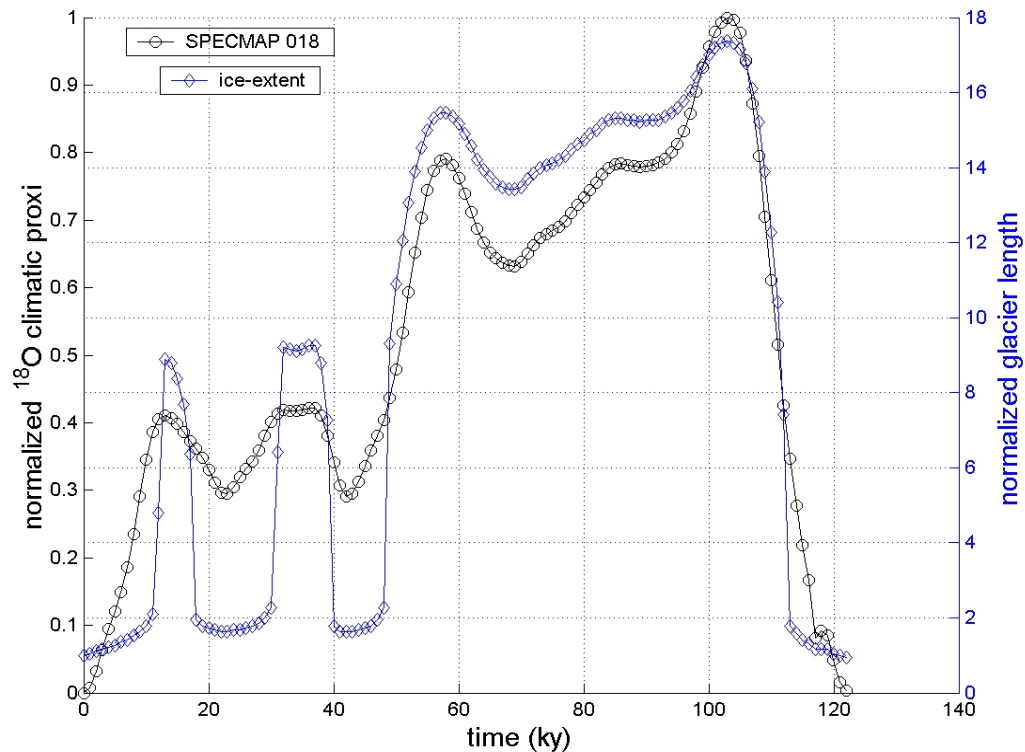
Figure 3.23: Normalized glacier extent (relative to maximum glacier extent) and paleoclimate proxy. Multiple glacial steady states when the glacier transitions beyond the main break in topographic slope translate into the fastest rates of advance and retreat.

in gradient for a valley of constant width is strongly reflected in the distribution of

terminus position, which can be divided between 2 states: 1) when the glacier is

contained within the region of steep bed slope and 2) the opposite. The sensitivity of

glacier response to climate change is inversely proportional to topographic slope and the

strength of the height mass balance feedback, which leads to the fastest increase in

glacier length as it transitions to more gently inclined regions. The glacier extends

beyond the major slope break for approximately 2/3 of the glacial cycle in this run. The

non-linear response of ice volume and the relative magnitude of oscillations in glacier

length in response to smoothly changing temperature and precipitation illustrate the effect

of longitudinal changes on glacial extent. Rates of terminus advance and retreat range over 3 orders of magnitudes (1-130 m/yr) with a mean of 10.5 m/yr. Since the height-mass balance feedback is the only implemented process response to the climatically induced variations in ice volume (i.e. no solid earth response to changes in loading induced by ice volume variations or thermo-mechanical dependence of ice flow on climate), the fluctuations of terminus positions along the valley profile respond to climate without a lag, and there is no hysteresis in ice volume as climate cools then warms.

Temperature of the basal interface: Despite the very large positive changes to South Alaskan air temperature introduced in the forcing to contain the size of the glacier, the upper 1600m of the region is below freezing temperature throughout the glacial cycle (figure 3.24). The existence of a thin protective cold ice cover at all times also avoids the cracking of rocks due to melt-freeze cycles or following periods with high freezing levels on all but the ice-free steepest slopes. This steep and high landscape is therefore mostly subject to lowering by mass wasting induced by gravitational and tectonic stresses. Model output suggests that the region of ice cover frozen to the substrate, therefore immune to significant glacier erosion, expands from 1 km during interglacial to 8 km away from the divide during periods of maximum climatic cooling. According to ice thickness and surface vertical velocity, the response time of the temperature at the basal interface to surface forcing could at times be a multiple of the time increment chosen between equilibrium conditions, which places uncertainty on the timing of the transition from a lubricated base to a frozen one as climate cools. About 8 km from the range divide, ice thickness varies from 350m during interglacial up to 900m during full glacial

153
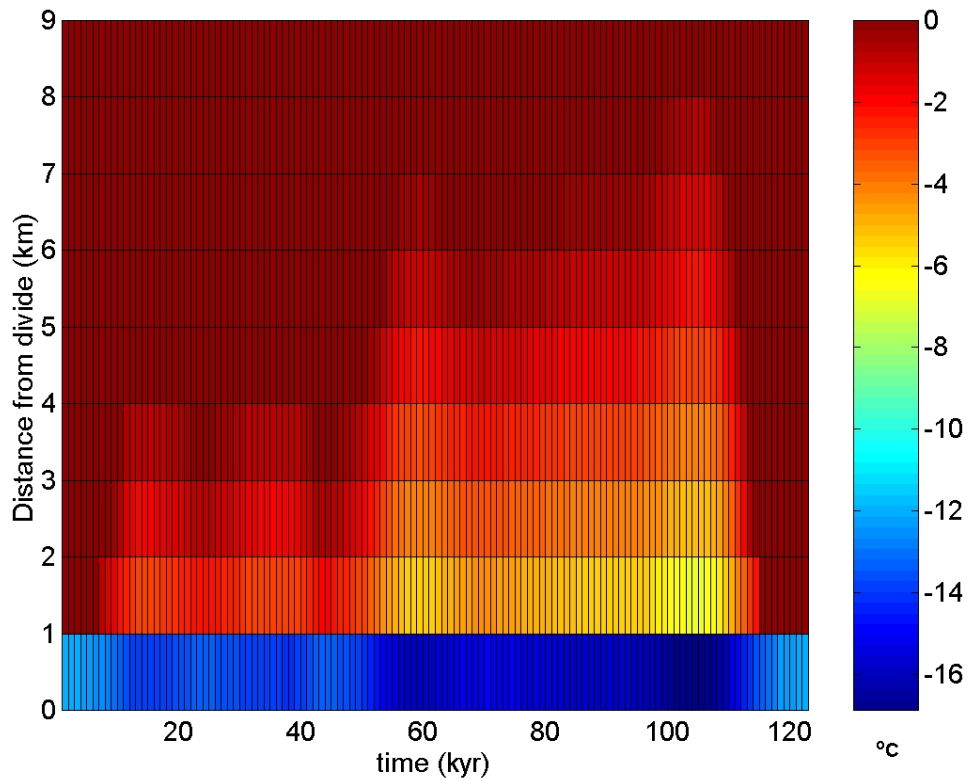
Figure 3.24: Temperature of the basal interface with the substrate and its evolution during a glacial cycle.

conditions; during half of the climatic cycle ice thickness is greater than 800m. Surface accumulation on that part of the domain is more than 2 m when ice is the thickest. Linear velocity estimates of the equilibrium response time for the temperature of the basal interface when ice is the thickest show that it is at most a small multiple of the modeled time step during the 55-110 kyr part of the climatic cycle. Therefore, the maximum modeled extent of frozen basal condition appears possible even though the timing of the glacier sole becoming frozen to the bed may differ from the model output by at most a few time increments. This modeled range of variation in basal temperature is likely to become greater when using air temperatures characteristic of South Alaska.

The distribution of erosion: Since the object of this run is to isolate the climatic controls on the pattern of erosion with minimal interference from topography, the free parameter in the quarrying rule is kept low so that erosion integrated over a glacial cycle doesn't appreciably alter basin hypsometry and glacier mass balance. For a mid-range α
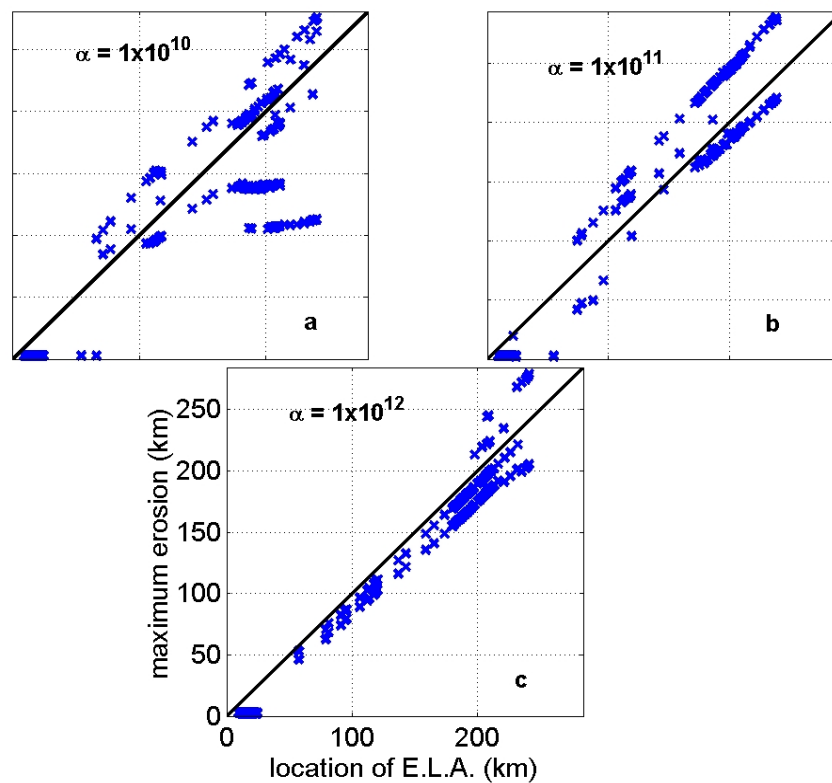
Figure 3.25: Bed regions where erosion is greater than 90% of maximum erosion versus the location of ELA for a range of α. Regions are defined by their proximal and distal boundaries relative to the range divide.

parameter value for hydraulic conductivity of 1×10^{11}, which for this topography and climate produces basal effective pressures most similar to those measured, the pattern of

erosion in regions of constant small bed slope and uniform width can be approximated by

an asymmetric bell shaped curve (fig 3.26). It has a broad maximum coinciding with the

domain that is swept by the snow line and extends upglacier beyond the ELA (fig 3.25,
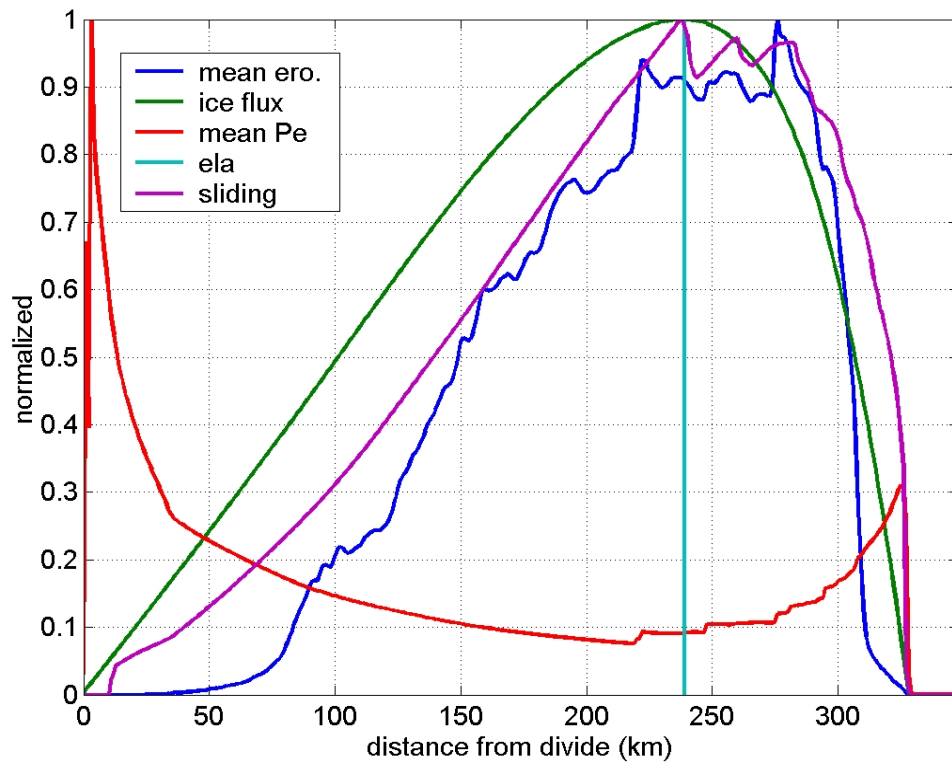
Figure 3.26: Longitudinal distribution of erosion under a glacier of uniform width during full glacial conditions ($\alpha = 1x10^{11}$). All variables displayed are mean annual quantities normalized by the yearly maximum occurring on the profile; mean annual sliding velocity reaches 235 m/yr and mean annual effective pressure is as low as 2.2 bars, whereas monthly mean values are as low as 0.5 bars. Spatially averaged effective pressure below the ELA (the September snowline) is prescribed to be halfway between computed R channel pressure and zero.

panel b). The distribution has a longer upglacier tail that reaches high into the

accumulation area whereas the downglacier part decreases sharply near the full winter

snow line; erosion rates approach maximum values over ~2/3 of the ablation area (figure

3.26). As seen in section 3.2.7, mean annual erosion are fastest near the seasonal snowline because it is where surface water input overwhelms the carrying capacity of the distributed subglacial network when effective pressures are low, yet not so low as to be outside the optimum range of conditions for quarrying to occur. Quarrying erosion is small to inexistent below the lowest elevation of the snow line where surface melt occurs throughout the year and high in the accumulation area where surface melt is low. Quarrying rates range over one order of magnitude along ~70% of the longitudinal profile. Erosion in the remaining 30% of the glaciarized area, 80% of which is at the glacier head, doesn't occur through quarrying induced by deviatoric stresses about subglacial cavities but through abrasion of the substrate. Mean annual erosion peaks near the location of the maximum in ice flux per unit width because maximum ice flux occurs at the ELA that is part of the domain subject to high sliding rate and low effective pressure. Quarrying is a function of sliding and effective pressure, while sliding is itself inversely proportional to effective pressure, yet there is not a systematic correlation throughout the year between the distribution of mean monthly basal motion and effective pressure, and that of mean annual quarrying rates (fig. 3.27). Most monthly mean quarrying rates correspond to the highest monthly rates of sliding except in early summer when effective pressure nearly vanishes and quarrying becomes less effective. This distribution of quarrying rates and its relationship to effective pressure, ice discharge, and sliding rate seen in figure 3.26 holds for all levels of glacierization when the glacier extends beyond the major break in slope.
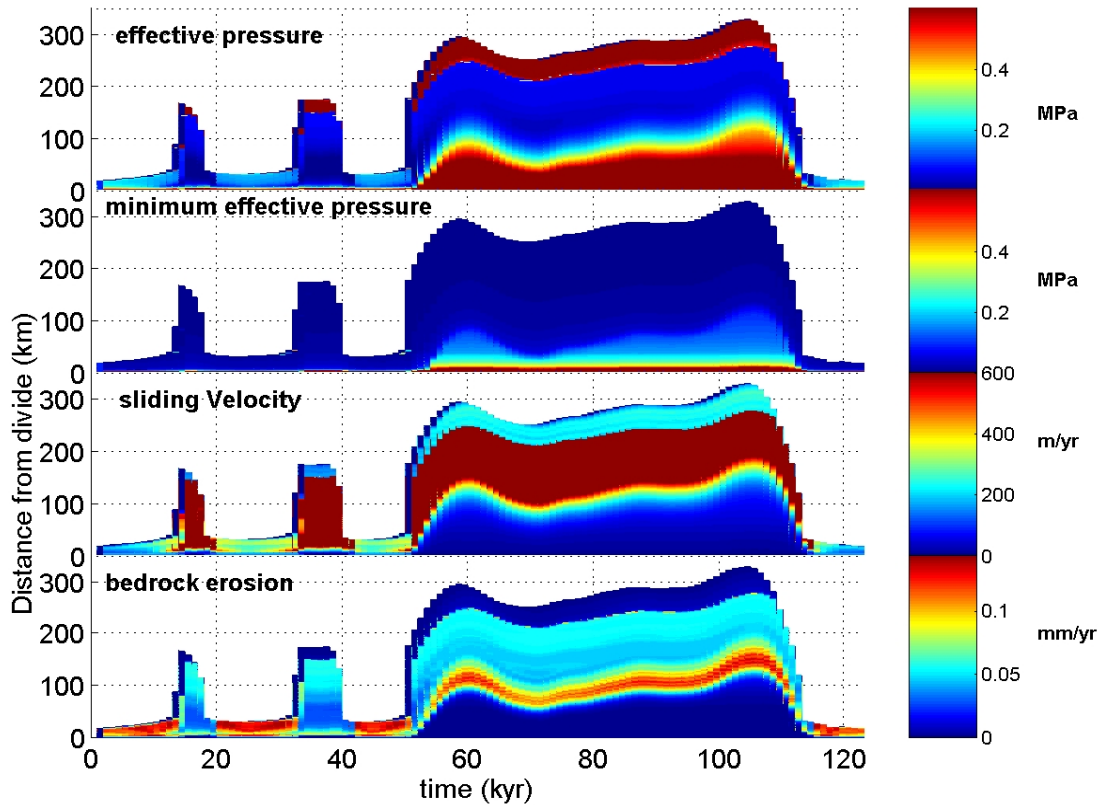
Figure 3.27: Average June basal conditions and relative quarrying rates for the duration of a glacial cycle. Rates are intentionally underestimated for reasons explained in the text. The range of effective pressure displayed is capped at 0.6 MPa to allow the variability at the lower end of the range to be visible. Note how the region of highest erosion doesn't correlate with the region of highest sliding from 50 kyr to 110 kyr.

During interglacial climate, when the glacier rests mostly within the region of steeper topography, the relationship between the yearly distribution of erosion and ice flux per unit glacier width is less predictable. Normal stress at the bed is small enough where ice is thin (<100 m) and sliding speed great enough to cause cavitation so that conditions are met for effective quarrying erosion without necessarily correlating to large ice flux (fig. 3.28); thus, quarrying can be fast both in the region swept by the snow line and in

158
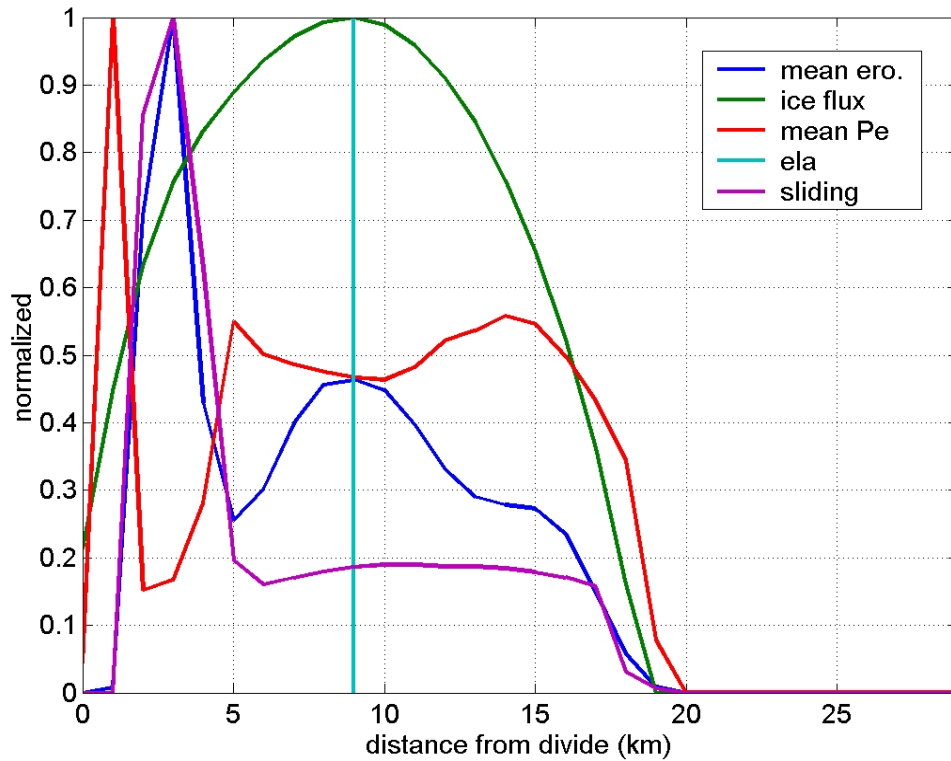
Figure 3.28: Annual distribution of quarrying and related basal conditions during interglacial conditions.

regions of thin sliding ice on steep slopes. Consequently, erosion can be fast over much of the interglacial glacierized area, including steep regions at basin headwaters during the ablation season (fig. 3.27).

In response to climate cooling and the lowering of the ELA, the regions of low effective pressure, high rates of sliding and erosion migrate down valley (fig. 3.27 and 3.29). As a result, effective pressures are higher and erosion is slower in the interglacial glacierized area during periods of significant glacier expansion that make up 2/3 of the climatic cycle.
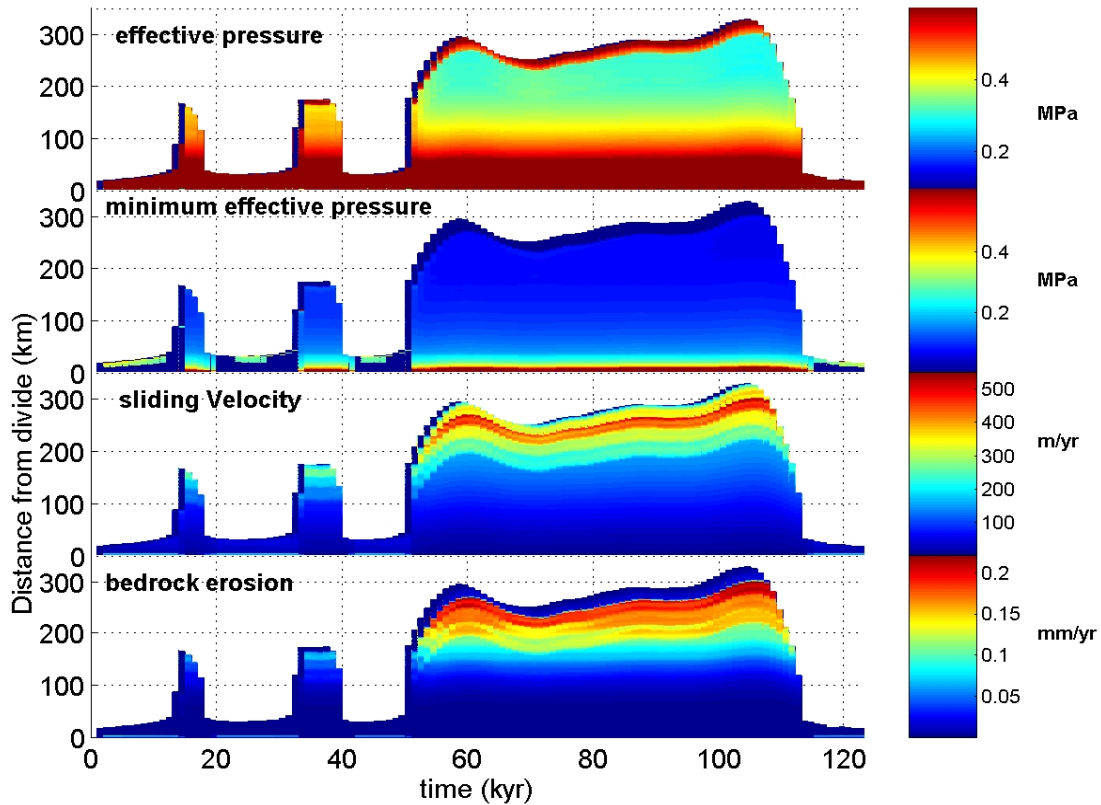
Figure 3.29: December basal conditions and quarrying erosion rates over the duration of a glacial cycle. The pattern of erosion coincides with that of monthly mean effective pressure and sliding rate during the winter season.

Average monthly and mean minimum subglacial water pressure decrease as climate cools and the glacier expands, due to a large increase in the cumulative quantity of water reaching the bed. As the glacier transitions from a retracted position essentially contained within the high mountains to a protracted one as it spreads onto the low gradient ramp for nearly similar climatic conditions (from 5kyr to 14kyr into a glacial cycle), the contributing melt area to water discharge scales with terminus advance; the cumulative water flux at the bed increases by nearly one order of magnitude. Model output suggests that despite a decreased surface melt rate and decreased precipitation, an increase in contributing melt area during cooler climate is sufficient to develop a more

160

efficient subglacial hydraulic system and induce lower water pressures during interglacial periods over a large portion of the valley that is occupied by ice. The monthly storage capacity indices near the ELA during glacier expansion are lower by only a few % thereby diminishing the effective transport capacity of the subglacial hydraulic network; however, the variation in the value of storage capacity index between these 2 states of glacierization is too small to account for the lowering in water pressure during cool periods. Running the model with lowered temperature and decreased precipitation show that this result is climate dependent. There is likely a threshold beyond which cooling and drying of climate results in a decrease in water routed at the bed and an increase in normal effective stress.

The relationship of cumulative longitudinal distribution of erosion for an entire glacial cycle to the distribution of ice discharge and basal speed that is slightly different to that observed for individual time steps (fig. 3.30). The maximum in cumulative erosion matches that of ice discharge for reasons cited previously: for a glacier of uniform width, ice discharge is at a maximum where ice is the thickest and where effective pressures are the lowest. As seen for each equilibrium state of glacier extent, the peak in erosion is downglacier of the ice discharge peak. For this configuration of geometry and climate, the maximum in erosion occurs a few 10's of km up valley from the location of the full glacial cycle ELA.

Even though the interglacial domain is covered by ice throughout the climatic cycle, it would be subjected to less erosion than the domain further downglacier that is only ice covered when climate cools (fig. 3.30).
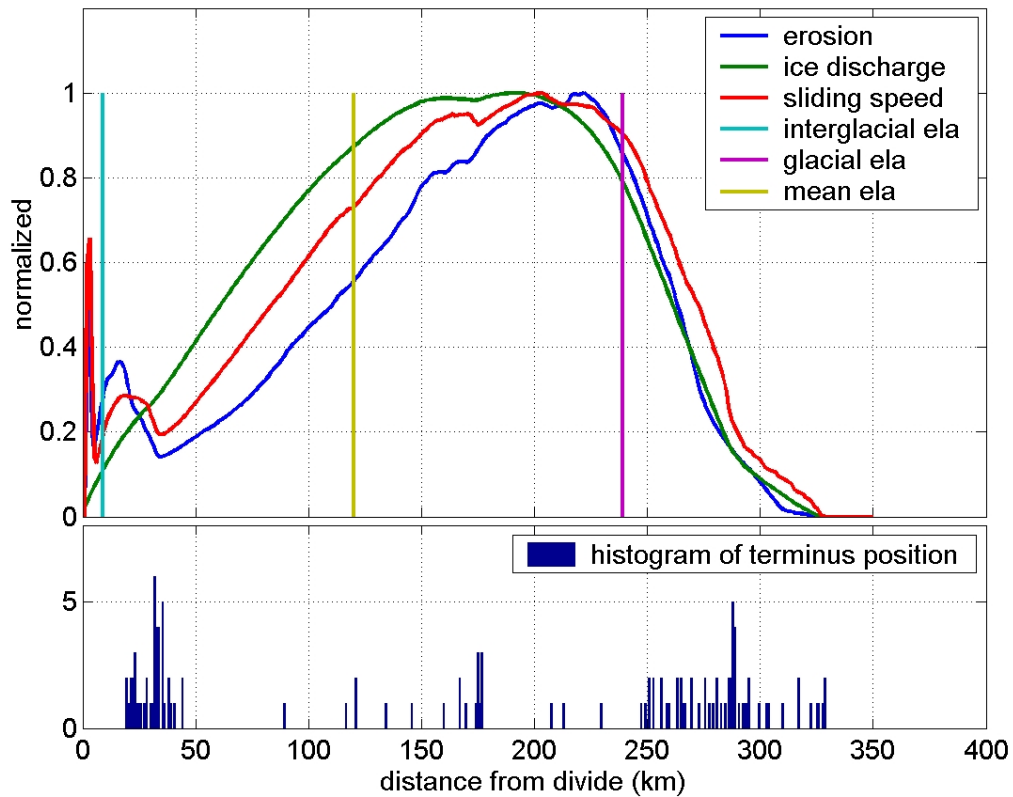
Figure 3.30: Spatial distribution of normalized erosion rates through quarrying and abrasion, ice discharge and sliding speed averaged over a glacial cycle. Vertical lines show the locations of the ELA at different parts of the cycle.

This result concurs with widespread evidence of greatly varying rates of plucking between two distinct sub-domains of glacial landscapes in sub-polar alpine regions: a) the bench-cirque zone immediately downstream from peaks where thin glaciers are found during interglacial quaternary climates and b) deeply incised trunk valleys and beyond where ice coalesces in thick ice masses.

3.7.2   Erosion by a glacier of variable width

Initial and full glacial conditions. Bed profile, precipitation and temperature

distributions with elevation, and their forcing are retained from the model discussed in

section 3.3.1. Like for the previous run, the resulting mass balance is similar in shape and
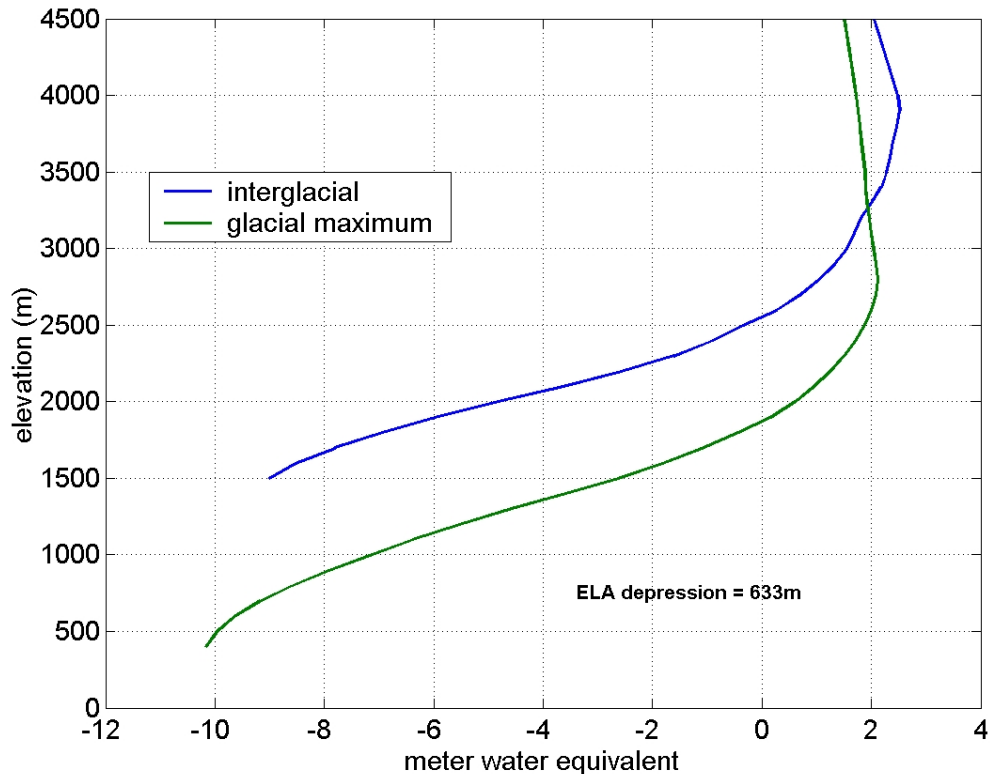
Figure 3.31: Mass balance during glacial minimum and maximum for a generic glacier of variable width.

maxima to that of the large South Alaskan glacial systems under study, except that

interglacial ELA is lifted by ~1500 m (fig. 3.31). Raising the ELA by this amount can be

thought of as simulating glacial systems with the dimensions of South Alaskan

topography at the latitude of the Northwestern coastal USA where average annual

precipitation and sea level temperature are close to that modeled in this exercise.

The only change from the previous section brought in the current model run is a

variable glacier width, with a longitudinal distribution similar to that of large south

Alaskan glacial systems (3.32). The width function consists of a broad, high accumulation area that narrows down to an entrenched valley, and then opens up onto a low gradient region where ice can spread laterally in a linear fashion with distance downstream until glacier width reaches a new maximum that is sustained for the remainder of the domain.

Due to the very broad accumulation area abruptly narrowing to a gorge, the interglacial ice mass extends easily beyond the region of steep topographic gradient, past the narrow valley outlet into the region where ice can spread laterally. In the upper 2/5 of the vertical domain (3000-5000 m), interglacial glacier thickness isn't great enough to decouple ice-driving stress from local topographic gradient. The velocity distribution reflects the first-order controls of steep valley gradient at basin headwaters and that of rapidly changing basin width as the valley narrows and broadens progressively further downstream. Due to ice flow convergence, the broad velocity maximum corresponds exactly to the region where the drainage narrows; sliding is fastest at the outlet of the gorge whereas the ice flux per unit width peaks a little past mid-point in the narrow valley (42 km down profile in figure 3.32, panel b).

During major glacial periods, the glacier extends much beyond the region where it is allowed to spread laterally (100 km from the divide in figure 3.34). The general velocity distribution is quite similar to that of the cumulative balance flux insofar it has 2 broad maxima. Like for the interglacial case, the first velocity high corresponds to the narrow gorge where ice flux per unit width is at an absolute maximum. The second

164
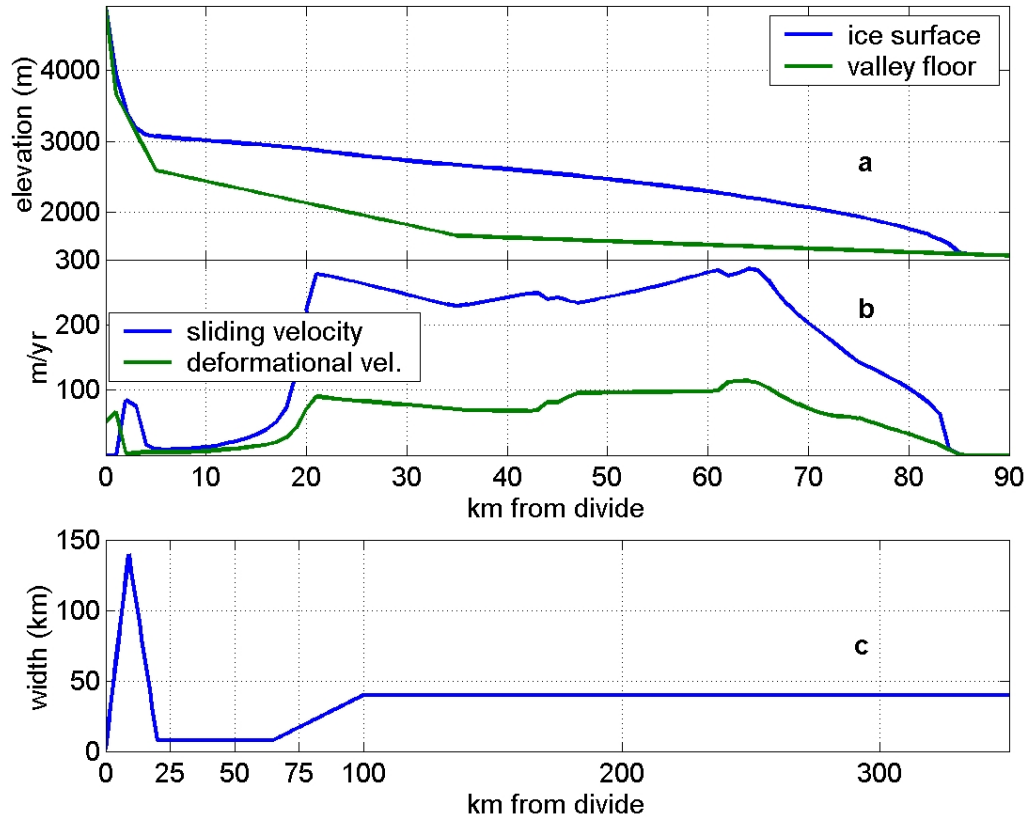
Figure 3.32: Initial conditions for a glacier of variable width ($\alpha = 1 \times 10^{11}$). Note the very large vertical exaggeration in the panel showing glacier geometry (a), and the change in horizontal scale for domain width (c). Over most of the profile, sliding accounts between 65-80% of total motion. Topographic long profile is the same as for the basin of constant width (fig. 3.22).

velocity high occurs in between the second relative high in ice flux per unit width (near km 215) and the maximum in driving stress (275 km). In this model run, sliding flux accounts for 60-80% of the total ice flux over 4/5 of glacier extent.
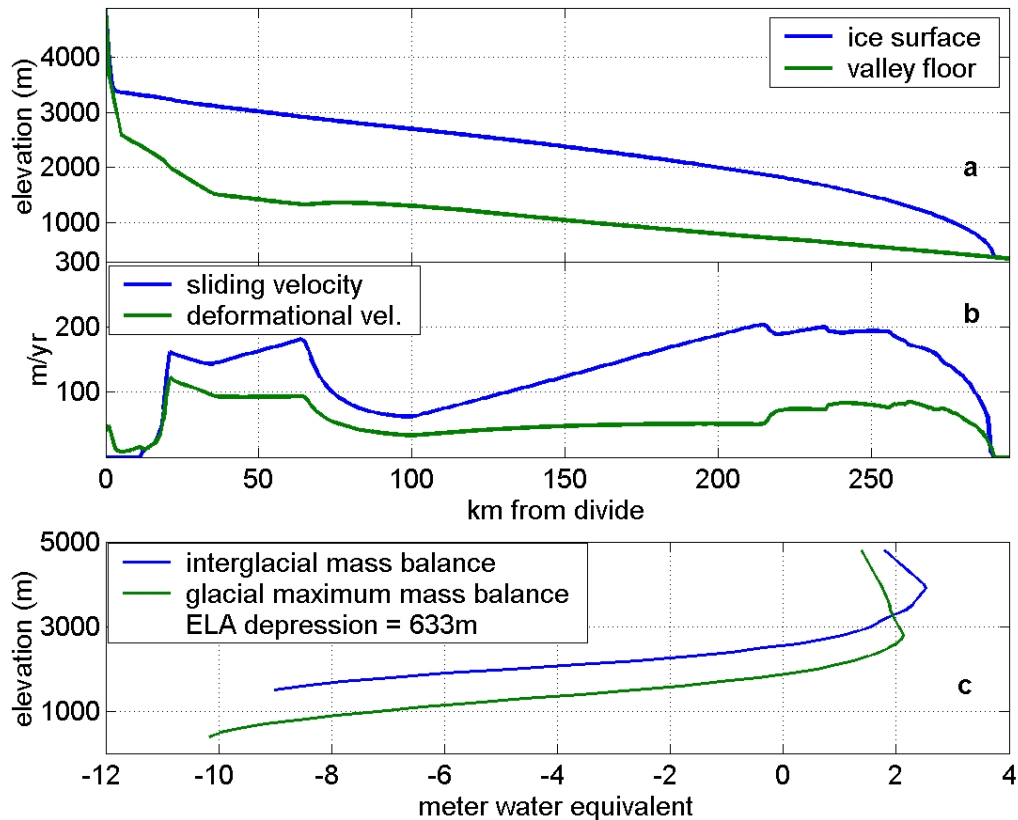
Figure 3.33: Glacier and valley profiles (a), and velocity partition (b) during the glacial maximum. Full glacial ELA is lowered to slightly above 2000 m, 200 km down from the divide during this run.

Glacier response to climatic forcing and topographic constraints: Due to the effect of valley geometry on ice flux divergence, the glacier reaches beyond the region of steep topographic gradient throughout the glacial cycle (fig 3.34). Consequently, the variation in terminus position doesn't show the high rates of terminus advance associated with the transition to lower topographic slope seen in the case of a glacier of constant width.

As is predictable, ice flux divergence in the section of the profile where the glacier can spread laterally dampens the response to climatic forcing while the terminus

is contained within that region. For the same prescribed mass balance, the amplitude of

fluctuations in glacier extent and rate of change in terminus positions with climate
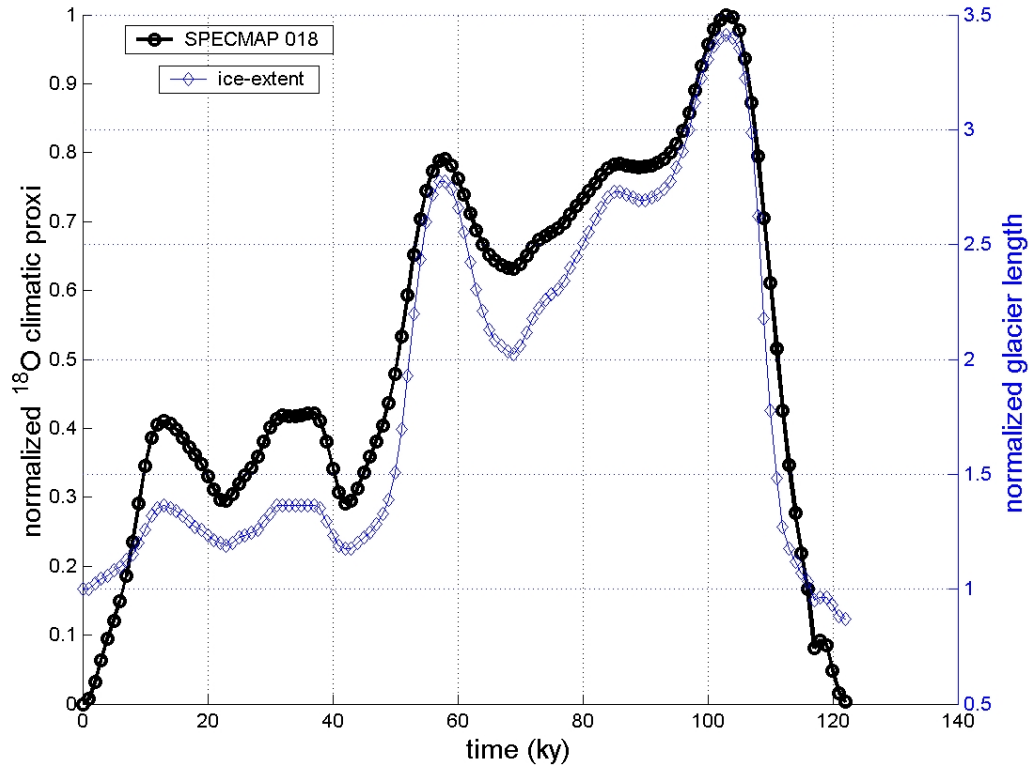
Figure 3.34: Normalized glacier extent and climatic proxy. Glacial response to climate is dampened by a variable width function.

fluctuations are significantly less than during the case of a glacier of constant width: the

difference in glacier length between interglacial and full glacial conditions is 210 km for

the variable width glacier versus 310 km for that of constant width. The respective mean

rates of terminus migration are 5.1 m/yr versus 10.5 m/yr. Changing mass balance by

raising the interglacial ELA so that minimum glacial extent is contained upstream from

the gorge outlet measurably decreases the difference in interglacial-glacial change in

glacier extent between the two discussed cases of width function; such an occurrence

would presumably be more representative of lower latitude glaciers.

The distribution of erosion: As for the glacier of constant width, the free parameter in the plucking rule is kept small to minimize the magnitude of erosion, thereby keeping basin hypsometry nearly constant throughout the model run in order to obtain a
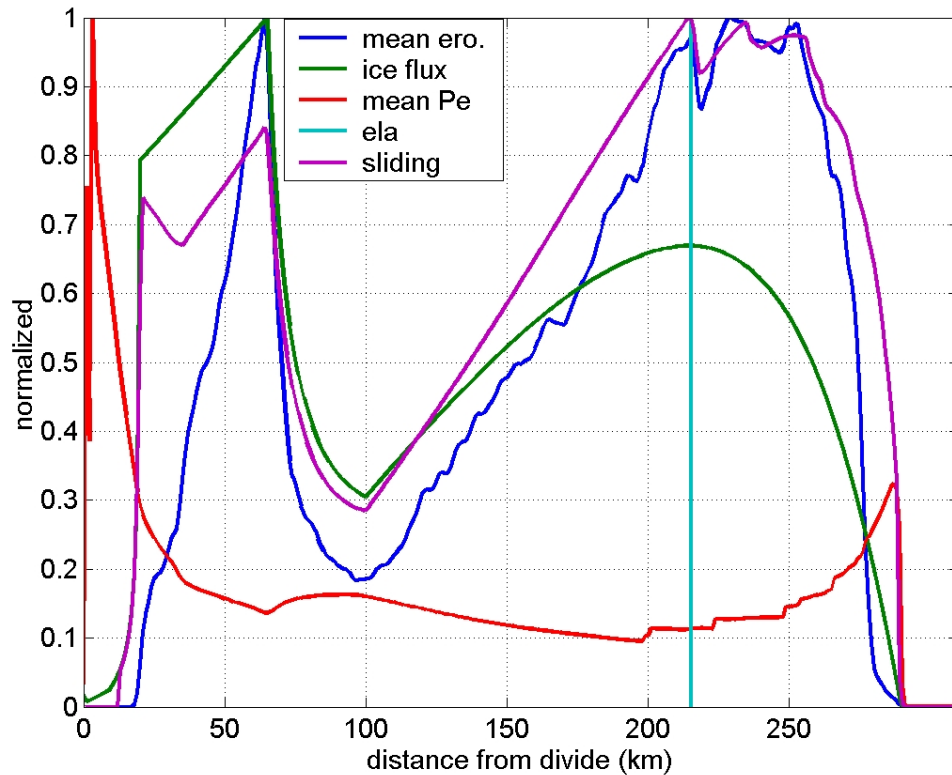
Figure 3.35: Longitudinal distribution of erosion, mean annual effective stress, sliding velocity and ice flux per unit width for a glacier of variable width during full glacial climatic conditions (for $\alpha = 1 \times 10^{11}$). Annual sliding velocity reaches 200 m/yr and mean annual and monthly effective pressures are as low as 2.4 and 0.47 bars, respectively.

distribution of erosion that varies solely with climate. Similarly to the distribution of sliding during higher levels of glacierization (fig. 3.33), all dependent variables displayed in figure 3.35 have double peaks along the longitudinal valley profile (a double minimum for effective pressure). The ensuing longitudinal pattern of erosion is a dual-peaked

168

curve; the first maximum in erosion occurs where drainage width narrows abruptly while the other maximum, like in the case of uniform width, has the shape of an asymmetric bell-shaped function reaching a broad maximum in the region swept by the snowline.

Although mean annual effective normal basal stress is lowest in the region swept by the snowline and just upstream from the ELA, it is nearly as low (approximately 1 bar greater for a mid-value α) in the narrow section of the long profile; the local minimum in effective pressure is at the gorge outlet located 65 km from the divide. In the narrows, ice flux per unit width reaches an absolute maximum and mean subglacial water flux per unit width increases rapidly relative to the region immediately downstream from the gorge outlet where both ice and water flux per unit width decrease. Despite keeping the erosional tuning parameter equal to the low value used in the constant width case, cumulated intensive quarrying in the narrows eventually produces a moderate sized trough in the bedrock profile (~80 m deep) by the time climatic forcing reaches full glacial conditions. This depression in bedrock profile results in thicker ice locally. Due to the effective pressure feedback on subglacial network conductivity, greater ice overburden in the gorge relative to the region immediately downstream from it (~80 m thicker ice in the gorge in this model run) accounts for part of the local effective pressure depression in the narrows. Comparing basal effective pressure with that obtained during a model run without bed overdeepening suggests that, for this particular valley profile geometry and climate, ~25% of the local effective pressure depression results from the constricting effect of greater ice overburden upon the subglacial network conveyance capacity. The remainder of the local water pressure high in the gorge can thus be imparted to increasing basal water pressure gradients due to the longitudinal variation in

169

cumulative water flux (and its transients implemented through the storage capacity index) that is induced by the variable width function.

As shown in previous sections, the relative amplitude of the maxima in erosion rate depends on the magnitude of mean monthly effective pressure, which is a function of
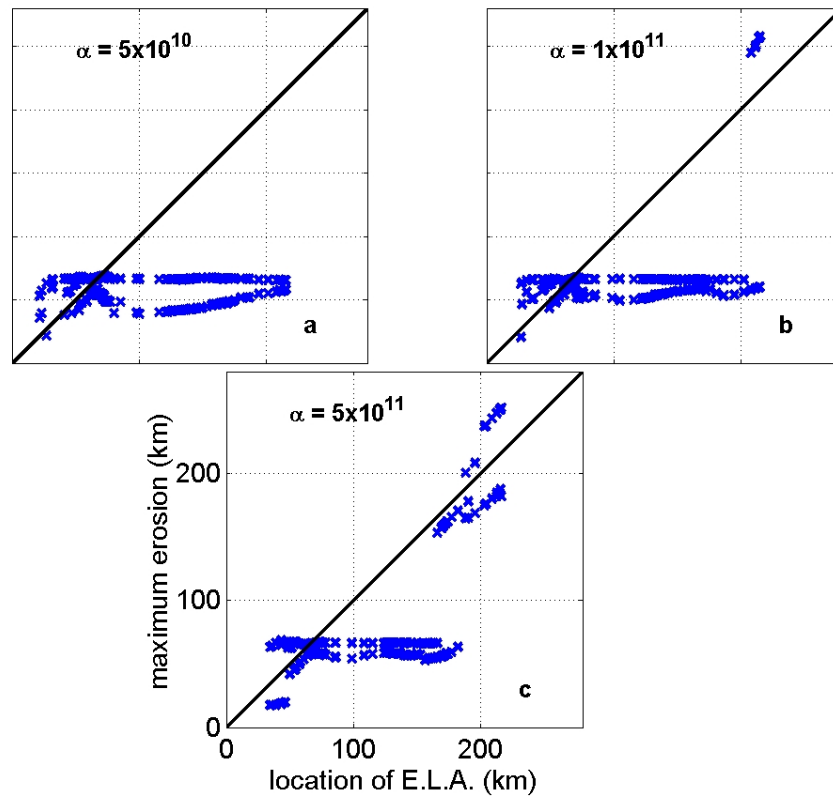
Figure 3.36: Bed regions for a glacier of variable width where erosion is greater than 90% of the maximum erosion incurred on the profile versus the location of ELA for a range of α. Regions are defined by their proximal and distal boundaries relative to the range divide. The output shown in fig. 3.35 is the furthest pair of points in the vertical dimension of panel b.

the hydraulic conductivity parameter α. Over the portion of the climate forcing cycle when the snowline is much further downstream from the gorge, like during the full glacial conditions illustrated in figure 3.35 (for $\alpha = 1\mathrm{x}10^{11}$), erosion rates reach similar maximum values both at the gorge outlet and in the region of the snowline. For the same

170

climate forcing but with $\alpha = 5 \times 10^{10}$, effective pressure nearly vanishes in the region of the ELA and erosion of the drainage area swept by the snowline becomes slower than in the gorge. Mean annual erosion rates reach an absolute maximum on the profile in the gorge rather than over the range of the snowline for much of the modeled α values (fig. 3.36). For the greater value of this parameter ($\alpha = 5 \times 10^{11}$), when mean annual effective pressures become a significant fraction of a MPa over much of the glaciated area, the broad high in erosion near the migrating snowline is relatively greater than in the gorge because increased basal water injection due to surface snow melt at the transition between subglacial hydraulic networks induces effective pressures that are in a range of values favoring more efficient quarrying.

For mid-range α (range: 5×10^{10}-5×10^{11}), mean effective pressure is very low (≤ 1 bar) in the subglacial region swept by the snowline during the first half of the melt season throughout the glacial cycle (fig. 3.37). In the gorge, basal effective pressure span from ~1bar during lower level of glacierization up to 4-5 bars during full glacial climate because of a decrease in surface melt rate high in the accumulation area during cooler climate. Excluding the regions at the highest and lowest elevations, erosion rates vary up to twice their values over much of the climate forcing cycle. Over the range in modeled α and for a constant tuning parameter in the quarrying rule, the rate of erosion varies by an order of magnitude. Although erosion rates are similar in value for the lower half of the range of α, it drops by an order of magnitude when α reaches 5×10^{11} as the corresponding effective stresses and sliding rates are more likely to be in the slower erosion region of the parameter space for the quarrying rule. For a mid-range $\alpha = 1 \times 10^{11}$ (fig. 3.38), erosion during the ablation season is fastest in the gorge section of the
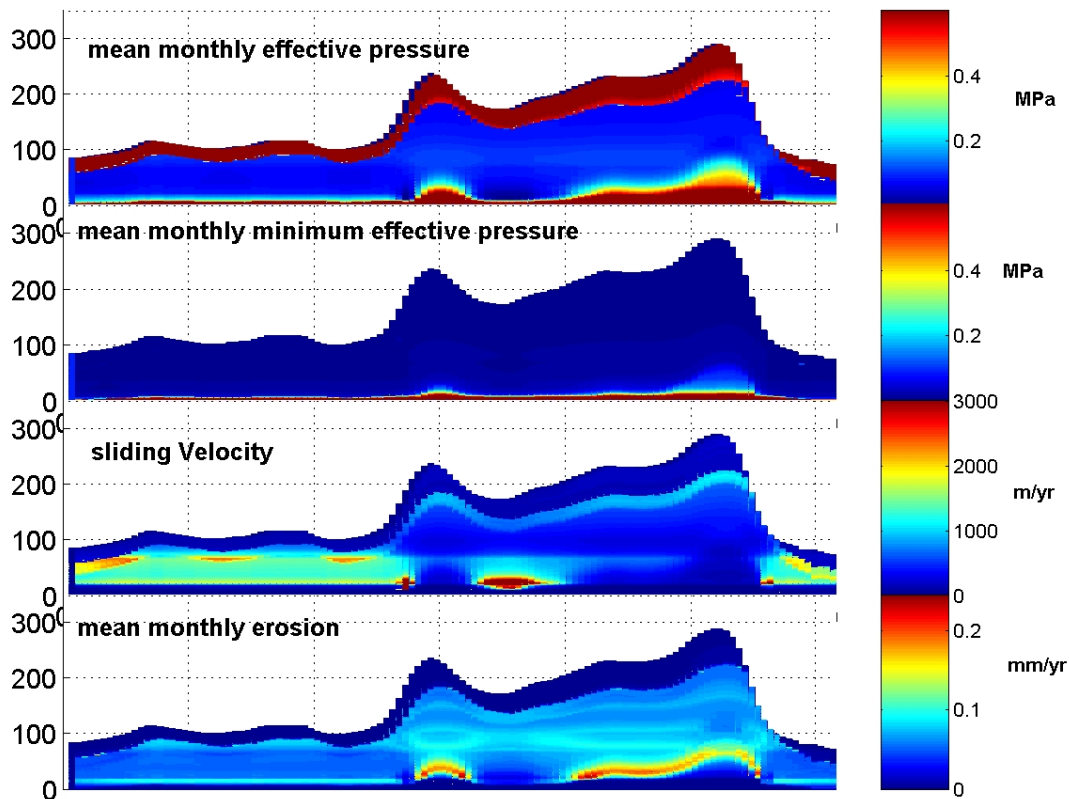
Figure 3.37: July distribution of basal conditions and erosion rates during a glacial cycle for a glacier of variable width (for $\alpha = 1 \times 10^{11}$). The absolute magnitude of erosion rates depends on a free parameter chosen to yield unrealistically slow erosion.

drainage during the cooler periods of the glacial cycle, whereas the concurrent annualized

sliding motion is much greater (about double) at the snowline much further downglacier

(more than 150 km downglacier from the peak in erosion). The maxima in sliding and

erosion are often better correlated for the accumulation season; peaks in erosion are then

respectively in the gorge and near the snowline during low and high levels of

glacierization. This seasonal agreement between maximum rates of sliding and erosion

results from higher basal effective pressures that fall within the range susceptible for

more effective quarrying during winter month whereas vanishing effective pressure

prevent active erosion during most of the ablation period. On monthly to seasonal time
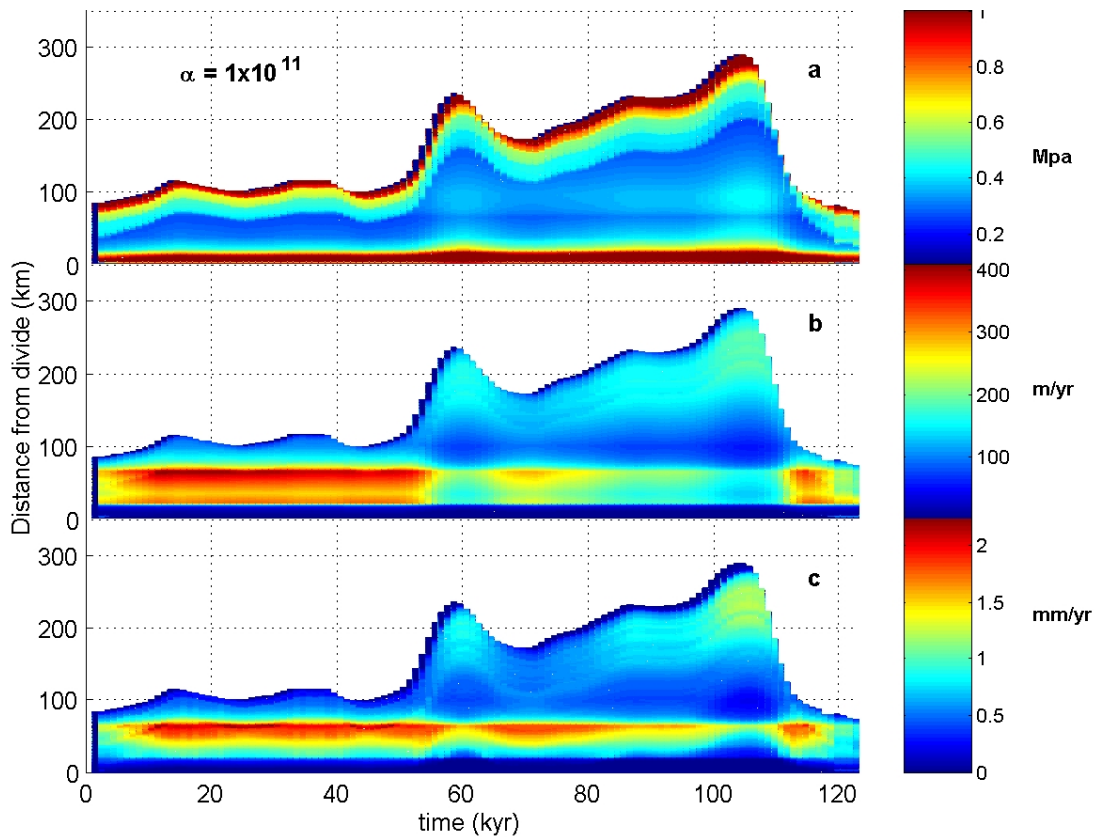
Figure 3.38: Mean annual basal effective pressure (a), sliding speed (b), and bedrock erosion (c) for a glacier of variable width for $\alpha=1x10^{11}$.

scales over the α range shown, sliding and quarrying rates are well correlated for the largest α when basal mean effective pressures are relatively high whereas they become progressively more uncorrelated as α decreases. On yearly to glacial cycles time scales, the fastest sliding result in the fastest mean erosion incurred over the period of climatic forcing (figure 3.38). Maximum cumulative erosion occurs at the outlet of the gorge (km 65) where basal speed is on average the greatest; significantly less erosion occurs at the upper end of the gorge (km 20) during the warmer half of the climate cycle than would be expected according to concurrent rates of sliding alone. Accounting for the effect of basal water transport on the coupling between a glacier and its bed to derive basal velocities

173

and stress distributions about bed roughness results into a variable degree of association between the temporal and spatial distributions of sliding speed and that of erosion rates.

The asymmetric distribution of erosion about low effective pressures likely to be found at glacier beds translates into sharply decreasing plucking rates at the low end of the range of useful effective stress and less sharply decreasing rates at its upper end. This result implies that on shorter time scales, the long valley profile distribution of erosion rates would vary a great deal according to changes in rate of water injection at the glacial interface; however, model output suggests that when integrated over a glaciation cycle, the relative distribution of cumulative erosion doesn't change very much (fig. 3.39). Irrespective of α, an index for the rate of water production and flow in the glacial system that sets the magnitude of water pressure, the general distribution of erosion rates for a glacier of complex geometry is retained. The rate of bedrock incision in the gorge is at least 2-5 times greater than anywhere else on the valley profile. The maximum in cumulated erosion occurs at the outlet of the gorge because effective pressures are among the lowest there for reasons noted above. Moreover, widening of the glacial valley dampens glacier response to climatic forcing thereby causing this region to be swept by the snowline for more than 72% of climatic cycles for this particular combination of hypsometry and climate. Another, less important locus of erosion further from the divide (between ~150-200 km in fig. 3.40) results from the seasonal migration of the hydraulic network transition at the snowline during periods of extensive glaciation. This secondary locus of erosion is also likely to produce an overdeepened bed region closer to maximum extent of the glacier.
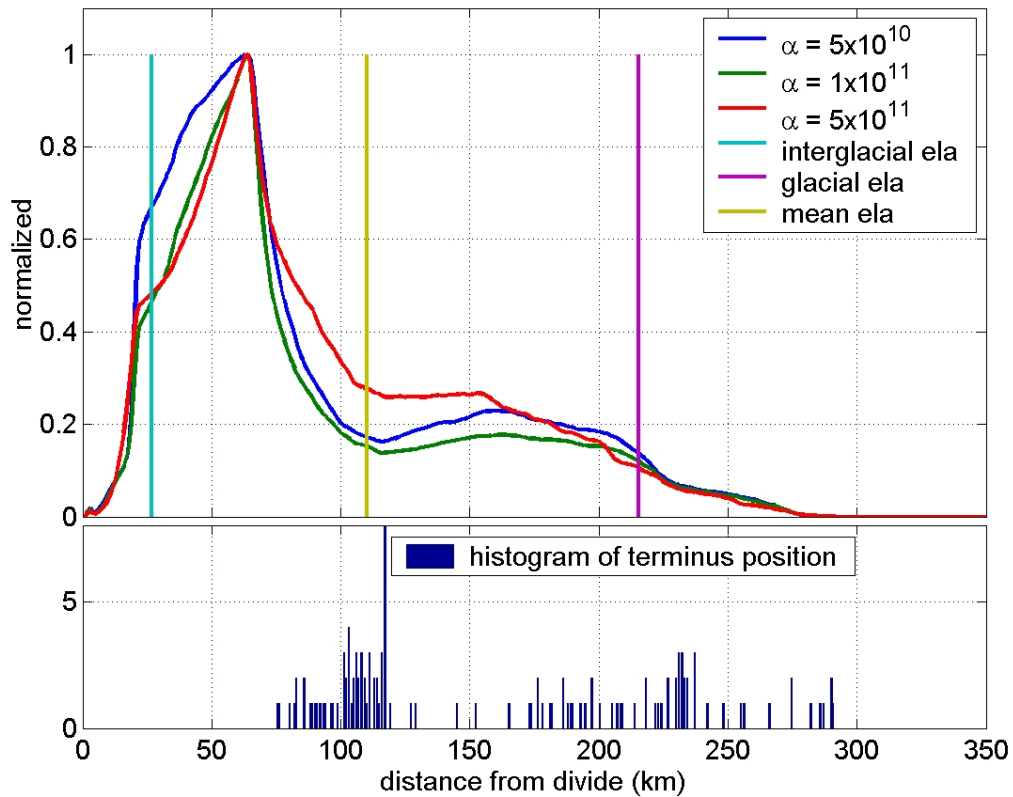
Figure 3.39: Cumulative distribution of erosion for a glacier of variable width for a likely range of α.

Although the relative distribution of erosion appears quite robust under a wide range of hydraulic regimes (fig. 3.39), cumulative bed erosion is sensitive to the relative extent of decoupling of the glacier from its substrate. Integrating model results in space and times shows that bedrock erosion under tested conditions conducive to extensive decoupling between the glacier and the substrate (low α) is twice that of the least decoupling (high α); the mid-range α produces nearly 80% of the bed excavation incurred for the low value of this parameter. This finding is altogether not entirely surprising since model formulation encapsulates the notion that low effective pressure regimes lead to higher quarrying rates; however, whether glaciers can be effective

eroding agents under conditions of very low effective stress (1 bar or less over much of the glacierized area) such as those at the low end of range modeled in this work is an outstanding question because it is likely to have significant implications for the rate of genesis of topography and its linkage to climatic regime.

For a mid-valued α, both potential sediment production rate per unit glacial area and total sediment production increases as climate cools (fig 3.40). Depending on climatic regime, minimum effective pressures may eventually rise slightly when climate
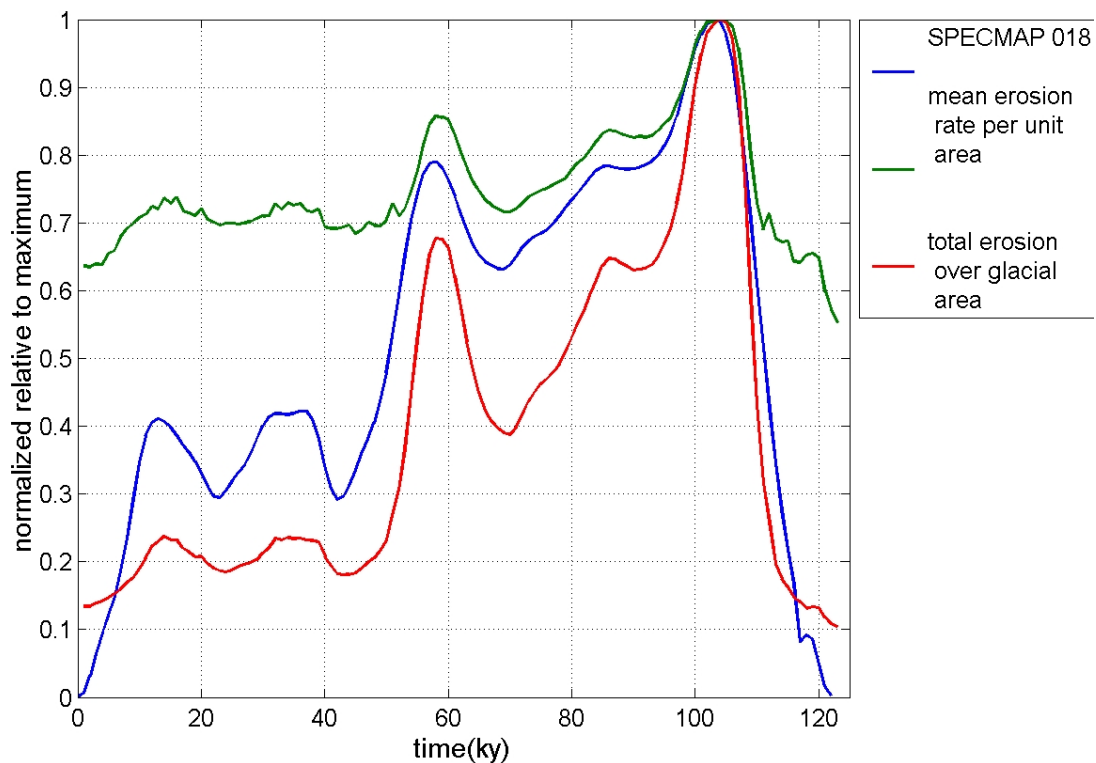
Figure 3.40: Evolution of potential sediment production rates as climate cycles for α = 1x10^{11}.

cools sufficiently to the point when the combination of decreased precipitation and lower air temperature offsets the effect of greater glacier extent on the cumulative amount of

water injected toward the bed. For most of the α range an increase in minimum effective stress increases erosive potential except for higher α values when increased minimum effective pressure enters the range where quarrying becomes less important. In such cases, lowered mean erosive potential per unit glacial area doesn't necessarily mean that total glacial area sediment production decreases since the increase in glacial area can offset in part or entirely decreased mean local sediment production.

3.7.3 Conclusions

For the lower 2/3 of the alpha range discussed when effective pressures are low to very low ($N \leq 3$ bars) over much of the glacial bed for much of the year (fig. 3.38), as is expected to be the case under many sub-polar glaciers, the peaks in velocity aren't always correlated to the peaks in erosion rate. Field observations of deglaciated landscapes indicate that glacial quarrying is a very significant erosional process, which combined with the lack of 1 to 1 correlation with sliding rate implies that accounting for sliding velocity and stress concentrations at the bed is critical for capturing the erosional signature of glaciers in numerical models.

The mean glacier length and its standard deviation over a climatic cycle are greater for the glacier of constant width than for the glacier of variable width (respectively 173 km and 162 km, standard deviation: 117 versus 64 km). The smaller mean glacier extent for a glacier of varying width implies that the erosional footprint is smaller but also that erosion is locally more rapid.

The distribution of cumulative erosion over a climate cycle for a glacier with a width function characteristic of that found in many high relief regions underscores both the role of water and ice flux convergence in focusing glacial erosion along a valley long profile,

especially in narrow valley sections that are regularly swept by the snowline over a large fraction of a glacial cycle. Valley narrows are therefore expected to develop overdeepened sections, as are all regions swept by the snowline over sustained periods of glacial occupation. In particular, temperate glaciers that extend significantly beyond the mountain front during cooler climate excavate an overdeepened region beyond the area of topographic confinement and in between the average glacial cycle ELA and that for full glacial conditions.

The rate at which debris is produced by bedrock erosion appears to increase with glacier extent for a range of normal basal stress likely to be found under temperate and sub-polar glaciers. Bedrock erosion will tend to slow, however, as debris accumulates at the bed thereby shielding it from erosion. Glacier sediment yields will nevertheless increase with glacier extent because of subglacial debris entrainment, which is a relatively rapid process (Motyka et al., 2006). The effect of debris is addressed explicitly in Chapter 4.

Chapter 4   Tidewater glaciers and sedimentary processes – Glacial erosion at Seward-Malaspina Glacier

4.1 Introduction

In order to address erosion by glaciers terminating in the sea more realistically, I now include important new elements to the model: sediment entrainment and deposition and calving (a large ice sink). There is much evidence that South Alaskan tidewater glaciers advanced and retreated asynchronously during the Late Holocene (Motyka and Beget, 1996; Calkin et al., 2001; Barclay et al., 2009). Thus, tidewater glacier retreat following the Little Ice Age that ended in the late 19th century in the region, took place throughout the 20th century. Glacier retreated at variable rates (10^2-10^3 m/yr) as glacier termini became ungrounded from terminal embankments and retreated in deeper water toward the heads of fjords until shallower sub-aqueous topography stabilized glacier termini (Meier and Post, 1987; Porter, 1989; Krimmel, 1997; Pfeffer et al., 2000). On decadal time scales, tidewater glaciers do not respond linearly to climatic variations because relative sea level controls the dynamics of ice fronts and the extent of glaciers that end in water; thus, although local sea level also depends on climate and tidewater glaciers eventually respond to climatic forcing, on shorter time scales their fluctuations reflect greater dependence on local non-climatic conditions.

The mass balance of temperate tidewater glaciers is substantially different than that of land-based glaciers not only because sub-artic maritime glaciers have steeper mass balance gradients but also because on average most annual mass loss occurs as iceberg calving rather than surface ablation (Van der Veen, 1996). From accounting for near 100% of ice loss in many tidewater polar glacial systems, and almost as much in

179

temperate systems retreating catastrophically in deep bodies of water, water driven melting and calving have been found to contribute up to ~50% of total annual loss for South Alaskan maritime glaciers near equilibrium (Motyka et al., 2003). The additional ice sink incurred in tidewater setting is reflected in the relatively large Accumulation Area Ratio (~0.7) found for most temperate tidewater glaciers ($AAR = \dfrac{A_{accum}}{A_{abl}}$). In temperate regions, where sea ice and ice shelves are absent to stabilize the ice front, rates of iceberg calving depend entirely on ice velocity, relative water depth (local water depth relative to topographically controlled ice thickness) that modulates basal effective pressure and longitudinal strain rates in the terminus region, and advection of heat in marine water to the ice front. For water depths approaching the ice thickness, buoyancy driven low basal traction leads to extensional stress regimes and the fracturing of ice that eventually breaks away through gravitational collapse to form icebergs at the ice front. Both terminus retreat in deeper water and glacier thinning through increased ice flux give rise to positive feedback processes on glacier sliding, ice streaming and eventual thinning until the glacier front starts to float and breaks away (Meier and Post, 1987; Hughes, 1986).

Tidewater glaciers have to be grounded on submarine substrate to be stable; the pace of glacier advance (10^0-10^1 m/yr) in water deep enough to create condition approaching buoyancy thus depends, on shorter time scales, on rates of ice thickening as well as the elevation of submarine topography that is in turn determined by the accumulation of sediment in a morainal embankment at the ice front (Cowan and Powell, 1991; Powell, 1991; Hunter et al., 1996). In order to model the evolution of coastal glacier extent as climate changes, it is therefore necessary to include mechanisms that

determine local, relative sea level (eustatic sea level change relative to the change in elevation of local topography) and the stability of ice fronts in tidal water. Besides ice thickness, eustatic sea level changes, sediment delivery at the glacier front, and tectonic forcing including isostatic adjustment to crustal load changes all factors affect the relative water depth at the glacier terminus and control whether the ice front is grounded. In this chapter, I consider first the effect of the tidewater environment on the evolution of Malaspina-Seward Glacier as climate changes and on the pattern of erosion rates using a stripped down version of the model that doesn't include sedimentary processes. Next, I introduce subglacial sedimentary remobilization and proglacial submarine deposition to model their impact on relative sea level and the stability of maritime temperate glaciers, and, eventually, how sediment changes the distribution of their erosional potential.

4.2 Tidewater environment

In this study, local sea level, like air temperature and precipitation rates in chapter 3 are assumed to parallel simply the benthic foraminifera $\delta^{18}O$ record (Imbrie et al., 1984). The total magnitude of sea level change over the course of a glacial cycle is relatively well established (Chappell et al., 1986), whereas significant uncertainties rest with the regional variance of other parameters affecting relative sea level. Variations in $\delta^{18}O$ from interglacial values are assumed to represent a proportional fraction of the maximum change in sea level during a glacial cycle (-130m). Sea surface temperature reconstructions show that ocean temperatures in the Gulf of Alaska were 3-4°C lower during the LGM than today and there was no sea ice (CLIMAP, 1981; Sabin and Pisias, 1996). Global Climate Models suggest a modest decrease in precipitation during the

LGM due to a 5-10° latitudinal shift toward the South in the polar front and the storm tracks that bring moisture to glaciers in South Central Alaska (Kutzbach, 1987; Kutzbach et al., 1993; Bamosky et al., 1987).

4.2.1 Glacier extent and iceberg calving

Whereas, temperate glaciers terminating on land simply extend to the point where ice discharge vanishes through the melting of ice, numerous other important but poorly understood processes determine the extent of lacustrine and tidewater glaciers. Observations and modeling studies suggest that ice velocities, bed processes, ice mechanics, and water depth and temperature all play a role in calving rates (Hughes, 1992; Van der Veen, 1996; Kirkbride and Warren, 1997; Vieli et al., 2000; Van der Veen, 2002). Although theoretical studies capture aspects of glacier calving, none can explain all of the available observations and considerable uncertainty exists as to whether water depth and temperature, or ice velocities drive calving rates as they correlate strongly with both (Van der Veen, 2002; Joughin et al., 2012). In this study, I do not attempt the difficult task of modeling stresses in ice at the terminus and the physics of fracturing, and concentrate on the role played by bed geometry and that of buoyancy. Similarly, although submarine melting calving are possibly a significant mass balance component of glaciers that end in bodies of water (Powell, 1988; Motyka et al., 2003), I do not model proglacial water convection and thermal oceanic melting but assume that they contribute directly to the ice loss at the tidewater margin by processes other than subaerial melting.

For a tidewater terminus, the calving rate (U_c) is usually defined as the difference between the ice velocity and the rate of advance of the terminus:

$$U_c = U - \frac{\partial L_g}{\partial t} \qquad \text{(Equation 4.1)},$$

where U is the velocity at the terminus and L_g, glacier length. When the glacier front is grounded on sub aqueous topography, Brown's empirical calving relation fit to Alaskan tidewater glaciers can be used to determine the calving flux (Brown et al., 1982; Van der Veen, 1996; Hughes and Fastook, 1997) according to:

$$U_c = k_3 h_w \qquad \text{(Equation 4.2)},$$

where h_w is mean water depth at the terminus, U_c is the calving velocity in km/yr, and k_3 is a constant estimated at 0.027 per yr. I chose to adopt the so-called height-above-buoyancy model to determine terminus position because it is simple, and appears robust for a wide range of applications. The position of the ice front is thus established by finding the most distal location wherever the terminus is grounded, which occurs where the ice flux diminished by an estimate of the calving flux allows for an ice thickness equal to the water depth plus freeboard sufficient to prevent floatation, according to:

$$h_t = \frac{\rho_w}{\rho_i} h_w + h_0 \qquad \text{(Equation 4.3)},$$

where the ice thickness at the terminus (h_t) is the ice column necessary to displace a water column equivalent to the water depth with the addition of a small value found to be near 50m in many tidewater systems (Van der Veen, 1996).

As the model time step is much greater than the time necessary for a tidewater terminus to stabilize at the appropriate water depth (order of 10^1 years), ice is simply truncated from the profile whenever it is too thin to be grounded. This scheme is iterated down profile during a glacier advance or up profile during a glacier retreat until water depth shallows and/or ice thickness increases sufficiently to allow grounding of the
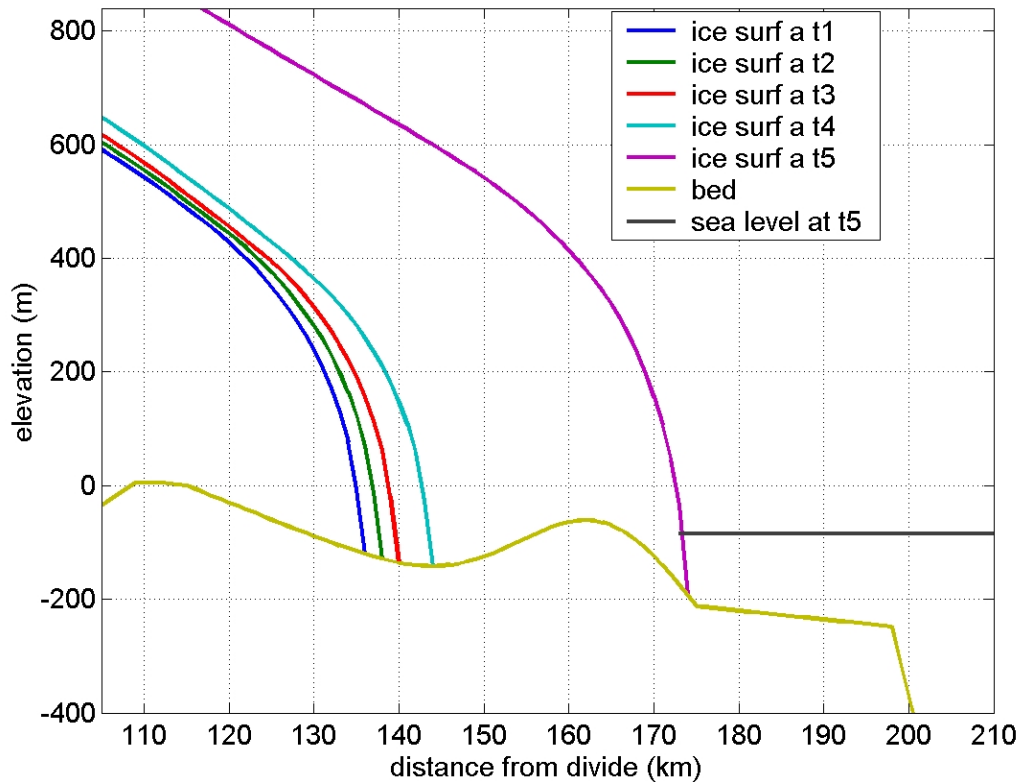
Figure 4.1: Progression of a tidewater glacier beyond a mostly sub-aqueous Gaussian topographic high in deeper water. Ice progresses slowly at first (evenly spaced times, t1 through t4), until shallower sub-aqueous topography and rapid ice growth due to the height mass balance feedback permit the terminus to advance quickly and stabilize in deeper water. Note that, in this illustrative run, width is uniform beyond the 120 km mark.

terminus. A new surface profile is then computed accounting for the calving loss incurred at the grounded terminus. To illustrate aspects of the behavior of a calving terminus, I consider a glacier advance in water over a Gaussian bump on the downglacier slopping bed representing the continental shelf; the advance is forced concurrently by a nearly constant rate of cooling-induced increase in glacier thickness and a decrease in water depth (fig. 4.1). Without concurrent modification of bottom topography through erosion or deposition, the glacier terminus stagnates and/or progresses forward very slowing into

the over-deepening (t1 through t4) until relative sea level decreases under the combined

effect of increasingly positive mass balance, eustatic sea level decrease, and shallower

topography (beyond the terminus position at t4 on the proximal side of the Gaussian

bump). The terminus is then able to advance at a much faster rate (t5) into deeper water

toward the shelf edge than before because of further cooling but also largely thanks to the
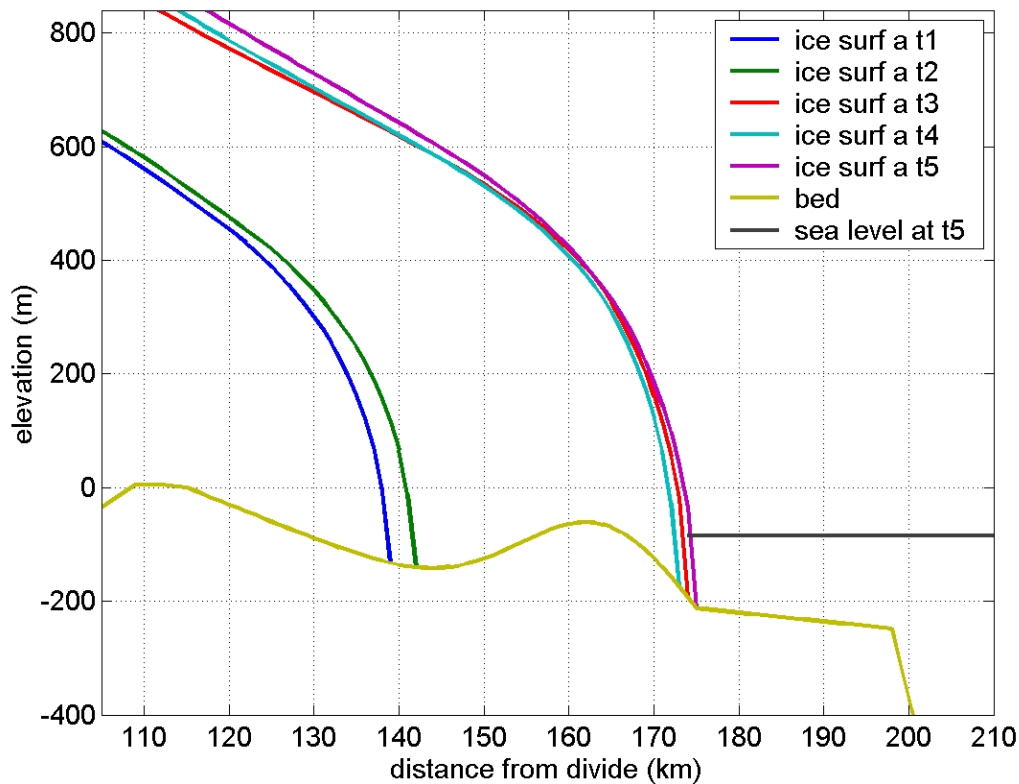
Figure 4.2: Tidewater glacier advance sequence when the constant in Brown et al.'s calving relation, k_3, is halved relative to the case illustrated in figure 4.1 and set at 13.5 per year. Halving the calving rate predictably results into much faster glacier advance.

height mass balance feedback process that results from the glacier finally being able to

progress beyond the over-deepening. The choice of calving rate constant has large

implications for the evolution of glacier extent. For example, halving the calving rate

185

constant from Brown et al to 13.5 per year enables the glacier to advance nearly twice as fast for the advance sequence illustrated previously (fig 4.2).

A floating ice shelf beyond the region of grounded terminus would provide some added stability to the ice front; however, the thermal limit under which ice shelves begin to form and persist, -5° to -9° C average annual air temperature (Vaughan and Doake, 1996; Cook et al., 2005), is likely to have been always exceeded in South Alaska over the course of the previous few million years according to previously mentioned climate reconstructions for the Northeast Pacific ocean. Hence, determining terminus position according to the floatation criterion assumption described above is likely to be a reasonable approximation throughout the glacial cycles of the Quaternary.

4.2.2 Modern mass balance at Seward-Malaspina Glacier

Mass balance is computed with the degree-day model described in chapter 3 that is applied to the area-altitude distribution of the hydrological drainage for the Seward-Malaspina Glacier. In Arc Info, I computed basin hypsometry from a 1m-altitude bin analysis of the USGS 3x3 arc-second digital elevation model (fig. 4.3). The mass balance as a function of elevation (Fig. 4.4) was derived based on available mass balance observations including the elevation of the snowline at the end of hydrological year and the widely accepted 10+ m.w.e. ice ablation rate at temperate sea level (Shuchman et al., 2010). Unfortunately, very little mass balance data have been collected for the Seward-
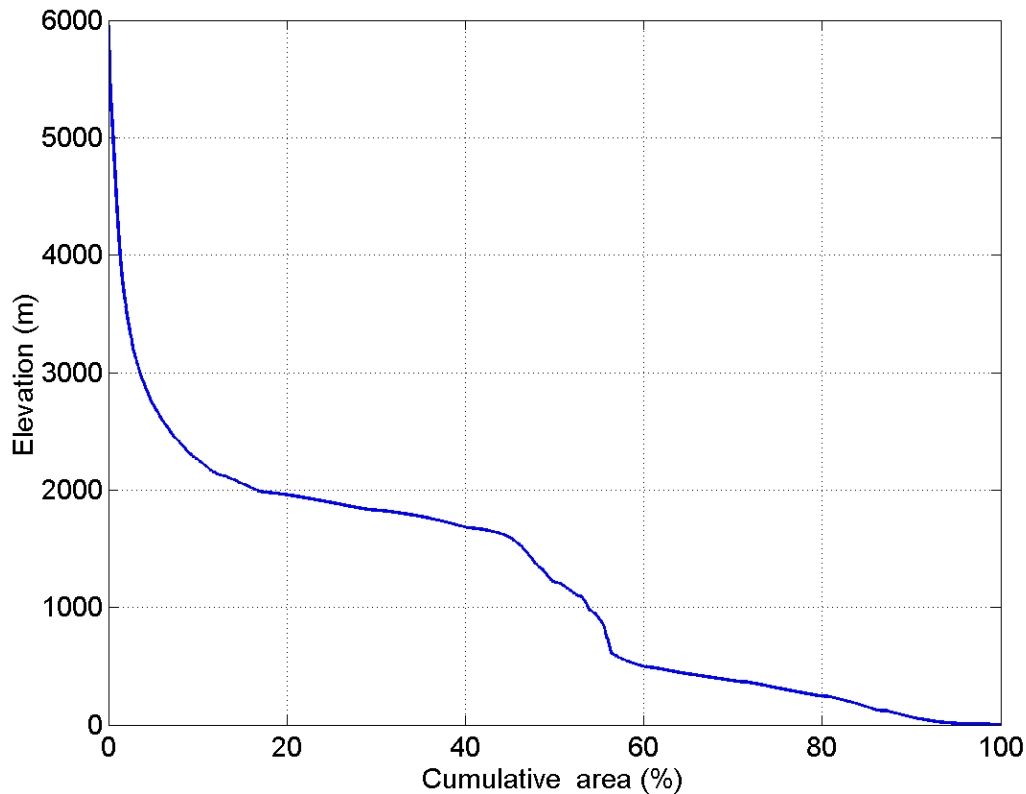
Figure 4.3: Hypsometric curve for the Seward-Malaspina Glacier drainage basin from the summit plateau of Mt. Logan down to sea level. Seward Throat features prominently between ~1700 m and ~600 m elevation. Recent snowlines at the end of the hydrological year have been near the 54% cumulative area threshold.

Malaspina glacial system and most published observations are now more than 40 years old (Sharp et al., 1951; Marcus and Ragle, 1970). Furthermore, ice melting in the ablation area of late Holocene glaciers is spatially extremely variable according to the extent and thickness of debris cover. When up to a few cm of debris cover the glacier surface, decrease in albedo increase heat absorption and transfer to the ice, thereby accelerating melt rates. On the other hand, insulation of the ice from atmospheric forcing (temperature and precipitation) by thicker deposits lead to decreasing melt rates. (Ostrem, 1959; Mattson and Gardner, 1989; Reznichenko et al., 2010). Much of the terminus area

of many glaciers is heavily covered with debris in South Alaska; it is often difficult to determine the part of the glacier that is active versus the stagnant ice. Malaspina Glacier is no exception: a terminal zone ~10 km wide appears currently inactive and is therefore considered a relic feature that isn't relevant to current climate and mass balance modeling of initial conditions. In this context above, the mass balance curve (fig. 4.4) represents the
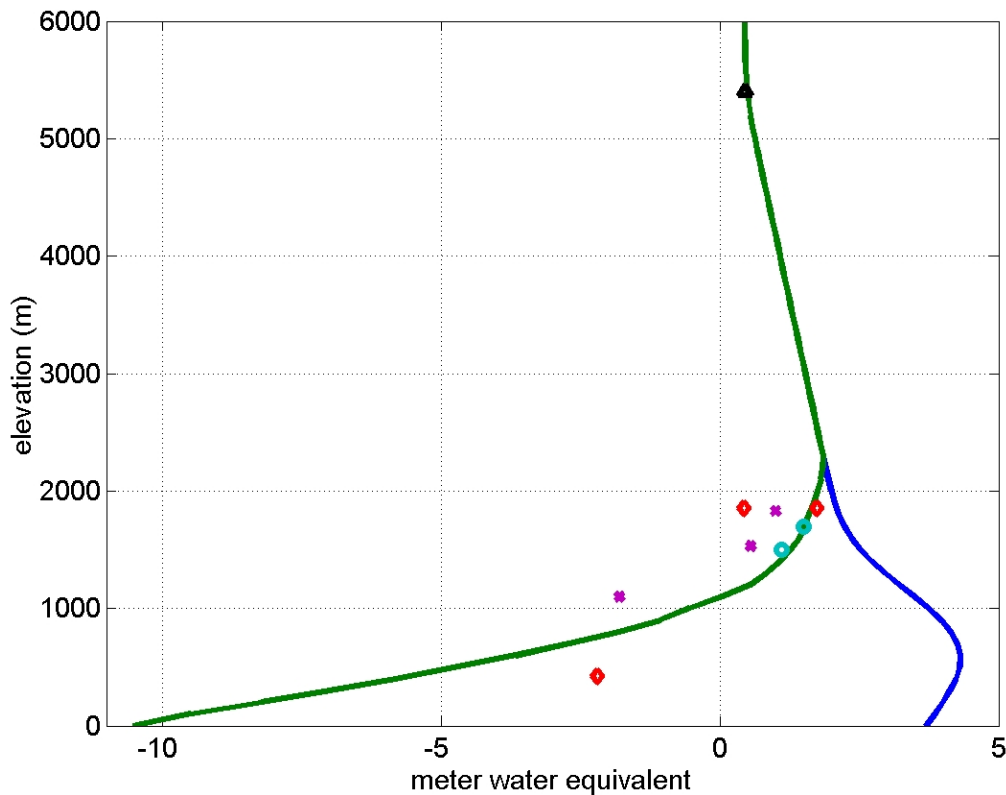
Figure 4.4: Modeled precipitation (blue) and mass balance (green) for modern conditions at Seward-Malaspina Glacier. Net accumulation data from Sharp (range of 1946-49, red diamonds), Marcus and Ragle (1968, cyan circle) on Seward Glacier, Holdsworth et al (average over 2nd half of 20th century, black triangle) and data acquired during the course of this study on Bagley Icefield (1992-96, magenta crosses).

essence of what is known for Malaspina Glacier. The firn line rose from an elevation of ~830 m in the mid 20th century (Sharp, 1951) to ~1000 m in the early 21st century, and

most coastal glacier have thinned (~50 m on average) in South Alaska (Post et al., 1962; Tangborn, 1999). Over the last decades, airborne and satellite measurements suggest that glacier wastage has accelerated: thinning rates for the 1999-2002 period were estimated to be -0.5 m/yr on Upper Seward Glacier and ~-2 m/yr for Malaspina lobe (Muskett et al., 2003; Sauber et al., 2005; Muskett et al., 2008)

Sharp (1951) measured net accumulation on the Seward glacier from 1946 to 1949; on average, net accumulation was nearly 1 m.w.e. in 3 locations between 1800m and 1900m on the eastern part of upper Seward Glacier (range of 0.43 to 1.75 m.w.e.), which is the accumulation area of Malaspina Glacier. In addition, during a late May-June 1965 snow pit-sampling traverse of the range, Marcus and Ragle (1970) recorded winter accumulation on the Seward glacier (1.7-2.1 m.w.e between 1500 and 1700 m on the upper Seward Glacier). When accounting for summer ablation by assuming 90 days of melt from mid-May to mid-September at a average rate of 0.007 mwe per day (Sharp's average snow and firn ablation rate), Marcus and Ragle's observations of winter accumulation give an estimate of net accumulation (~1.1-1.5 m.w.e.) that is broadly consistent with the mean of Sharp's observations. The somewhat higher net accumulation of Marcus and Ragle can be attributed to annual variability that is high according to Sharp's data or to their sampling directly above the 4-6 km wide gorge of Lower Seward Glacier where moisture is likely to be funneled by topography. An ice core drilled by Holdsworth et al. (1989) at an elevation of 5340 m on the summit plateau of Mt. Logan at the head of the Seward Glacier shows 0.45 m w.e. per year of accumulation averaged over the 1950-2000 period; Mt. Logan is a much more continental setting than Malaspina Glacier. Multi-year data (1992-96) we collected during the course of this study at 2 sites

189

in the accumulation area of the adjacent Bagley Icefield in late August 1996 are the only additional measurements in close proximity to Seward Glacier (~65–85 km away). Based on measurements of snow accumulation above an obvious ash layer likely deposited during the June 1992 Mt. Spurr eruption and the snow densities recorded by Sharp over a 4 year period, net annual accumulation averages 0.55 m.w.e and 1 m.w.e. at elevations of 1510m (60.4938N, 141.8042W) and 1830m (60.4330N, 141.2343W) on the Bagley Icefield. This upper most data point is similar to the mean value found by Sharp on the Upper Eastern Seward Glacier, which is similar to the sampling site on Bagley Icefield in being in the lee (north) of the first major topographic barrier to the Pacific.

Unfortunately, the nearest existing multi-decadal mass-balance data are that collected in the Juneau Icefield, ~400 km to the East, and Wolverine Glacier, ~300 km to the West. The resulting mass balance curve is comparable to that found in Meier and Post (1962) for Seward-Malaspina Glacier. Reproducing the large ablation rate found at sea level while keeping the firn line within the required elevation range demanded an increase of precipitation with elevation until the 700 m level. The degree-day coefficients are effectively used as tuning parameters and chosen to be 0.0034 m/K for snow and 0.0065 m/K for ice, which is within the ranges of parameter values cited in the literature. Allowing the degree-day coefficients to vary with elevation may have permitted a different precipitation profile; however, gradients in ablation rate constants are even more uncertain due to the dearth of data for the region.

4.2.3   Initial conditions

I assume that the hypsometry of the Malaspina-Seward basin hasn't changed
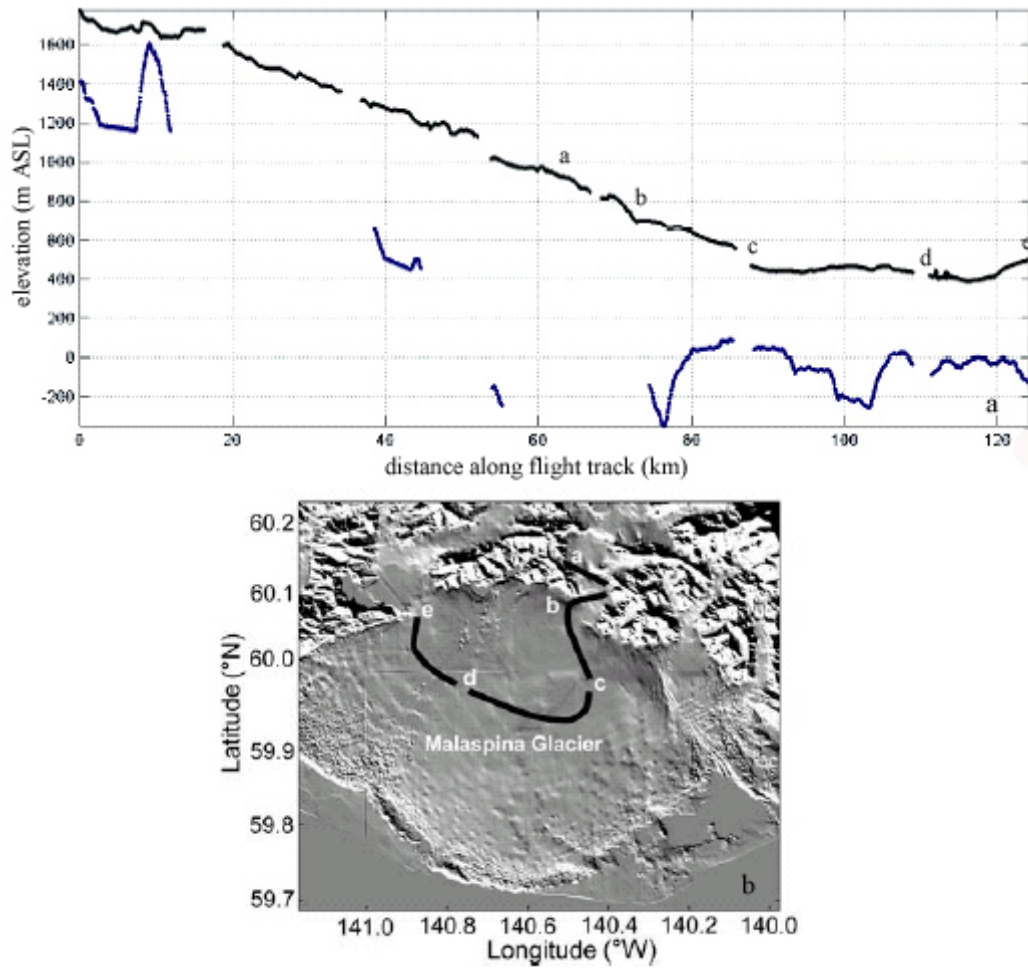
Figure 4.5: a) Estimates of surface and bed elevations from Conway et al's airborne ice-penetrating radar survey at Seward-Malaspina Glacier. b) Flight line overlain on shaded relief map of Malaspina Glacier.

significantly since the previous interglacial period, which allows making use of elevation

data for much of the current subglacial profile (Conway et al., 2009; Trabant, D.,

personal communication, figures 4.5 and 4.7). The procedure used to derive the modern

width function based on basin hypsometry and surface profile is described in section

3.2.1; however, significant uncertainty exists with regard to glacier width once the glacier

advances on the continental shelf. The submarine glacial trough in front of Malaspina

glacier, Yakutat Sea Valley, is narrower than the current Malaspina lobe: Yakutat sea

Valley is on average 30km wide whereas Malaspina lobe is 45km across, which suggests that shelf morphology may not be a good indicator of total glacier width. On the continental shelf, the width of Malaspina Glacier is to first order likely constrained laterally by large ice masses flowing out of Agassiz Glacier and Icy Bay drainages to the West and out of Yakutat Bay to the East (outlet for Hubbard and other major glaciers). Yakutat sea valley is on average ~100m deeper than surrounding bed topography indicating that a different flow regime likely takes place within the shelf trough. Modern analogs suggest that during glacial times fast moving ice in the trough is surrounded by wide expanses of slower moving ice grounded in shallow water. Such complexity is impossible to capture with a one-dimensional model, so I chose to first model ice spreading on the shelf without the submarine trough (referred to as TOPO1) and second, model ice flowing toward the Gulf of Alaska on topography TOPO2 at the elevation of Yakutat Sea Valley (fig 4.6). Assuming that glacier width keeps increasing on the continental shelf at the rate that width currently increases on Malaspina lobe up to the point where it is contained by lateral ice masses, I estimate that Seward-Malaspina Glacier would have a maximum width of 65 km, which I chose as the uniform glacier width on the shelf for the no-shelf trough model run (TOPO1). For the run with shelf trough floor elevation (TOPO2), I chose a maximum glacier width equal to that of the current Malaspina lobe (45km). Model results presented below will be based on the base model (no shelf trough) initial conditions unless noted otherwise.
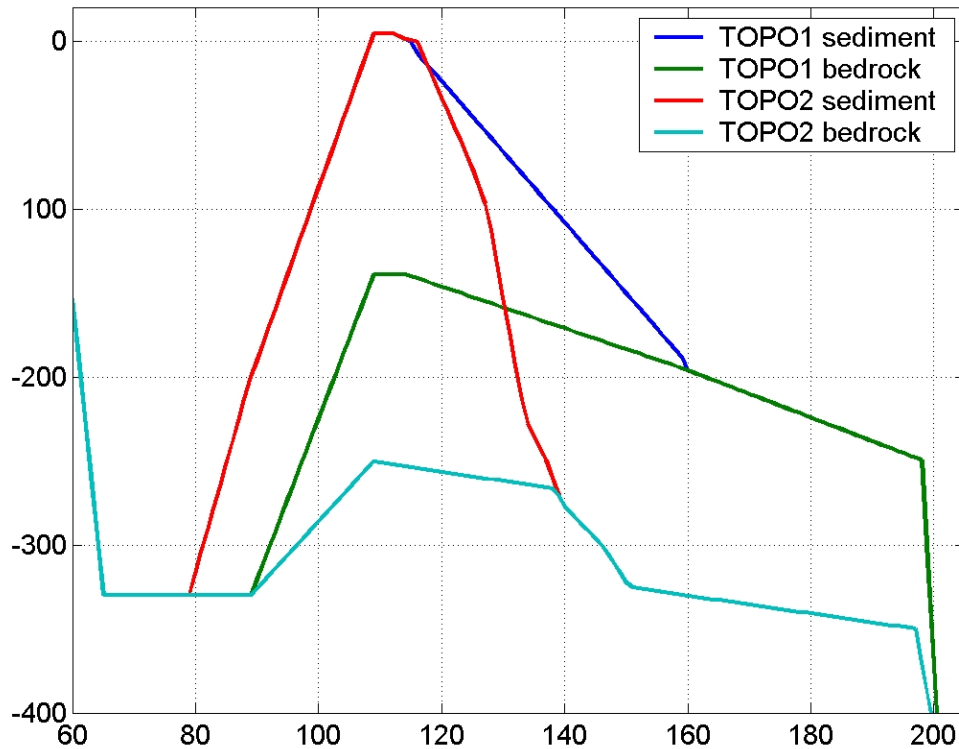
Figure 4.6: TOPO1 and TOPO2 models of substrate elevations under modern Malaspina lobe and on the continental shelf. TOPO2 glacier width on the continental shelf (>110km from the divide) is ~1/3 narrower than in TOPO1 (45km versus 65km).

Similar difficulty in choosing initial conditions exists regarding sub-bottom topography under the Malaspina lobe because it is very uneven as shown by several 100's of meter lateral variation in elevation according to radar data that suggest a prominent trough-like zone of lower elevation extending from the Seward gorge outlet toward the modern shoreline (fig 4.5 and 4.7). Based on SAR data, Molnia and Jones (1989) inferred extensive subglacial basins and valleys under Malaspina. Thus, for the model, the base of the glacier is set at -330 m, close the minimum sub-bottom elevation found between location b and c in figure 4.5; this is likely representative of the upglacier half of section
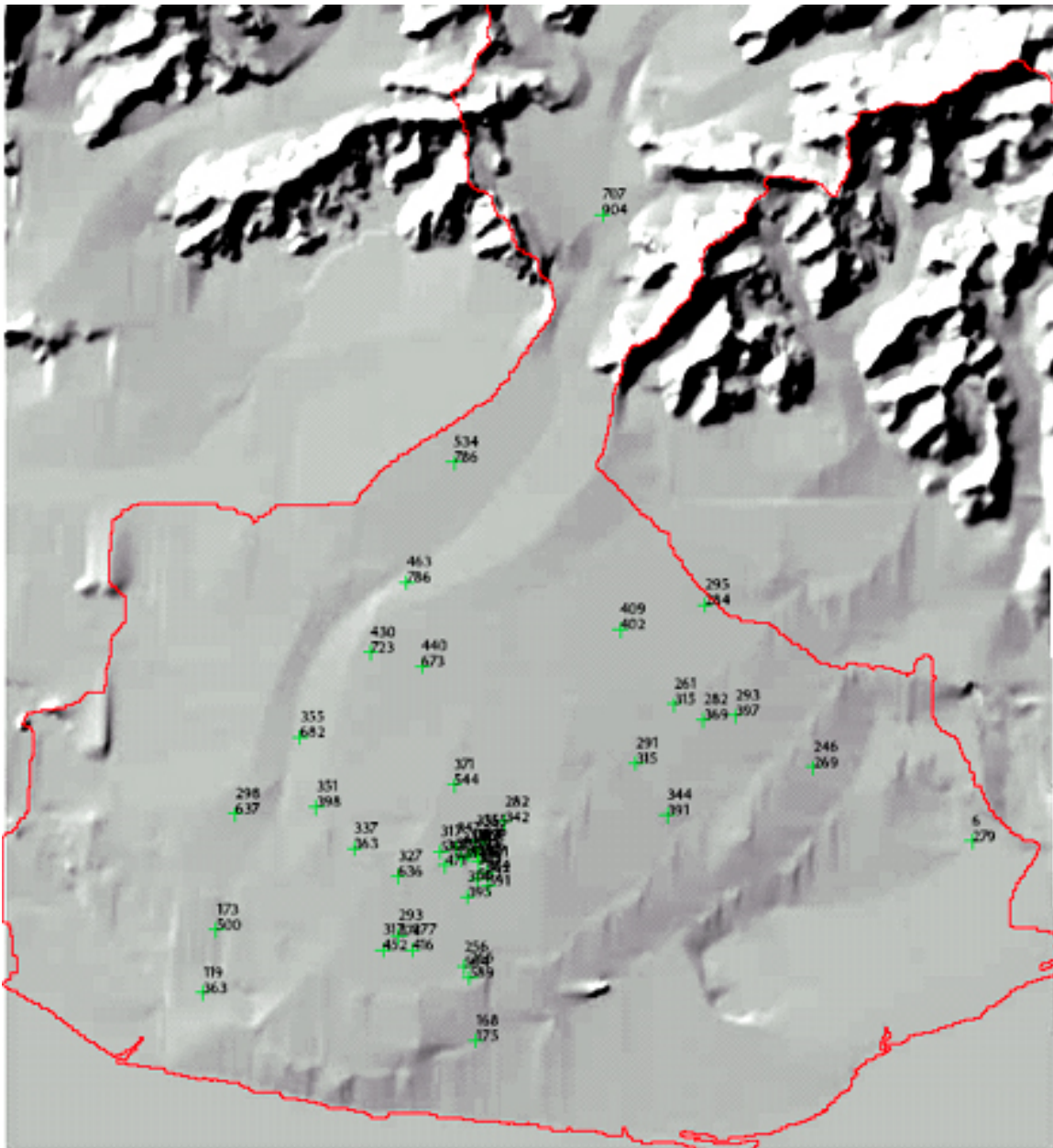
Figure 4.7: Spot radar data at Malaspina Glacier collected by D. Trabant. Each data pair is surface elevation and ice thickness in m.

underlying Malaspina lobe. The 330 m depth also appears fairly representative of bottom

elevations recorded by Dennis Trabant (spot radar data in fig. 4.7) in the trough-like zone

mentioned above although it is a significant overestimate for the extensive shallow

regions revealed by field data. The thickness of Holocene sediment immediately beyond

Malaspina Glacier ranges from ~125 m to 250 m according to seismic reflection data

(figure 4 in Sheaf et al., 2003). If little to no older poorly consolidated sediment underlies

the Holocene sediment package (as suggested by the prominent angular unconformity

noted immediately below Holocene deposits in part of this region of the shelf), the basin

beneath Malaspina lobe as inferred from radar data would be deeper than the adjacent

shelf by ~0-200 m. To reflect this range of possibilities, in TOPO1 I assume that bedrock

elevation reaches within 140 m of modern sea level at the shoreline, whereas TOPO2

assumes that bedrock rises up to 250 m below the modern sediment surface (fig, 4.6). The

overdeepening under Malaspina lobe relative to the continental shelf is therefore assumed

to be ~100m greater in TOPO1 than in TOPO2.

Malaspina-Seward Glacier is thought to have surged at least 4 times since the

beginning of the 20th century (Sharp, 1958; Post, unpublished; Jones et al., 1989; Muskett

et al., 2008); surge-related changes in surface elevation are commonly on the order of 100

m. Modeling surface elevation and glacier extent averaged over time increments much

longer than the decadal period of surges will produce a glacier geometry that deviates

from the real world glacier. It should also be noted that the values of temperature and

precipitation used to force the model's initial run are averaged over the last 50 years; a

period during which the ice surface elevation has decreased by several 10's of meters

(Muskett et al., 2003; Muskett et al., 2008). Panel a of figure 4.8 shows that differences in

surface elevation between model and real world glacier range from 3 to 50 m, or at most

6% of ice thickness, for the 4 locations chosen; with this simple approximation of the

glacier bed geometry, the model reproduces the ice surface elevation relatively well in

most places along the longitudinal profile (Fig. 4.8). As expected because large
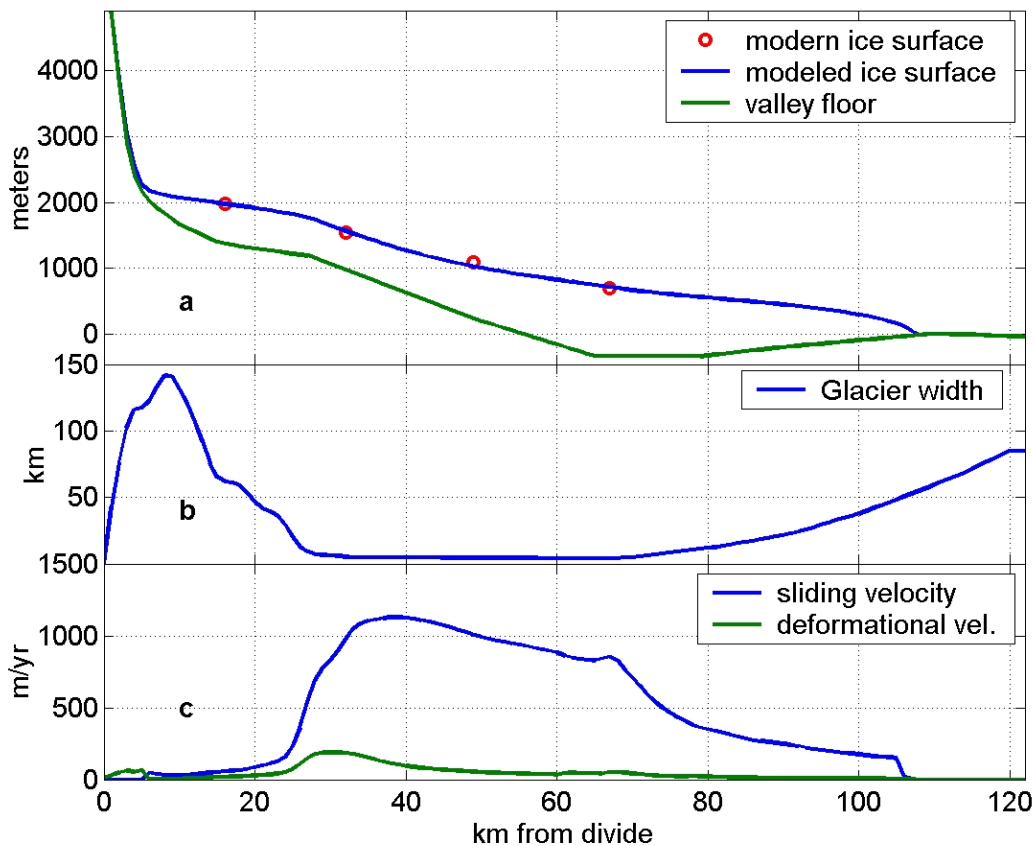
Figure 4.8: Initial ice surface at Seward-Malaspina glacier compared to current elevation surface data (panel a). Width function is derived from basin hypsometry (panel b); width is approximated to be ~4 km within Seward Throat as much of the ice seems to flow as an ice stream of uniform width with distinct shear margins.

volumes of ice funnel through Seward Throat, interglacial glacier velocities are highest

there, reaching as much as 1250 m/yr near the upstream end of the gorge and 900 m/yr at

its lower end. Although, effective pressure is lower by ~1 bar near the downstream end,

higher surface slope at the upper entrance appears to explain this counter-intuitive model

result. Faster ice flow at the up-stream end of the gorge rather than at the bottom is

counter-intuitive because the modern snow line and maximum in ice discharge fluctuates

between the lower and mid-reaches of Seward throat while glacier width decreases

slightly in the down flow direction (from 5 to 4 km wide over the extent of the gorge).

Surface observations and analysis of Synthetic Aperture Radar (SAR) images over the

last 30 years indicate surface velocities of 1000-1500 m/yr at the upper entrance of

Seward Throat, and 1500-1800 m/yr at its lower end (Post and Plafker, 1971,

unpublished; Headley et al., 2012; Burgess, 2013). Post and Plafker report one data point

averaging 2 years of motion, whereas Headley and co-workers report on a 2-week long

observation period of glacier transects during summer. In turn, Burgess analyzed SAR

images of a 46 days winter window. Model velocity output for the upper gorge is within

the range of observations but modeled velocities near the outlet onto Malaspina lobe are

on average 45% lower than those reported in the literature. Attempts to model higher

velocities similar to those observed in the lower gorge while reproducing the current

glacier extent and surface elevation proved impossible without assuming a large increase

in net mass balance, which isn't supported by the available accumulation data. Mass

conservation suggests that either of the motion, glacier thickness or the mass balance

observations at Seward-Malaspina are inaccurate or not representative of mean spatio-

temporal conditions. The available mass balance data for Seward Glacier is sparse in

space and time but seem robust and broadly consistent with those inferred from our own

data on neighboring Bagley Icefield. Since floor elevation are poorly known, I assumed

that bedrock floor elevation within the gorge rises linearly with decreasing distance from

the divide, but multiple tectonic faults, such as the Malaspina Fault and the Chaix Hill

Fault, probably extend across Seward Throat and could sustain high bedrock topography

in the process. My modeling strategy may therefore not account for shallower and steeper

regions in the lower reaches of the gorge, which would demand higher local ice velocities

to observe continuity. Finally, the few velocity measurements are probably accurate since they are reasonably consistent with one another while they document local surface velocities at different times over a ~40 year period yet they may not represent well space and time averaged ice dynamics within the gorge.

4.2.4 Response to climatic forcing

Lowering mean air temperature by 3ºC or 4ºC, and decreasing precipitation by
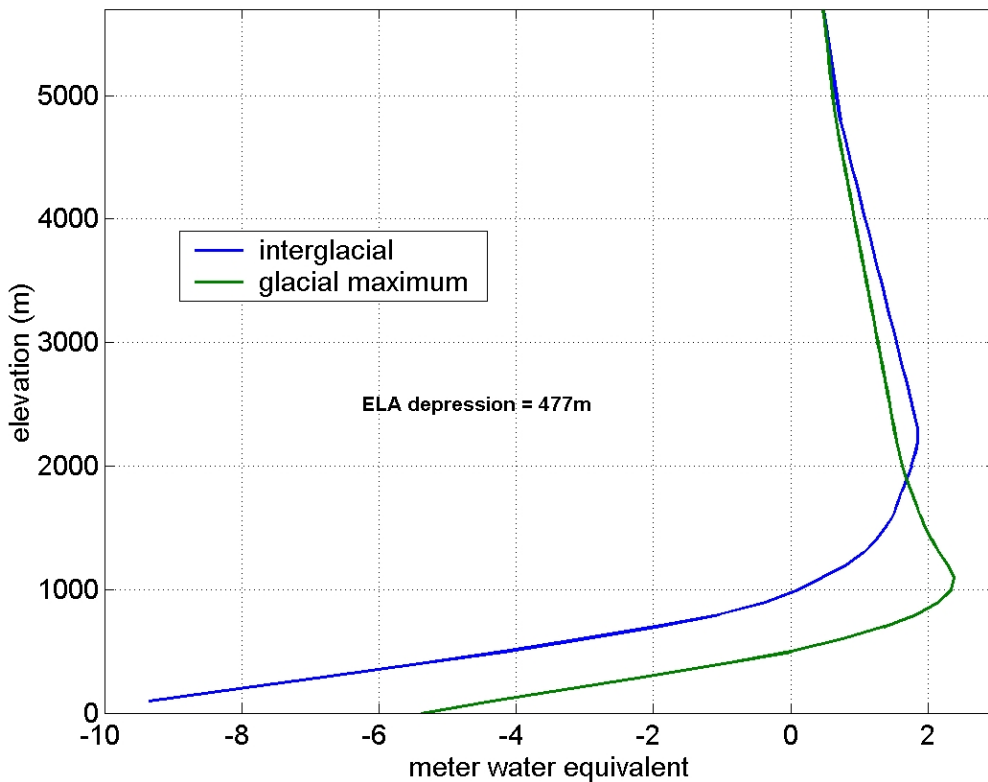
Figure 4.9: Modeled glacial and interglacial mass balance at Seward-Malaspina Glacier. Full glacial mass balance shown corresponds to a lowering of temperature of 3ºC and a decrease in precipitation of 20% relative to interglacial conditions.

20% over the course of a glacial sequence depressed the ELA by 477m or 620 m, respectively (figure 4.9). Although there is no ELA reconstruction in the Chugach-St.

Elias Mountains for the LGM, the ELA is likely to have dropped between the 400 and 600m based on studies in other regions ringing the Northwestern Gulf of Alaska such as Prince Williams Sound, the Kenai Peninsula, Kodiak Island, and the Alaska Peninsula (Detterman, 1986; Mann and Peteet, 1994; Mann and Hamilton, 1995; Porter et al., 1983). Glacier behavior when forced by climate will be tested for the range of departure in sea surface temperature (3-4°C), and for a decrease in precipitation of 20% to reflect a small latitudinal shift of storm tracks toward the south.

Under the parameters and processes chosen for this model run, Seward-Malaspina Glacier advances only a total of 52km toward the edge of the continental shelf from the interglacial moraine (fig. 4.10). From interglacial times through Maritime Isotope Stage 4 (MIS 4: 70 kyr.b.p.), the glacier advances slowly onto the continental shelf as allowed by eustatic sea level changes. During the first major cooling of MIS3 (60 kyr.b.p.), the glacier advances rapidly to a region of the shelf where it nearly stagnates throughout MIS3 and MIS2 (24 kyr.b.p.), ~50 km further from the position currently occupied by the late Holocene moraine but still nearly 40km away from the continental shelf edge (fig. 4.10). As a comparison, the same glacier without the significant ice loss due to calving penalty would spill onto the continental slope by ~60kyr into a glacial cycle. The same tidewater system subject to decreasing mean air temperature by –4°C instead of –3°C would result in the glacier advancing a few kilometers further during the LGM yet still not allow it to reach the edge of the continental shelf.
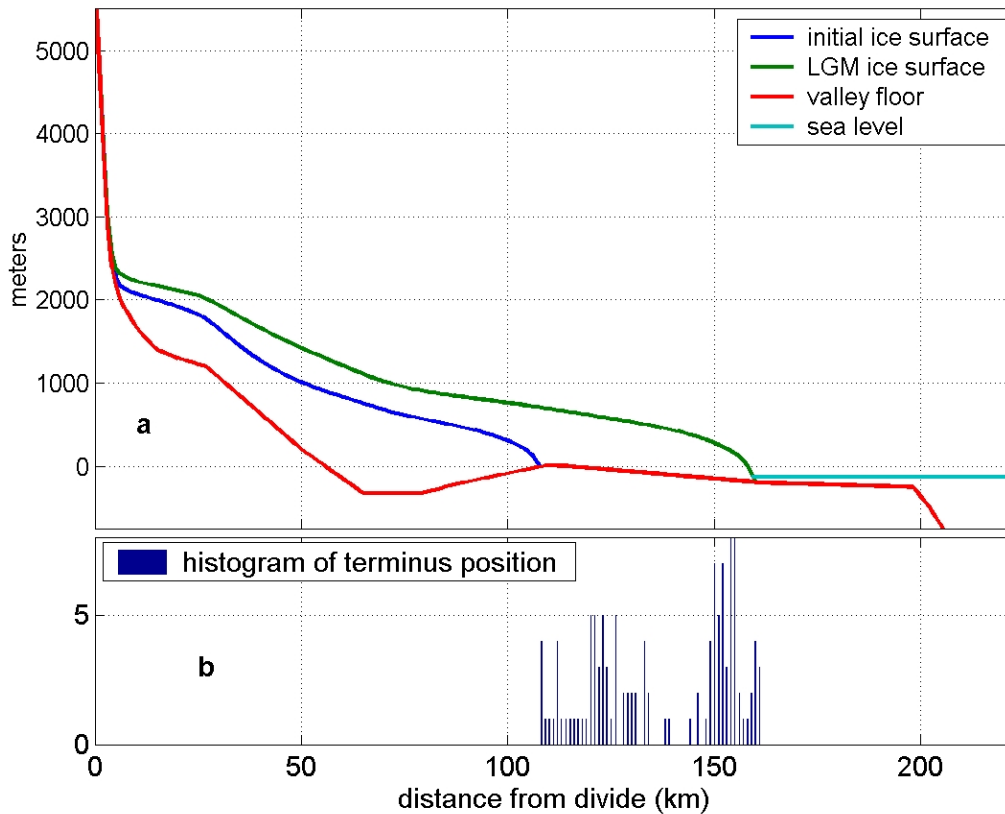
Figure 4.10: Minimum and maximum glacier extent for a tidewater system without sediment deposition (panel a). Locations of the glacier terminus during a 123 kyr glacial cycle are shown in panel b.

Topographic troughs that cross the continental shelf in front of South Alaska's major glaciers show, however, that massive glaciers can reach the edge of the continental shelf at least during the colder part of glacial cycles. The lack of modification of the bed under the glacier by erosional processes during this model run insures the terminus will not encounter regions of water deeper than were encountered during glacier advance and prevent catastrophic retreats toward the proximal end of the over-deepening; however, excavation of overdeepenings by extremely efficient sub-glacial water channels when sediment is over-run during advance could create the conditions necessary for very rapid glacier retreat as witnessed throughout this century in Southern Alaska. Similarly, rates of

200

proglacial sediment delivery and shoal building would greatly affect grounding of the terminus in water, decrease its dependence on glacier width and increase rates of glacier advance. The subglacial entrainment, transport, and deposition of sediment are addressed in the following section.

4.3   Sediment transfer

The distribution of sediment packages under and in front of a tide water glacier controls 1) the dynamics of the glacier front by changing water depth and 2) the spatial distribution of bedrock erosion since significant sediment accumulation shields the bed from physical erosion. It is therefore necessary to account for sediment deposition in the proglacial environment and remobilization during glacial advance to determine glacier extent, erosional footprint and sediment fluxes toward the oceans.

Glacial sediment deposited in the proglacial environment, including that deposited in fjords and on the continental shelf, is eventually overrun by ice and remobilized during subsequent glacier advances. Temperate glaciers are very efficient at removing debris fills especially wherever ice and subglacial water flow are relatively confined: incision rates into sediment of 1-4 meters per year sustained from one to several decades since the mid-50's have been documented in South Alaska at Taku Glacier (Motyka et al., 2006). Such high sediment entrainment rates suggest that most deposits would be washed away in a few 100 of years unless overridden by a glacier lacking highly efficient water channels. It is probable that glaciers stayed in protracted positions on the continental shelf for many thousands of years during the LGM, providing plenty of time for subglacial processes to excavate much of the sediment deposited during the previous interglacial. In

201

fact, an analysis of seismic reflection profiles collected on the continental shelf and industry borehole data by Berger and co-workers (2008), indicate that ~200 meters of sediment has accumulated above a shelf wide unconformity thought to represent the intensification of glaciations in the middle Pleistocene (~800 kyr bp), which suggests that most of the sediment deposited during interglacial times over the last 8 glacial cycles has been removed during glacial advances and flushed onto the continental slope. Sediment excavation by subglacial water channels is so rapid in confined valleys that bottom fjord fills are commonly assumed to mostly represent erosional product post-dating the last advance to the fjord mouth. Nevertheless, even in temperate ice system where debris transfer is rapid local long-term storage can occur in topographic overdeepenings or at the sides of wide valleys (Figs 5 and 6, Cowan et al., 2010) under the ice. Between the modern shoreline and the St Elias mountain front, some sediment packages found on interfluves between glacial troughs predate the LIA glacial advance in South coastal Alaska, but none have been found to be deposited before the last glacial maximum retreat off the continental shelf over 14,000 y.b.p. (Calkin, 1988; Ager, 2007). In fact, little sediment found near the bottom of fjords appears to predate the LIA retreat during the 20th century even though glaciers probably weren't in protracted position at the modern shoreline for much of the Holocene (Porter, 1986; Calkin et al., 2001; Barclay et al., 2006; Barclay et al., 2009; Cowan et al., 2010; Pasch et al., 2010).

4.3.1 Glacial sediment entrainment and marine sedimentation

Glaciofluvial transport is by far the most important mode of delivery to the glacier margin of South Alaska's temperate glaciers. Transport in subglacial water accounts for 84-99% of all sediment flux in Glacier Bay, whereas bed deformation, basal freeze-on,

englacial and surface transport account for the remaining balance (Hunter et al., 1996 a & b; Alley et al., 1997; Lawson et al., 1998; Alley et al., 2003). The overwhelming importance of glacial fluvial sediment transfer in South Alaskan glacial systems is to be expected considering the high sediment transport capacity of subglacial hydraulic networks characterized by the seasonal nature of meltwater discharge and large total hydraulic head gradients ($O[10^{-1}-10^{-2}]$ from glacier head to terminus). Quickly decreasing water pressure head due to rapidly decreasing ice overburden as one approaches the terminus induces the largest piezometric head gradient along the profile even though topographic slopes at the bed tend to be smaller near the terminus of glaciers. The large downglacier increase in subglacial water discharge, a 3 orders of magnitude increase in the ablation area, is largely responsible for the marked increase in sediment transport capacity near the terminus that will be examined below.

Other transport processes like sediment entrainment due to ice sliding over the bed and basal freeze on of debris are likely to become significant only locally where glacier melt is insufficient to cause major sediment removal, such as above the snowline where a distributed hydraulic network dominates, or in overdeepenings where subglacial water can be conveyed by englacial channels or can be injected toward the bed due to freezing conduits (Hooke et al., 1988; Hooke, 1991; Hooke and Pojohla, 1994). Whenever a reverse bed slope (a bed slope rising toward the glacier terminus) is ~1.5 times greater (1.2-1.7) than the negative of the glacier surface slope, the pressure release-induced rise of the freezing point of ice water cause frazzle ice formation, thereby reducing the carrying capacity of subglacial channels, and/or causing the freezing of supercooled water in debris rich basal layers (Lawson et al., 1998; Alley et al., 2003).

Secondary glacier sediment transport processes in South Alaska, like basal freeze on of sediment and englacial and surpraglacial transports, which represent a few percent of all sediment transport, are beyond the reach of this exercise and are therefore neglected in this work. Although I chose to not solve for glaciohydraulic cooling and basal freeze on processes explicitly, the bedrock erosion function I use features a reverse slope angle threshold; all reverse bed slopes exceeding the glacier surface slope do not incur any bedrock erosion, due to the presence of sediment suggested by theory irrespective of whether or not sediment exists at that location in the model. Sediment entrainment through shearing of a sediment layer is assumed to occur wherever the ice isn't frozen to the bed as determined by the basal thermal model. Considering the complexity of the task at hand and the modest means available to simulate subglacial sediment mobilization, I focus on the first order contribution of sediment transport systems to tidewater glacier variations. My modeling strategy addresses first subglacial fluvial sediment transport because it overwhelms all other modes of sediment transfer, and second sliding-induced sediment transport not only because it likely occurs where the glacier overrides sediments but also because it effectively represents a host of sliding-dependent entrainment phenomena (Hunter, 1996a&b) where the carrying capacity of subglacial water networks is small or where it decreases substantially because of adverse bed slope or of channel freezing.

In one dimension, the continuity equation for the sedimentary cover over the glacier bed can be expressed as:

$$\frac{dh_s}{dt} + \frac{1}{w\rho_s}\frac{dQ_s}{dx} = \overset{\bullet}{e}\frac{\rho_r}{\rho_s} \qquad \text{(Equation 4.4)},$$

which relates changes in thickness of the subglacial sediment layer, h_s, to the divergence

of the mass transport rate, Q_s, and the sediment source, $\dot{e}$, the subglacial bedrock erosion

rate modulated by the shielding of a sedimentary cover greater than a threshold thickness

(see equation 4.7). By inspection of the continuity equation, it is apparent that where

bedrock erosion is insignificant, sediment cover thickens wherever sediment flux

divergence is negative and vice versa.

In the model, following Bagnold's (1966) work on bedload transport, I

approximate subglacial fluvial transfer as simply increasing linearly with the stream

power of the subglacial hydraulic network. I take this approach because it is simple and

accounts for the basic physics of sediment transport insofar as the potential energy to

entrain sediment is proportional to the discharge-slope product of the flow; yet, it ignores

the explicit mechanics of sediment entrainment that are beyond the scope of this work.

This treatment of debris transfer doesn't differentiate between bedload and suspended

load, and model calibration accounts for total load concentration. Sediment transfer is the

sum of glacifluvial and basal entrainment mass transport rates, with glacifluvial transport

simply scaling with subglacial stream power according to:

$$Q_s = -k_1 \rho_w Q_w G + Q_{sd} \qquad \text{(Equation 4.5)},$$

where Q_s is the sediment mass transport rate resulting from fluvial and deforming bed

processes, k_1 is a dimensionless proportionality constant that is assumed uniform along

the profile, Q_w is the subglacial discharge resulting from surface melt and liquid

precipitation, G is the hydraulic potential gradient and Q_{sd} is the mass flux due to bed

deformation. k_1 is effectively used as a tuning parameter to induce sediment yields that

are consistent with the wide range of mean annual rates of terminus sediment delivery

found in the literature and of sediment concentrations in rivers emerging from glaciers (Chernova, 1981; Gustavson and Boothroyd, 1987; Bezinge et al., 1989; Booth, 1994). Presumably because sediment delivery in maritime environment is more difficult to observe, these field observations were almost all made in continental settings (European Alps, Korakorum, Pamirs) over time intervals of a few years at most; they allowed computing total sediment concentrations ranging 0.2-10 g/l of water. In initial model runs, k_1 was first selected to deliver mean annual terminus concentrations near the middle of the range and yearly average total sediment concentrations were allowed to fluctuate about this mean; however, evacuating most of the bedrock debris eroded concurrently required total sediment concentrations on the average significantly greater than that found by field workers. In order to reproduce the lack of significant long-term accumulation of debris observed under South Alaskan glaciers, the range of possible total sediment outflux concentrations was thus increased to 14g/l (fig. 4.11). Following Shreve (1072), the dimensionless hydraulic potential gradient in one dimension is:

$$G = \frac{1}{\rho_w g}\frac{d}{dx}\left(P_w + \rho_w gz\right) \qquad \text{(Equation 4.6)}$$

where the water pressure is P_w and the elevation head $\rho_w gz$. Bedrock erosion, the source term in equation (4.4), is assumed to be an exponentially decreasing function of sediment thickness when it exceeds an arbitrarily small threshold of 0.2 m, according to:

$$\dot{e} = \dot{e}_o \exp\left(-\frac{h_s}{a}\right) \text{ when } h_s > 0.2m \text{ and } \dot{e} = \dot{e}_o \text{ when } h_s \leq 0.2m \text{ (equation 4.7),}$$

where $\dot{e}_o$ is bedrock erosion in the absence of sediment shielding the bed, h_s is sediment thickness and a is a dimensionless constant less than unity (0.5) chosen so that erosion is nearly $1/10^{th}$ its sediment free value with 1 m of sediment protecting the bed.
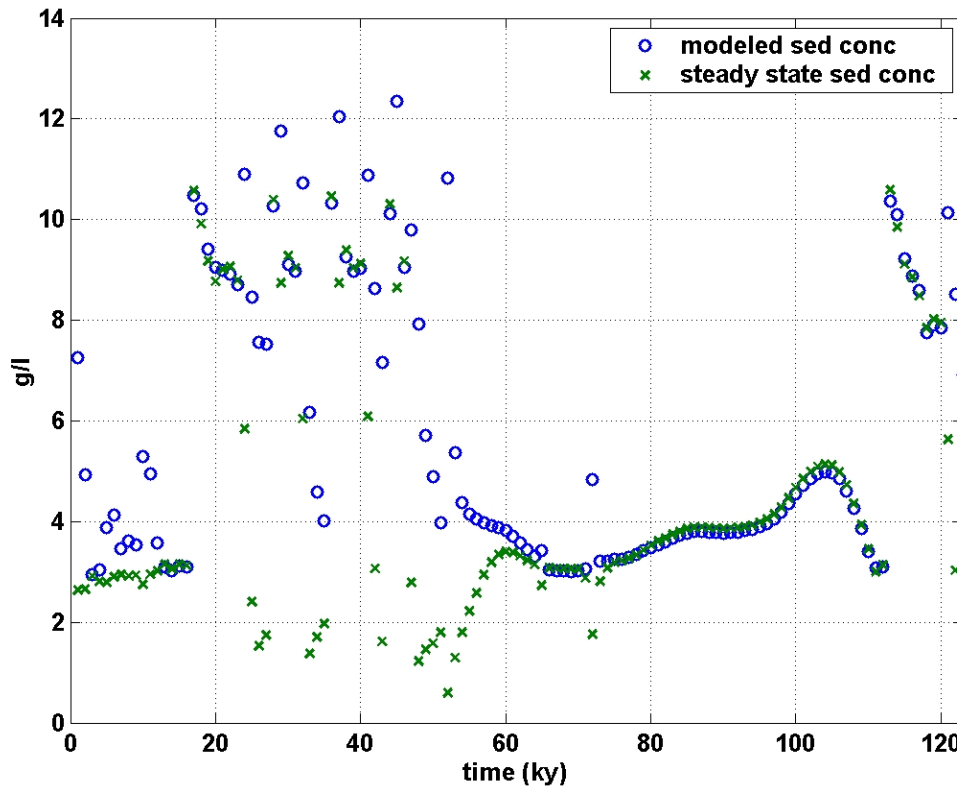
Figure 4.11: Modeled mean annual total sediment concentration in water at the terminus over the course of a complete glacial cycle (circles) and sediment concentrations that are required to keep sediment thickness unchanged by flushing out all concurrently produced sediment from under the glacier (i.e. steady state sediment concentration). Sediment transport approaches sediment production during colder climate (60-110ky), but modeled concentrations also reflect remobilization of pre-existing sediment during interglacial times.

Choice of *a* is arbitrary but represents the notion that sediment layers less than 1 meter thick are unlikely to drown all bed roughness and prevent all quarrying from occurring.

Substituting potential gradient (eqn 4.6) into the expression for sediment transport (eqn 4.5), then substituting the outcome and sediment source (eqn 4.7) into the continuity equation (eqn 4.4) results in a diffusion equation. I simply solve this equation numerically by an explicit finite difference method. I approximate the time derivative of sediment thickness through a forward differencing scheme, and use a 2nd order central

difference approximation to estimate the product of water discharge with the spatial derivative of hydraulic potential. For each time step, after computing effective bedrock erosion as a function of sedimentary cover, a sweep down the profile first compares transport capacity to sediment supply because transport is supply limited in many subglacial channel reaches. Equating transport capacity with sediment transport would grossly overestimate the quantity of sediment within the subglacial network of channels so wherever supply is less than transport potential, sediment leaving a reach is set to the volume of sediment available within the reach. Once sediment transport and the new bed elevation have been computed, sediment concentration in water at the terminus averaged over the time step (1000 years) for the ice dynamics model is limited to be within the range of sediment concentrations representative of modern delivery of sediment to the proglacial environment. If the model yields a sediment flux outside the prescribed range, the proportionality constant k_1 in the glacifluvial transport equation (eqn. 4.5) is accordingly adjusted and the numerical scheme iterated until the sediment concentration meets the prescribed conditions. Although the grid spacing for sediment mobilization is that of the main model routine (dx = 1000 m), the time step is reduced to one year, which is sufficiently small to permit a stable evolution of the sediment cover while tracking the annual cycle of meltwater discharge.

The object of this portion of the model is to simulate fluvial mobilization of the subglacial bed and how it affects the distribution of erosion controlled by climate. To model discharge, I assume that lateral stream migration over the entire glacier bed combined with convergence of sediment toward subglacial rivers is bound to occur within the millennial time scale of each model step. I further assume that on average the

208

discharge of subglacial water for a glacier cross-section is partitioned into equidistant

subglacial streams with uniform 100 m spacing. As water emerges from under the ice in a

subaerial or submarine setting, the hydraulic head gradient reduces to the streambed

gradient. Accordingly, stream power generally drops quickly as subglacial rivers emerge

from under the ice causing sediments to accumulate near the terminus (fig. 4.12). At that
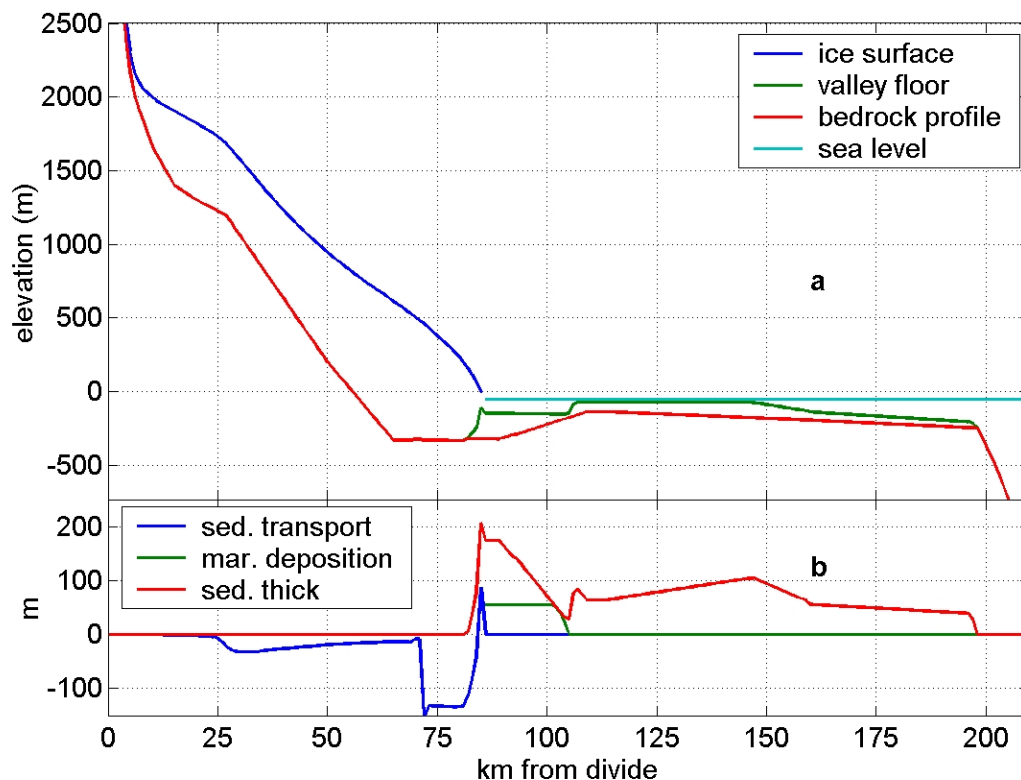
Figure 4.12: Sediment remobilization and deposition when the glacier terminus is within an overdeepened region. The spatial variability of sediment transport reflects first the supply-limited nature of subglacial sediment mobilization. Exclusive sedimentation within the overdeepening occurs when the terminus doesn't extend onto the continental shelf, which reflects current knowledge about fjords acting as very efficient sediment traps. Sediment transport in panel b is in m/yr.

stage in the routine, half the sediment load is assumed to be suspended load that will

bypass the terminal embankment and settle out of the water column away from the

terminus within the fjord and on the continental shelf. The other half, the bedload, however is spread evenly over the cell immediately beyond the terminus, which results in an unrealistically thin terminal shoal since the km-grid scale is quite large relative to the active depositional zone for bed load at the glacier terminus. As sediment transport is controlled by the availability of sediment, and thus it often equates the sediment production by erosion of bedrock wherever prior sediment accumulation is small or inexistent.

Although South Alaskan sediment entrainment rates through shearing of basal sediment are 1-2 orders of magnitude smaller than in subglacial streams (Hunter et al., 1996a & 1996b), the process likely plays a significant local role in preventing debris accumulation on the bed wherever glacifluvial transport capacity is small. Ice shearing on top of a bed of sediment is simply implemented by assuming that a layer is entrained on average at a fraction of the ice sliding velocity according to:

$$Q_{sd} = k_2 w \rho_s h_2 U_{slid} \qquad \text{(Equation 4.8)},$$

where k_2 is a dimensionless constant, w is glacier width, h_2 is the thickness of the layer in motion that is chosen to be at most 1 m thick as the sediment is likely often not a classic matrix supported soft deforming bed, and U_{slid} is the sliding velocity. k_2 is typically used to set the slope of the vertical velocity profile within the deforming layer although I effectively use it as a tuning parameter to set the magnitude of ice shear-induced transport relative to that of fluvial transport. The model is calibrated so the yield of sediment through shearing amounts to ~2% of total yield to reflect observations in South Alaska.

I treat sedimentation beyond the glacier margin simply. Rock debris supplied by subglacial processes at the glacier terminus is first allowed to fill proglacial

overdeepenings at the ice front. Excess sediment can settle in fjords and on the

continental shelf, at a rate that is a function of distance from the modern shoreline

dictated by Holocene sedimentation rates derived from acoustic surveys or from

radioisotope studies of cores taken on the continental shelf (Carlson et al., 1975; Jaeger

and Nitrouer, 1998). Rapid tidewater retreat due to the combined effect of negative net

mass balance and rising eustatic sea-level during deglaciation of the continental shelf

~14,000 y.b.p. (Ager, 2007) implies that sediment above the uppermost hard acoustic

reflector in the sediment column represents Holocene sedimentation mostly issued from

point sources near the existing shoreline since retreat was likely very rapid. Since the

post-LIA retreat during the 20th century, most sediment has been trapped in fjords, as it

was probably also the case during much of the Holocene including the mid-Holocene

thermal Optimum (Barclay et al., 2006). Holocene sediment thickness inferred from the

continental shelf seismic data is converted to a mean yearly accumulation rate by

assuming rapid glacier retreat 14,000 y.b.p. and fitted to a 2nd order polynomial as a

function of distance away from the modern shoreline. Sediment is thus spread on the

shelf according to this polynomial. Sedimentation on the continental slope leads to rapid

shelf progradation as can be seen in seismic sensing of the South Alaska continental shelf

(Carlson et al., 1982; Berger et al., 2008); however, sediment deposition beyond the

shelf-slope break is ignored. This deposition and the time evolution of trough mouth fans

processes are beyond the scope of this study.

4.3.2 Evolution of interfluves and landsliding

Mass transfer due to slope failure is a key erosional process in tectonically active

regions and where relief is high, it contributes significantly to the sediment budget. In this

model, the width of interfluves is constant through time. On actual slopes, the limit to local relief is a function of structure, lithology, jointing, and hydrology. It is thus difficult to simply characterize a generic hillside at the point of failure while accounting for the variability found in nature. For simplicity, I assume that slopes are linear and remain close to the angle of repose once they have attained it. Following Anderson (1994), I parameterize the sediment flux on interfluves so that it increases exponentially as the slope nears the threshold slope angle at which all slopes fail (Sc), thereby simulating the non-linear dependence of landsliding on slope. The volume flux per unit width of slope is given by:

$$Q_s = k_{sl} L Sc \exp\left(-\left(\frac{Sc - S}{Sc - Si}\right)\right)$$ (Equation 4.7),

where S is the hillslope angle, Si is the angle at which landslides start to occur, and k_{sl} a transport coefficient. The slope length, L, is the difference between ridge top and ice surface elevation and is thus susceptible to thinning of the ice during deglaciation. The slope is assumed to lower uniformly as glaciers transport all detached bedrock to the ice front. The critical and initiation slope angles are obtained through DEM analysis of deglaciated terrain whereas the value of the proportionality constant k_{sl} results from a steady-state model calibration where ridge lowering rates match incision of the valley bottom. The neglect of slope diffusion processes reflects the observation that incision rates of valley floors during glacial occupation are great enough to oversteepen hillslopes in the region so that rockfall and landsliding are the main mode of transport on ice-free slopes.

4.3.3 Initial conditions and forcing

Initial conditions and climatic forcing ($\delta T=+3^oC$, $\delta P=-20\%$) are the same as those used for the generic tidewater case (section 4.2), except for differentiating the nature of the substrate between either of bedrock or sediments. There is, however, little to no information about sediment thickness underneath the terminus region or any other location at Malaspina Glacier, which calls for a judicious choice of initial conditions. As shown in section 4.2, tidewater glacier extent is sensitive to the factors that affect relative sea level, including sediment thickness. South Alaskan glaciers are known to be very efficient at removing these deposits, which suggests that any sustained glacier advance is likely to lower the bottom boundary thereby affecting glacier mass balance and, perhaps, the ability of the terminus to be grounded. Indeed, during a hypothetical period with constant climate forcing, sustained sediment evacuation would result in glacier retreat due to lowering elevation of the substrate unless sediment production keeps up with the rates of sediment evacuation.

Although within a few hundred meters from the ocean at Sitkagi Bluff, Malaspina glacier doesn't currently terminate in tidewater today but it calves into, and melts below the water line at Malaspina Lake (fig. 4.13). In contrast with Bering Glacier, the other great contemporary piedmont coastal glacier in the region, relatively little is known about Holocene glacier chronology of the Seward-Malaspina Glacier due to the modern ice limit being very close to that of the LIA maximum at the present shoreline; however, an early 19th century glacier advance was recorded by trees killed by outwash aggradation at Caetanie River that pours into Icy Bay (Sharp, 1958b; Barclay et al., 2006) and the existence of Holocene-age marine shells within recent ice limits indicates that a marine

embayment existed on the Malaspina foreland at some point between the LGM retreat

and the LIA advance, much as has been identified at Bering and Yakutat Glaciers

(Barclay et al., 2009; Pasch et al., 2010). The Icy Bay glacier complex, Malaspina's

westerly neighbor, and the Yakutat Bay glacier complex, on Malaspina's eastern flank, as

well as many other South Alaskan Glaciers, including Bering Glacier 200 km to the

Figure 4.13: Terminus region at Malaspina Glacier from Anderson and Molnia, 1989. Fresh water lakes and thousands of kettles have appeared since the mid-20th century on the lower reaches of the Malaspina lobe likely initiating the formation of a tidally influenced system of lakes on the foreland like Vitus lake at Bering Glacier.

West, are known to have fluctuated between the mountain front and the modern shoreline

several times since the LGM retreat; they provide useful analogs for Seward-Malaspina

Glacier over the same time period (Porter, 1986; Molnia and Post, 1995, Muller and

Fleisher, 1995; Calkin et al., 2001; Barclay et al., 2009; Pasch et al., 2010).

Terminus oscillations between the mountain front and the modern shoreline

during the Holocene, and by inference for all interglacial periods of the Quaternary,

214

suggest more consistent occupation and greater erosion of the low elevation foreland than

immediately further out onto the continental shelf; therefore, an overdeepened bedrock

subsurface similar to the observed topographic depression under the ice is likely to exist.

Although, I assume, as in the preceding sediment-less case, that the width-averaged

bedrock elevation of the overdeepening under the foreland is –330 m, I now assume that
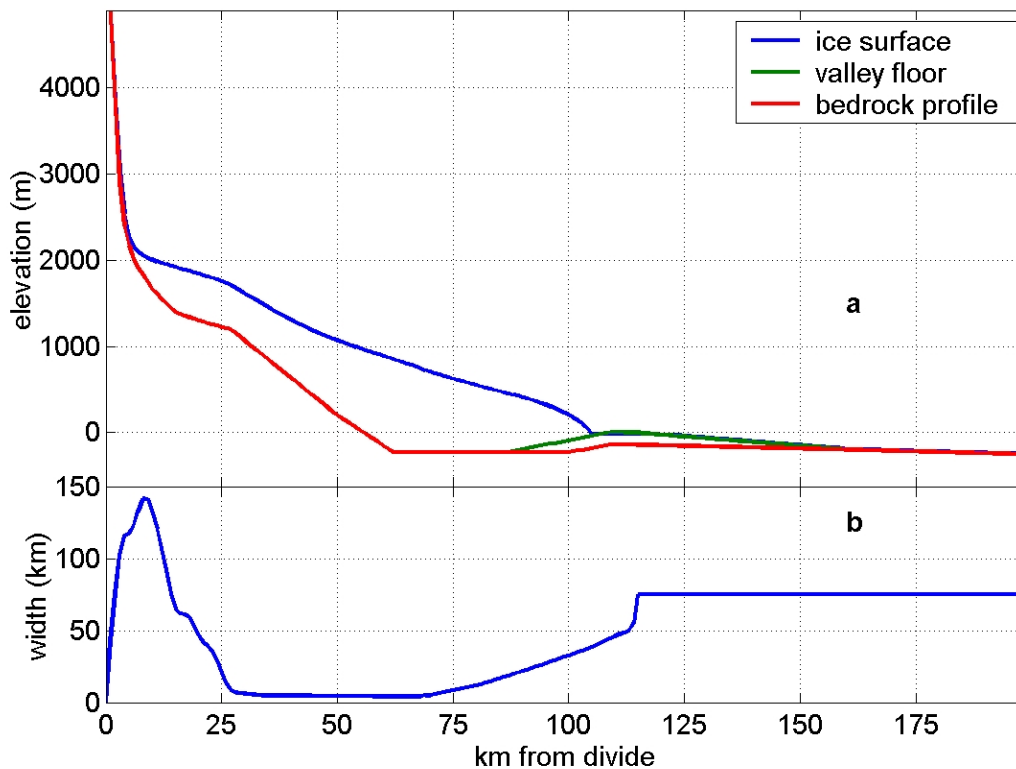
Figure 4.14: Initial long profile with sediment apron blanketing the sill of the overdeepening under the Malaspina foreland (a), and effective width function of Seward-Malaspina glacial valley derived from analysis of basin hypsometry (b).

a thick sediment package initially covers the distal portion of the overdeepening (fig.

4.14). The gradient of the reverse distal slope of the overdeepening is set as somewhat

smaller than what was estimated from data found in the literature so as to not use an

initial boundary condition that would preclude bedrock erosion at that location through

glaciohydraulic supercooling and sediment accumulation; the reverse bedrock slope is thus set at less than 1%, whereas the mean distal reverse slope was estimated to be as high as ~2.5% in the Swiss Alps (from subsurface sounding data in Preusser et al., 2010) and greater than 3% at Columbia Glacier (from a bathymetric long-profile in Pfeffer, 2007). In turn, modeled ice surface slope during the initial time step averages -2.5% (the negative sign indicates surface elevation decreasing with distance from the divide) over the region underlain by the reverse slope of the overdeepening.   For the reasons outlined in chapter 1 (mainly extreme topography and intense erosion sustained for millions of years at the syntactic corner), mass fluxes in and out of the orogen are assumed to be at equilibrium, and that the valley floor topography is in a steady state. These assumptions enable me to infer a pattern of uplift along the length of the glacier that exactly offsets the pattern of erosion incurred during the previous model time step.

4.3.4 Glacier response to climatic forcing and topographic constraints

Ignoring the prominent oscillations in glacier extent that appear to occur on decadal to century time scales irrespective of climate change as expected, modeled variations in terminus position of Seward-Malaspina glacier averaged over longer time scales (O[10^4] yr) follow climatic forcing (fig. 4.15). For the initial ~50 kyr of the climate cycle, the glacier terminus location fluctuates between the mountain front at the entrance to Seward throat at 68 km from the divide (nearly 0.7 of normalized glacier extent in figure 4.15) and the modern shoreline (located at 1 on the right vertical axis of figure 4.15 or 109 km from the divide). Before each of the 4 advances toward the modern shoreline, the terminus nearly stagnates close to the mountain front (the lower end of Seward

Throat) for a few thousand years until the interplay of climatic change (mass balance and

eustatic sea level) and topographic evolution of the valley floor (sediment production
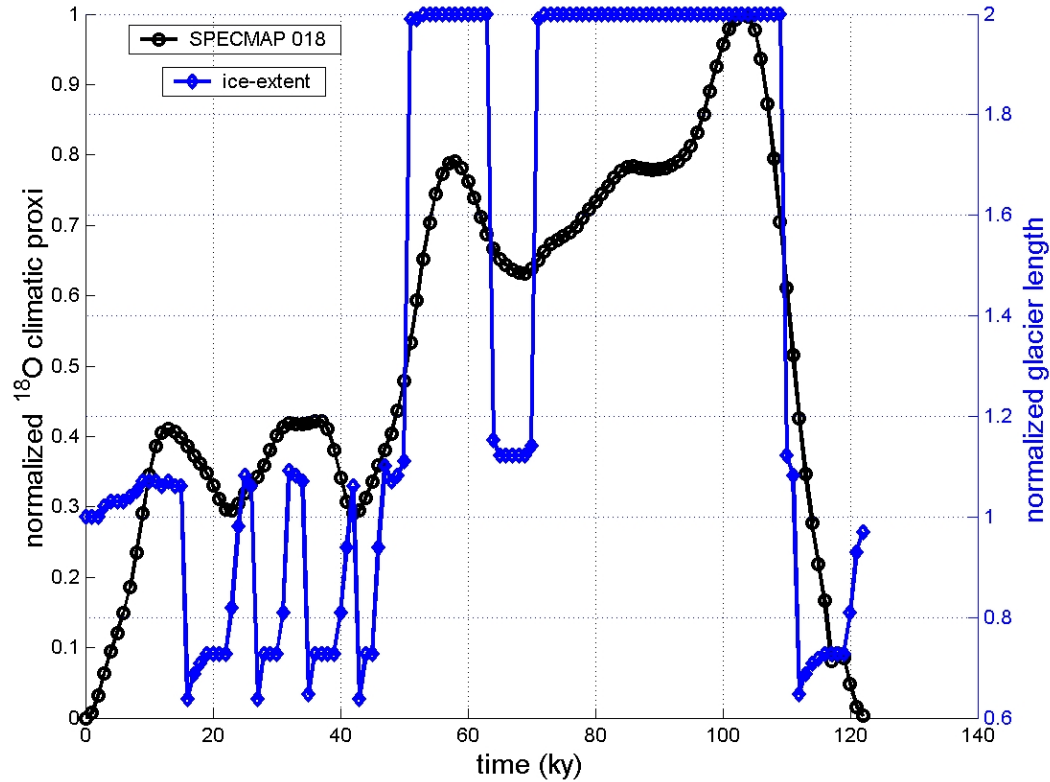
Figure 4.15: Normalized glacier extent and ^{18}O climatic proxy over a 123 kyr glacial cycle on TOPO1. The entrance to Seward throat, the modern shoreline and the shelf edge are respectively located at 0.69, 1.1 and 2 on the normalized right-hand scale.

and accumulation) results in a relative sea level sufficiently low to allow for the terminus

to be grounded in marine water at which point the glacier advances rapidly across the

overdeepening (fig. 4.15). As seen in section 4.2.1, relative water depth at the terminus

controls sensitively the rate of glacier advance into tidewater. Without modeling

proglacial sedimentation explicitly, however, the relative importance of four possible

contributing factors (eustatic sea level, mass balance, ice dynamics and floor topography)

has been unclear, especially since the individual processes involved are interdependent.

On a short time scale ($\leq O[10^3]$ yr) and over the spatial domain subject to glacier oscillations (the ~50-km long section that is today the Malaspina foreland), relative sea level is determined primarily by rates of terminal shoal recycling and infilling of an overdeepening with sediment since the modeled glacier oscillates in the same fashion seemingly irrespective of eustatic sea level and mass balance changes. The domain interval over which the glacier oscillates also features the major break in slope at the mountain front and a rapid increase in drainage width downstream from Seward throat. These topographic features exerted the greatest influence on rates of glacier advance in the discussion of a generic land-based glacier in Chapter 3; however, the height mass balance feedback is also a function of tidewater processes. Significant calving fluxes prevent the height mass balance feedback by drawing down the surface elevation in the ablation area, thus mitigating the very large ice volume increase that results from applying a steep mass balance gradient to low gradient topography when the glacier transitions from steep mountain slopes to the foreland. The rapid widening below Seward Glacier also affects rates of infilling of the overdeepening, thereby further delaying glacial advance because of the ice flux divergence. Infilling of the overdeepening by proglacial sediment deposition shortens the glacial response time imposed by drowned basal basins and ice flux divergence due to positive rates of change in valley confinement. Thus, the response time of the glacier to climatic forcing also becomes a function of sediment production and delivery to the ice front, as well as the divergence of sediment flux when the glacier advances onto what is the Malaspina foreland today.

Identifying processes that can delay glacial advance in tidewater is not difficult since, as already noted, this issue has been identified and discussed in the literature for

many years. However, the oscillations during the retreat phase are less intuitive because the model suggests that some retreats from the modern shoreline are not controlled by climate or eustatic sea level on any time scale since they occur during a cooling phase. A handful of modern tidewater glaciers are known to be advancing today or were doing so in the recent past (for example, Pio XI and Perito Moreno glaciers in Patagonia, or Taku glacier in Alaska) while regional climate is warming, and many Alaskan tidewater glaciers started their post-LIA retreat at least decades after land-based glaciers (Meier and Post, 1987; Warren et al., 1997). Thus, the ability of tidewater glaciers to stagnate or advance while climate warms has already been widely recognized by researchers (Warren, 1999). In the more intuitive case of glacial retreat when climate warms and eustatic sea level rises, the model shows that, as glacier mass balance grows increasingly negative, the glacier eventually pulls away from the morainal shoal; thus, within the first few thousand years of warming and sea level rise, the glacier terminus starts withdrawing into water that is too deep for the terminus to be firmly grounded, thereby triggering catastrophic retreat. For example, the first rapid retreat off the terminal shoal occurs 4000 years past the first peak in cooling (fig. 4.15) during which eustatic sea level increased by ~2.5 m; most of the rise is incurred during the last time step of this sequence before rapid retreat takes place (sea level increased only ~1 m during the first 3000 years of this retreat phase). At the time of retreat, climate is still colder than it was when the ice reached near the modern shoreline during initial conditions, but sustained sediment evacuation during the advance phase lowered the sediment bed under the glacier over the foreland. In addition, decreasing sediment yield as stores of subglacial sediment become depleted during the times steps subsequent to reaching a protracted position reduces the

219

ability to sustain a terminal embankment sufficiently large for the terminus to be

grounded (fig. 4.16). Once the terminus pulls away from the terminal embankment,
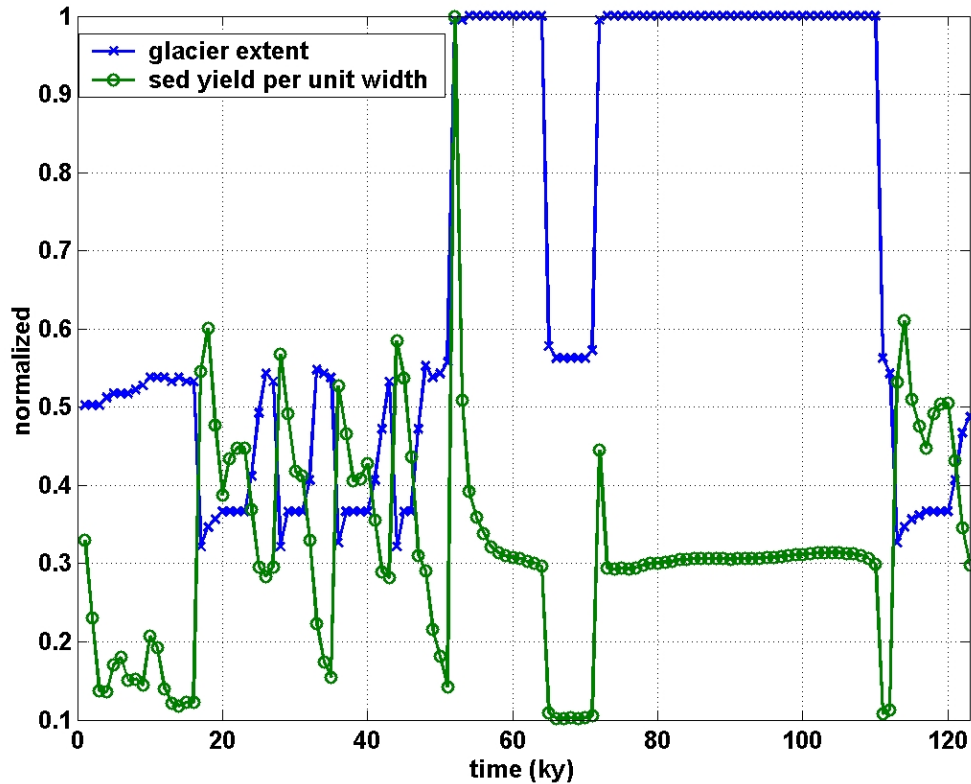
Figure 4.16: Glacier extent and sediment yield per unit of terminus width for an entire glacier cycle. Delivery of sediment to the terminus per unit width of terminus is a proxy for the glacier capacity to sustain a terminal moraine and be grounded. Sediment yield per unit width first reflects the drainage width function and second how recently previously deposited sediment was overridden. Sediment yield decreases with increasing occupation time until in situ sediment is almost completely evacuated.

glacier withdrawal all the way to the lateral confinement of Seward Throat is almost

assured because no basal topographic pinning point exists within the zone of terminus

oscillation as most of the sediments have already been evacuated from the

overdeepening. Moreover, lowering of the subglacial valley floor through sediment

evacuation alone appears to trigger glacial retreats modeled during periods of climatic

cooling modeled between 20 and 50 kyr of the glacial cycle (fig. 4.15). A slight decrease

in net mass balance, due to the lowering of ice surface elevation caused by removal of

10-100s meters of substrate under the glacier ablation area, forces terminus retreat off the

terminal shoal and subsequent catastrophic withdrawal in deep water. This sequence of

events holds for all simulated glacial retreats that occur during a cooling phase while the

frequency of terminus oscillations depends sensitively on the rate of subglacial sediment

remobilization; for example, doubling the sediment transport by doubling the

proportionality coefficient k_1 of the stream power equation results in twice the number of

oscillations over the Malaspina foreland. Alley (1993) has suggested that tidewater

glaciers could retreat without external forcing when sediment transport toward the ice

front by subglacial processes is insufficient to supply the additional debris needed to

sustain the required thickness of the morainal shoal as the ice front moves forward into

deeper water; deepening water without a commensurate increase in size of the marine

embankment would thus induce a greater calving flux, thinning of the glacier and

eventual retreat. The process invoked by Alley is substantially different from that

emerging from the model herein: the initial retreat off the shoal is forced by 1) a more

negative mass balance induced by a change in basin hypsometry caused by massive

subglacial removal of unlithified sediment and 2) a decreasing sediment delivery per unit

width of ice front caused by a rapidly depleting supply of subglacially stored sediment.

Model formulation, especially time discretization of valley floor evolution into 1000-year

steps makes it difficult to fully assess whether the quasi continuous processes of

transport, shoal building and sedimentation combined with progressive climate cooling

would enable the glacier to adapt to rapid evolution of subglacial basin hypsometry

221

without negatively affecting mass balance. Nevertheless, the effect on net mass balance of lowering basin hypsometry throughout the ablation area due to the removal of 10-100s meters of sediment over a few thousand years is likely to outpace that of lowering the ELA through climatic cooling because average lowering of ELA is ~3.7 m/1000 yr during this model run. The mean rate of ELA lowering is therefore up to 2 orders of magnitude less than plausible lowering rates of valley bottom through sediment removal, thereby suggesting that subglacial sediment removal significantly reduces mass balance even during cooling phases. Moreover, slight glacial retreat induced by these competing controls on mass balance calls into question the capacity of the glacier to retreat off its morainal shoal and rapidly rebuild another shoal to prevent continued retreat in deepening water; rebuilding a moraine requires sustained sediment delivery to the terminus, which decreases with occupation time in the model and depends strongly on high sediment production rates. Taku Glacier is probably the only tidewater ice mass that is thought to have retreated (~1650 y.b.p.) while neighboring land-based glaciers of the Juneau Icefield remained in an advanced position for 200 years (Motyka and Beget, 1996). Taku Glacier's asynchronous retreat has been interpreted as the withdrawal phase part of the tidewater glacier cycle (Meier and Post, 1987; Post and Motyka, 1995) because a modest retreat into deeper water was followed by catastrophic pull back to the head of the fjord where it remained for several centuries. The trigger to Taku Glacier's major retreat 1650 y.b.p. is likely to remain elusive; however, this retreat contrasts with the behavior of practically all neighboring glaciers, suggesting that an internal mechanism like decreasing sediment delivery to the terminal shoal and possibly glacier entrenchment through removal of the substrate may have played a role in rapid retreat.

The lack of direct observation of asynchronous retreat of tidewater glacier during a climatic stasis or cooling may well be due to warming sub-polar climates over most of the period of human observations.

In the second part of the climate cycle (post 50 kyr, Fig. 4.15), the glacier proceeds to reach the edge of the continental shelf at 53 kyr due to the strong cooling, and then retreats to the modern shoreline during a period of climate warming at 65 kyr, to return and remain at the shelf edge for the coldest part of the climate cycle. 13 kyr before present the glacier rapidly retreats near the modern shoreline and oscillates between that position and the mountain front as it did during the previous interglacial period.

Accounting for the role of sedimentation in this run enables the modeled glacier to reach the edge of the continual shelf, which it could not do in the previous model run without sediment mobilization and deposition. Again, this suggests that sediment delivery to the proglacial environment is the rate-limiting step for tidewater glacier advances in South Alaska. Modeled mean rates of terminus variations range over 2 orders of magnitude (0-80 m/yr). Rates of advance reach only ~28 m per year within the region of overdeepening and valley widening, but peak on the continental shelf, a region with a gentle and steady incline in the direction of ice flow in TOPO1. Despite the rapid retreat rates of actual tidewater glaciers, which reach hundreds of meters per year, the magnitude of modeled mean retreat rate is only nearly 2-3 times greater than the mean glacial cycle rate of advance (-26 m/yr versus +11 m/yr) likely because retreat rates are averaged over a time step much greater than the time needed for catastrophic tidewater glacier recession.

Substituting initial topography for that described in TOPO2 (topography with shelf trough) results in markedly different glacier fluctuations (fig 4.17 vs. fig. 4.14). Although, variations are very similar in shape and timing through the first 50ky of
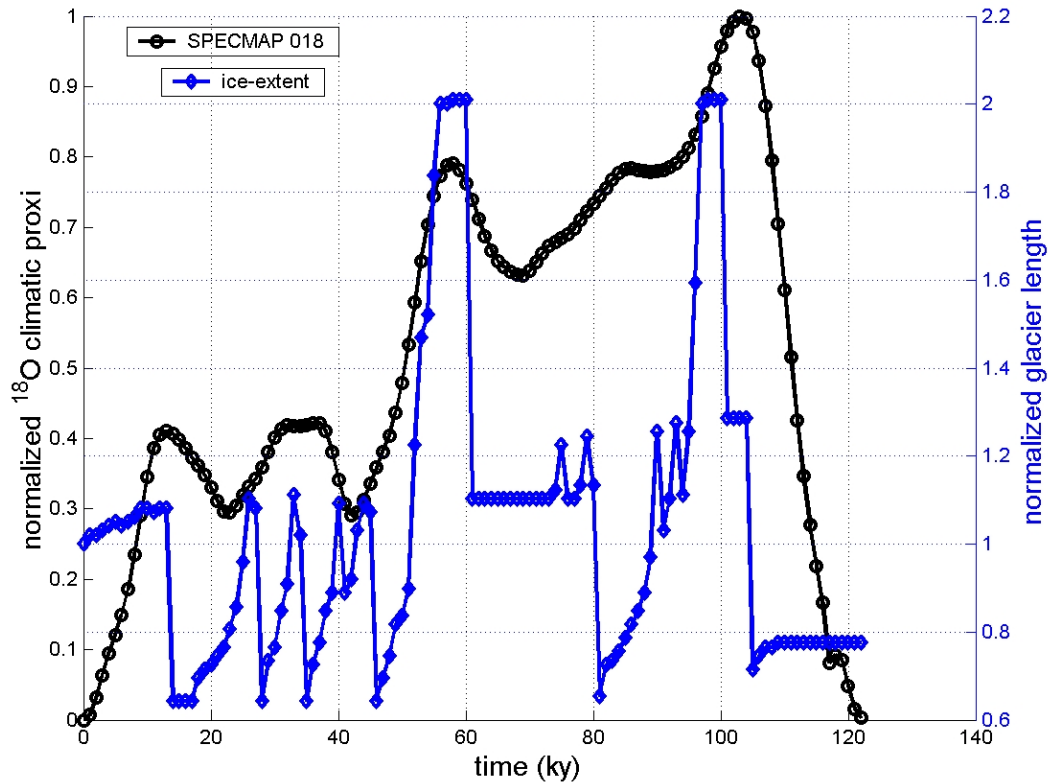
Figure 4.17: Variations in glacier extent over the course of glacial cycle with TOPO2 topographic model. TOPO2 includes a less pronounced overdeepening under the Malaspina foreland due to a lower sill elevation and continental shelf elevation similar to that found in Yakutat sea valley.

forcing when the glacier doesn't extend beyond the current shoreline, ice occupies the continental shelf during the colder part of the climate cycle only a fraction of the time than in the TOPO1 model with the shallower water. In fact, the glacier terminus is unexpectedly in a retracted position at the gorge outlet during the beginning of MIS2 (24 kyr.b.p.). Lower bedrock sill elevation near the modern shoreline and lower elevation of the continental shelf within Yakutat Sea Valley (fig. 4. 4) demand greater rate of outwash

deposition in order to advance the grounding line in the tidewater environment. Everything beside initial topography being equal, notably bedrock and sediment erosion tuning parameters, means that relative sea level as defined herein is on average higher when TOPO2 is the initial condition. Removal of sediment overlying the bedrock sill that was deposited during interglacial time accounts for both the small oscillations about 41 kyr and retreat to the gorge outlet at the 81 kyr mark. The ability of the glacier to remain in an advanced position at the edge of the continental shelf is also lesser than for TOPO1 since the calving flux is much greater with TOPO2 thereby preventing sufficient glacier thickening through the height mass balance feedback. Once the glacier retreats after full glacial conditions to the gorge outlet, it is never able to regain its interglacial position near the modern shoreline, which suggests that rates of sediment productions and/or rates of sediment mobilization may have been underestimated by the model.

4.4 The spatial distribution of erosion

In chapter 3, modeled bed incision by a generic land-based glacier was shown to vary with the stress distribution at the glacier interface with the substrate, which depends strongly on effective pressure and sliding speed, and on glacier geometry due to the strong dependence of ice flux per unit width on ice surface slope and glacier width. By modulating rates of glacial advance and the distribution of sedimentary cover as climate changes, the inclusion of tidewater and sedimentary processes in the model is expected to impact the spatial distribution of bedrock erosion by affecting the extent of the basin area subject to glacial erosion and the time the bedrock subject to erosive ice; the impact arises from the two distinct effects of sediments in modulating glacier fluctuations in the tidewater environment and in shielding the rock bed from erosion. First, I describe and

compare the model outputs to differentiate between the distributions of potential and effective erosion during the interglacial and full glacial conditions characteristic of Quaternary climate extremes. Potential erosion is defined as resulting from the distribution of effective pressure and sliding, whereas effective erosion also includes the shielding effect of subglacial sediment. Like in previous model runs, mean annual erosion is computed by averaging monthly mean erosion. The water pressure non-dimensional parameter, α, is first set at an average value of 1×10^{11}, and it is subsequently allowed to vary within the range previously considered in chapter 3. The tuning factor in the quarrying rule, k_c (eqn. 3.2.7x), is adjusted so that glacierized basin-wide erosion rates during modern climate conditions reach 2.5-3 mm/yr ($k_c = 300$). This rate is a fraction of that found (~ 10 mm/yr) for several South Alaskan glaciers as discussed in chapter 2. The dimensionless proportionality constant, k_1, for the sediment mass transport rate is set at 3×10^{-7}.

4.4.1 Bedrock erosion during interglacial climate

Although the glacier extends to near the modern shoreline during the glacial minimum, effective bedrock erosion occurs almost exclusively within Seward Throat, the region containing the ELA that is characterized by high ice flux per unit width, and a broad low in mean annual effective pressure and high rates of sliding (fig. 4.18). On
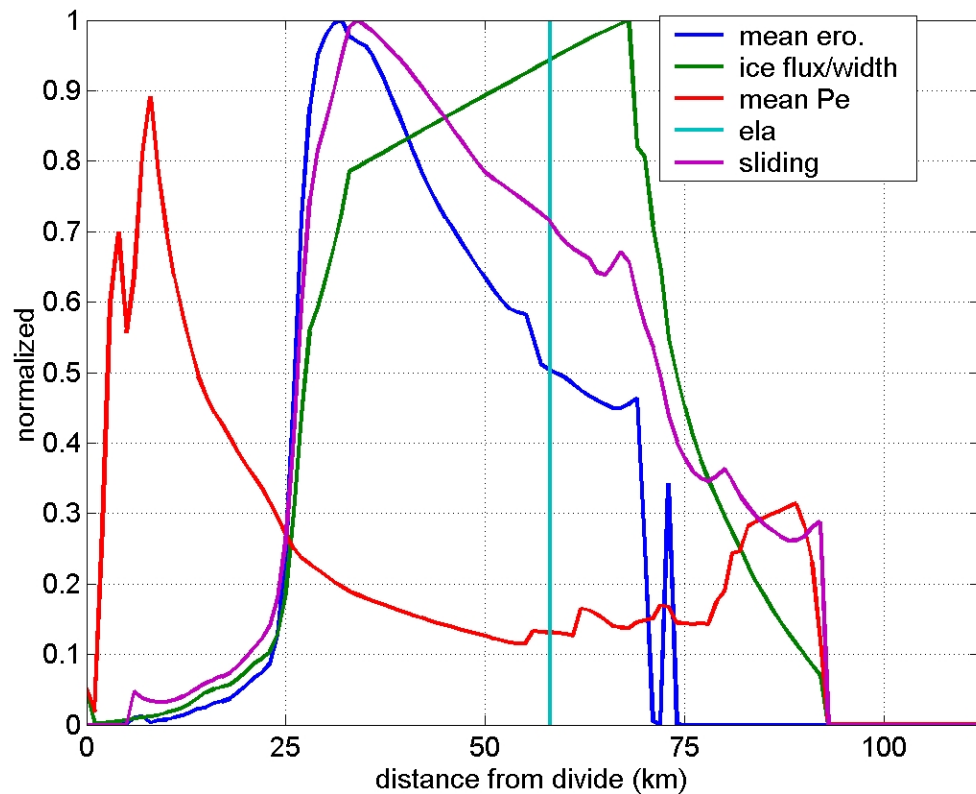
Figure 4.18: The distribution of effective mean annual erosion and key variables during interglacial conditions. Seward Throat extends from 33 to 68km as shown by its effect on the flux of ice per unit width. Ice flux per unit width increases throughout the gorge and beyond the ELA (location of vertical line) since Seward Throat is on average slightly narrower at its lower end than at its upper entrance (~4 km versus 5 km)

Upper Seward Glacier (0-33 km from the divide), effective pressure first rises abruptly

with ice overburden in the zone of no basal meltwater production (0-6 km from the

divide). Due to high mean annual effective pressure (up to 1.6 MPa) notwithstanding

moderate ice thickness, little erosion occurs on much of upper Seward Glacier; however,

rock incision increases sharply upstream from Seward Throat to attain a prominent

absolute basin maximum 32 km from the divide, just before the upstream entrance to the

gorge. In the example shown (fig. 4.18), the maximum erosion rate along the entire

glacier profile is ~27 mm/yr, which coincides with mean monthly effective pressures in the optimum range of a few bars (0.3-0.5 MPa). Although, the peak in erosion corresponds to the maximum in annual sliding speed (1195 m/yr), most erosion is incurred during months when sliding is significantly less (350 to 950 m/yr from September through May) due to the inverse relation between sliding and effective pressure. As one progresses down the gorge, erosion slows to nearly half of the maximum rate found in the upper reaches of the gorge. Water pressure varies the most with the seasonal evolution of water production at the lower end of the gorge: basal water pressures approach ice pressures before the seasonal migration of the snow line, and effective stress exceeds 5 bars when a Rothlisberger channel network drains this part of the subglacial landscape. Mean annual sliding rate along with ice surface slope decrease toward the gorge outlet onto Malaspina lobe: from the upper entrance to the lower end, the yearly sliding rate decreases by ~33%, from 1200 m/yr to 800 m/yr, while surface slope decreases by more than 54%, from –0.035% to –0.016%. The annual sliding velocity decrease is matched by a near doubling of ice thickness over the span of Seward Throat (from 550 m to 970 m). Ice motion due to ice deformation near the gorge outlet increases its modest upstream contribution to total speed by a few percent over that interval (from 6 to 8%), which isn't sufficient to offset a ~33% decrease in sliding incurred over the length of Seward Throat. As seen in chapter 3, the entire N-Us parameter space of the quarrying rule isn't available under glaciers due to the inverse relation between effective pressure and sliding (fig. 3.13); thus, seasonal variations in
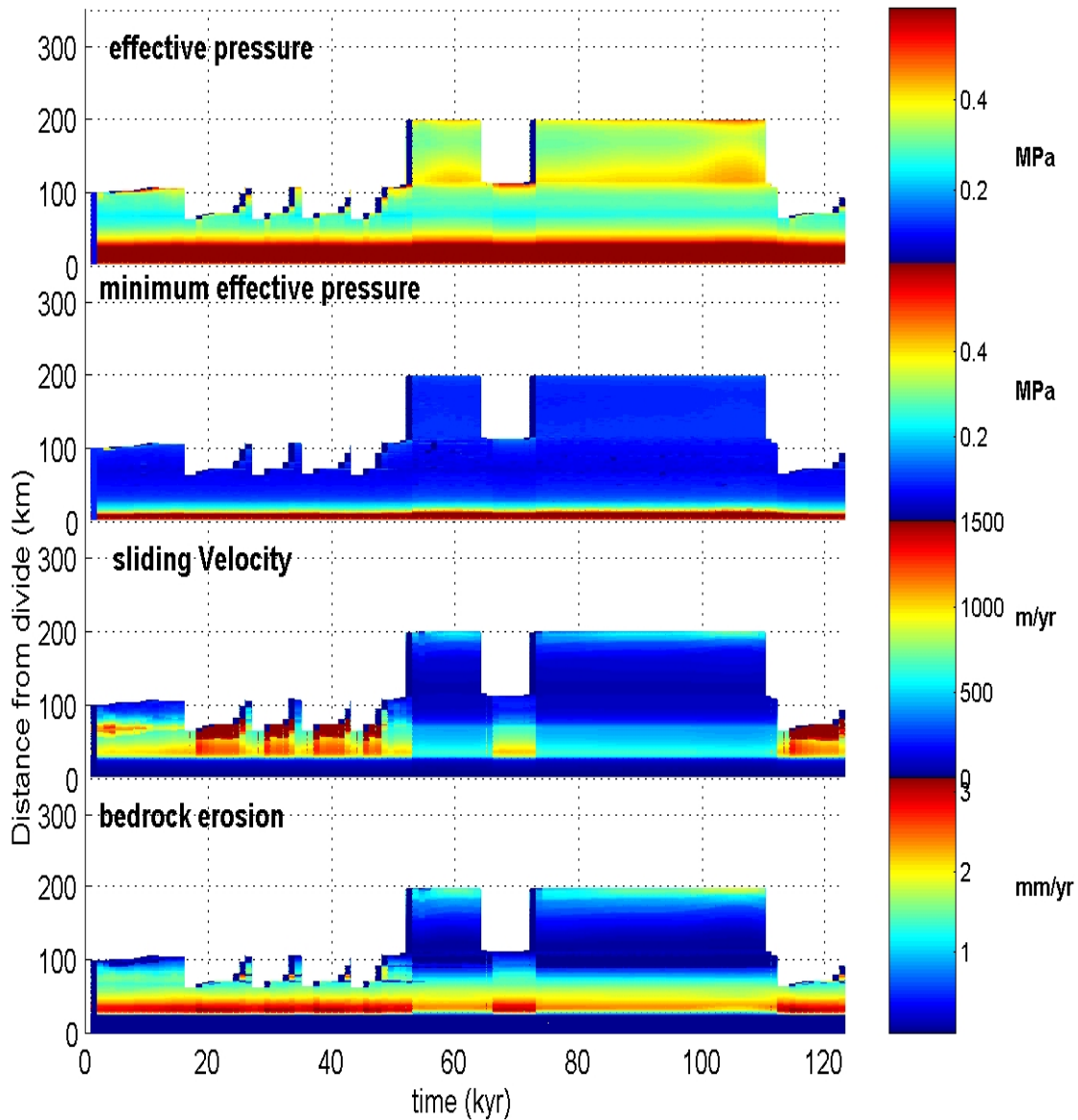
Figure 4.19: Monthly mean effective pressure, sliding speed and potential erosion rate during January for an entire glacial cycle. Potential erosion is fastest in the upper gorge throughout the climatic cycle due to favorable combinations of effective pressure (~ 5bars) and sliding (500-1200 m/yr) whereas low effective pressure and high sliding rate result into lower rates in the lower gorge. Slower erosion potential during the cooler part of the glacial cycle is mainly due to lower rate of sliding. Note, this figure doesn't take into account shielding of the bed by sediment.
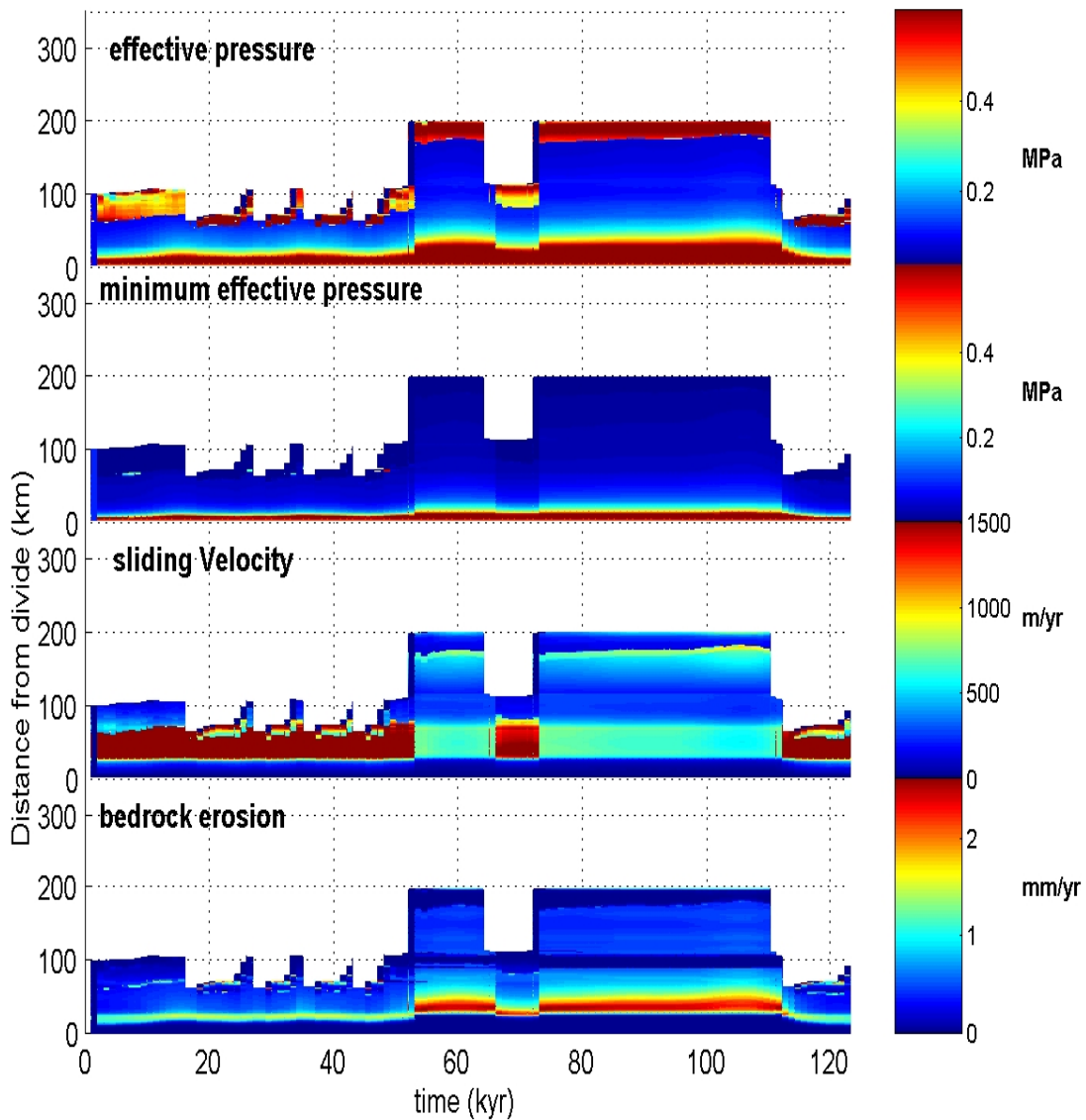
Figure 4.20: Monthly mean effective pressure, sliding speed and potential erosion rate in August during a full glacial cycle. Vanishing effective pressure and very high sliding speed (>1500 m/yr) in the gorge during summer result in little potential erosion relative to the winter season (fig. 4.17). Lower rates of sliding and modest effective pressures during the cooler part of the cycle combine to produce the highest erosion potential in the gorge.

effective pressure decrease quarrying rates both during periods of high and very low water pressures. During interglacial conditions in the lower gorge, high sliding velocity-extremely low effective pressure combinations during the onset of melt and vice versa

after the melt result in lower erosion rates for at least part of the year, whereas in the

upper gorge region, effective pressure is never vanishing and the erosion potential is

greater (Fig. 4.19 and 4.20).

Downstream from the transition between a sub-freezing and melting basal contact
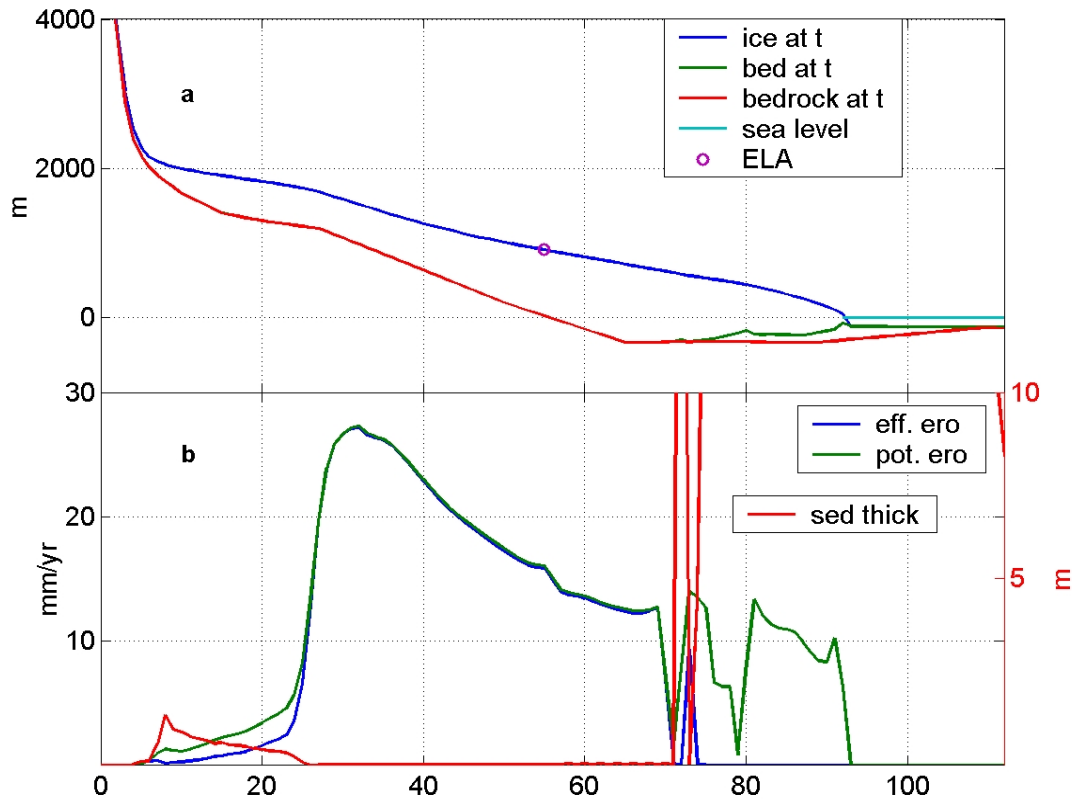
Figure 4.21: Model run of Seward-Malaspina glacier during interglacial conditions after a full climate cycle (panel a). Panel b shows the sediment thickness under and immediately in front of the glacier (right-hand vertical axis), and the distribution of potential and effective bedrock erosion (left-hand vertical axis). Sediment thickness beyond ~75 km is greater than 10 m.

(at 6 km from the divide during interglacial time), potential erosion under upper Seward

glacier is not negligible (1-4 mm/yr); however, subglacial sediment transfer there is

transport limited, which results in a sediment layer sufficiently thick to slow erosion.

Shielding of the substrate by a sediment layer up to 1.5 m thick keeps bedrock erosion to

the fraction of 1 mm/yr (fig 4.21). Similarly, under Malaspina lobe at the end of the 123 kyr climate cycle, a sediment cover greater than 100 m thick extends over much of the overdeepening in the profile, including its distal reverse slope. Consequently, sediment packages prevent bedrock incision processes from 5 km beyond the Seward throat gorge outlet onto Malaspina Glacier (73 km) down to the terminus despite significant potential erosion induced by sliding and effective pressure. Thus, although, bed slope is opposite and of greater absolute magnitude than the chosen threshold surface slope necessary to prevent glaciohydraulic supercooling at least for one node (79 km), modeled sediment accumulation through subglacial fluvial transport alone is sufficient to prevent bedrock incision at that location. Erosion in the gorge is rapid (12-27 mm/yr) but erosion rate averaged over the glacierized area is moderate in the example depicted (2.1 mm/yr) because bedrock incision is mostly confined to Seward Throat, which accounts only for ~6% of the glacial area.

4.4.2 Bedrock erosion during the glacial maximum

From headwaters to the glacier terminus, the mean annual distribution of erosion rates shows two main peaks during full glacial conditions: the largest and most prominent peak at the edge of the continental shelf and a smaller maximum in Seward Throat (fig. 4.22). As in similar cases when the glacier extends much beyond a drastic valley narrow, effective pressure has 2 minima down the glacier profile: one low is located at the gorge outlet and the absolute minimum (1.8 bar) is found slightly upstream from the ELA on the continental shelf (fig. 4.22). Over the extent of the gorge, the yearly mean effective pressure distribution ranges from 2.5 bar to 5.5 bar, which is slightly higher than during

interglacial conditions (by ~ 1 bar), whereas the mean annual sliding speed (615-445

m/yr) is approximately halved relative to interglacial conditions. These conditions of low
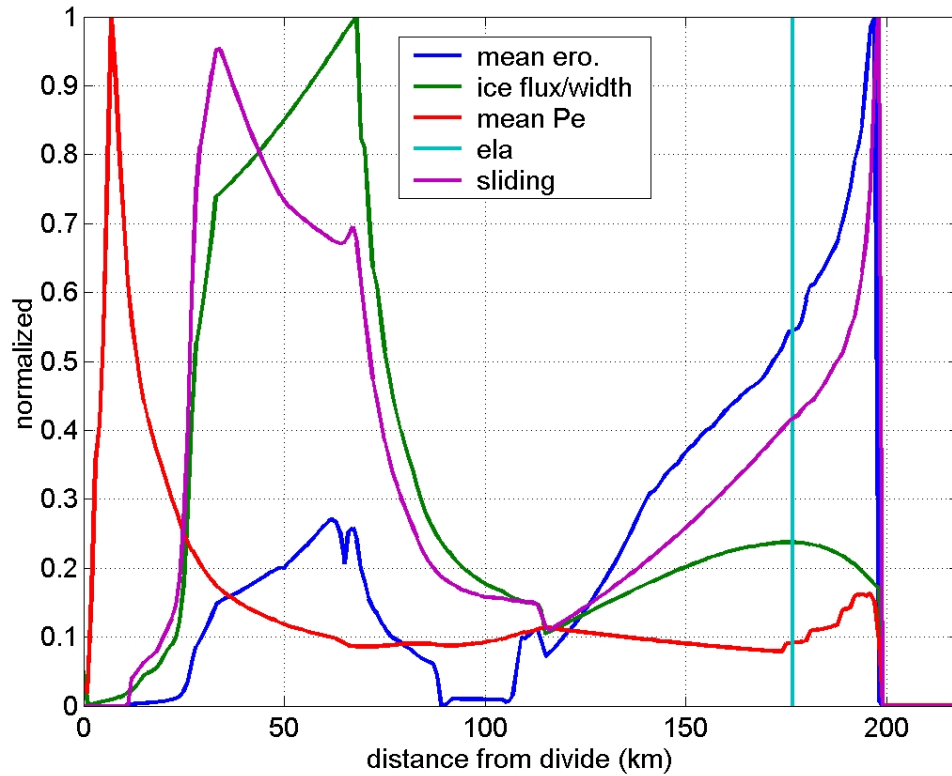
Figure 4.22: The distribution of net mean annual bedrock erosion and other key variables during full glacial conditions for TOPO1.

but not vanishing effective pressures and moderate sliding rates lead to high erosion

potential over much of the domain (fig. 4.23). By opposition to interglacial conditions,

mean effective pressure varies little from month to month within the gorge, which means

that erosion takes place at a similar rate throughout the year. Beyond the gorge outlet

toward the shelf edge, however, monthly effective pressure ranges from 0.5 bar during

the melt season to 2.5-5 bar during colder months, which indicates that most erosion

takes place during winter months. In Seward Throat, the full glacial potential erosion

curve is similar in form but of ~35% greater magnitude and it is displaced downstream

by 6 km relative to the interglacial case (fig. 4.23); thus, the location of the steep
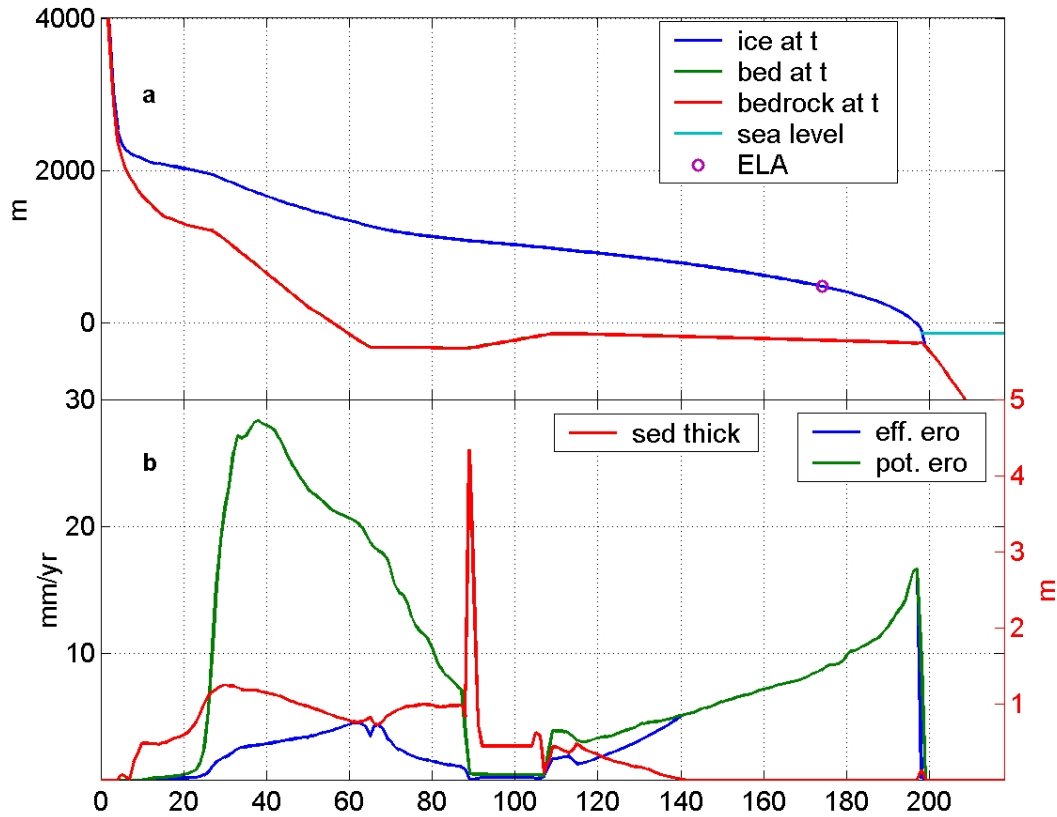
Figure 4.23: Bed and glacier long profiles (a) and (b) the distributions of potential and effective erosion rates, and sediment thickness (respectively the left and right vertical axes of panel b) during full glacial conditions.

rise in potential erosion under upper Seward Glacier is moved down glacier as climate

cools and surface meltwater production decreases with the lowering of the ELA. Surface

meltwater production is an order of magnitude smaller during full glacial conditions over

the extent of the modern glacier. Potential erosion on the continental shelf rises and

reaches a secondary peak at the terminus near the shelf-continent slope break; similarly to

the interglacial case, potential erosion is at a maximum where effective pressure is within

the critical range of 3-5 bars and velocity is near a local maximum. Sediment shielding of

the bed is very significant from the range divide to the modern shoreline (110 km from the divide), which greatly slows bedrock erosion (fig. 4.23). This region includes both the gorge and the distal slope of the overdeepening, which due to its steepness (0.01) relative to the shallow and opposite ice surface slope (0.004-0.005) accumulates significant debris and undergoes little to no erosion. Within Seward Throat, the sediment layer is thickest at the upstream end, due to low subglacial stream power induced by the small meltwater discharge, thereby causing effective erosion to be larger near the downstream outlet. On the continental shelf however, the sedimentary cover progressively thins to vanish almost entirely because of rapidly increasing subglacial water discharge with distance from the divide; thus, little to no shielding of the substrate by sediment occurs starting at 140 km away from the divide to the shelf edge. Sediment protecting the bed under much of the accumulation area leads to greater effective erosion rates on the shelf even though favorable quarrying conditions favor potential erosion in the gorge where it attains a regional maximum that is nearly twice as great as on the shelf. Mean glacierized area (the maximum basin area during full glacial conditions) erosion rate is 4.6 mm/yr, which is more than twice as much as during interglacial conditions. 97% of erosion occurs on the continental shelf that represents 67% of the glacierized area.

4.4.3 Distribution of erosion during a glacial cycle

Although model results indicate that sedimentary cover profoundly affects the magnitude and longitudinal distribution of effective erosion, for ~2/3 of the alpha range modeled, the loci of fastest erosion still depends strongly on the glacier width function, as well as the distribution of sliding and effective pressure (fig. 4.24). While, at very low
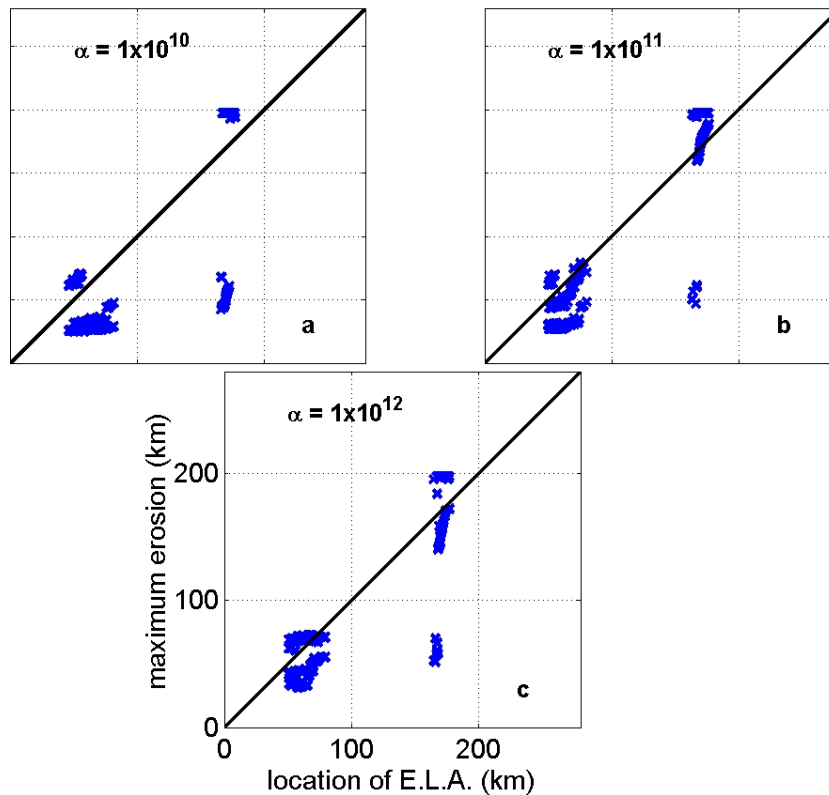
Figure 4.24: Bed regions where erosion is within 10% of the maximum cumulative effective erosion incurred on the profile versus the location of ELA for a range of water pressure parameter (α). Loci of maximum erosion are defined by their proximal and distal boundaries relative to the range divide. Seward Throat is between 33-68 km, the modern coastline is at 110km, and the shelf edge at 200 km.

effective pressure ($\alpha = 1 \times 10^{10}$), erosion rates are highest in Seward Throat, 10's of km upstream from the ELA for much of the glacial cycle, they are highest where relative mean yearly effective pressure is lowest for the rest of the alpha range. The cumulative relative distributions of potential and effective erosion are very similar for the entire α range modeled (fig. 4.25). In all cases, effective erosion over a glacial cycle is fastest in Seward Throat with a maximum at the upper entrance to the gorge for the lower 2/3 of the α range (1×10^{10}-1×10^{11}; figure 4.25, panels a & b) and a maximum near the gorge outlet for $\alpha = 1 \times 10^{12}$ (panel c). In all cases, erosion is significant under Upper

236
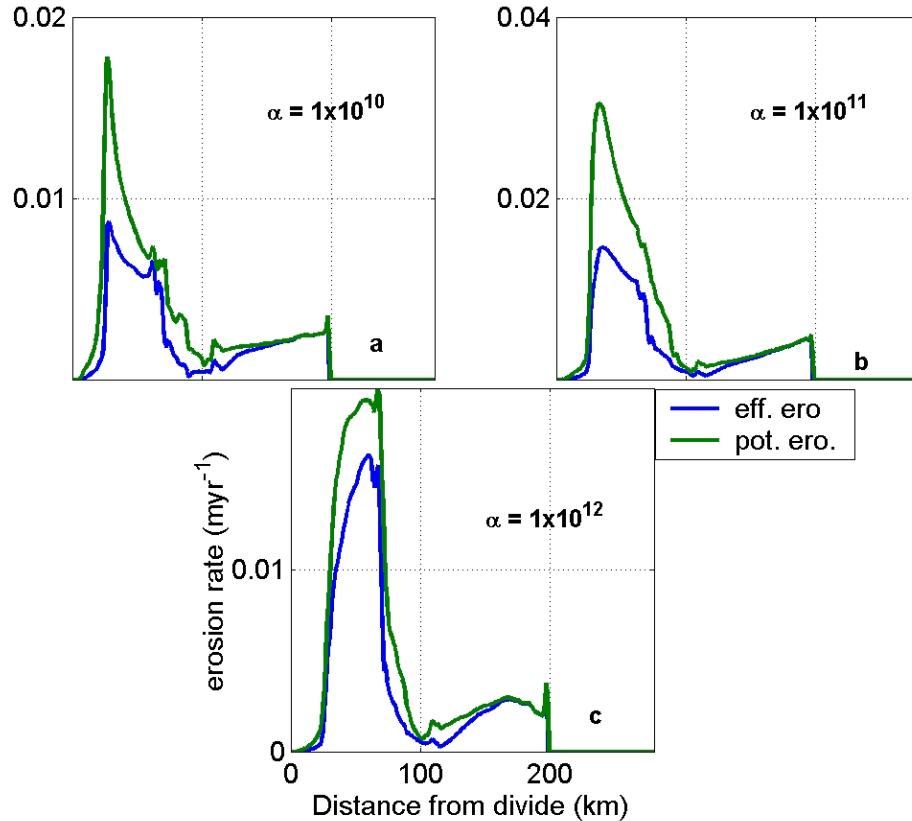
Figure 4.25: Distribution of cumulative effective and potential erosion rate averaged over a 10^5-year glacial cycle for a range of water pressure parameter for TOPO1.

Seward Glacier below the transition between a frozen and melted basal contact (6-8 km from the range divide) although sediment accumulation during cooler periods shields the bed from the thermal transition to the lower reaches of the gorge. Erosion in the region of inferred overdeepening under modern Malaspina lobe is a small fraction (0.05%-0.25%) of what is incurred in Seward Throat, due to sediment accumulation. On the other hand, erosion rates increase across the continental shelf, reaching high values (~30% of maximal values) at the shelf break. Sediments shield the bed throughout the profile at some point during a glacial cycle except for the distal ~50 km before the continental

slope. Although contemporaneous, sediment shielding of bedrock above the gorge outlet and on the continental shelf results from different processes. Whereas on the shelf, sediments deposited when the glacier is in a retracted position have to be remobilized before the substrate becomes available for erosion, upstream of the gorge outlet decreasing subglacial stream power as climate cools leads to sediment accumulation where there was none during warmer climate. The modeled cumulative distribution of erosion is consistent with that inferred from thermochronological data (Enkelmann et al., 2008 and 2009; Berger and Spotila, 2009) insofar a broad peak in erosion is located under Seward Glacier with an absolute maximum at the upstream end of Seward gorge for most of the range in water pressure parameter, α (fig. 4.25). The absolute maximum is displaced toward the lower end of the gorge for $\alpha = 1 \times 10^{12}$ that gives mean basal effective pressures that appear unrealistically high based on sparse data from under a massive temperate glacial system like Seward-Malaspina Glacier (Humphrey et al., 1993; Kamb et al., 1994). The cumulative maximum in erosion occurs 10's of km (20-30 km depending on α) upstream from the modern ELA because of vanishing effective pressure under the annual snowline.

Cumulative erosion for the TOPO2 profile (fig. 4.26) is markedly different from that incurred with the TOPO1 model run shown in figure 4.25, panel b. Even though, the spatial distribution of quarrying and abrasion is almost the same (TOPO1 erosion is 20% less) over the modern extent of Seward-Malaspina Glacier (0-110 km), erosion of the continental shelf is up to 90% less in TOPO2. Erosion of the continental shelf in TOPO2 is reduced due to the smaller glacial occupation time caused by the greater amount of

238

sediment infilling needed for the glacier to be grounded and the additional time required

to remove the thicker sediment infill before bedrock erosion can resume. I stress that
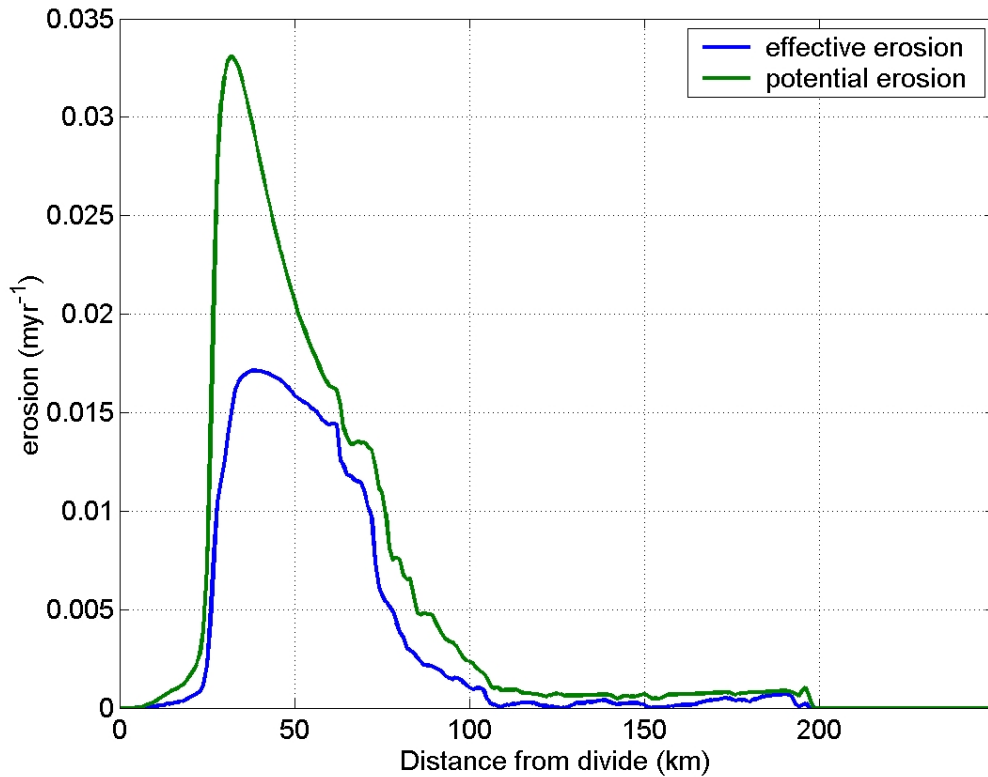
Figure 4.26: Cumulative potential and effective erosion of TOPO2 profile over the course of a climatic cycle for water parameter $\alpha = 1e^{11}$. Sediments shield the bed, nearly halving the potential erosion over the extent of lower Seward Glacier (Seward Throat). Although erosion of TOPO2 is similar to that of TOPO1 over the interglacial domain (from the divide down to 110 km), erosion of the continental shelf is much less for TOPO2 profile.

removal of basal sediments is also the primary cause of several tidewater catastrophic

retreats in this model, which shortens occupation time of the continental shelf and

suggests that the potential to erode deep troughs on the continental shelf is limited. The

modeled erosion of the continental shelf is unexpected in view of the seismic surveys,

which indicate that modest sediment accumulation has occurred over the last ~1 Myr (Berger et al., 2008). It is likely that this part of my modeling effort needs considerable improvement, potentially including an alternate subglacial sediment remobilization scheme less dominated by glacifluvial processes on the continental shelf.

4.5   Sediment yields

As discussed in Chapter 2, sediment delivery at the terminus isn't necessarily a good measure of sediment production by bedrock erosion. Although, on average rock debris has a short subglacial residence time in glacifluvial dominated systems, remobilization of pro-glacial deposits during glacial advance and of subglacial sediment accumulations during cooler periods imply that transport limited conditions dominate at times over part of the glacial domain and that sediment yields do not reveal concurrent sediment production rates. Sediment yields per unit drainage area in unglaciated drainage basins tend to decrease with increasing basin area (Schumm, 1977; Milliman & Meade, 1983; Church et al., 1989; Milliman and Syvitski, 1992), which is largely explained by the decrease in mean basin slope associated with increasing basin area. Lower slope translates into slower average erosion and greater sediment storage in large basins. In contrast, some workers have noted an increase in specific sediment yield with area for some mountain river basins and glacial drainages (Church et al., 1989; Debkov and Moszherin, 1992; Hallet et al., 1996). Although, remobilization of stored sediment is largely responsible for many observations of a positive relationship between drainage area and specific yield, increase in glacierized area can result in greater erosion rates as seen in section 4.4.2 when the basin wide erosion rate during full glacial conditions is twice the interglacial value for the time steps illustrated. Larger, more massive temperate

ice masses are possibly more erosive because negative water pressure transients result into greater deviatoric stresses on bed roughness elements under thicker ice.
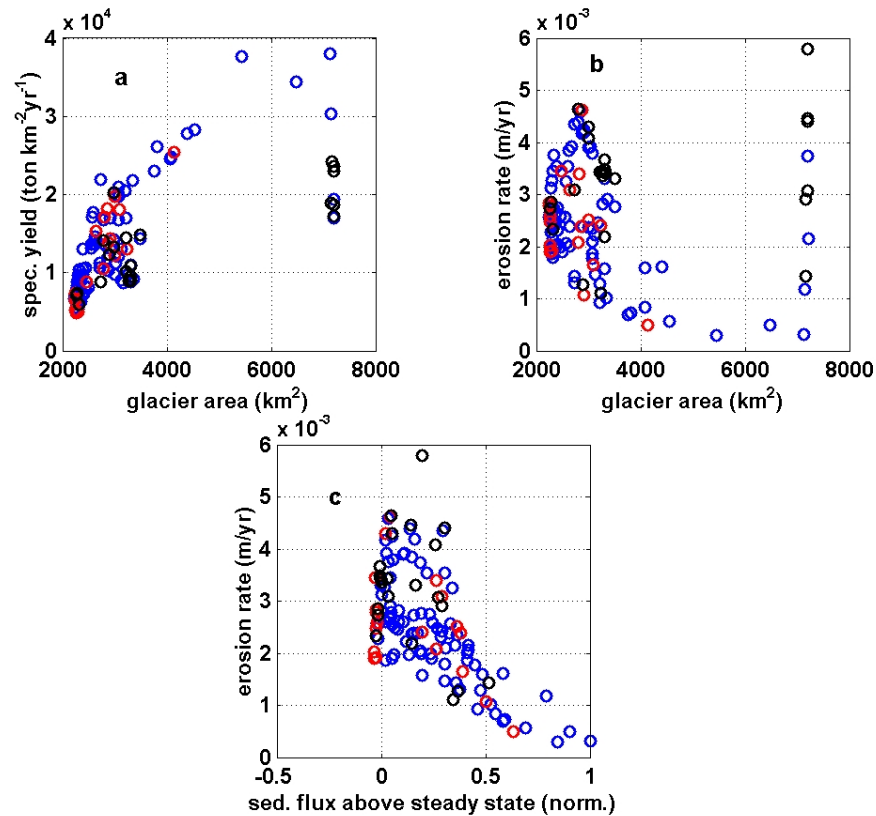
Figure 4.27: (a) Specific sediment yield versus glacier area. Glacier is advancing when blue, at a stand still when black and retreating when red. (b) Mean bedrock erosion rates as a function of glacierized area. (c) Relationship between erosion rates and sediment flux in excess of the flux necessary to evacuate the product of concurrent bedrock erosion illustrates how erosion rates are conditioned by transport-limited conditions at the glacier bed.

The distributions of sediment yields and erosion rates as a function of glacier extent are shown for quarrying and sediment transport parameter values at the low end of the range of modern sediment yields and erosion rates for South Alaskan glaciers (fig. 4.27). Specific sediment yields tend to increase with the extent of the modeled glacier (panel a). Almost all the highest specific yields ($>2 \times 10^4$ ton km^{-2} yr^{-1}) during the 123 kyr

241

glacial cycle occur when the ice is advancing over sediment; yet, specific yield and drainage area are also correlated during the standstill and retreat phases of the glaciation cycle. Mean erosion rates tend to decrease with increasing drainage area (fig. 4.27, panel b) largely because of sediment protecting the bed as the glacier advances over proglacial sediment accumulations, as shown by the negative trend in panel c. Although mean basin erosion appears to decrease with increasing drainage area, some of the highest mean erosion rates occur when the glacier is in an advanced position suggesting that without sediment shielding, basin-wide erosion rates would increase with drainage area. This possibility is confirmed by the positive trend shown between potential erosion (without sediment shielding) and glacier area (fig. 3.40). Interestingly, some of the highest sediment yields in excess of steady state occur when the glacier is retreating and erosion rates are lowest (fig. 4.27, panel c) suggesting that subglacial stores of sediment decrease when ice surface lowers and/or climate warms.

Due to the shielding effect, variations in sediment flux and basin-averaged erosion rate are positively correlated only when the transport capacity of the subglacial hydraulic network is mostly supply-limited (fig. 4.28). For example, during the first advance-retreat sequence to the shelf-break (between 49 and 60 kyr), total sediment yield reaches a maximum as the glacier over-rides sediment previously deposited on the continental shelf. Meanwhile, the bedrock-derived sediment yield (the flux of debris concurrently eroded off the bed) initially decreases for the first 5000 years of this sequence. The bedrock-derived yield eventually starts increasing (at 55 kyr) when transport-limited conditions become more prevalent at the glacier sole. The total sediment yield begins to decline as availability of debris decreases (55 kyr), and rises again because concurrent

bedrock erosion reaches a maximum when average shielding of the bed decreases. Interestingly, bedrock erosion slows at the beginning of the advance sequence because sediment accumulates under the interglacial extent of the glacier (erosion within Seward Throat decreases by ~1 order of magnitude). Both a more positive
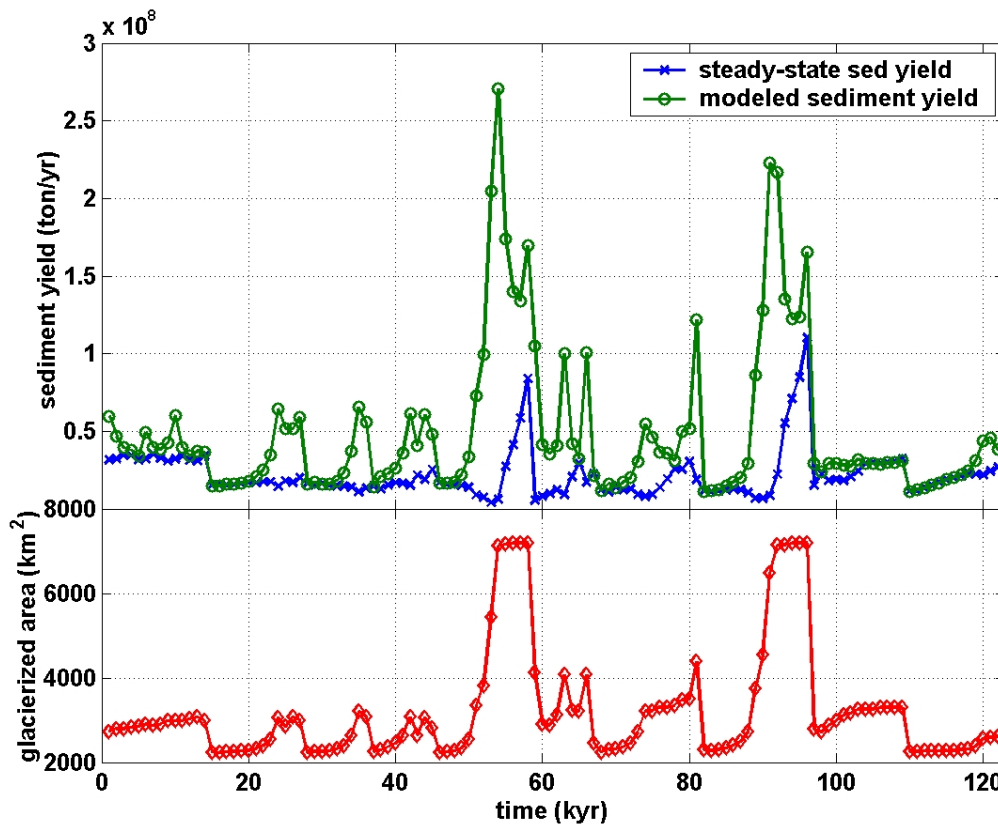
Figure 4.28: Total and bedrock-derived sediment yields over the course of a climate cycle (upper panel) and glacier extent (lower panel). The bedrock-derived or steady state yield is that which correspond to concurrent bedrock erosion. Total yield increases rapidly as the ice overrides proglacial sediment.

net mass balance when climate cools and the height-mass balance feedback when the glacier extends beyond the mountain front combine to raise ice surface elevation, diminish surface melt and lowers the transport capacity of the subglacial fluvial network. The glacier surface rises 200-600 m respectively at the top and bottom of Seward Throat from 50 to 54 kyr, which induces a thickening of the bottom sediment layer that is stored

until the retreat phase of the fluctuation sequence. This sequence, and as seen in panel c of figure 4.27, also illustrate that specific sediment yields increase during the retreat phase of the tidewater glacier cycle even though erosion rates may decrease.

4.6 Discussion, conclusions and caveats

The extent and timing of glaciation on the South Alaskan continental shelf during climatic cooling are significant, unresolved questions because they control the spatio-temporal distribution of sediment accumulation and the loading of the earth crust by ice, sediments and water. The history of this loading impacts the interpretation of geodetic measurements (Elliott et al., 2010), and bears on studies of the neotectonics and geodynamics of the region (Chapman et al., 2007), as well as on research of local to global sea level (Shennan, 2011). As already noted, the large glacial troughs indicate that tidewater glacial systems reach the edge of the shelf for at least part of a 123 kyr glacial cycle. Sediments deposited within the troughs while glaciers are in a retracted position are therefore likely to be at least partially transferred to the shelf edge and onto the continental slope during glacial advances. Implementing tidewater processes with sediments in the numerical model had a profound impact on the ability of Seward-Malaspina Glacier to advance toward the shelf-slope break. Without sediments, the glacier never reached the edge of the shelf, whereas a comparable land-based glacier would have done so by 60 kyr into a glacial cycle. In the absence of deep sea valleys (TOPO1 topographic model), water depths on the shelf are moderate everywhere, particularly during low eustatic sea level stands; yet, large calving losses along the wide ice front prevented the glacier from coming any closer than 40 km from the shelf-slope break. While the Gulf of Alaska is the source of the copious amount of moisture that

sustains some of the largest temperate ice masses on the planet, it is also a giant ice sink, as well as a repository for massive volumes of ice rafted and other glacigenic debris that has accumulated for 5 Myr (Krissek, 1995).

Modeling the fluctuations of tidewater glacier advance into the Gulf of Alaska merits further attention for a number of reasons. Brown's calving rate constant, which is used in the model, was determined through observing Alaskan tidewater glaciers that had already retreated in fjords by the 1980's. It is unlikely that this value (27 yr^{-1}) adequately accounts for open marine ice loss processes on the Alaskan continental shelf, where without the protection of an ice shelf, the glacier terminus is fully exposed to storm surges and constant ice erosion by waves. Moreover, the isostatic response to changes in loads (ice, sediment, water) has not been included in the model to compute relative sea level. Preliminary results, not presented herein, indicate that it could significantly contribute to local water depth and instability of calving glacier fronts.

Sediment transfer to the glacier margin and proglacial submarine deposition decrease water depth at the terminus, thus enabling faster glacier progression into tidewater. Model results also indicate that the response time of the glacier to climatic forcing, and the amplitude and frequency of glacial fluctuations depend sensitively on sediment production and delivery to the ice front. Sediment yields are rate limiting for glacier variations insofar as the changes in the elevation of the basal interface (due to a divergence in subglacial sediment transport) occur 1-2 order of magnitude faster than changes in ELA elevation, and several more orders of magnitude faster than changes in eustatic sea level. Glacier mass balance is thus more sensitive to changes in basin hypsometry caused by sediment entrainment than to climatic variations. These results are

consistent with a numerical model of Columbia Glacier (Southern coast of Alaska) by Nick and others (2007) who found that the rate of tidewater glacier advance in deep water increases with sediment yields and erosion rates.

Evacuation of massive volumes of sediments from under the ice gives rise to prominent non-climatic glacier retreats when sediment input from upglacier is insufficient to sustain both subglacial accumulations of sediment and a terminal shoal large enough to significantly reduce water depth at the ice front; the glacier then becomes entrenched in the substrate and recedes. This sequence of events could cause glacier retreat during a period of continuous cooling or climatic stasis, which to my knowledge, has been documented only once in the literature at Taku Glacier (Motyka and Beget, 1996). The important consequences of the tidewater glacier cycle for levels of glacierization, cumulative erosional footprint and sediment transfer imply that further study of sediment entrainment by glaciers be conducted with a time dependent model of glaciation. Remobilization of large subglacial sediment stores occur on a shorter time scale (10^2 yr) than the time step chosen for this steady state glacier model (10^3 yr); it is therefore not clear whether the mass balance of tidewater glaciers can adapt to lowering of basin hypsometry in the ablation area without triggering catastrophic retreat.

Ice occupies the continental shelf for a significantly shorter portion of a glacial cycle when the modeled shelf topography includes glacial troughs than when they are absent because greater water depth induces greater calving loss and demands higher sediment yields to stabilize the terminus. This shorter occupation time implies that less cumulative erosion occurs on the continental shelf but also that a smaller volume of sediment is evacuated from the shelf, and sediments remain on the shelf for a longer

period of time. The underlying bedrock is thus protected from erosion for a longer portion of a glacial cycle as seen in the output for the TOPO2 model runs. This scenario is consistent with the post mid-Pleistocene sediment accumulation inferred at Bering trough (Gullick et al., 2008) as well as shelf-wide (Berger et al., 2008). Implementing proglacial sedimentation and subglacial sediment storage evolution delivers much valuable insight into glacier variations in the glacimarine environment of South Alaska, which underlie the topographic evolution of the massive continental shelf (~5 km thick, 100 km wide, and hundreds of kms in E-W extent) and the redistribution of marine sediment toward extensive fans covering much of the North eastern Pacific.

Like in Chapter 3, the spatial distribution of erosion rates for a glacier of highly variable width such as Seward-Malaspina Glacier depends on the longitudinal variation of ice flux per unit width determined by topographic constraints and mass balance, as well as on basal conditions that control potential erosion rates (effective pressure and sliding velocity). Potential erosion at Seward-Malaspina is consequently always very large within the narrows of Seward throat, especially at its upper end where conditions of effective pressure and sliding are both optimal for rapid erosion for much of the hydrological year. As discussed above, erosion of the continental shelf first depends strongly on terminus stability in tidewater and on whether the glacier can advance in deep water. Shielding of bedrock by sediment drastically slows erosion. Although more effective erosion (accounting for sediment shielding) still occurs at the upper entrance of the Seward throat, it is more uniform throughout the gorge than is suggested solely by erosional potential. The sediment transport capacity of the subglacial network decreases relatively more at higher elevation when climate cools, ice surface elevation swells, and

surface melt plummets, which leads to relatively fast sediment accumulation and a large reduction in erosion rates for that part of the glacial domain. Flushing of this sediment during the following retreat phase of the tidewater cycle and a deflating ice surface provides an alternative hypothesis to increasing erosion rates (Koppes and Hallet, 2006) to explain the large modern specific yields during glacial retreat following the LIA in South Alaska.

The modeled distribution of glacial erosion at Seward-Malaspina Glacier reproduces relatively well the pattern of exhumation derived from thermochronology, in particular the maximum in exhumation rate near the Chugach-St. Elias fault at the upstream end of Seward Throat. This maximum occurs significantly upstream (~30km) from both the modern ELA and the maximum in ice flux per unit width. The spatial variation of erosion along the Seward-Malaspina glacier long profile over a full glacial cycle is therefore significantly more complex than suggested by simple association with ice flux per unit width and the current and past location of the ELA since basal decoupling between ice and the bedrock substrate, as conditioned by water pressure and sediment, impacts the spatial distribution of bedrock erosion rates.

Chapter 5   Summary of findings

This dissertation investigates the spatial and temporal distribution of the rate of glacial erosion as a function of climate in an active compressive orogen. It addresses quantitatively the controls on the distribution of glacial erosion rates by temperate ice masses at convergent margins, with guidance from the large South Alaskan glacial systems found at the syntaxis between the North American and Pacific tectonic plates. Modeling these systems yielded new insights into the role of climate in shaping the Seward-Malaspina sector of the St. Elias range, as well as temperate coastal glacial regions in general. Climate influences glacial erosion in diverse ways in addition to glacier mass balance; they include meltwater generation, sediment production and transfer, and sea level. After a brief overview of the results in Chapter 2 of a field study defining erosion rates for Bering Glacier, the largest glacier in this orogen, I summarize findings from my numerical model that are broadly applicable to generic cases, and then those that pertain to the large modern piedmont glaciers of the South Alaska coast, in particular the Seward-Malaspina glacier.

In Chapter 2, a survey of the volume of sediments accumulated in a lake in front of Bering Glacier, enabled estimating the basin-wide glacial erosion rate of nearly 6 mm/yr averaged over a 30-year period that includes a massive surge. This rate is consistent with Holocene rates of South Alaskan erosion for other glacial systems, as well as with estimates of the range-wide rate from Holocene sediment accumulation on the continental shelf.

In chapter 3, a new numerical model is developed and shown to be a useful tool for studying the spatial and temporal distribution of glacial erosion rates. Model results show how rates of erosion by glaciers of variable width vary longitudinally and tend to be high in regions of high ice flux per unit width, of low basal effective pressure in topographic narrows, in steep valleys, and/or in the ablation area. Under a broad range parameterizations of the subglacial hydraulic regime, the mean annual erosion rate peaks near the seasonal snowline where percolating surface melt water overwhelms the carrying capacity of the distributed subglacial network thereby causing low effective pressure at the basal interface. In some instances, however, glacial erosion rates vanish as the ice disconnects from the bed due to basal water pressure approaching ice pressure. Consequently, the fastest erosion does not necessarily correlate with the fastest sliding along a glacier. Peaks in potential erosion rates (rates in the absence of sediments) that are associated with narrow sections of the basin due to lateral topographic constraints are characterized both by 1) rapid sliding that accommodate the large ice flux per unit width and 2) increased water pressure caused by water flux convergence in bottom conduits and/or the feedback on erosion rates due to the increase in ice pressure in overdeepened regions. For the latter, the increase in ice thickness associated with lowering of the bed in an erosional hotspot decreases the transport capacity of the subglacial hydraulic network, boosts water pressure and increases erosion rates. The low effective pressure and rapid sliding necessary for efficient quarrying were found in steep upper regions of the accumulation area covered with thin ice. More generally, complex longitudinal variations in glacial erosion rates are to be expected even for idealized glaciers of uniform width with maximal values in regions of steep topography and near the ELA. These controls on

the erosion potential by glaciers indicate that, in addition to sliding speed, accounting for the degree of decoupling between ice and the bed should be an important component of any model of the distribution of erosion rates under temperate glaciers.

In chapter 4, the glacier mass balance and basin geometry are guided by those of Seward-Malaspina Glacier, and two additional elements are added to the model developed in the previous chapter to represent the dynamics of the glacier terminus in the tidewater environment and subglacial sediment transport. These are important because sediment accumulation both shields the bedrock from erosion and affects the extent of the glacier and domain subject to glacial erosion. Glacier mass balance and terminus stability in tidewater were shown to be especially sensitive to changing basin hypsometry caused by rapid removal of subglacial sediments during glacier advances. Greater terminus instability in tidewater translates into fast and sustained terminus retreat, even during relatively cool climates. Decreased occupation time of the continental shelf by ice leads to less erosion of the lower reaches of the glacier basin (the continental shelf) than for a comparable land-based ice mass. Rates of sediment removal and accumulation are shown to have much greater control on local relative sea level than eustatic sea level change and isostatic compensation to load changes.

Shielding of bedrock by a sediment layer is especially effective in the upper reaches of the glacier when climate cools and less surface melt percolates to the basal interface thereby decreasing the sediment transport capacity of the subglacial fluvial network. Sediment shielding also tends to be important in overdeepened regions of the bed where thick sediment accumulations form because of decreasing stream power on the reverse slope of overdeepenings. Overdeepened regions are thus shown to be self-sustaining

without necessitating the explicit implementation of glaciohydraulic supercooling processes.

Topographic constraints, tidewater control of glacier extent and sediment shielding of the bed at Seward-Malaspina overwhelm climatically forced variables like effective pressure in determining the pattern of exhumation insofar maximum erosion always occurs where ice funnels through a narrow passage through a transverse range, the Seward Throat, irrespective of climatic forcing; yet, the maximum in erosion at the upstream end of the gorge is ultimately determined by the locus of low but not vanishing effective pressure.

This numerical study highlights the importance of two processes that are generally absent from large-scale models of glacial erosion. First is the flow of water below the glacier that controls not only the sliding speed, but also quarrying rates and evacuation of sediments. Second is the transport of sediments that controls the accumulation of subglacial debris that can shield the bedrock from erosion for extensive periods. Moreover, for tidewater glaciers, proglacial sediment accumulation plays a central role in modulating the glacial extent. Future research on the interplay of climate, tectonics and topography must recognize that climate influences glacial erosion in diverse ways in addition to glacier mass balance (meltwater generation, sediment transfer, and sea level).

In addition, this study provides a first quantitative examination at how large temperate coastal glaciers interact with convergent tectonics to shape the quasi-steady state distribution of rock uplift from range divide to shelf edge. In particular, modeling mass transfers of water, ice and sediment and their timing relative to glacial-interglacial climate fluctuations provided insight into the processes and feedback controlling the form

of topographic long profile and the architecture of the accretionary wedge at the South Alaska margin. Moreover, such a numerical tool should prove useful in interpreting the growing thermochronological record of exhumation within the range, the sedimentary record in the Northeast Pacific and the climatic signature contained in the spatial and temporal distribution of sediment depocenters.

References

Ager, T., 2007, Vegetation response to climate change in Alaska: Examples from the fossil record: U.S. Geological Survey Open-File Report 2007-1096, 44 p.

Ahnert, F., 1970, Functional relationships between denudation, relief, and uplift in large mid latitude drainage basins: American Journal of Science, v. 268, p. 243–263.

Alley, R., 1991, Deforming-bed origin for southern Laurentide till sheets?: Journal of Glaciology, v. 37, no. 125, p. 67-76.

Alley, R. B., 1991, Sedimentary processes may cause fluctuations of tidewater glaciers: Annals of Glaciology, v. 15, p. 119-124.

Alley, R.B., Meese, D.A., Shuman, C.A., Gow, A.J., Taylor, K.C., Grootes, P.M., White, J.W.C., Ram, M., Waddington, E.D., Mayewski, P.A., and G.A. Zielinski, 1993, Abrupt increase in Greenland snow accumulation at the end of the Younger Dryas event, Nature, v. 362, p. 527 – 529.

Alley, R.B., 1997, Water, sediment and tidewater glaciers: Simplistic review and weakly constrained speculations, *in* Van der Veen, C.J., ed., Calving Glaciers: Byrd Polar Research Center Report no. 15, p. 51-55.

Alley, R.B., Cuffey, K.M., Evenson, E.B., Strasser, J.C., Lawson, D.E., and Larson, G.J., 1997, How glaciers entrain and transport basal sediment: Physical constraints: Quaternary Science Reviews, v. 16, no. 9, p. 1017-1038.

Alley, R.B., Lawson, D.E., Evenson, E.B., Strasser, J.C., and Larson, G.J., 1998, Glaciohydraulic supercooling: A freeze-on mechanism to create stratified, debris-rich basal ice: II. Theory: Journal of Glaciology, v. 44, no. 148, p. 563-569.

Alley, R.B., Lawson, D.E., Evenson, E.B., and Larson, G.J., 2003, Sediment, glaciohydraulic supercooling, and fast glacier flow: Annals of Glaciology, v. 36, p. 135–141.

Alley, R.B., Dupont, T.K., Parizek, B.R., and Anandakrishnan, S., 2005, Access of surface meltwater to beds of sub-freezing glaciers: Preliminary insights: Annals of Glaciology, v. 40, p. 8-14.

Anders, A.M., Roe, G.H., Hallet, B., Montgomery, D.R., Finnegan, N.J., and Putkonen, J., 2006, Spatial patterns of precipitation and topography in the Himalaya, in Willett, S.D., et al., eds., Tectonics, climate and landscape evolution: Geological Society of America Special Paper 398, p. 39–53.

Anders, A.M., Mitchell, S.G., and Tomkin, J.H., 2010, Cirques, peaks, and precipitation patterns in the Swiss Alps: Connections among climate, glacial erosion, and topography: Geology,
v. 38, p. 239-242.

Anderson, J.B., and Molnia, B., 1989, Glacial-marine sedimentation, *in* Crawford, M.L., and Padovani, E., eds., Short Course in Geology: Volume 9: Washington, D.C., American Geophysical Union.

Anderson, R.S., Hallet, B, Walder, J., and B.F. Aubry, 1982, Observations in a cavity beneath the Grinnell Glacier, Montana: Earth Surface Processes and Landforms, v. 7, p.63-70.

Anderson, R.S., 1994, Evolution of the Santa Cruz Mountains, California through tectonic growth and geomorphic decay: Journal of Geophysical Research, v. 99, no. B10, p. 20,161-20,179.

Anderson, R.S., Anderson, S.P., MacGregor, K.R., Waddington, E.D., O'Neel, S., Riihimaki, C.A., and Loso, M.G., 2004, Strong feedbacks between hydrology and sliding of a small alpine glacier: Journal of Geophysical Research, v. 109, F03005, p. 1-17.

Anderson, R.S., Molnar, P., and M.A. Kessler, 2006, Features of glacial valley profiles simply explained, Journal of Geophysical Research: Earth Surface, v. 111, F01004, doi:10.1029/2005JF000344.

Atkinson, B.K., 1984, Subcritical crack growth in geological materials, Journal of geophysical research, v. 89, p. 4077-4114.

Atkinson, B.K., 1987, Fracture mechanics of rock, Academic press, Orlando.

Bagnold, R.A., 1966, An approach to the sediment transport problem from general physics: Geological Survey Professional Paper 442-I, p. 1-37.

Balise, M.J., and Raymond, C.F., 1985, Transfer of basal sliding variations to the surface of a linearly viscous glacier: Journal of Glaciology, v. 31, no. 109, p. 333-344.

Bamosky, C.W., Anderson, P.M., and Bartlein, P.J., 1987, The northwestern U.S. during deglaciation: Vegetational history and paleoclimatic implications, *in* Ruddiman, W.F., and Wright, H.E., eds., North America and Adjacent Oceans During the Last Deglaciation: Boulder, Colorado, Geological Society of America, Geology of North America, v. K-3, p. 289-321.

Barclay, D.J., Gloss, J., Calkin, P., and Wiles, G., 1997, Late Holocene advance and retreat of tidewater glaciers in Yakutat Bay and Icy Bay, Gulf of Alaska, *in* Van

der Veen, C.J., ed., Proceedings of a Workshop on Tidewater Glaciers, February 28-March 2, 1997: Byrd Polar Research Center Publication No. 15, p. 61-66.

Barclay, D.J., Barclay, J.L., Calkin, P.E., and Wiles, G.C., 2006, A revised and extended Holocene glacial history of Icy Bay, Southern Alaska, U.S.A.: Arctic, Antarctic, and Alpine Research, v. 38, no. 2, p. 153–162.

Barclay, D.J., Wiles G.C. and Calkin, P, 2009, Holocene glacier fluctuations in Alaska: Quaternary Science Review, v. 28, p. 2034-2048.

Bayer, K.C., Mattick, R.E., Plafker,G., and Bruns,T.R., 1978, Refraction studies between Icy Bay and Kayak Island, eastern Gulf of Alaska: U.S. Geological Survey Journal of Research, v.6, p.625-636.

Beaumont, C., Fullsack, P., and Hamilton, J., 1991, Erosional control of active compressional orogens, *in* McClay, K.R., ed., Thrust Tectonics: London, Chapman and Hall, p. 1-18.

Berger, A.L., Spotila, J.A., Chapman, J.B., Pavlis, T.L., Enkelmann, E., Ruppert, N.A., and J.T. Buscher, 2008a: Architecture, kinematics, and exhumation of a convergent orogenic wedge: A thermochronological investigation of tectonic-climatic interactions within the central St. Elias orogen, Alaska, Earth and Planetary Science Letters, v. 270, p. 13-24.

Berger, A.L., Gulick, S.P., Spotila, J., Upton, P, Jaeger, J., Chapman, J.B., Worthington, L.A., Pavlis, T.L., Ridgway, K.D., Willems, B.A., and McAleer, R.J. 2008b, Quaternary tectonic response to intensified glacial erosion in an orogenic wedge: Nature Geoscience v. 1, p.793-802.

Berger, A.L., and Spotila, J. A. 2008, Denudation and deformation in a glaciated orogenic wedge: The St. Elias orogen, Alaska: Geology, v. 36, p. 523-526.

Bezinge, A., Clark, M., Gurnell, A.M., and Warburton, L., 1989, The management of sediment transported by glacial melt-water streams and it significance for the estimation of sediment yield: Annals of Glaciology, v. 13, p. 1-5.

Bindschadler, R., 1983, The importance of pressurized subglacial water in separation and sliding at the glacier bed: Journal of Glaciology, v. 29, p. 3–19.

Biswas, N.N., Aki, K., Pulpan, H. and Tytgat, G., 1986, Characteristics of regional stresses in Alaska and neighboring areas, Geophysical Research Letters, v. 13, p. 177-180.

Bjornsson, H., 1996, Scales and rates of glacial sediment removal: A 20 km long x 300 m deep trench created beneath Breidamerkurjokull during the Little Ice Age: Annals of Glaciology, v. 22, p. 141-146.

Blake, E.W., Fischer, U.H, and Clarke, G.K.C., 1994, Direct measurement of sliding at the glacier bed: Journal of Glaciology, v.40, no. 136, p.595-599

Blum J. D., 1997, The effect of late Cenozoic glaciation and tectonic uplift on silicate weathering rates and the marine 87Sr/86Sr record, *in* Ruddiman, W.F., ed., Tectonic Uplift and Climate Change: New York, Plenum, p. 259–288.

Booth, D.B., 1994, Glaciofluvial infilling and scour of the Puget lowland, Washington, during ice-sheet glaciation: Geology, v. 22, no.8, p. 695-698.

Boulton, G.S., 1974, Processes and pattern of glacial erosion, *in* D.R.Coates (ed.) Glacial Geomorphology, Binghampton, New York, pp. 41-87.

Boulton, G. S., Armstrong, A. A., Morris, E. M., and A. Thomas, 1979, Direct measurement of stress at the base of a glacier, Journal of Glaciology, v. 22, p. 3-24.

Boulton, G.S., 1979, Processes of glacier erosion on different substrata, Journal of Glaciology, v. 23, p. 15-37.

Braithwaite, R.J. 1985. Calculation of degree-days for glacier-climate research, Zeitschrift fue Gletscherkunde und Glazialgeologie, v. 20, p. 1-8.

Braithwaite, R.J., 1995, Positive degree-day factors for ablation on the Greenland ice sheet studied by energy-balance modeling: Journal of Glaciology, v. 41, p. 153–160.

Briner, J.P., and Swanson, T.W., 1998, Using inherited cosmogenic 36Cl to constrain glacial erosion rates of the Cordilleran ice sheet, Geology, v. 26, p. 3-6.

Brocher, T.M., Fuis, G.S., Fisher, M.A., Plafker, G., Moses, M.J., Taber, J., and N.I. Christensen, 1994, Mapping the megathrust beneath the northern Gulf of Alaska using wide-angle seismic data, Journal of Geophysical Research, v. 99, p. 11663-11685.

Brocklehurst, S. H., and K. X. Whipple, 2002, Glacial Erosion and Relief Production in the Eastern Sierra Nevada, California, Geomorphology, v. 42, no. 1. p. 1-24.

Brocklehurst, S. H., and K. X. Whipple, 2004, Hypsometry of glaciated landscapes, Earth

Surface Processes Landforms, v. 29, no. 7, p. 907–926.

Broecker, W.S., Turekian, K.K., and Heezen, B.C., 1958, The relation of deep sea sedimentation rates to variations in climate: American Journal of Science, v. 256, p. 503-517.

257

Brown, C.S., Meier, M.F., and Post, A., 1982, Calving speed of Alaska tidewater glaciers, with application to Columbia Glacier. U.S. Geological Society Professional Paper 1258-C, C1-C13 p.

Brozovic, N., Burbank, W.B., and Meigs, A.J., 1997, Climatic limits on landscape development in the Northwestern Himalaya: Science, v. 276, p. 571-574.

Bruhn, R.L., Pavlis, T.L., Plafker, G., and Serpa, L., 2004, Deformation during terrane accretion in the Saint Elias orogen, Alaska: Geological Society of America Bulletin, v. 116, p. 771-787.

Bruhn, R.L., Forster, R.R., Ford, A.L.J., Pavlis, T.L., and Vorkink, M., 2009, Structural geology and glacier dynamics, Bering and Steller Glaciers, Alaska, *in* Shuchman, R.A., and Josberger, E.G., eds., Bering Glacier: Interdisciplinary Studies of Earth's Largest Temperate Surging Glacier: GSA Special Paper 462, p. 217-233

Bruns, T.R., and Schwab, W.C., 1983, Structure maps and seismic stratigraphy of the Yakataga segment of the continental margin, northern Gulf of Alaska: U.S. Geological Survey Miscellaneous Field Studies Map MF-1424, 20 p.,4 sheets, scale 1:250,000.

Budd, W.F., Keague, P.L., and N.A. Blundy, 1979, Empirical studies of ice sliding, Journal of Glaciology, v. 23, p. 157-170.

Burgess, E., 2013, Ice flow dynamics of Alaska glaciers, PhD dissertation, Department of Geography, The University of Utah. p. 144

Calkin, P.E., 1988, Holocene glaciation of Alaska (and adjoining Yukon Territory, Canada): Quaternary Science Reviews, v. 7, p. 159-181.

Calkin, P.E., Wiles, G.C., and Barclay, D.J., 2001, Holocene coastal glaciation of Alaska: Quaternary Science Reviews, v. 20, p. 449-461.

Carlson, P.R., Molnia, B.F., Kittelson, S.C., and Hampson, J.C., Jr., 1977, Distribution of bottom sediments on the continental shelf, northern Gulf of Alaska: U. S. Geological Survey Miscellaneous Field Studies Map, MF- 876, 2 sheets, 13 p.

Carlson, P.R,. Bruns, T.R., Molnia, B.F. and S.C. Schwab, 1982, Submarine valleys in the northeastern Gulf of Alaska: Characteristics and probable origin, Marine Geology, v. 47, p. 217-242.

Chamberlin, T.C., 1899, An attempt to frame a working hypothesis of the cause of glacial periods on an atmospheric basis: Journal of Geology, v. 7, p. 545-584, 667-685, 751-787.

Chapman, J.B., Haeussler, P.J., and T.L. Pavlis, 2007, Quaternary history of Wingham Island, South-Central Alaska, United States Geological Survey, Professional Paper 1760-B, p. 1-19.

Chappell, J., and Shackleton, N.J., 1986, Oxygen isotopes and sea level: Nature, v. 324, p. 137–140.

Chapple, W.M. 1978. Mechanics of a thin-skinned fold and thrust belt. Geological Society of America Bulletin, v. 89, p. 1189–1198.

Chernova, L.P., 1981, Influence of mass balance and run-off on relief-forming activity of mountain glaciers: Annals of Glaciology, v. 2, p. 69-70.

Church, M., and Ryder, J.M., 1972, Paraglacial sedimentation: A consideration of fluvial processes conditioned by glaciation: Geological Society of America Bulletin, v. 83 no. 10, p. 3059-3072.

Church, M., and Slaymaker, O., 1989, Holocene disequilibrium of sediment yield in British Columbia: Nature, v. 327, p. 452–454.

Church, M., Kellerhals, R. and Day, T. J., 1989, Regional clastic sediment yield in British Columbia: Canadian Journal of Earth Science, v. 26, p. 31-45.

Climap Project Members, 1981, Seasonal reconstructions of the earth's surface at the last glacial maximum: Geological Society of America Map and Chart Series MC-36, scale 1:50,000,000, 9 sheets.

Cohen, D., Hooke, R.LeB., Iverson, N.R., and Kolher, J., 2000, Sliding of ice past an obstacle at Engabreen, Norway: Journal of Glaciology, v. 46, no. 155, p. 599-610.

Cohen, D., Hooyer, T. S., Iverson N. R., Thomason, J. F., and Jackson, M., 2006, Role of transient water pressure in quarrying: A subglacial experiment using acoustic emissions: Journal of Geophysical Research, v. 111, p. 3006-3019.

Collins, D.N., 1989, Seasonal development of subglacial drainage and suspended sediment delivery to meltwaters beneath an alpine glacier: Annals of Glaciology, v. 13, p. 45-50.

Collins, D.N., 1990, Seasonal and annual variations of suspended sediment transport in meltwaters draining from an alpine glacier: International Association of Hydrological Sciences Publication, v. 193, p. 439-446.

Collins, D.N., 1996, A conceptually-based model of the interaction between flowing meltwater and subglacial sediment: Annals of Glaciology, v. 22, p. 224-232.

Conway, H., Smith, B., Vaswani, P., Matsuoka, K., Rignot, E., and Claus, P., 2009, A low frequency ice-penetrating radar system adapted for use from an airplane: test results from Bering and Malaspina Glaciers, Alaska, USA: Annals of Glaciology, v. 51, p. 93-97.

Cook, A.J., Fox, A.J., Vaughan, D.G., and Ferrigno, J.G., 2005, Retreating glacier fronts on the Antarctic Peninsula over the past half-century: Science, v. 308, p. 541-544.

Cosma, T., and Hendy, I.L., 2008, Pleistocene glacimarine sedimentation on the continental slope off Vancouver Island, British Columbia: Marine Geology, v. 255, p. 45-54.

Cowan, E.A. and Powell, R.D., 1991, Ice-proximal sediment accumulation rates in a temperate glacial fjord, southeastern Alaska, *in* Anderson, J.B., and Ashley, G.M., eds., Glacial Marine Sedimentation: Paleoclimatic Significance: Geological Society of America Special Paper 261, p. 61-74.

Cowan, E.A., Seramur, K., Powell, R., Williams, B., Gullick, S., and Jaeger, J.M., 2010, Fjords as temporary sediment traps: History of glacial erosion and deposition in Muir Inlet, Glacier National Park, Southeastern Alaska: Geological Society of America Bulletin, v. 122, no. 7-8, p. 1067-1080.

Crossen, K.J., and Lowell, T.V., 2010, Holocene history revealed by post-surge retreat: Bering Glacier forelands, Alaska*:* Geological Society of America Special Papers, v. 462, p. 235-250.

Cuffey, K.M. and Alley, R.B., 1996, Erosion by deforming subglacial sediments: Is it significant? (Toward Till Continuity): Annals of Glaciology, v. 22, p. 126-133.

Cuffey, K.M. and Clow, G.D., 1997, Temperature, accumulation, and ice sheet elevation in central Greenland through the last deglacial transition, Journal of Geophysical Research, v. 102, p. 26383-26396.

Dahlen, F. A., Suppe, J., Davis, D. M., 1984, Mechanics of fold-and-thrust belts and accretionary wedges: Cohesive Coulomb theory: Journal of Geophysical Research, v. 89, p. 10,087-10,101.

Dahlen, F. A., 1990. Critical taper model of fold-and-thrust belts and accretionary wedges: Annual Review of Earth and Planetary Sciences, v. 18, p. 55-99.

Dahlen, F.A., and Suppe, J., 1988, Mechanics, growth, and erosion of mountain belts, *in* Clark, S.P.J., Burchfiel, B.C., and Suppe, J., eds., Processes in Continental Lithospheric Deformation: Geological Society of America Special Paper 218, p. 161–178.

Davis, W.M., 1899, The geographical cycle, Geographical Journal, v. 14, p. 481-500.

Davis, D., Suppe, J., and Dahlen, F.A., 1983, Mechanics of fold-and-thrust belts and accretionary wedges, Journal of Geophysical Research, v. 88, p. 1153–1172.

Debkov, A.P., and Moszherin, V.I., 1992, Erosion and sediment yield in mountain regions of the world *in* Walling, D.E., Davies, T.R., and Hasholt, B., eds., Erosion, Debris Flows and Environment in Mountain Regions, Proceedings of the Chengdu Symposium, July 1992, IAHS Publication no. 209, p. 29-36.

DeMets, C., Gordon, R.G., Argus, D.F., and Stein, S., 1990, Current plate motions: Geophysical Journal International, v. 101, p. 425–478.

Denner, J.C., Lawson, D.E., Larson, G.J., Evenson, E.B., Alley, R.B., Strasser, J.C., and Kopczynski, S., 1999, Seasonal variability in hydrologic system response to intense rain events, Matanuska Glacier, Alaska, U.S.A.: Annals of Glaciology, v. 28, p. 267–271.

Dettennan, R.L., 1986, Glaciation of the Alaska Peninsula, *in* Hamilton, T.D., Reed, K.M., and Thorson, R.M., eds., Glaciation in Alaska: Alaska Geological Society, p. 151-170.

Dodds, C.J., and Campbell, R.B., 1988, Potassium-argon ages of mainly intrusive rocks in the Saint Elias Mountains, Yukon and British Columbia: Geological Survey of Canada Paper 87-16, 43 p.

Doser, D.I., Pelton, J.R. and Veilleux, A.M., 1997, Earthquakes in the Pamplona zone, Yakutat block, south central Alaska. Journal of Geophysical Research, v. 102, p. 24,499–24,511.

Doser, D.I., and R. Lomas, 2000, The transition from strike-slip to oblique subduction in southeastern Alaska from seismological studies, Tectonophysics, v. 316, p. 45-65.

Drewry, D.J., 1986, Glacial geological processes: London, England, Edward Arnold, 276 p.

Egholm, D. L., Nielsen, S. B., Pedersen, V. K., and Lesemann, J. E., 2009, Glacial effects limiting mountain height: Nature, v. 460, p. 884-888.

Elverhoi, A., Hooke, R.LeB., and Solheim, A., 1998, Late Cenozoic erosion and sediment yield from the Svalbard-Barents sea region: Implications for understanding erosion for glacierized basins: Quaternary Science Reviews, v. 17, p. 209-241.

Elliott, J. L., Larsen, C. F., Freymueller, J. T. and Motyka, R. J., 2010, Tectonic block motion and glacial isostatic adjustment in southeast Alaska and adjacent Canada constrained by GPS measurements, Journal of Geophysical Research, v. 115, pp.

Enkelmann, E., Garver, J.I. and Pavlis, T.L., 2008, Rapid exhumation of ice-covered rocks of the Chugach St. Elias orogen, SE-Alaska: Geology, v. 36, p. 915-918.

Enkelmann, E., Zeitler, P.K., Pavlis, T.L, Garver, J.I., Ridgway, K.D., 2009, Intense localized rock uplift and erosion in the St Elias orogen of Alaska. Nature Geoscience, v. 2, p. 360-363.

Enkelmann, E., Zeitler, P.K., Garver, J.I., Pavlis, T.L. and Hooks, B.P., 2010, The thermochronological record of tectonic and surface process interaction at the Yakutat-North American collision zone in Southeast Alaska, American Journal of Science, v. 310, p. 231–260.

Estabrook, C., Nabelek, J., and Lerner-Lam, A., 1992, Tectonic model of the Pacific-North American plate boundary in the Gulf of Alaska from broadband analysis of the 1979 St. Elias, Alaska, earthquake and its aftershocks: Journal of Geophysical Research, v. 97, p. 6587-6612.

Eyles, C. H., Eyles, N., and Lagoe, M. B., 1991, The Yakataga Formation; A late Miocene to Pleistocene record of temperate glacial-marine sedimentation in the Gulf of Alaska, in Anderson, J. B., and Ashley, G. M., eds., Glacial Marine Sedimentation: Paleoclimatic Significance: Boulder CO, Geological Society of America, p. 159-180.

Fahnestock, M.A, 1991, Hydrologic control of sliding velocity in two Alaskan glaciers; observation and theory, Ph.D. thesis, California Institute of Technology.

Firestone, J.E., Waddington, E.D, and J. Cunningham, 1990, The potential for basal melting under Summit, Greenland, Journal of Glaciology, v. 36, p. 163-168.

Fleisher, P.J., Gardner, J.A., and Franz, J. M., 1993, Bathymetry and sedimentary environment in proglacial lakes at the eastern Bering Piedmont Glacier of Alaska: Journal of Geological Education, v. 41, p. 267–274.

Fleisher, P.J., Cadwell, D.H., and Muler, E.H., 1998, Tsivat Basin conduit system persists through two surges, Bering Piedmont Glacier, Alaska: Geological Society of America Bulletin, v. 110, p. 877-887.

Fletcher, H., and J. T. Freymueller, 1999, New GPS constraints on the motion of the Yakutat block, Geophysical Research Letters, v. 26, p. 3029-3032.

Flint, R.F., 1957, Glacial and Pleistocene geology. Wiley, New York, p. 553.

Flowers, G.E., and Clarke, G.K.C., 2002, A multi-component coupled model of glacier hydrology 1. Theory and synthetic examples,; Journal of Geophysical Research, v. 107, no. B11, p. 2287.

Fountain, A.G., 1989, The storage of water in, and hydraulic characteristics of, the firn of South Cascade Glacier, Washington State, U.S.A.: Annals of Glaciology, v. 13, p. 69–75.

Fountain, A.G., 1993, Geometry and flow conditions of subglacial water at South Cascade Glacier, Washington State, U.S.A.: An analysis of tracer injections: Journal of Glaciology, v. 39, no. 131, p. 143–156.

Fountain, A.G., 1994, Borehole water-level variations and implications for the subglacial hydraulics of South Cascade Glacier, Washington state, U.S.A., Journal of Glaciology, v. 40, p. 293-304,

Fountain, A.G., and Walder, J.S., 1998, Water flow through temperate glaciers: Review of Geophysics, v. 36, no. 3, p. 299–328.

Fountain, A.G., Jacobel, R.W., Schlichting, R., and Jansson, P., 2005, Fractures as the main pathways of water flow in temperate glaciers: Nature, v. 433, p. 618-621

Fowler, A.C., 1987, Sliding with cavity formation: Journal of Glaciology, v. 33, no. 115, p. 255–267.

Gardner, A.S., Moholdt, G., Cogley, J.G., Wouters, B., Arendt, A.A., Wahr, J., Berthier, E., Hock, R., Pfeffer, W.T., Kaser, G., Ligtenberg, S.R.M., Bolch, T., Sharp, M., Hagen, J.O., van den Broeke, M.R., and F. Paul, 2013, A reconciled estimate of glacier contributions to sea level rise: 2003-2009, Science, v. 340, no. 6134, p. 852-857.

Gilbert, G.K., 1877, Geology of the Henry Mountains: U.S. geographical and geological survey of the Rocky Mountain region: U.S. Government Printing Office, Washington, D.C., 160 p.

Gilchrist, A.R., Kooi, H. and Beaumont, C., 1994. Post-Gondwana geomorphic evolution of southwestern Africa: Implication for the controls on landscape development from observations and numerical experiments, Journal of Geophysical Research, v. 99, p. 12211-12228

Gordon, S., Sharp, M., Hubbard, B., Smart, C., Ketterling, B., and Willis, I., 1998, Seasonal reorganization of subglacial drainage inferred from measurements in boreholes: Hydrological Processes, v. 12, p. 105–133

Gordon, S., Sharp, M., Hubbard, B., Willis, I., Smart, C., Copland, L., Harbor, J., and Ketterling, B., 2001, Borehole drainage and its implications for the investigation of glacier hydrology: Experiences from Haut Glacier d'Arolla: Hydrological Processes, v. 15, no. 5, p. 797–813.

Griscom, A., and Sauer, P.E., 1990, Interpretation of magnetic maps of the northern Gulf of Alaska, with emphasis on the source of the Slope anomaly: U.S. Geological Survey Open File Report 90–348, 18 p.

Gulick, S.P.S., Lowe, L.A., Pavlis, T.L., Gardner, J.V., and Mayer, L.A., 2007, Geophysical insights into Transition fault debate: Propagating strike-slip in response to stalling Yakutat block subduction in the Gulf of Alaska, Geology, v. 35, p. 763-766.

Gurnell, A.M., 1982, The dynamics of suspended sediment concentration in a proglacial Stream, *in* Hydrological Aspects of Alpine and High Mountain Areas: (Proc. Exeter Symp., July 1982), International Association of Hydrological Sciences Publication 138, p. 319-330.

Gustavson, T.C., and Boothroyd, J.C., 1987, A depositional model for outwash, sediment sources, and hydrologic characteristics, Malaspina Glacier, Alaska: A modern analog of the southeastern margin of the Laurentide Ice Sheet: Geological Society of America Bulletin, v. 99, no. 2, p. 187-200.

Hack, J.T., 1960, Interpretation of erosional topography in humid landscape regions: American Journal of Science, Bradley Volume, v. 258-A, p. 80-97.

Hallet, B., 1979, A theoretical model of glacial abrasion. Journal of Glaciology v. 23, p. 39–50.

Hallet, B., 1981, Glacial abrasion and sliding: their dependence on the debris concentration in basal ice, Annals of Glaciology, v. 2, p. 23-28.

Hallet, B. and Anderson, R.S., 1981, Detailed glacial geomorphology of a proglacial bedrock area at Castleguard Glacier, Alberta, Canada: Zeitschrift fur Gletscherkunde und Glazialgeologie, v.16, p.171-184.

Hallet, B., 1996, Glacial quarrying: A simple theoretical model: Annals of Glaciology, v. 22, p. 1–8.

Hallet, B., Hunter, L. and Bogen, J., 1996, Rates of erosion and sediment evacuation by glaciers: A review of field data and their implications: Global and Planetary Change, v. 12, p. 213-235.

Hamilton, E.L., and Bachman, R.T., 1982, Sound velocity and related properties of marine sediments: Journal of the Acoustical Society of America, v. 72, p. 1891-1904.

Hamilton, E.L., 1985, Sound velocity as a function of depth in marine sediments: Journal of the Acoustical Society of America, v. 78, p. 1348-1355.

Hanson, B., Hooke, R., LeB., Edmund M., Grace, Jr., 1998, Short term and water pressure variations down glacier form a riegel, Storglaciären, Sweden, Journal of Glaciology, v. 44, p. 359-367.

Harbor, J., and Warburton, J., 1993, Relative rates of glacial and nonglacial erosion in alpine environments: Arctic and Alpine Research, v. 25, p.1–7.

Harbor, J., Sharp, M,. Copland, L., Hubbard, B., Nienow, P., and Mair, D., 1997, Influence of subglacial drainage conditions on the velocity distribution within a glacier cross section: Geology, v. 25, no. 8, p. 739-742.

Harper, J.T., Humphrey, N.F., and Greenwood, M.C., 2002, Basal conditions and glacier motion during the winter/spring transition, Worthington Glacier, Alaska, USA.: Journal of Glaciology, v. 48, no. 160, p 42-50.

Harper, J.T., Humphrey, N.F., Pfeffer, T.D., Fudge, T., and O'Neel, S., 2005, Evolution of subglacial water pressure along a glacier length: Annals of Glaciology, v. 40, p. 30-36.

Harper, J.T., Humphrey, N.F., Pfeffer, W.T., and Brian L., 2007, Two modes of accelerated glacier sliding related to water: Geophysical Research Letters, v. 34, no. 12, p. L12503.

Headley, R., Hallet, B., and Rignot, E., 2007, Measurements of fast ice flow of the Malaspina Glacier to explore connections between glacial erosion and crustal deformation in the St. Elias Mountains, Alaska: Eos, Transactions, American Geophysical Union, v. 88, C41A-0050.

Headley, R., Roe, G., and B. Hallet, 2012, Glacier longitudinal profiles in regions of active uplift: Earth and Planetary Science Letters, v. 317-318, p. 354–362.

Headley, R., Hallet, B., Roe, G., Waddington, E.D., and E. Rignot, 2012, Spatial distribution of glacial erosion rates in the St. Elias range, Alaska, inferred from a realistic model of glacier dynamics, Journal of Geophysical Research Earth Surface, v. 117, doi: 10.1029/2011JF002291.

Herman, F., and J. Braun, 2008, Evolution of the glacial landscape of the Southern Alps of New Zealand: Insights from a glacial erosion model: Journal of Geophysical Research, v. 113, F02009, doi: 10.1029/2007JF00080.

Herman, F., Beaud, F., Champagnac, J.D., Lemieux, J.M., and Sternai, P., 2011, Glacial hydrology and erosion patterns: A mechanism for carving glacial valleys: Earth and Planetary Science Letters, v. 310, p. 498–508.

Hicks, D.M., McSavaney, M.J., and Chinn, T.J.H., 1990, Sedimentation in proglacial Ivory Lake, Southern Alps, New Zealand: Arctic and Alpine Research, v. 22, p. 26-42.

Hildes, D.H., 2001, Modelling subglacial erosion and englacial sediment transport of the North American ice sheets [Ph.D. thesis]: Vancouver, University of British Columbia, 155 p.

Hoffman, P., Kaufman, A.J., Halverson, G.R., and Schrag, D.P., 1998, A Neoproterozoic snowball earth: Science, v. 281, no. 5381, p. 1342-1346.

Holdsworth, G., Krouse, H.R., Nosal, M., Spencer, M.J., and Mayewski, P.A., 1989, Analysis of a 290-year accumulation time-series from Mt. Logan, Yukon: International Association of Hydrological Sciences Publication No. 183, p. 71-79.

Holmlund, R., and Hooke, R.LeB., 1983, High water-pressure events in moulins, Storglaciaren, Sweden: Geografiska Annaler, v. 65 A, no. 1-2, p. 19-25.

Holmlund, R., 1988, Internal geometry and evolution of moulins, Storglaciaren, Sweden: Journal of Glaciology, v. 34, no. 117, p. 242-248.

Hooke, R.LeB., Brzozowski, I., and Bronge, C., 1983, Seasonal variations in surface velocity, Storglaciären, Sweden: Geografiska Annaler, v. 65A, no. 3-4, p. 263-277.

Hooke, R.LeB., Miller, S.B., and Kohler, J., 1988, Character of the englacial and subglacial drainage system on Storglaciären, Sweden, as revealed by dye trace studies: Journal of Glaciology, v. 34, p. 228–31.

Hooke, R.LeB., Calla, P., Holmlund, P., Nilsson, M., and Stroeven, A., 1989, A 3 year record of seasonal variations in surface velocity, Storglaciaren, Sweden: Journal of Glaciology, v. 35, no. 120, p. 235-247.

Hooke, R.LeB., Laumann, T., and Kohler, J., 1990, Subglacial water pressures and the shape of subglacial conduits: Journal of Glaciology, v. 36, no. 122, p. 67–71.

Hooke, R.LeB, 1991, Positive feedbacks associated with erosion of glacial cirques and overdeepenings: Geological Society of America Bulletin, v. 103, no. 8, p.1104-1108.

Hooke, R.LeB. 1998. Principles of glacier mechanics: New Jersey, Prentice Hall, p. 119-134

Hooke, R.LeB., and Pohjola, V.A., 1994, Hydrology of a segment of a glacier situated in an overdeepening, Storglaciaren, Sweden: Journal of Glaciology, v. 40, no. 134, p. 140-148.

Hubbard, B.P., Sharp, M.J., Willis, I.C., Nielsen, M.K., and Smart, C.C., 1995, Borehole water-level variations and the structure of the subglacial hydrological system of Haut Glacier d'Arolla, Valais, Switzerland: Journal of Glaciology, v. 41, no. 139, p. 572–583.

Hubbard, B., Siegert, M.J. and McCarroll, D., 2000, Spectral roughness of glaciated bedrock geomorphic surfaces: Implications for glacier sliding. Journal of Geophysical Research, v. 105, p. 21,295-21,303.

Hunter, L.E., Powell, R.D., and Lawson, D.E., 1995, Morainal-bank sediment budgets and their influence on the stability of tidewater termini of valley glaciers entering Glacier Bay, Alaska, U.S.A.: Annals of Glaciology, v. 22, p. 211-216.

Hunter, L.E., Powell, R.D., and Lawson, D.E., 1996, Morainal-bank sediment budgets and their influence on the stability of tidewater termini of glaciers entering Glacier Bay, Alaska, U.S.A.: Annals of Glaciology, v. 42, p.123-135.

Hughes, T., 1992, Theoretical calving rates from glaciers along ice walls grounded in water of variable depths: Journal of Glaciology, v. 38, no. 129, p.282–294.

Hughes, T., 1986, The Jakobshavn effect: Geophysical Research Letters, v. 13, p.46–48.

Hughes, T.J. and Fastook, J.L., 1997, The relationship between calving rates, ice velocities and water depths, *in* Van der Veen, C.J., ed., Calving Glaciers: Report of a Workshop, February 28–March 2, 1997: Byrd Polar Research Center Report No. 15, p.77–84.

Humphrey, N.C., Raymond, C.F., and Harrison, W.D., 1986, Discharges of turbid water during mini-surges of Variegated Glacier, Alaska: Journal of Glaciology, v. 32, no. 111, p. 195-207.

Humphrey, N.F., 1987, Basal hydrology of a surge-type glacier: Observations and theory relating to Variegated Glacier [Ph.D. thesis]: Seattle, University of Washington.

Humphrey, N.F., Kamb, B., Fahnestock, M., and Engelhardt, H., 1993, Characteristics of the bed of the lower Columbia Glacier, Alaska: Journal of Geophysical Research, Vol. 98, p. 837-846.

Humphrey, N.F. and Raymond, C.F., 1994, Hydrology, erosion and sediment production in a surging glacier, Variegated Glacier, Alaska, 1982-83: Journal of Glaciology, v. 40, no. 136, p. 539--552.

Hunter, L.E., Powell, R.D., and Lawson, D. E., 1996, Flux of debris transported by ice at three Alaskan tidewater glaciers: Journal of Glaciology, v. 42, no. 140, p. 123-135.

Hunter, L.E., Powell, R.D., and Lawson, D. E., 1996, Morainal-bank sediment budgets and their influence on the stability of tidewater termini of valley glaciers entering Glacier Bay, Alaska, U.S.A.: Annals of Glaciology, v. 22, p.211-216.

Iken, A., 1981, The effect of the subglacial water pressure on the sliding velocity of a glacier in an idealized numerical model: Journal of Glaciology, v. 27, no. 97, p. 407–421.

Iken, A., Rothlisberger, H., Flotron, A., and Haeberli, W., 1983, The Uplift of Unteraargletscher at the beginning of the melt season – a consequence of water storage at the bed?: Journal of Glaciology, v. 29, no. 101, p. 28-47.

Iken, A., and Bindschadler, R.A., 1986, Combined measurements of subglacial water pressure and surface velocity of Findelengletscher, Switzerland: Conclusions about drainage system and sliding mechanism: Journal of Glaciology, v.32, no.110, p.101-119.

Iken, A., and M. Truffer, 1997, The relationship between subglacial water pressure and velocity of Findelengletscher, Switzerland, during its advance and retreat: Journal of Glaciology,v. 43, no. 144, p. 328–338.

Imbrie, J., Hays, J.D., Martinson, D.G., McIntyre, A., Mix, A.C., Morley, J.J., Pisias, N.G., Prell, W.L., Shackleton, N.J., 1984, The orbital theory of Pleistocene climate: Support from a Revised chronology of the marine d18O record, *in* Berger, A., Imbrie, J., Hays, J., Kukla, G., and Saltzman, B., eds., Milankovitch and climate: Dordrecht, Reidel Publishing Company, p. 269–305.

Iverson, N.R., 1990, Laboratory simulations of glacial abrasion: comparison with theory, Journal of Glaciology, v. 36, p. 304-314.

Iverson, N.R., 1991. Morphology of glacial striae: implications for abrasion of glacier beds and fault surfaces. Geological Society of America Bulletin, v. 103, p. 1308-1316.

Iverson, N.R., 1991, Potential effects of subglacial water-pressure fluctuations on quarrying: Journal of Glaciology, v. 37, no. 125, p. 27-36.

Iverson, N.R., 2012, A theory of glacial quarrying for landscape evolution models: Geology, v. 40, p. 679-682.

Jaeger, J.M., Nitrouer, C.A., Scott, N.D, and Milliman, J.D., 1998, Sediment accumulation along a glacially impacted mountainous coastline—North-east Gulf of Alaska: Basin Research, v. 10, p. 155–173

Jahns, R.H., 1943, Sheet structure in granites: its origin and use a measure of glacial erosion in New England, Journal of Geology, v. 51, p. 71-98.

Jansson, P., 1996, Dynamics and hydrology of a small polythermal valley glacier: Geografiska Annaler, v. 78A, no. 2-3, p.171-180.

Jansson, P., Hock, R., and Schneider, T., 2003, The concept of glacier storage: A review: Journal of Hydrology, v. 282, no. 1–4, p.116–129.

Johannesson, T., Raymond, C., and Waddington, E.D., 1989, Time-scale for adjustment of glaciers to changes in mass balance: Journal of Glaciology, v. 35, p. 355–369.

Jones, J.E., B.F. Molnia and J.W. Schoonmaker, Jr. 1989. The Malaspina Glacier radar study: a SLAR investigation of glacier and periglacier features. USGS Year Book, p. 34–40.

Jordan, P., and Slaymaker, O., 1991, Holocene sediment production in Lillooet River basin: A sediment budget approach: Géographie physique et Quaternaire, v. 45, p. 45–57.

Josberger, E.G., Shuchman, R.A., Meadows, G.A., Savage, S. and John Payne, J., 2006, Hydrography and Circulation of Ice-Marginal Lakes at Bering Glacier, Alaska, U.S.A: Arctic, Antarctic, and Alpine Research, Vol. 38, No. 4, p. 547–560

Joughin, I., Alley, R.B., and D.M. Holland, 2012, Ice-sheet response to oceanic forcing, Science, v. 338, p. 1172-1176.

Kamb, B., Raymond, C.F., Harrison, W.D., Engelhardt, H., Echelmeyer, K.A., Humphrey, N., Brugman, M.M., and Pfeffer, T., 1985, Glacier surge mechanism: 1982-1983 surge of Variegated glacier, Alaska: Science, v. 227, no. 4686, p.469-479.

Kamb, B., 1987, Glacier surge mechanism based on linked cavity configuration of the basal water conduit system: Journal of Geophysical Research, v. 92, no. B9, p. 9083–9100.

Kamb, B. and H. Engelhardt, 1987, Waves of accelerated motion in a glacier approaching surge: the mini-surges of Variegated Glacier, Alaska, U.S.A., Journal of Glaciology, v. 33, p27-46

Kamb, B., and Echelmeyer, K. A., 1986, Stress-gradient coupling in glacier flow, I, Longitudinal averaging of the influence of ice thickness and surface slope: Journal of Glaciology, v. 32, p.267-284.

Kamb, B., Engelhard, H., Fahnestock, M.A., Humphrey, N., Meier, M. and D. Stone, 1994, Mechanical and hydrologic basis for the rapid motion of a large tidewater glacier, 2. Interpretation, Journal of Geophysical Research, v. 99, p. 15,231-15,244.

Kirkbride, M.P. and Warren, C.R., 1997, Calving processes at a grounded ice cliff: Annals of Glaciology, v. 24, p.116–121.

Kooi, H. and Beaumomt, C., 1994, Escarpment evolution on high-elevation rifted margins: Insights derived from a surface processes model that combines diffusion, advection, and reaction, Journal of Geophysical Research, v. 99, p. 12191-12209

Koons, P.O., 1989, The topographic evolution of collisional mountain belts: A numerical look at the southern Alps, New Zealand: American Journal of Science, v. 289, p. 1041-1069.

Koppes, M.N., and Hallet, B., 2002, Influence of rapid glacial retreat on the rate of erosion of tidewater glaciers: Geology, v. 30, no. 1, p. 47-50.

Koppes, M.N., and Hallet, B., 2006, Erosion rates during rapid deglaciation in Icy Bay, Alaska: Journal of Geophysical Research, v. 111, p. 1–11.

Koppes, M. N., and Montgomery, D. R., 2009, The relative efficacy of fluvial and glacial erosion over modern to orogenic timescales, Nature Geoscience, v. 2, p. 644-647.

Krimmel, R.M., 1997, Documentation of the retreat of Columbia Glacier, Alaska, *in* Van der Veen, C.J., ed., Calving glaciers: report of a workshop, February 28–March 2, 1997:Byrd Polar Research Center Report No. 15, p. 105–108.

Krissek, L.A., 1995, Late Cenozoic ice-rafting records from leg 145 sites in the North Pacific: Late Miocene onset, late Pliocene intensification and Pliocene-Pleistocene events, *in* Rea, D.K., Basov, I.A., Scholl, D.W., and Allan, J.F. (Eds.), Proceedings of the Ocean Drilling Program, Scientific Results, v. 145, p. 179-194.

Kutzbach, J.E., 1987, Model simulations of the climatic patterns during the deglaciation of North America, *in* Ruddiman, W.F., and Wright, H.E., eds., North America and Adjacent Oceans During the Last Deglaciation: Boulder, Colorado, Geological Society of America, Geology of North America, v. K-3, p. 425-446.

Kutzbach, J.E., Guetter, P.J., Behling, PJ., and Selin, R., 1993, Simulated climatic changes: Results of the COHMAP climate- model experiments, *in* Wright, H.E., Kutzbach, J.E., Webb, T. III, Ruddiman, W.F., Street-Petrott, EA., and Bartlein, P.J., eds., Global Climates Since the Last Glacial Maximum: Minneapolis, University of Minnesota Press, p. 24-93.

Lagoe, M.B., Eyles, C.H., and Eyles, N., 1989, Paleoenvironmental significance of foraminiferal biofacies in the glaciomarine Yakataga Formation. Middleton Island, Gulf of Alaska: Journal of Foraminiferal Research, v. 19, p. 194–209.

Lagoe, M.B., Eyles, C.H., Eyles, N., and C. Hale, 1993, Timing of Late Cenozoic tidewater glaciation in the Far North Pacific: Geological Society of America Bulletin, v. 105, p.1542-1560.

Larsen, C., Motyka, R., Freymueller, J.T., Echelmeyer, K.A., and E. R. Ivins, 2005, Rapid viscoelastic uplift in southeast Alaska caused by post-Little Ice Age glacial retreat: Earth and Planetary Science Letters, v. 237, p. 548– 560.

Lawson, D. E., Strasser, J. C., Evenson, E. B., Alley, R. B., Larson, G. J., and Arcone, S.A., 1998, Glaciohydraulic supercooling: A freeze-on mechanism to create stratified, debris-rich basal ice: I. Field evidence: Journal of Glaciology, v.44, no.148, p. 547-562.

Lawson, D.E. and U.S. Army Cold Regions Research and Engineering Laboratory, 1993, Glaciohydrologic and Glaciohydraulic Effects on Runoff and Sediment Yield in Glacierized Basins: Hanover, New Hampshire, U.S. Army Corps of Engineers, Cold Regions Research and Engineering Laboratory, 108 p.

Le Meur, E., Gagliardini, O., Zwinger, T., and Ruokolainen, J., 2004, Glacier flow modelling: a comparison of the Shallow Ice Approximation and the full-Stokes solution, Comptes Rendus Physique, v. 5, p. 709-722.

Lliboutry, L., 1968, General theory of subglacial cavitation and sliding of temperate glaciers: Journal of Glaciology, v. 7, no. 49, p. 21-58.

Lliboutry, L. A., 1971, Permeability, brine content and temperature of temperate ice, Journal of Glaciology, v. 10, p. 15-29.

Loso, M., Anderson, R.S., and S. Anderson, 2004, Post-little ice age record of coarse and fine clastic sedimentation in and Alaskan proglacial lake: Geology, v. 32, no.12, p. 1065-1068.

Ma, C., Sauber, J.M., Bell, L.J., Clark, T.A., Gordon, D., Himwich, W.E., and J.W. Ryan, 1990, Measurement of horizontal motions in Alaska using very long baseline Interferometry, Journal of Geophysical research, v. 95, p. 21991–22011.

MacGregor, K.R., Anderson, R.S., Anderson, S.P., and Waddington, E.D., 2000, Numerical simulations of glacial-valley longitudinal profile evolution: Geology, v. 28, p. 1031–1034.

MacGregor, K.R., Anderson, R.S., and Waddington, E.D., 2009, Numerical modeling of glacial erosion and headwall processes in alpine valleys: Geomorphology, v. 10, p. 189–204.

Mair D., Nienow, P., Willis, I., and Sharp, M., 2001. Spatial patterns of glacier motion during a high-velocity event: Haut glacier d'Arolla, Switzerland: Journal of Glaciology, v. 47, no.156, p. 9-20.

Mair D., Willis, I., Fischer, U., Hubbard, B., Nienow, P., and Hubbard, A., 2003, Surface, internal and basal motion during spring events: Journal of Glaciology, v. 49, no.167, p. 555-567.

Manabe, S., and A. J. Broccoli, 1985: The influence of continental ice sheets on the climate of an ice age. Journal of Geophysical Research, v. 90, p. 2167-2190.

Mann, D.H., and Peteet, D.M., 1994, Extent and time of the last glacial maximum in southwest Alaska: Quaternary Research, v. 42, p.136-148.

Mann, D.H., and Hamilton, T.D., 1995, Late Pleistocene and Holocene Paleoenvironments of the North Pacific Coast: Quaternary Science Reviews, v. 14, p.449–471.

Marcus, M.G., and Ragle, R.H., 1970, Snow accumulation in the Icefield Ranges, St. Elias Mountains, Yukon: Arctic and Alpine Research, v. 2, no. 4, p. 270-292.

Masek, J.G., Isacks, B.L. Gubbels, T.L., and E.J. Fielding, 1994, Erosion and tectonics at the margins of continental plateaus: Journal of Geophysical Research, v. 99, p. 13941-13956

Mattson, L.E., and Gardner, J.S., 1989, Energy exchange and ablation rates on the debris-covered Rakhiot Glacier, Pakistan: Zeitschrift fur Gletscherkunde und Glazialgeologie, v. 25, no. 1, p.17–32.

Meier, M.F., and Post, A.S., 1962, Recent variations in mass net budgets of glaciers in western North America: International Association of Hydrological Sciences, v. 58, p.63–77.

Meier, M., and A. Post, 1987, Fast tidewater glaciers: Journal of Geophysical Research, v. 92, no. B, p. 9051-9058.

Meigs, A., and Sauber, J., 2000, Southern Alaska as an example of the long-term consequences of mountain building under the influence of glaciers: Quaternary Science Reviews, v. 19, p. 1543-1562.

Meigs, A., Krugh, W. C., Davis, K. and Bank, G., 2006, Ultra-rapid landscape response and sediment yield following glacier retreat, Icy Bay, southern Alaska: Geomorphology, v. 78, no. 3-4, p. 207-221.

Merrand, Y., and Hallet, B., 1996, Water and sediment discharge from a large surging glacier: Bering Glacier, Alaska, U.S.A., summer 1994: Annals of Glaciology, v. 22, p. 233-240.

Merrand Y., and Hallet, B., 2000, A physically based numerical model of orogen-scale glacial erosion: Importance of subglacial hydrology and basal stress regime: GSA Abstracts with Programs, v. 32, p. A329.

Milliman, J. A. & Meade, R. H., 1983, World wide delivery of river sediment to the oceans: Journal of Geology, v. 91, pp. 1-21.

Milliman, J.D., and Syvitski, J.P.M., 1992, Geomorphic/tectonic control of sediment discharge to the ocean: The importance of small mountainous rivers: Journal of Geology, v. 100, no. 5, p. 525–544.

Mitchell, S.G., and D.R. Montgomery, 2006, Influence of a glacial buzzsaw on the height and morphology of the Washington Cascade Range, Washington State, USA. Quaternary Research, v. 65, no. 1, p. 96-107.

Molnar, P., and England, P., 1990, Late Cenozoic uplift of mountain ranges and global climate change: chicken or egg?: Nature, v. 346, p. 29-34.

Molnia, B.F., and J.E. Jones, 1989, View through the ice: are unusual airborne radar backscatter features from the surface of Malaspina Glacier, Alaska, expressions of subglacial morphology?, EOS Transactions, American Geophysical Union, v. 70, p. 701-710.

Molnia, B.F., Post, A., Carlson, P.R., and Trabant, D.C., 1991, Evolution and morphology of proglacial Lake Vitus, Bering Glacier, Alaska: American Geophysical Union, Eos, Program and Abstracts, v. 72, p. 158-159.

Molnia, B.F., Post, A., Trabant, D.C., and Krimmel, R.M., 1994, The 1993-1994 surge of the Bering Glacier, Alaska: An overview: Eos, Transactions, American Geophysical Union, v. 75, p. F62.

Molnia, B.F, and A. Post, 1995, Holocene history of Bering Glacier, Alaska: A prelude to the 1993-1994 surge: Physical Geography, v. 16, p.87-117.

Molnia, B.F., Post, A., and Carlson, P.R., 1996, 20th Century glacial-marine sedimentation in Vitus Lake, Bering Glacier, Alaska, U.S.A.: Annals of Glaciology, v. 22, p.205-210.

Molnia, B.F, 2001, Glaciers of Alaska, Alaska Geographic, v. 28, no. 2, 112 p.

Molnia B.F., and Snyder, L.E., 2012, Bed Morphology and Ice Thickness, Bering Glacier, Alaska: AGU Poster C23B-0649, San Francisco, 3-7 December.

Montgomery, D.R., Balco, G., and Willet, S.D., 2001, Climate, tectonics, and the morphology of the Andes: Geology, v. 29, p. 579–582

Montgomery, D.R., and Brandon, M.T., 2002, Topographic controls on erosion rates in tectonically active mountain ranges; Earth and Planetary Science Letters, v. 201, p. 481-489.

Morland, L.W. and Boulton, G.S., 1975, Stress in an elastic hump: The effects of glacier flow over elastic bedrock: Proceedings of the Royal Society of London, Series A, Mathematical and Physical Sciences, v. 344, no. 1637, p. 157-173.

Motyka, R.J., and Begét, J.E., 1996, Taku Glacier, Southeast Alaska, U.S.A.: Late Holocene History of a Tidewater Glacier: Arctic and Alpine Research, v. 28, p. 42-51.

Motyka, R.J. and Echelmeyer, K.A., 2003, Taku Glacier (Alaska, U.S.A.) on the move again: active deformation of proglacial sediments: Journal of Glaciology, v. 49, p. 50–58.

Motyka, R.J., Hunter, L., Echelmeyer, K., and Connor, C., 2003, Submarine melting at the terminus of a temperate tidewater glacier, LeConte Glacier, Alaska: Annals of Glaciology, v. 36, p. 57-65.

Motyka, R.J., Truffer, M., Kuriger, E.M., and Bucki, A.K., 2006, Rapid erosion of soft sediments by tidewater glacier advance: Taku Glacier, Alaska, USA.: Geophysical Research Letters, v. 33, L24504, doi:10.1029/2006GL028467.

Müller, F. and A. Iken, 1973, Velocity fluctuations and water regime of arctic valley glaciers, IAHS Publication 95, p. 165-182

Muller, E.H., Post, A., Fleisher, P.J., Franzi, D.A., Stuckenrath, R., and Cadwell, D.H., 1991, Buried forest beds exposed by lowering of glacial lake Tsiu reveal late Holocene history of Bering Glacier, Alaska: Geological Society of America Abstracts with Programs, v. 23, no. 1, p. 106.

Muller, E.H., and Fleisher, P. J., 1995, Surge history and potential for renewed retreat, Bering Glacier, Alaska: Arctic and Alpine Research, v. 27, p. 81–88.

Murray, T., Stuart, G.W., Fry, M., Gamble, N.H., and Crabtree, M.D., 2000, Englacial water distribution in a temperate glacier from surface from borehole radar velocity analysis: Journal of Glaciology, v. 46, no.154. p.389-398.

Muskett, R.R., Lingle, C.S., Tangborn, W.V., and R.T., Rabus, 2003, Multi-decadal elevation changes on Bagley Ice Valley and Malaspina Glacier, Alaska: Geophysical Research Letters, v. 30, no. 16, p. 1857-1859.

Muskett, R.R., Lingle, C.S., Sauber, J.M., Post, A.S., Tangborn, W.V., And B.T. Rabus, 2008, Surging, accelerating surface lowering and volume reduction of the Malaspina Glacier system, Alaska, USA, and Yukon, Canada, from 1972 to 2006, Journal of Glaciology, v. 54, p. 788-800.

Nakamura, K., and Uyeda, S., 1980, Stress gradient in arc-back arc regions and plate subduction, Journal of Geophysical Research, v. 85, p. 6419-6428.

Nick, F.M., van der Veen, C.J., and J. Oerlemans, 2007: Controls on advance of tidewater glaciers: Results from numerical modeling applied to Columbia Glacier, Journal of Geophysical Research, v. **112**, doi: 10.1029/2006JF000551.

Nienow, P., Sharp, M., and Willis, I., 1996, Temporal switching between englacial and subglacial drainage pathways: Dye tracer evidence from the Haut Glacier d'Arolla, Switzerland: Geografica Annler, v. 78A, no. 1, p. 51–60.

Nienow, P., Sharp, M., and Willis, I., 1998, Seasonal changes in the morphology of the subglacial drainage system, Haut Glacier d'Arolla, Switzerland: Earth Surface Processes and Landforms, v. 23, no. 9, p. 825–843.

Nienow, P.W., Hubbard, A.L., Hubbard, B.P., Chandler, D.M., Mair, D.W.F., Sharp, M.J., and Willis, I.C., 2005, Hydrological controls on diurnal ice flow variability in valley glaciers: Journal of Geophysical Research, vl. 110, F04002, doi: 10.1029/2003JF000112.

Nishenko, S.P. and Jacob, K.H., 1990, Seismic potential of the queen Charlotte, Alaska, Aleutian seismic zone. Journal of Geophysical Research 95: doi: 10.1029/89JB03279,

Nolan, M., Echelmeyer, K., Motyka, R., and Trabant, D., 1995: Ice thickness measurements of Taku Glacier, Alaska, USA, and their relevance to its recent behavior, Journal of Glaciology, v. 41, p. 541–552.

Nye, J.F., 1953, The flow law of ice from measurements in glacier tunnels, laboratory experiments and the Jungfraufirn Borehole Experiment, Proceedings of the Royal Society of London Series A-Mathematical And Physical Sciences, v. 219, p. 477-489.

Nye, J.F., and Martin, P.C.S., 1967, Glacial erosion: Bern, International Union of Geodesy and Geophysics: Commission of Snow and Ice, v. 79, p. 78–86.

Nye, J.F., 1969, A Calculation on the Sliding of Ice Over a Wavy Surface Using a Newtonian Viscous Approximation, Proceedings of the Royal Society of London. Series A, Mathematical and Physical Sciences, v. 311, no. 1506, p. 445-467.

Nye, J. F. and Frank, F.C., 1973, Hydrology of the intergranular veins in a temperate glacier, in Symposium on the Hydrology of Glaciers: Proceedings of the symposium held at Cambridge, England, 7–13 September 1969, International Association of Hydrological Sciences Publication No. 95, p. 157–161.

Oerlemans, J., 1984, Numerical experiments of large scale glacial erosion: Zeitschrift für Gletscherkunde und Glazialgeologie, v. 20, p. 107–126.

Østrem, G., 1959, Ice melting under a thin layer of moraine, and the existence of ice cores in moraine ridges: Geografiska Annaler, v. 41, no. 4, p.228–230.

O'Sullivan, P. B., and Currie, L. D., 1996, Thermotectonic history of Mt. Logan, Yukon Territory, Canada: Earth and Planetary Science Letters, v. 144, p. 251-261.

O'Sullivan, P. B., Plafker, G., and Murphy, J.M., 1997, Apatite fission-track thermotectonic history of crystalline rocks in the northern St. Elias Mountains, Alaska, in Dumoulin, J. A., and Gray, J. E., eds., Geological studies inAlaska by the U.S. Geological Survey, 1995: Reston, United States Geological Survey, p. 283-293.

Page, R.A., Stephens, C.D., and J.C. Lahr, 1989, Seismicity of the Wrangell and Aleutian Wadati-Benioff Zones and the North American Plate Along the Trans-Alaska Crustal Transect, Chugach Mountains and Copper River Basin, Southern Alaska, Journal of geophysical research, v. 94, p. 16059-16082.

Pasch, A.D., Foster, N.R., and Irvine, G.V., 2010, Faunal analysis of Late Pleistocene-early Holocene invertebrates provides evidence for paleoenvironments of a Gulf of Alaska shoreline inland of the present Bering Glacier margin, *in* Shuman R.A., and Josberger, E.G., eds., Bering Glacier: Interdisciplinary Studies of Earth's Largest Temperate Surging Glacier: Geological Society of America Special Paper 462, p. 251-274.

Paterson, W.S.B., 1994. The physics of glaciers, 2d ed.: Oxford, Pergamon, 136 p.

Peterson, J.A., and Robinson, G. 1969. Trend surface mapping of cirque floor levels, Nature, v. 222, no. 5188, p. 75-76.

Pearce, J., Pazzaglia, F, Evenson, E., Lawson, D., Alley, R., Germanoski, D., and Denner, J., 2003, Bedload component of glacially discharged sediment: Insights from Matanuska Glacier, Alaska: Geology, v. 31, no. 1, p. 7–10.

Pfeffer, W.T., Cohn, J., Meier, M., and Krimmel, R.M., 2000, Accelerated retreat of Columbia Glacier, Alaska: Eos, Transactions, American Geophysical Union, v. 81, no. 48, p. 577–584.

Plafker, G., and M. Rubin, 1978, Uplift history and earthquake recurrence as deduced from marine terraces on Middleton Island, Alaska, in *Proceedings of Conference VI Methods and Identification of Seismic Gaps,* pp. 687–721.

Plafker, G., Hudson, T., Burns, T., and M. Rubin, 1978, late Quaternary offsets along the Fairweather fault and crustal plate interactions in southern Alaska, Canadian Journal of Earth Science, v. 15, p. 805– 816.

Plafker, F., Hudson, T., Rubin, M., and K. Dixon, 1981, Holocene marine terraces and uplift history in the Yakataga seismic gap near Icy Cape, Alaska, U.S. Geological. Survey Circular 844*,* p. 111–115.

Plafker, G., Moore, J.C., and Winkler, G.R., 1994, Geology of the southern Alaska margin, *in* Plafker, G., and Berg, H.J.C., eds., The Geology of Alaska, Vol. G-1: Boulder, Colorado, Geological Society of America, Geology of North America, p. 389-449.

Porter, S.C., 1964, Composite Pleistocene snowline of Olympic mountains and Cascade Range, Washington: Geological Society of America Bulletin, v. 75, p. 477–482.

Porter, S.C., 1977, Present and past glaciation threshold in the Cascade Range, Washington, U.S.A.: Topographic and climatic controls and paleoclimatic implications: Journal of Glaciology, v. 18, p. 101–116.

Porter S.C., Pierce K.L., and Hamilton, T.D., 1983, Late Wisconsin mountain glaciation in the western United States, *in* Porter, S.C., ed., Late Quaternary Environments of the United States, Vol. 1, The Late Pleistocene: Minneapolis, University of Minnesota Press, p.71–111.

Porter, S.C., 1986, Chronology of fjord-glacier fluctuations in Icy Bay, Alaska, during the last two millennia: Geological Society of America Abstracts with Programs, v. 16, no. 6, p. 721.

Porter, S.C., 1989, Late Holocene fluctuations of the fjord glacier system in Icy Bay, Alaska, U.S.A.: Arctic Alpine Research, v. 21, p. 364-379.

Post, A., and Motyka, R.J., 1995, Taku and LeConte Glaciers, Alaska: calving speed control of late Holocene asynchronous advances and retreats. In Nelson, E E.

(ed.), Glaciers and Late Quaternary Environments of Alaska: I, Essays in Honor of William O. Field. Physical Geography, v. 16: p. 59-82.

Powell, R.D., 1988, Processes and facies of temperate and subpolar glaciers with tidewater fronts: Short Course Notes, Denver, Colorado, Geological Society of America, 114 p.

Powell, R.D., 1991, Grounding-line systems as second-order controls on fluctuations of tidewater termini of temperate glaciers, In: Anderson, J.B. & Ashley, G.M. (eds.), Glacial marine sedimentation; Paleoclimatic significance, The Geological Society of America, Special Paper 261, p. 75-93.

Rasmussen, L.A., 1989, Surface velocity variations of the lower part of Columbia Glacier, Alaska, 1977-1981: Geological Survey Professional paper 1258-H, 52 p.

Raymo, M.E., Ruddiman, W.F., and Froelich, P.N., 1988, Influence of the late Cenozoic mountain building on ocean geochemical cycles: Geology, v. 16, p. 649-653.

Raymo, M.E., and W.F. Ruddiman, 1992, Tectonic forcing of late Cenozoic climate, Nature, v. 359, p. 117-122.

Raymond, C. F., 1980, Valley glaciers, in Colbeck, S.C.,(ed.) Dynamics of snow and ice masses, Academic Press, New York, p. 79-139.

Raymond, C. F., 1983, Deformation in the vicinity of ice divides, Journal of Glaciology, v. 39, p. 357-373.

Raymond, C.F., and Harrison, W.D., 1987, Fit of ice motion models to observations from Variegated Glacier, Alaska, in Waddington, E.D., and Walder, J.S., eds., The Physical Basis of Ice Sheet Modeling: Proceedings of the Vancouver Symposium, August 1987, International Association of Hydrological Sciences Publication No. 170, p. 153-168.

Raymond, C.F., Benedict, R.J., Harrison, W.D., Echelmeyer, K.A., and Sturm, M., 1995, Hydrological discharges and motion of Fels and Black Rapids Glaciers, Alaska, U. S. A.: Implications for the structure of their drainage systems: Journal of Glaciology, v. 41, no. 138, p. 290– 304.

Rea, D. K., and Snoeckx, H., 1995, Sediment fluxes in the Gulf of Alaska; paleoceanographic record from Site 887 on the Patton-Murray Seamount Platform, in Rea, D. K., Basov, I. A., Scholl, D. W., and Allan, J. F., eds., Proceedings of the Ocean Drilling Program, Scientific Results: College Station, TX., Ocean Drilling Program, p. 247-256.

Reznichenko, N., Davies, T., Shulmeister, J. and M. McSaveney, 2010, Effects of debris on ice surface melting rates: an experimental study, Journal of Glaciology, v. 56, p. 384-394.

Rothlisberger, H., 1972, Water pressure in intra- and subglacial channels: Journal of Glaciology, v. 11, no. 62, p. 177–203.

Rothlisberger, H., Iken, A., and Spring, U., 1979, Piezometric observations of water pressure at the bed of Swiss glaciers: Journal of Glaciology, v. 23, no. 89, p. 429–430.

Rothlisberger, H., and Iken, A., 1981, Plucking as an effect of water-pressure variations at the glacier bed: Annals of Glaciology, v. 28, no. 100, p. 475-481

Rothlisberger, H., and Lang, H., 1987, Glacial hydrology, *in* Gurnell, A.M., and Clark, M.J., eds., Glacio-fluvial sediment transfer: An alpine perspective: Chichester, Wiley and Sons, p. 207–284.

Sabin, A., and Pisias, N., 1996, Sea surface temperature changes in the Northeastern Pacific Ocean during the past 20,000 years and their relationship to climate change in Northwestern North America: Quaternary Research, v. 46, p. 48–61.

Saltzman, B., and Verbitsky, M., 1994, Late Pleistocene climatic trajectory in the phase space of global ice, ocean state, and CO2: Observations and theory, Paleoceanography, v. 9, p. 767–779.

Sauber, J.M., McClusky, S., and R. King, 1997, Relation of ongoing deformation rates to the subduction zone process in southern Alaska, Geophysical Research Letters, v. 24, p. 2853–2856.

Sauber, J.M, B. Molnia, C. Carabajal, S. Luthcke, and R. Muskett, 2005, Ice elevations and surface change on the Malaspina Glacier, Alaska, Geophysical Research Letters, v. 32, L23S01, doi: 10.29/2005GL023943.

Schumm, S. A., 1977,cd The Fluvial System. John Wiley and Sons, New York.

Schneider, T., 1999, Water movement in the firn of Storglaciären, Sweden: Journal of Glaciology, v. 45, no. 150, p. 286–294.

Schuler, T., Fischer, U.H., and Gudmundsson, G.H., 2004, Diurnal variability of subglacial drainage conditions as revealed by tracer experiments: Journal of Geophysical Research, v. 109, no. F2, F02008, doi: 10.1029/2003JF000082.

Sharp, M., Richards, K., Willis, I., Arnold, N., Nienow, P., Lawson, W., and Tison, J.L., 1993, Geometry, bed topography and drainage system structure of the haut glacier

d'Arolla, Switzerland: Earth Surface Processes and Landforms, v. 18, no. 6, p. 557-571.

Sharp, M., Tranter, M., Brown, G.H., Hubbard, B.P., and M. Skidmore, 1995, Rates of chemical denudation and CO_2 drawdown in a glacier-covered alpine catchment, Geology, v. 23, p. 61-64.

Sharp, R. 1951, Accumulation and ablation on the Seward-Malaspina glacier system, Canada-Alaska: Geological Society of America Bulletin, v. 62, no. 7, p. 725-743.

Sharp, R.P., 1958, The latest major advance of Malaspina Glacier, Alaska: Geographical Review, v. 48, p.16–26.

Sheaf, M.A., Serpa, L., and Pavlis, T.L., 2003, Exhumation rates in the St. Elias Mountains, Alaska: Tectonophysics, v. 367, no. 1-2, p 1-11.

Shennan, I., 2009, Late Quaternary sea-level changes and palaeoseismology of the Bering Glacier region, Alaska: Quaternary Science Reviews, v. 28, p. 1762–1773.

Shennan, I., 2011, Sea level from global to local, Nature Geoscience, v. 4, p. 283–284.

Shoemaker. E.M., 1986, Debris-influenced sliding laws and basal debris balance, Journal of Glaciology, v. 3, p. 224-231.

Shreve, R.L., 1972, Movement of water in glaciers: Journal of Glaciology, v. 11, no. 62, p. 205-214.

Shushman, R.A., Josberger, E.G., Hatt, C.R., Roussi, C., Fleisher, P.J., and S. Guyer, 2010, Bering glacier ablation measurements, The Geological Society of America, Special Paper 462, p. 83-97.

Souchez, R.A., and Lemmens, M., 1987, Solutes in Glacio-fluvial sediment transfer, Gurnell, A.M., and. Clark, M.J., eds.: New York, J. Wiley and Sons Ltd, p. 285-303.

Spotila, J.A., Buscher, J.T., Meigs, A.J., and P.W. Reiners, 2004, Long term glacial erosion of active mountain belts: example of the Chugach-St. Elias range, Alaska, Geology, v. 32, no. 6, p. 5-1-504.

Spotila, J.A., and Berger, A.L., 2010. Exhumation at orogenic indentor corners under long-term glacial conditions: example of the St. Elias orogen, southern Alaska. Tectonophysics, v. 490, p. 241–256.

Sternai, P., Herman, F., Fox, M.R., and S. Castelltort, 2010, Hypsometric analysis to identify spatially variable glacial erosion: Journal of Geophysical Research, v. 116, p. 17.

Sugden, D, Glasser, N., and C.M. Clapperton, 1992, Evolution of large roches moutonnees: Geografiska Annaler, v. 74A, no. 3, p.253-264.

Sugiyama, S., and Gudmundsson, G.H., 2004, Short-term variations in glacier flow controlled by subglacial water pressure at Lauteraargletscher, Bernese Alps, Switzerland: Journal of Glaciology, v. 50, no. 170, p. 353–362.

Sugiyama, S., Bauder, A., Weis, P., and Funk, M., 2007, Reversal of ice motion during the outburst of a glacier-dammed lake on Gornergletscher, Switzerland: Journal of Glaciology, v. 53, no. 181, p.172-180.

Summerfield, M.A., 1991, Global geomorphology, An introduction to the study of landforms: New York, Wiley, 537 p

Summerfield, M. A., and Kirkbride, M. P., 1992, Climate and landscape response: Nature, v. 55, p. 306.

Tangborn, W. V., 1999, A mass balance model that uses low-altitude meteorological observations and the area – altitude distribution of a glacier: Geografiska Annaler: Series A, v. 81, p.753–765.

Tomkin, J. H., and Braun, J., 2002, The influence of alpine glaciation on the relief of tectonically active mountain belts: American Journal of Science, v. 302, p. 169–190.

Tomkin, J.H., and Roe, G.H., 2007, Climate and tectonic controls on glaciated critical-taper orogens: Earth and Planetary Science Letters, v. 262, p. 385–397.

Trabant, D.C., Molnia, B.F., and Post, A., 1991, Bering Glacier, Alaska-Bed configuration and potential for calving retreat: Eos, Transactions, American Geophysical Union, Program and Abstracts, v. 72, p. 159.

Trabant, D.C., and Molnia, B.F., 1992, Ice thickness measurements of Bering Glacier, Alaska, and their relation to satellite and airborne SAR image patterns: Eos, Transactions, American Geophysical Union, v. 72, no. 44-supplement, p. 159.

Tucker, G. E., and R. L. Slingerland, 1994, Erosional dynamics, flexural isostasy, and long-lived escarpments: A numerical modeling study, Journal of Geophysical Research, v. 99, p. 12,229 –12,243.

Van der Veen, C.J., 1996, Tidewater calving: Journal of Glaciology, v. 42, no. 141, p. 375–385.

Van der Veen, C.J., 2002, Calving glaciers: Progress in Physical Geography, *v.* 26, no. 1, p. 96–122.

Vaughn, B.H., and Fountain, A. G., 2005, Stable isotopes and electrical conductivity as keys to understanding water pathways and storage in South Cascade Glacier, Washington, USA.: Annals of Glaciology, v. 40, p. 107-112

Vaughan, D.G., and Doake, C.S.M., 1996, Recent atmospheric warming and retreat of ice shelves on the Antarctic Peninsula: Nature, v. 379, p. 328-331.

Vieli, A., Funk, M., and Blatter, H., 2000, Tidewater glaciers: Frontal flow acceleration and basal sliding: Annals of Glaciology, v. 31, p. 217–221.

Vivian, R., and Bocquet, G., 1973, Subglacial cavitation phenomena under the Glacier d'Argentiere, Mont Blanc, France: Journal of Glaciology, v. 12, no. 66, p. 439–451.

Walder, J., and Hallet, B., 1979, Geometry of former subglacial water channels and cavities: Journal of Glaciology, v. 23, no. 89, p. 335-346.

Walder, J. S., 1986, Hydraulics of subglacial cavities: Journal of Glaciology, v. 32, no. 112, p. 439–445.

Warren, C.R., Rivera, A., and A. Post, 1997, Greatest Holocene advance of Glaciar Pio XI, Chilean Patagonia: Possible causes: Annals of Glaciology, v. 24, p. 11-15.

Warren, C., and Masamu, A., 1999, The calving glaciers of southern South America: Global and Planetary Change, v. 22, p. 59–77.

Weertman, J., 1964, The theory of glacier sliding: Journal of Glaciology, v. 5, no. 39, p. 287-303.

Whipple, K., Kirby, E. and S. Brocklehurst, 1999, Geomorphic limits to climatically induced increases in topographic relief, Nature, v. 401, p. 39–43.

White, J. M., Ager, T. A., Adam, D. P., Leopold, E. B., Liu, G., Jette, H., and Schweger, C. E., 1997, An 18 million year record of vegetation and climate change in northwestern Canada and Alaska: Tectonic and global climatic correlates: Palaeogeography Palaeoclimatology Palaeoecology, v. 130, no. 1-4, p. 293-306.

Wiles, G.C., and Calkin, P.E., 1994, Late-Holocene, high-resolution glacial chronologies and climate, Kenai Mountains, Alaska: Geological Society of America Bulletin, v. 106, p. 281-303.

Willenbring, J.K. and F. von Blanckenburg, 2010, Long-term stability of global erosion rates and weathering during late Cenozoic cooling, Nature, v. 465, p. 211-214.

Willett, S., Beaumont, C., and Fullsack, P., 1993, Mechanical model for the tectonics of doubly vergent compressional orogens: Geology, v. 21, p. 371–374.

Willett, S.D., 1999. Orogeny and orography: The effects of erosion on the structure of mountain belts: Journal of Geophysical Research, v. 104, no. B12, p. 28,957-28,981.

Willett, S.D., and Brandon, M.T., 2002, On steady states in mountain belts: Geology, v. 30, p. 175–178.

Willis, I.C., 1995, Intra-annual variations in glacier motion: A review: Progress in Physical Geography, v. 19, no. 1, p. 61-106.

Worthington, L. A., Gulick, S. P. S. and Pavlis, T.L., 2008, Localized deformation zones in the offshore leading edge of the Yakutat microplate, Gulf of Alaska, in Active Tectonics and Seismic Potential of Alaska, edited by J.T. Freymueller, P.J. Haeussler, R.L. Wesson, G. Ekström, Geophysical Monograph Series, Volume 179, 350 pp

Worthington, L. L., S. P. S. Gulick, and T. L. Pavlis, 2010, Coupled stratigraphic and structural evolution of a glaciated orogenic wedge, offshore St. Elias orogen, Alaska, Tectonics, v. 29, TC6013, doi: 10.1029/2010TC002723.

Zoback, M.L., Zoback, M.D., Adams, J., Assumpcao, M., Bell, S., Bergman, E.A., Bluemling, P., Denham, D., Ding, J., Fuchs, K., Gregersen, S., Gupta, H.K., Jacob, K., Knoll, P., Magee, M., Mercier, J.L., Muller, B.C., Paquin, C., Stephansson, O., Udias, A., and Xu, Z.H., 1989, Global patterns of intraplate stress: A status report on the world stress map project of the International Lithosphere Program: Nature, v. 341, p. 291–298.

Zwally, H.J., Abdalati W., Herring T., Larson K., Saba J., and Steffen K., 2002, Surface melt-induced acceleration of Greenland ice-sheet flow: Science, v. 29**7**, no. 5579, p. 218–222.

Model Variables and coefficients

a_o	Ablation at sea level (10 m.w.e./yr)
α	Dimensionless water pressure parameter (1×10^{10}-1×10^{12})
A	Arhenius flow law coefficient (5×10^{24} s^{-1}kPa^{-3})
A_s	Sliding rule coefficient
b	Specific mass balance (m.w.e./yr)
c_i	Positive degree-day coefficient for the melting of ice (0.0055 m/d ^{o}C)
c_s	Positive degree-day coefficient for the melting of snow (0.0033 m/d ^{o}C)
dP	Precipitation departure from interglacial conditions
dT	Temperature departure from interglacial condition
f	Valley shape factor
G	Water potential gradient
h_i	Ice thickness
h_w	Water depth
H	Reference maximum ice thickness
H_{ref}	Reference ice thickness
I_s	Storage capacity index
k_c	Dimensionless quarrying rate coefficient
k_i	Ice closure rate constant (1.59×10^{-25} Pa^{-3}s^{-1})
k_1	Stream power coefficient
k_2	Sediment entrainment coefficient
k_3	Calving coefficient (0.027 1/yr)
Kic	Critical crack intensity stress (1.07×10^6Pa)
κ	Ice thermal diffusivity (1.09×10^{-6} m^2/s)
l_r	Lapse rate (5.5×10^{-3} ^{o}C/m)
L	Latent heat of fusion for ice (3.34×10^5 J/kg)
n	Power flow law coefficient
N	Effective normal stress
P_i	Ice overburden pressure
P_w	Water pressure
q	Ice flux per unit width
Q_{bal}	Ice balance flux
Q_{dyn}	Ice dynamic flux
Q_{df}	Basal melt flux
Q_{gf}	Geothermal heat flux (0.05 J/m^{2}s)
Q_w	Surface melt flux
Q_{wi}	Viscous deformation water flux
ρ_t	Ice density (910 kg/m^3)
ρ_r	Rock density (2650 kg/m^3)
ρ_s	Sediment density (1700 kg/m^3)
ρ_w	Water density (1000 kg/m^3)

U_c	Calving flux (km/yr)
U_d	Deformation velocity
U_{slid}	Sliding velocity
W	Glacier width
W_{ref}	Reference glacier width